Doctoral Dissertation
Doctoral Program in Metrology (34th Cycle)

In silico models for biomedical applications of magnetic nanoparticles

By

Marta Vicentini

******

Supervisor(s):
Dr. A. Manzin, Supervisor

Doctoral Examination Committee:
Prof. M. D'Aquino, Referee, Università degli Studi di Napoli Federico II
Prof. R. Gerbaldo, Politecnico di Torino
Prof. J. Leliaert, Ghent University
Dr. W. Rocchia, Istituto Italiano di Tecnologia
Dr. N. Smith, Referee, National Physical Laboratory

Politecnico di Torino
2022

Declaration

I hereby declare that, the contents and organization of this dissertation constitute my own original work and does not compromise in any way the rights of third parties, including those relating to the security of personal data.

Marta Vicentini

2022

* This dissertation is presented in partial fulfillment of the requirements for **Ph.D. degree** in the Graduate School of Politecnico di Torino (ScuDo).

Acknowledgment

I would like to express my sincere gratitude to all the people that helped me during my Ph.D. studies. In particular, to my supervisor, Dr. Alessandra Manzin (INRiM), who gave me valuable support during these three years and provided me with a set of results from the micromagnetic modelling analysis, which increased the quality of this Thesis. To Dr. Riccardo Ferrero (INRiM) for the CAD geometries and for the results of the micromagnetic modelling analysis. To the research group of Dr. Paola Tiberto (INRiM) and Dr. Hüseyin Sözeri (TÜBİTAK) for the experimental data. To Ioannis Androulakis (Erasmus MC Cancer Institute) for providing me with the numerical simulations that were used for the validation of two in-house developed solvers that are presented in this Thesis. Moreover, the results here reported were developed in the framework of the Project 18HLT06 RaCHy that has received funding from the European Metrology Programme for Innovation and Research (EMPIR), which is co-financed by the participating states, and from the European Union's Horizon 2020 program.

Abstract

In this Thesis, we focus on the application of magnetic nanoparticles (MNPs) in magnetic hyperthermia, with the aim of presenting a modeling approach to provide information to plane and optimize *in vivo* experiments conducted on small animals. Magnetic hyperthermia is a therapeutic technique, which is generally applied as an adjuvant to standard therapies for the cure of cancer, e.g. radiotherapy or chemotherapy. With this technique, MNPs are excited by the application of an AC magnetic field (with frequency from 50 kHz to 1 MHz) to release heat in diseased regions and thus promote the damage of cancer cells, enhancing their sensitivity to standard therapies. The target temperatures should be in the range of 40-45 °C). Although promising results have been obtained in clinical trials, further research is required to optimize this therapeutic technique and acquire a deeper knowledge of its potential advantages and limitations. The main critical aspects are the capacity of guaranteeing safe levels of field exposure, the achievement of a proper MNP thermal dose, and the monitoring of temperature distribution within the tumor and the surrounding tissues.

In this context, we have developed a set of in-house numerical tools for the simulation of the heating process generated by magnetic hyperthermia (also considering side effects) and of the MNP transport in microvascular networks and their release to target tissues. For each solver, we present its implementation and the numerical validation by means of comparison to analytical solutions or solutions obtained with commercial solvers. The first solver simulates the eddy current effects induced by the exposure to low-frequency electromagnetic (EM) fields, evaluating the electric field induced in the body/domain of calculation. The second solver is based on the heat transfer equation and calculates the spatial-temporal distribution of temperature of MNP-containing samples to support thermometric measurements and the characterization of MNP heating efficiency, as a function of MNP concentration and heating time. The third solver is based on the Pennes' bioheat equation and evaluates the thermal response of living tissues as a result of blood perfusion, metabolic heat, EM field exposure (whose contribution is calculated with the EM solver), and MNP activation under AC magnetic fields. The simulations are performed on two high-resolution digital phantoms of murine models, a 28 g mouse and a 503 g rat. The last solver is based

on classical Newtonian dynamics and simulates the motion of an ensemble of spherical micro/nanoparticles circulating in a 3D reconstruction of a real blood vessel segment, under the influence of an external magnetic field.

The first three models, all based on the finite element method (FEM), enable us to test the heating efficiency of MNPs, and to select the treatment conditions to guarantee a proper temperature increase in tumor-affected regions and to avoid the appearance of hot-spots in healthy tissues. Specifically, with the EM solver and the thermal solver based on the Pennes' equation, we have investigated the effects of the only EM field exposure, in terms of specific absorption rate (SAR) and temperature increase, in relation to the field parameters (frequency and peak amplitude), the animal size, the body-field orientation (considering uniform fields), and the applicator geometry (i.e. non-uniform field distribution). Then, we have analyzed the heating effects of several MNP types as a function of diseased region type (size and position in the body), MNP concentration, and field configuration. Finally, with the last model, we have investigated the importance of magnet configuration (size and position with respect to the blood vessel geometry) and particle properties (size and magnetic moment) to properly guide particle motion towards the target regions, comparing the trajectories of three different particle types, with radius from 10 nm to 500 nm.

Contents

List of Figures

List of Tables

Chapter 1

Introduction

Nanomedicine is a branch of nanotechnology that has been emerging over the last 30 years, thanks above all to the promising results obtained in the treatment of tumors and chronic diseases [1]. In nanomedicine, nanoscale structures are employed as site- and target-specific therapeutic agents and/or diagnostic tools. The use of nanoparticles (NPs) has played a crucial role in the development of nanomedicine due to their ability to interact with biological components, thanks to their suitable sizes, and their adaptability in a wide range of biomedical applications. In particular, NPs are employed as biosensors, carriers in drug delivery and gene delivery, contrast agents in imaging, and heating agents in therapeutic hyperthermia. Other fields of application are cell labeling to track cells in living tissues or cell cultures, and bioseparation to isolate macromolecules (e.g. antibodies, DNA, RNA, and enzymes) [2-20].

NPs are particles that range in size from a few nanometers to hundreds of nanometers [21] and are typically made up of an inner core that can be functionalized by covering the surface with the most appropriate coating (e.g. biotargeting agents, antibodies, and proteins) to promote drug delivery in target tissues, or binding and interactions to biomaterials (DNA, proteins, cells), depending on the application.

In the following sections, we focus on magnetic nanoparticles (MNPs) as heating agents in magnetic hyperthermia. First, we provide a brief overview of the MNPs utilized in biomedical applications, describing the basis of MNP activation under alternating current (AC) magnetic fields and the MNP research process, from preparation to preclinical testing. The basic features of magnetic hyperthermia are then discussed, including the relevance of biophysical limits for AC magnetic field exposure, MNP heating efficiency, and the importance of achieving an appropriate thermal dose in the diseased area to treat. Particular attention is paid to the role of computational simulations as predictive tools to support preclinical tests of magnetic hyperthermia, in terms of temperature evaluation within biological media and particle targeting in microvascular networks. In the last part of the Introduction, the outline of the Thesis is presented, where we summarize the content of each Chapter.

1.1 Magnetic nanoparticles

Thanks to their magnetic properties, magnetic nanoparticles (MNPs) show the potential advantage of being manipulated by external magnetic fields. The application of an external magnetic field can be used to influence the motion and the activation of MNPs, e.g. guiding their direction to a target area of the body and inducing the release of the carried drugs in specific tissues or regions of interest. In particular, small magnetic nanoparticles with sizes lower than 20-30 nm exhibit superparamagnetic behavior (the critical size corresponding to the transition from superparamagnetism to ferromagnetism depends on the material type). This aspect finds great interest in biomedical applications due to the fact that superparamagnetic NPs do not have remanent magnetization when the applied field is turned off, maintaining their colloidal stability and avoiding unwanted clustering or aggregation processes in absence of the field [2,22].

Particular attention has been paid to iron oxide NPs, which present optimal chemical and physical properties in terms of chemical stability, good biocompatibility, almost no toxicity, and high saturation magnetization [21]. Among the iron oxides, the types mostly used in biomedical applications are maghemite (γ-Fe_2O_3) and magnetite (Fe_3O_4), because their biocompatibility is proven. However, also other MNPs, made of cobalt ferrite or zinc ferrite, have been investigated for several biomedical applications [23-25].

1.1.1 Activation of magnetic nanoparticles under AC magnetic fields

The magnetic behavior of a material placed into a magnetic field **H** is the overall response of each atomic moment inside it. This magnetic response can be described in terms of the magnetic induction **B** or of the magnetization vector **M**, as a function of **H**. The corresponding **M**-**H** curve is different for each material and depends on its composition and its physical and geometrical properties. In particular, the **M**-**H** curve has a typical shape in accordance with the magnetic behavior of the material, i.e. diamagnetic, paramagnetic and ferromagnetic. For what concerns MNPs, they present a ferromagnetic behavior that is strongly influenced by the MNP size. Particles larger than 100 nm and smaller than a few microns are considered to be multi-domain, whereas particles with a size lower than 100 nm are assumed to be single-domain. These MNPs can exhibit hysteresis, which means that the magnetization process is irreversible, and the **M-H** relationship is described by a loop with a non-negligible area, known as hysteresis loop. In Figure 1.1a we report the typical shape of the **M**-**H** curve for ferromagnetic materials, where H_C indicates the coercivity, which measures the resistance of the material to be demagnetized, M_R is the remanent magnetization, which is the remained magnetization when the applied field is zero, and M_S is the magnetic saturation that defines the asymptote that the curve approaches when it increases. The hysteresis loss, which is the energy dissipated as heat, is proportional to the area of the hysteresis loop. Smaller particles, which have a size lower than 20-30 nm (critical size depending on the material type), exhibit another

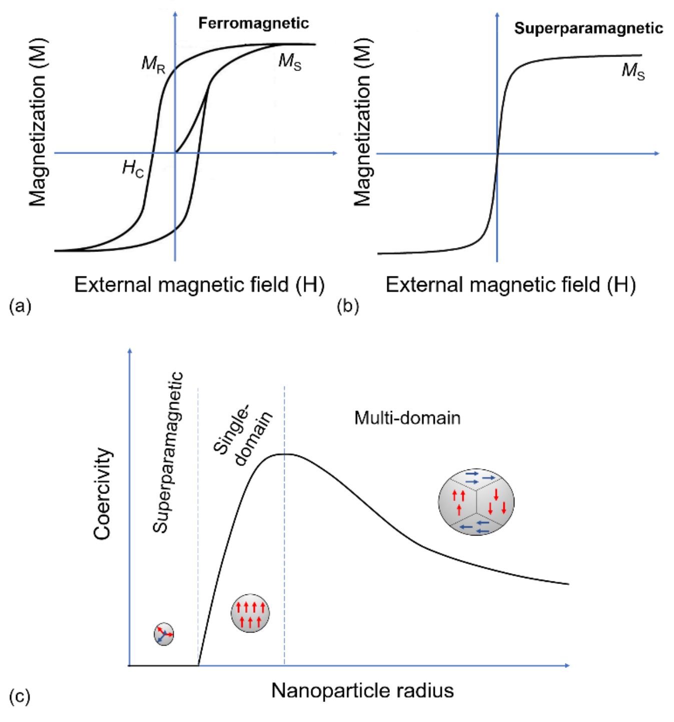

Figure 1.1. Magnetization versus applied field curves for (a) ferromagnetic nanoparticles, and (b) superparamagnetic nanoparticles, with M_S the magnetic saturation, M_R the remanent magnetization, and H_C the coercivity. (c) Transitions from superparamagnetic behavior to single domain and multi domain in relation to particle size and coercivity.

magnetic behavior that is called superparamagnetic. Superparamagnetic materials are characterized by the absence of hysteresis (the remanent magnetization is null) and magnetization randomly switches direction in response to thermal energy, also in the absence of an applied field. Figure 1.1b reports the typical **M-H** curve shape for superparamagnetic NPs, whereas Figure 1.1c shows a schematic of the transition from superparamagnetic behavior to single-domain and multi-domain in relation to NP size and coercivity.

When a magnetic material is exposed to an AC magnetic field, heat dissipation occurs via different mechanisms of energy loss: eddy current, hysteresis, Néel relaxation, and Brownian relaxation [26,27]. Eddy current effects are the dominant heating mechanisms in bulk materials and are negligible in microparticles and nanoparticles, due to their reduced dimension and low conductivity of iron oxides. The other heating mechanisms involve the alignment of the MNP magnetic moment along the direction of the AC magnetic field by the rotation of the magnetization vectors within MNPs (hysteresis and Néel relaxation) or by the mechanical rotation of the MNPs in the medium with generation of frictional losses (Brownian relaxation). The latter is typically inhibited in the tumor microenvironment, apart from small oscillations allowed by tissue elasticity.

The magnetic behavior and the consequent heating properties are strongly influenced by MNP size, with the presence of two critical dimensions, which are material dependent. The lowest critical size is associated with the transition from superparamagnetic to single-domain ferromagnetic behavior, above which the coercivity (zero for the superparamagnetic state), and thus, the hysteresis losses gradually increase reaching a maximum. This occurs in correspondence of the highest critical size, which corresponds to the transition to multi-domain ferromagnetic behavior, after which coercivity and hysteresis losses start to decrease with dimension.

The heating efficiency of MNPs is usually quantified by the specific loss power (SLP), which expresses the thermal power dissipated per unit mass of magnetic material. This parameter depends on several factors, which comprise not only the dimensional and physic-chemical properties of MNPs (composition and magnetic behavior, state of dispersion, size, and shape) but also the magnetic field exposure conditions (in particular field amplitude and frequency). To evaluate the SLP of MNPs, thermometric measurements are typically conducted, recording the temperature evolution in a sample of MNP suspension contained in a vial exposed to an AC magnetic field. Generally, the recorded data in a fixed point of the sample, which correspond to the time vs temperature exponential curve, are used to estimate the SLP according to the following equation, considering that the process is conducted under adiabatic conditions and that no changes occur within the sample, [28]

$$SLP = \frac{\Delta T}{\Delta t}\frac{C}{m_{Fe}} \tag{1.1}$$

where $\Delta T/\Delta t$ is the initial slope of the curve, C is the volumetric heat capacity of the sample and m_{Fe} is the mass of magnetic material in the sample.

The evaluation of SLP is important because a high value of SLP is necessary for efficient hyperthermia therapy, in order to reduce the injected dose of MNPs in the body and obtain a temperature increment suitable for therapeutic treatment.

1.1.2 Magnetic nanoparticles preparation and characterization

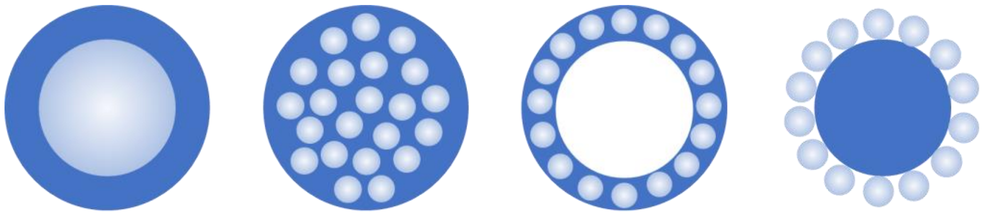

Figure 1.2. Different structures of magnetic nanoparticles. From left to right: magnetic core-polymer shell, nanoparticles homogeneously distributed in a polymer matrix, nanoparticles distributed within a ring-shape polymer shell, magnetic shell-polymer core.

For a successful application of MNPs, syntheses of stable colloidal NP suspensions are needed to guarantee MNP stability in biological media. Moreover, it is the methods of synthesis and the following functionalization that determine the physicochemical behavior of MNPs. The synthesis of MNPs for biomedical applications is in general a chemical (bottom-up) method, including co-precipitation, solvothermal, or microwave-assisted processes. As iron oxide tends to oxidize, NPs are generally coated with biocompatible shells made of diamagnetic materials, such as polymers, ceramics, or some metals [29-31]. Shells are also used to prevent aggregation phenomena between NPs and shells of noble metals, e.g. gold, are used to improve biocompatibility [32]. In addition, to enhance their magnetic properties, MNPs are also combined with magnetically susceptible elements, e.g. cobalt, nickel, and manganese [2]. Then, MNPs are functionalized, adding bioactive molecules, such as peptides and proteins. MNPs typically have a magnetic core surrounded by an inorganic shell, but different structures are possible as illustrated in Figure 1.2. For example, in some situations, it is preferred to embed small MNPs in matrices of inorganic or organic materials, e.g. a polymeric matrix. These structures, which can have a size varying from a few nanometers to a few microns, take the name of beads [25].

After the preparation, MNPs are characterized to investigate their geometrical and physical properties [33], helping in the understanding of their performances during applications. Scanning electron microscopy (SEM) and transmission electron microscopy (TEM) are commonly used to examine MNP morphology and size distribution. SQUID magnetometry and vibrating sample magnetometry (VSM) can be used to quantify the magnetization of a sample of MNPs, and thermometric or calorimetric measurements can be used to determine the heating capacity. Then, *in vitro* studies are performed to investigate the potential toxicity of MNPs and MNP-cell interactions, in terms of cell viability and proliferation [34].

1.1.3 Preclinical trials and the 3R principle

The majority of preclinical trials are conducted on rodents, especially on mice with a weight lower than 30 g. Larger animals, such as rats and rabbits, are also considered in some oncological studies because they can develop larger tumors, usually induced from human cell lines [35]. In Europe, animal studies must be conducted in compliance with the European Union (EU) legislation, which since 1986 has adopted directives to improve the protection and the welfare of animals. In September 2010, the EU adopted the Directive 2010/63/EU regarding the use of animals for scientific purposes, on the basis of the principle of the Three Rs. This principle was first described by W. M. S. Russell and R. L. Burch [36] and is based on the:

- Reduction of the number of animals used;
- Refinement of methods and procedures to minimize and avoid any source of pain and discomfort in animals;
- Replacement of animal experiments with alternative methodologies (if possible).

Examples of alternative methods that can be used to replace animal experiments are the use of organoids, which are cells growing in a 3D *in vitro* environment to form clusters that reiterate the function and structure of organs

[37], and *in silico* experiments, which are computational simulations of real experiments. The main advantages of *in silico* experiments are the repeatability of the experiments a potentially infinite number of times under the same conditions, and the possibility to study physical phenomena not easily reproducible or observable. In fact, *in silico* experiments are widely used to simulate chemical or biological processes. Moreover, *in silico* modeling approaches can be a useful tool to predict dangerous experimental conditions and subsequently avoid their occurrence, minimizing the number of animals sacrificed in preclinical tests.

1.2 Magnetic hyperthermia

Hyperthermia is a therapeutic technique applied in oncology as an adjuvant to standard therapies, such as radiotherapy or chemotherapy [38,39]. With this technique, a temperature elevation is induced in tumor areas to enhance cell sensitivity to therapies, without increasing the collateral effects due to the cytotoxicity of radio- and chemotherapies. The therapeutic temperature range is 40-45 °C [39,40] and it has to be maintained in the diseased area for a sufficient period of time (up to one hour [38,41]), in order to promote the damage of cancer cells. In particular, hyperthermia increases the immune system response, inhibits DNA repair mechanisms and cell proliferation, and induces membrane damage. The adverse impacts are reduced in healthy cells because they present less susceptibility to temperature increments [42].

Hyperthermia is classified on the basis of the heated surface area or volume: local hyperthermia (for the treatment of a small area, e.g. a not very extended tumor), regional hyperthermia (for larger areas of treatment, such as entire organs or limbs), and whole-body hyperthermia (for metastatic cancers that are hinder and spread through the body). The induced heating can be achieved in different ways, for example, hyperthermia can be induced by electromagnetic radiations, therapeutic ultrasounds, laser application, and MNPs as heat mediators. Among these modalities, magnetically mediated hyperthermia is becoming a promising candidate for hyperthermia, as it can guarantee more selective heating with reduced side effects in the surrounding tissues [40].

In magnetic hyperthermia, an AC magnetic field is applied to reorient the MNP magnetic moment in the tumor mass. The excitation induced in the MNPs leads to the generation of heat, as a result of different processes (hysteresis, Néel relaxation, Brownian relaxation) that contribute to thermal energy and that have been described in the section above. Since the applied magnetic fields generally pass harmlessly through tissues, magnetic hyperthermia is particularly suitable for the treatment of both superficial and deep cancers. Thanks to their size, MNPs can easily pass blood-brain barriers, making magnetic hyperthermia an appropriate technique for the treatment of brain tumors. Magnetic hyperthermia presents other important advantages in comparison to the types of hyperthermia mentioned earlier: MNPs can be absorbed by cancer cells and can deliver heat directly to them, and MNPs can be coated with molecules to enhance the binding with cancer cells, leading to a more selective heat deposition and a more homogeneous local temperature distribution [43].

The first application of MNPs for selective heating of tumors was attempted in 1957 by Gilchrist *et al*. [44]. In these *in vitro* studies, magnetic particles with a size ranging from 20 nm to 100 nm were used to induce heat in the lymph nodes of dogs, and a noteworthy temperature increment of about 14 °C was obtained. But only between 2003 and 2005, the first phase 1 trial was conducted at the Charité Hospital in Berlin, on 14 patients with glioblastoma multiforme, and showed the tolerability and feasibility of magnetically mediated hyperthermia with MNPs [45]. In the following years, phase 1 and phase 2 clinical studies have demonstrated the improvement of the survival time from the diagnosis of the first glioblastoma recurrence [46] and have been successfully carried out also for patients with prostate cancer [47].

Although promising results have been obtained in clinical trials, further research is required to optimize this complex therapy strategy and acquire a deeper knowledge of the potential aspects and limitations of magnetic hyperthermia treatments. Regarding the type of MNPs used for magnetic hyperthermia preclinical tests, the most used are coated superparamagnetic iron oxide nanoparticles (SPIONs), because they are currently approved for some biomedical treatments, e.g. as contrast agents in MRI [48]. At present, only in Europe there are commercially available SPIONs that are clinically approved for magnetic hyperthermia, the ferrofluid NanoTherm®. This ferrofluid consists of NPs with an average diameter of 15 nm dispersed in a water-based solution and is manufactured by MagForce (MagForce® Nanotechnologies AG, Berlin) [49]. SPIONs present important properties, such as a weak tendency to agglomeration and good biocompatibility, but at the same time they have limited heating efficiency. For this reason, different MNPs are being studied to improve the heating efficiency and reduce the required dosage, above all the interest is focused on MNPs composed of materials with higher saturation magnetization or with different nanostructure geometry, in order to enhance hysteresis losses. Examples of promising studies are: cobalt ferrite nanoparticles [50,51], iron oxide nano-octopods [52], nanorods [53], iron oxide nanoflowers [54].

In biomedical applications, the role of additional parameters has to be in-depth investigated, such as the cytotoxicity mechanisms and the effects of MNP interactions with biological media and cells on the heating efficiency of the MNPs [55]. Other critical aspects of *in vivo* applications that need further research and that we will discuss in the following sections are:

- the optimization of AC magnetic field application and the capacity of guaranteeing a safe level of field exposure;
- the achievement of an optimal MNP thermal dose in tumors;
- the monitoring of temperature increase due to MNP excitation;
- the monitoring of MNPs distribution within the tumor and the surrounding tissues, after injection.

1.2.1 Magnetic field exposure

The applied AC magnetic fields have a frequency that typically varies from 50 kHz to 1 MHz. A careful selection of field peak amplitude and frequency is needed to guarantee an optimal activation of MNPs and a safe level of patient exposure to AC magnetic fields. Even in the absence of injected MNPs, the only exposure to fields EM with large frequency and/or amplitude can induce excessive thermal responses within the patient body, such as hotspots, as a result of the heat produced by the induced eddy currents, and can result in burns, discomfort, or pain. In fact, tissues are largely composed of diamagnetic components and magnetic effects on them are in general negligible. However, the application of electromagnetic (EM) fields can generate eddy currents in any conducting media. The eddy currents rise radially with respect to the direction of the applied field and are subject to losses that are maximum in the peripheral body regions. Considering a cylindrical volume totally placed inside a uniform AC magnetic field applied along its longitudinal axis, the rate of heat production can be expressed by the specific heating power due to the induced eddy currents [56]

$$P = \sigma\left(\pi\mu_0\right)^2\left(\hat{H}_{\mathrm{a}} \times f\right)^2 r^2 \tag{1.2}$$

where σ is the electrical conductivity of the cylindrical sample exposed to the electromagnetic (EM) field, μ_0 is the magnetic permeability of the vacuum, $\hat{H}_a$ is the peak amplitude of the AC magnetic field, f is its frequency and r is the distance from the axis of the cylinder. From Equation 1.2, it can be seen that eddy current heating is directly proportional to the square of the product $\hat{H}_a \times f$ and the square of the distance. In particular, the equation explains how significant heating can occur in peripheral areas of large bodies, also when the product $\hat{H}_a \times f$ is limited [56]; but at the same time a higher value of $\hat{H}_a \times f$ can be applied if the size of the region to be treated is small.

To reduce side effects as much as possible, a first biophysical constraint has been proposed on the AC magnetic field exposure in 1984, imposing a threshold on the product $\hat{H}_a \times f$. This limitation, known as the Atkinson-Brezovich limit, suggests that the product of the field frequency f and the peak amplitude $\hat{H}_a$ should not exceed the value of $4.85 \cdot 10^8$ A/(m·s) [56]. The acquisition of this value was obtained by conducting experiments where volunteers were exposed to an AC magnetic field generated by a single-turn coil with a diameter of 30 cm, which surrounded their thorax. The field amplitude and frequency were increased until they were tolerated for more than 1 hour without significant discomfort. Subsequently, in 2007 Hergt and Dutz introduced a less rigid limit that was determined considering a frequency range of 100-500 kHz and an EM field exposure of body parts (e.g. limbs) less large than the thorax. This criterion, which is the result of extended theoretical calculations, recommends a field exposure with $\hat{H}_a \times f < 5 \cdot 10^9$ A/(m·s) [57]. Since MNPs have a heating efficiency that depends on the values of $\hat{H}_a$ and f [27], a careful choice of field parameters is necessary to guarantee efficient heating while respecting these limits. In particular, when hysteresis heating is dominant, it is critical to predict the minimum field required to achieve the irreversible jumps of the hysteresis loop, in order to generate a suitably large area of the loop and hence achieve a good heating efficiency, but this limits the selection of the applicable frequency. The selection of field frequency and amplitude should also be done in accordance with the type of EM field applicators. The applicator geometry and positioning, with respect to the target region, should be optimized to generate fields that are primarily focused on the diseased area and have negligible exposure to the surrounding healthy tissues, thus leading to safer treatment conditions. Although the above limitations are fulfilled in the few studies conducted on human patients [45-47], there are many preclinical tests on animals that exceed even the Herg-Dutz criterion [55, 58-71], as listed in Table 1.1, raising questions on the preservation of animal welfare. The reported studies are mainly conducted on mice that are totally placed inside solenoids and have a heating time that does not exceed 1 hour of field application.

Table 1.1. Preclinical studies of magnetic hyperthermia exceeding the limit of Hergt-Dutz.

Ref.	Animal model	Tumor size (location)	Applicator and exposure type	$\hat{H}_a \times f$ [A/(m·s)]	Heating time (min)
[61]	Athymic nude mouse	100-250 mm^3 (backside area)	Helical coil (backside external exposure)	$6.7 \cdot 10^9$	60
[62]	Athymic nude mouse	200 mm^3 (backside area)	Helical coil (backside external exposure)	$6.7 \cdot 10^9$	60
[63]	Athymic nude mouse (~30 g)	200 mm^3 (flank area)	Helmholtz coil (body inside)	$6.7 \cdot 10^9$	5
[64]	Athymic nude mouse (~30 g)	500 mm^3 (flank area)	Helmholtz coil (body inside)	$6.7 \cdot 10^9$	30
[65]	Athymic nude mouse (~20 g)	125 mm^3 (flank area)	Helmholtz coil (body inside)	$6.7 \cdot 10^9$	30
[66]	BALB/c nude mouse (~29-32 g)	100-150 mm^3 (flank area)	Helical coil (body inside)	$7.6 \cdot 10^9$	25
[67]	HSP70-LucF transgenic mouse (~20 g)	N/A (back area)	Helical coil (body inside)	$7.7 \cdot 10^9$	10
[68]	Mouse	21-30 mm^3 (femoral area)	Helical coil (body inside)	$8.2 \cdot 10^9$	30
[69]	C3H/HeJ mouse	220±40 mm^3 (breast)	Helical coil (body inside)	$8.4 \cdot 10^9$	15
[70]	BALB/c nude mouse (~18 g)	60 mm^3 (breast)	Helical coil (body inside)	$8.4 \cdot 10^9$	8
[71]	Nude mouse (~26 g)	50 mm^3 (flank area)	Helical coil (posterior half inside)	$11.3 \cdot 10^9$	30
[72]	SCID Mouse (~18-19 g)	200 mm^3 (flank area)	N/A	$11.6 \cdot 10^9$	10
[73]	BALB/c nude mouse (~20 g)	100 mm^3 (abdomen)	Helical coil (body inside)	$18.7 \cdot 10^9$	10
[74]	Rat (~250-270 g)	0.41 (±0.22) mm^3 0.46 (±0.19) (liver)	Helical coil (body inside)	$8.5 \cdot 10^9$	>21

Other important constraints for human exposure to radiofrequency EM fields to mention are reported in the guidelines of the International Commission on Nonionizing Radiation Protection (ICNIRP) [72]. The guidelines establish exposure limits based on a large number of studies, comprising recently published papers, research results reviewed by the World Health Organization (WHO), and the reports of the Scientific Committee on Emerging and Newly Identified Health Risks (SCENIHR) and of the Swedish Radiation Safety Authority (SSM). In particular, ICNIRP suggests limitations to the specific absorption rate (SAR), which expresses the power absorbed per unit of mass by a body exposed to EM fields,

$$\mathrm{SAR} = \frac{1}{V}\int_{\Omega} \frac{\sigma|\mathbf{E}|^2}{2\rho} dv \tag{1.3}$$

where V is the volume of the body, Ω is the domain occupied by the body, $\mathbf{E}$ is the induced electric field vector and ρ is the density of the tissue. The guidelines consider two different types of exposure scenarios: occupational exposure and general public exposure. As written in [72], *"occupationally-exposed individuals are defined as adults who are exposed under controlled conditions associated with their occupational duties, trained to be aware of potential radiofrequency EMF [i.e. electromagnetic field] risks and to employ appropriate harm-mitigation measures"*; whereas the *"general public is defined as individuals of all ages and of differing health statuses, which includes more vulnerable groups or individuals, and who may have no knowledge of or control over their exposure to EMFs"*. Exposure to EM fields with frequencies between 100 kHz and 300 GHz is considered, taking into account results from in vivo experiments conducted on both animals (the majority) and humans. According to the ICNIRP guidelines, in animals, harm was only found under conditions of exposure characterized by a whole-body average SAR substantially higher than 4 W/kg; this value is considered the threshold below which adverse effects would not be expected. Consequently, for human exposure, a precautionary threshold for the whole-body SAR is set at 0.4 W/kg for the occupational scenario, and at 0.08 W/kg for the general public scenario (applying a reduction factor of 50), in order to avoid any potential risk. These limitations guarantee a safe field exposure with a large margin of safety and mainly refer to general applications of EM fields and have no medical purposes. However, these SAR thresholds can be considered as a starting point to avoid any possible health effects due to field exposure. In particular, SAR limitations could be useful in medical applications such as magnetic hyperthermia, where the AC magnetic field should be exploited only to activate MNPs and not to increase tissue temperature through electromagnetic induction phenomena. Moreover, in biomedical treatments, SAR thresholds could be relaxed to enhance therapeutic results [73], after a careful analysis of potential harm and benefits, especially if the patients present metallic implants that can perturb the EM fields.

The biophysical constraints put in evidence the importance of a priori analysis of the EM field exposure to select the field parameters, i.e. frequency and amplitude, that can avoid eddy current effects and that can properly activate MNPs at the same time. In this Thesis, the eddy current effects produced in biological tissues during AC magnetic field application are evaluated by solving a low-frequency EM field problem [74], in order to calculate the electric field induced within an exposed body. The developed model, which will be described in detail in the following Chapter, is employed to calculate the whole-body SAR and the heating power produced by the applied field on computational anatomical phantoms of murine models.

1.2.2 AC magnetic field applicators

AC magnetic fields are generated by means of inductive coils, however there are currently no standards for the manufacturing of field applicator setup for *in vivo* and *in vitro* magnetic hyperthermia applications. The unique commercially available magnetic field applicator for humans is the MFH300F system that was fabricated by MagForce® [49] specially for the trials conducted at the Charité Medical School in Berlin, and it has the potential to be used for tumors in all parts of the body [45-47]. The system generates AC magnetic fields with a fixed frequency of 100 kHz and a field amplitude that can vary up to18 kA/m and is designed for the use of the NanoTherm® fluid. The phase 1 and phase 2 trials conducted with the MagForce® system [45-47] have proved the validity of the Atkinson-Brezovich and Hergt-Dutz limits in terms of tolerable field parameters. In fact, in the studies on glioblastoma [45] patients tolerated fields with a value of $\hat{H}_a \times f$ lower than $1.35 \cdot 10^9$ A/(m·s), with a median value of $8.5 \cdot 10^8$ A/(m·s). In patients with prostate cancer [47] the tolerable fields correspond to values of $\hat{H}_a \times f$ lower than $5 \cdot 10^8$ A/(m·s), because beyond this threshold they presented discomfort in the perineal region, which has a large exposure area with respect to the head and this clarifies the lower value of tolerable fields, in accordance to Equation 1.2.

Commercial applicators fabricated for preclinical trials are also available and are customized especially for small animals, such as mice. An example is nB nanoscale Biomagnetics [75], which provides applicators for *in vivo* applications with a working frequency range from 100 kHz to 800 kHz and furthermore it manufactures tools for magnetic characterization. Most of the provided setups have single- or multi-solenoid coils (diameter up to 48 mm) where mice can be placed inside. Pancake coils are also available but are provided for cell culture experiments. However, many research groups build their own setups in order to better adapt the applicators to the animal body and tumor location. The most commonly used are simple helical coils, Helmholtz type coils, and pancake coils, which are typically placed in the closest proximity of the tumor site or totally surround the animal body [75-79].

1.2.3 Thermal dose and temperature distribution

The achievement of an optimal thermal dose within the treated tumor has a key role in the efficiency of the treatment. The enhancement of radio- and chemo-therapy induced by magnetic hyperthermia depends on several thermometric parameters that could be used as predictors of tumor response [80]. These comprise the temperature reached during hyperthermia sessions (e.g. in terms of maximum, minimum, and average temperature within the treated volume), the time interval of heating, the number of sessions, and the time interval between consecutive sessions [80-82]. It is proven that also the temperatures achieved in a certain percentage of the target tumor volume (e.g. 10%, 50%, or 90%) might be useful metrics of tumor response and hyperthermia efficiency [83].

A critical aspect is that thermal response depends on the physical properties of tissues and the body's physiological response, and is complex to predict. In hyperthermia sessions, temperature monitoring is needed to control if the temperature reaches the therapeutic temperature range in the treated area and if does not achieve dangerous high values. Temperature evolution can be monitored by thermal cameras in the case of very superficial tumors, otherwise fiber optic temperature probes are usually inserted inside the tumor to record temperature, but this type of measurement is invasive and can measure temperature at discrete points only. For this reason, bioheat transfer numerical models are developed to estimate the temperature increase within the diseased areas. Many models are based on the solution of the Pennes' bioheat transfer equation [84], which takes into account the heat generated by the metabolic processes, the heat exchange between blood flow and solid tissues, and the heat exchange between the skin and the environment. In this Thesis, we will describe in Chapter 4 a thermal model based on the Pennes' equation that considers the heat due to an external source defined by an applied EM field, and the heat released by MNPs administered to the body and excited by the field. Through this model, the temperature increase is estimated inside the whole body, not only in the diseased area but also in the surrounding healthy tissues, to study the effects of heating within all tissues and avoid the possible unwanted formation of hotspots in parts of the body far from the malignant area. The model is first used to establish the eddy current effects due to the only EM field exposure, in terms of the thermal response of tissues, to assess safe exposure conditions. Then, it is used to evaluate the heating efficiency of different MNPs.

1.3 Particle transport

In *in vivo* applications of MNPs, but of NPs in general, the control of particle transport from injection to release is a challenging task. The distribution of MNPs within the tumor has a significant impact on the success of magnetic hyperthermia treatments. Guaranteeing a homogenous distribution of MNPs inside the tumor with a concentration sufficiently high to maximize the thermal response, is nontrivial. The MNP diffusion is determined by a plethora of complex phenomena not directly manipulable. For hyperthermia treatments, MNPs are usually injected directly into the tumor; in this way, a larger NP concentration can be guaranteed in the diseased area. Whereas intravenous injections are employed mainly for systemic drug delivery or to reach regions not otherwise achievable with a local administration. After the injection, most of the NPs could not reach or stay in the tumor and could be captured by the mononuclear phagocyte system or accumulate in healthy tissues (in general in the liver and spleen) [85,86]. For this reason, the knowledge and prediction of the NP motion within the microvascular network of the tumor or other target areas are crucial aspects. NP distribution can be monitored with imaging techniques, such as *in vivo* optical imaging, magnetic resonance imaging, and magnetic particle imaging (which is an emerging and promising modality) [87,88].

1.3.1 MNP targeting

An external magnetic field can manipulate MNPs circulation in blood flow influencing the motion and activities of the particles, such as immobilizing them, controlling their direction towards a specific area of the body, and activating the release of carried drugs in a precise region of the body. The magnetic fields are generated by means of a magnetic source, such as electromagnets, single permanent magnets, permanent magnet arrays, and combinations of permanent magnets and electromagnets [89]. Permanent magnets are the most used and are typically placed externally to the body, in proximity to the target region, or internally under the skin. The magnetic force exercised by the magnets on the single MNPs could result in minimal, in the range of piconewtons or less, and rapidly decay over the increase of the distance between the magnet and the MNP location [90]. To influence the MNP motion and promote MNP accumulation within the target site, the magnetic force has to overcome the drag force, due to blood flow, that tends to sweep MNPs away. Moreover, the magnetic field has to be focused on the region of interest only, in order to not accumulate MNPs or induce drug release in healthy tissues. For this reason, the choice of magnet geometry and positioning is critical and is strictly related to the location of the target site and the strength of the blood flow (which depends on the vessel type). Particular attention must be focused on the MNP interactions, because even if MNPs are designed to minimize agglomeration, some degree of accumulation could occur and help the increase of the magnetic force, with is directly proportional to particle volume, but at the same time the MNP concentration must not be sufficiently high, in order to avoid obstructions within blood vessels. Besides these aspects, MNPs trajectory is also influenced by the interactions between nearby MNPs (e.g. magnetic dipolar interaction and steric repulsion due to the MNP surface coating layer), and the interactions with the vessel epithelium that bring to adhesion or collision processes, making the prediction of MNP motion even more difficult.

1.3.2 Numerical models for particle transports

Regarding the prediction of MNP transport in carrier fluids, *in silico* models represent essential tools for the understanding of NP motion within the circulatory system and extravasation processes. Two main numerical approaches can be used to simulate particle motion [91]:

- models based on a drift-diffusion equation for the evaluation of particle volume concentration,
- models based on the classical Newtonian dynamics to calculate the trajectory of individual NPs.

The second one is the approach used in this Thesis to analyze MNP transport mediated by the application of an external magnetic field generated by a permanent magnet. With the models, a parametric analysis can be done to elucidate the influence of NP properties (size and particle-particle interaction), blood flux, and geometrical structure of blood vessels. When MNPs are employed, other important aspects to study are the MNP magnetic behavior, and the spatial distribution of the applied magnetic field, in order to support and optimize both MNP properties and configuration of field sources.

1.4 Outline of the Thesis

This Thesis was carried out at the Istituto Nazionale di Ricerca Metrologica (INRiM) in Torino, in the framework of the 18HLT06 RaCHy Joint Research Project, which received funding from the European Metrology Programme for Innovation and Research (EMPIR) program (co-financed by the Participating States), and from the European Union's Horizon 2020 Research and Innovation Program. The objective of the Thesis is the development of modeling approaches to study magnetic hyperthermia and its effects on biological media. The focus is the implementation of *in silico* models to mimic *in vivo* experiments and in particular to

- simulate the heating process generated by magnetic hyperthermia in living tissues and possible adverse effects;
- simulate MNP transport in microvascular networks and release to target tissues.

All simulations are performed by means of in-house codes that have been implemented in MATLAB®. The main part of the Thesis is devoted to the study of the thermal response of biological media due to MNP activation under AC magnetic field exposure, whereas the last chapters concern the problem of MNP transport in blood vessels. Chapters 2, 3, 4, and 8 present the implementation of the developed numerical models, and the simulations obtained with the models are presented in Chapters 5, 6, 7, and 9. In the following, we present the contents of the chapters in more detail.

In Chapter 1, we have described the main characteristics of MNPs and we have given an overview of the challenging aspects that magnetic hyperthermia treatments present.

In Chapter 2, we introduce the low-frequency EM field problem that models the electric field induced by low-frequency magnetic fields in living tissues. Then, we describe the numerical implementation of the problem through the finite element method (FEM). Finally, we compare the results obtained with our developed model, an analytical solution, and the results of the software Sim4Life®, in the case of simple domain geometries.

In Chapter 3, first we introduce the transient problem of heat transfer, which is used to reproduce thermometric measurements of MNP heating efficiency in vials containing MNP suspensions exposed to EM fields. Second, we describe how we implement FEM for the spatial discretization of the problem and how we apply the θ-method for the time integration. The obtained numerical model is validated by comparison to the results obtained by means of the MATLAB®'s Partial Differential Equation Toolbox, for the same geometry that reconstructs an Eppendorf test tube containing a water-based suspension of MNPs.

In Chapter 4, we introduce the Pennes' bioheat transfer equation that describes the temperature distribution within living tissues. In analogy to Chapter 3, we show how we implement FEM and θ-method for this transient problem. Then, we compare the results obtained with our solver with the solutions obtained with Sim4Life in a simplified geometry. Finally, we describe the two computational anatomical animal models and the tissue parameter database that are used in this Thesis to mimic magnetic hyperthermia preclinical tests on animals.

In Chapter 5, we present the numerical simulations obtained with the numerical solver described in Chapter 3. First, we simulate the spatial-temporal temperature distribution of magnetic nanodisk suspensions contained in a polypropylene vial, varying MNP concentration, heat transfer coefficient, and media. Then, we described how the model has been used to support thermometric measurements through comparison to experimental data.

In Chapter 6, we present the numerical results obtained on the two animal models where we evaluate the possible eddy current effects due to the only exposure to EM fields. We calculate the whole-body SAR and the temperature increments for the two models for different EM field exposure. First, we assume a uniform field distribution within the whole body, varying field parameters (amplitude and frequency), and field orientation with respect to the body. Then, we evaluate the effects of non-uniform field distributions generated by EM applicators with different sizes and geometrical structures.

In Chapter 7, we present the numerical results obtained by applying the model, described in Chapter 2 and 4, to the computational animal models to evaluate the heating efficiency of different types of MNPs, calculating the spatial-temporal distribution of temperature within the entire animal body. We analyze several parameters: dose of MNPs, target region size and location, thermal properties of the target tissue, field amplitude and distribution, and MNP distribution within the diseased volume.

In Chapter 8, we describe the physical model considered for the simulation of MNP and magnetic bead transport in viscous media magnetically manipulated by an external permanent magnet.

In Chapter 9, we present the simulations of MNP and magnetic bead transport performed in a 3D reconstruction of a segment of a real blood vessel network. We compare the transport of different magnetic particles (from 20 nm sized MNPs to micrometer magnetic beads) to analyze the influence of particle size and magnetic properties.

1.5 References

[1] J. K. Patra *et al.*, “Nano based drug delivery systems: recent developments and future prospects,” Journal of Nanobiotechnology, *J. Nanobiotechnology*, vol. 16, no. 1, p. 71, 2018. DOI: 10.1186/s12951-018-0392-8.

[2] M. Colombo *et al.*, “Biological applications of magnetic nanoparticles,” *Chem. Soc. Rev.*, vol. 41, no. 11, pp. 4306–4334, 2012. DOI: 10.1039/C2CS15337H.

[3] J. Estelrich, M. J. Sánchez-Martín, and M. A. Busquets, “Nanoparticles in magnetic resonance imaging: from simple to dual contrast agents,” *Int. J. Nanomedicine*, vol. 10, pp. 1727–1741, 2015. DOI: 10.2147/IJN.S76501.

[4] Y. Zhang *et al.*, “Synthesis of PVP-coated ultra-small Fe3O4 nanoparticles as a MRI contrast agent,” *J. Mater. Sci. Mater. Med.*, vol. 21, no. 4, pp. 1205–1210, 2010. DOI: 10.1007/s10856-009-3881-3.

[5] J. H. Maeng *et al.*, “Multifunctional doxorubicin loaded superparamagnetic iron oxide nanoparticles for chemotherapy and magnetic resonance imaging in liver cancer,” *Biomaterials*, vol. 31, no. 18, pp. 4995–5006, 2010. DOI: 10.1016/j.biomaterials.2010.02.068.

[6] S. Mohammadi-Samani, R. Miri, M. Salmanpour, N. Khalighian, S. Sotoudeh, and N. Erfani, “Preparation and assessment of chitosan-coated superparamagnetic Fe3O4 nanoparticles for controlled delivery of methotrexate,” *Res. Pharm. Sci.*, vol. 8, no. 1, pp. 25–33, 2013.

[7] P. Sharma, S. Rana, K. C. Barick, C. Kumar, H. G. Salunke, and P. A. Hassan, “Biocompatible phosphate anchored Fe3O4 nanocarriers for drug delivery and

hyperthermia," *New J Chem*, vol. 38, no. 11, pp. 5500–5508, 2014. DOI: 10.1039/C4NJ01431F.

[8] Y. Ding *et al.*, "Design and construction of polymerized-chitosan coated Fe3O4 magnetic nanoparticles and its application for hydrophobic drug delivery," *Mater. Sci. Eng. C Mater. Biol. Appl.*, vol. 48, pp. 487–498, 2015. DOI: 10.1016/j.msec.2014.12.036.

[9] Z. Bakhtiary, A. A. Saei, M. J. Hajipour, M. Raoufi, O. Vermesh, and M. Mahmoudi, "Targeted superparamagnetic iron oxide nanoparticles for early detection of cancer: Possibilities and challenges," *Nanomedicine*, vol. 12, no. 2, pp. 287–307, 2016. DOI: 10.1016/j.nano.2015.10.019.

[10] S. Senapati, A. K. Mahanta, S. Kumar, and P. Maiti, "Controlled drug delivery vehicles for cancer treatment and their performance," *Signal Transduct. Target. Ther.*, vol. 3, no. 1, pp. 1–19, 2018.

[11] A. Bhirde, J. Xie, M. Swierczewska, and X. Chen, "Nanoparticles for cell labeling," *Nanoscale*, vol. 3, no. 1, pp. 142–153, 2011.

[12] O. Betzer *et al.*, "In-vitro optimization of nanoparticle-cell labeling protocols for in-vivo cell tracking applications," *Sci. Rep.*, vol. 5, no. 1, p. 15400, 2015.

[13] Z. Farka, T. Juřík, D. Kovář, L. Trnková, and P. Skládal, "Nanoparticle-based immunochemical biosensors and assays: Recent advances and challenges," *Chem. Rev.*, vol. 117, no. 15, pp. 9973–10042, 2017. DOI: 10.1021/acs.chemrev.7b00037.

[14] H. Malekzad, P. S. Zangabad, H. Mirshekari, M. Karimi, and M. R. Hamblin, "Noble metal nanoparticles in biosensors: recent studies and applications," *Nanotechnol. Rev.*, vol. 6, no. 3, pp. 301–329, 2017. DOI: 10.1515/ntrev-2016-0014.

[15] V. Vijayanathan, T. Thomas, and T. J. Thomas, "DNA nanoparticles and development of DNA delivery vehicles for gene therapy," *Biochemistry*, vol. 41, no. 48, pp. 14085–14094, 2002. DOI: 10.1021/bi0203987.

[16] R. Rai, S. Alwani, and I. Badea, "Polymeric nanoparticles in gene therapy: New avenues of design and optimization for delivery applications," *Polymers (Basel)*, vol. 11, no. 4, p. 745, 2019. DOI: 10.3390/polym11040745.

[17] Z. W. Tay *et al.*, "Magnetic Particle Imaging: An emerging modality with prospects in diagnosis, targeting and therapy of cancer," *Cancers (Basel)*, vol. 13, no. 21, p. 5285, 2021. DOI: 10.3390/cancers13215285.

[18] A. J. Giustini, A. A. Petryk, S. M. Cassim, J. A. Tate, I. Baker, and P. J. Hoopes, "Magnetic nanoparticle hyperthermia in cancer treatment," *Nano Life*, vol. 1, no. 1n02, pp. 17–32, 2010. DOI: 10.1142/S1793984410000067.

[19] B. Thiesen and A. Jordan, "Clinical applications of magnetic nanoparticles for hyperthermia," *Int. J. Hyperthermia*, vol. 24, no. 6, pp. 467–474, 2008. DOI: 10.1080/02656730802104757.

[20] M. Bañobre-López, A. Teijeiro, and J. Rivas, "Magnetic nanoparticle-based hyperthermia for cancer treatment," *Rep. Pract. Oncol. Radiother.*, vol. 18, no. 6, pp. 397–400, 2013. DOI: 10.1016/j.rpor.2013.09.011.

[21] K. McNamara and S. A. M. Tofail, "Nanoparticles in biomedical applications," *Adv. Phys. X.*, vol. 2, no. 1, pp. 54–88, 2017. DOI: 10.1080/23746149.2016.1254570.

[22] K. L. McNerny, Y. Kim, D. E. Laughlin, and M. E. McHenry, "Chemical synthesis of monodisperse γ-Fe–Ni magnetic nanoparticles with tunable Curie temperatures for self-regulated hyperthermia," *J. Appl. Phys.*, vol. 107, no. 9, p. 09A312, 2010. DOI: 10.1063/1.3348738.

[23] H. M. Joshi *et al.*, "Effects of shape and size of cobalt ferrite nanostructures on their MRI contrast and thermal activation," *J. Phys. Chem. C Nanomater. Interfaces*, vol. 113, no. 41, pp. 17761–17767, 2009. DOI: 10.1021/jp905776g.

[24] L. An *et al.*, "Dextran-coated superparamagnetic amorphous Fe–Co nanoalloy for magnetic resonance imaging applications," *Mater. Res. Bull.*, vol. 49, pp. 285–290, 2014. DOI: 10.1016/j.materresbull.2013.09.004.

[25] O. Philippova, A. Barabanova, V. Molchanov, and A. Khokhlov, "Magnetic polymer beads: Recent trends and developments in synthetic design and applications," *Eur. Polym. J.*, vol. 47, no. 4, pp. 542–559, 2011.DOI: 10.1016/j.eurpolymj.2010.11.006.

[26] A. G. Kolhatkar, A. C. Jamison, D. Litvinov, R. C. Willson, and T. R. Lee, “Tuning the magnetic properties of nanoparticles,” *Int. J. Mol. Sci.*, vol. 14, no. 8, pp. 15977–16009, 2013. DOI: 10.3390/ijms140815977.

[27] Q. A. Pankhurst, J. Connolly, S. K. Jones, and J. Dobson, “Applications of magnetic nanoparticles in biomedicine,” *J. Phys. D Appl. Phys.*, vol. 36, no. 13, pp. R167–R181, 2003. DOI: 10.1088/0022-3727/36/13/201.

[28] X. Liu et al., “Comprehensive understanding of magnetic hyperthermia for improving antitumor therapeutic efficacy,” *Theranostics*, vol. 10, no. 8, pp. 3793–3815, 2020. DOI: 10.7150/thno.40805.

[29] D. Valdeperez *et al.*, “Polymer-coated nanoparticles: Carrier platforms for hydrophobic water- and air-sensitive metallo-organic compounds,” *Pharmacol. Res.*, vol. 117, pp. 261–266, 2017. DOI: 10.1016/j.phrs.2016.12.034.

[30] E. S. D. T. de Mendonça et al., “Effects of silica coating on the magnetic properties of magnetite nanoparticles,” *Surf. Interfaces*, vol. 14, pp. 34–43, 2019. DOI: 10.1016/j.surfin.2018.11.005.

[31] G. Barrera *et al.*, “Surface modification and cellular uptake evaluation of Au-coated Ni80Fe20 nanodiscs for biomedical applications,” *Interface Focus*, vol. 6, no. 6, p. 20160052, 2016.

[32] S. Sabale, P. Kandesar, V. Jadhav, R. Komorek, R. K. Motkuri, and X.-Y. Yu, “Recent developments in the synthesis, properties, and biomedical applications of core/shell superparamagnetic iron oxide nanoparticles with gold,” *Biomater. Sci.*, vol. 5, no. 11, pp. 2212–2225, 2017. DOI: 10.1039/C7BM00723J.

[33] M. Faraji, Y. Yamini, and M. Rezaee, “Magnetic nanoparticles: Synthesis, stabilization, functionalization, characterization, and applications,” *J. Iran. Chem. Soc.*, vol. 7, no. 1, pp. 1–37, 2010. DOI: 10.1007/BF03245856.

[34] S. V. Spirou *et al.*, “Recommendations for in vitro and in vivo testing of magnetic nanoparticle hyperthermia combined with radiation therapy,” *Nanomaterials (Basel)*, vol. 8, no. 5, 2018. DOI: 10.3390/nano8050306.

[35] V. Vilas-Boas, F. Carvalho, and B. Espiña, “Magnetic hyperthermia for cancer treatment: Main parameters affecting the outcome of in vitro and in vivo

studies," *Molecules*, vol. 25, no. 12, p. 2874, 2020. DOI: 10.3390/molecules25122874.

[36] W.M.S Russell, and R.L Burch, "The principles of humane experimental technique," *Med. J. Aust.*, vol. 1, no. 13, pp. 500–500, 1960. DOI: 10.5694/j.1326-5377.1960.tb73127.x.

[37] C. Corrò, L. Novellasdemunt, and V. S. W. Li, "A brief history of organoids," *Am. J. Physiol. Cell Physiol.*, vol. 319, no. 1, pp. C151–C165, 2020. DOI: 10.1152/ajpcell.00120.2020.

[38] Z. Behrouzkia, Z. Joveini, B. Keshavarzi, N. Eyvazzadeh, and R. Z. Aghdam, "Hyperthermia: How can it be used?," *Oman Med. J.*, vol. 31, no. 2, pp. 89–97, 2016. DOI: 10.5001/omj.2016.19.

[39] N. R. Datta *et al.*, "Local hyperthermia combined with radiotherapy and-/or chemotherapy: recent advances and promises for the future," *Cancer Treat. Rev.*, vol. 41, no. 9, pp. 742–753, 2015. DOI: 10.1016/j.ctrv.2015.05.009.

[40] S. Jha, P. K. Sharma, and R. Malviya, "Hyperthermia: Role and risk factor for cancer treatment," *Achiev. Life Sci.*, vol. 10, no. 2, pp. 161–167, 2016. DOI: 10.1016/j.als.2016.11.004.

[41] J. Crezee, N. A. P. Franken, and A. L. Oei, "Hyperthermia-based anti-cancer treatments," *Cancers (Basel)*, vol. 13, no. 6, p. 1240, 2021. DOI: 10.3390/cancers13061240.

[42] A. LeBrun, T. Joglekar, C. Bieberich, R. Ma, and L. Zhu, "Identification of infusion strategy for achieving repeatable nanoparticle distribution and quantification of thermal dosage using micro-CT Hounsfield unit in magnetic nanoparticle hyperthermia," *Int. J. Hyperthermia*, vol. 32, no. 2, pp. 132–143, 2016. DOI: 10.3109/02656736.2015.1119316.

[43] C. S. S. R. Kumar and F. Mohammad, "Magnetic nanomaterials for hyperthermia-based therapy and controlled drug delivery," *Adv. Drug Deliv. Rev.*, vol. 63, no. 9, pp. 789–808, 2011. DOI: 10.1016/j.addr.2011.03.008.

[44] R. K. Gilchrist, R. Medal, W. D. Shorey, R. C. Hanselman, J. C. Parrott, and C. B. Taylor, "Selective inductive heating of lymph nodes," *Ann. Surg.*, vol. 146, no. 4, pp. 596–606, 1957. DOI: 10.1097/00000658-195710000-00007.

[45] M. Johannsen *et al.*, “Clinical hyperthermia of prostate cancer using magnetic nanoparticles: presentation of a new interstitial technique,” *Int. J. Hyperthermia*, vol. 21, no. 7, pp. 637–647, 2005. DOI: 10.1080/02656730500158360.

[46] K. Maier-Hauff *et al.*, “Efficacy and safety of intratumoral thermotherapy using magnetic iron-oxide nanoparticles combined with external beam radiotherapy on patients with recurrent glioblastoma multiforme,” *J. Neurooncol.*, vol. 103, no. 2, pp. 317–324, 2011. DOI: 10.1007/s11060-010-0389-0.

[47] M. Johannsen *et al.*, “Thermotherapy of prostate cancer using magnetic nanoparticles: feasibility, imaging, and three-dimensional temperature distribution,” *Eur. Urol.*, vol. 52, no. 6, pp. 1653–1661, 2007. DOI: 10.1016/j.eururo.2006.11.023.

[48] J. E. Rosen, L. Chan, D.-B. Shieh, and F. X. Gu, “Iron oxide nanoparticles for targeted cancer imaging and diagnostics,” *Nanomedicine*, vol. 8, no. 3, pp. 275–290, 2012. DOI: 10.1016/j.nano.2011.08.017.

[49] https://www.magforce.com/en/home/our_therapy/

[50] S. Gandhi, S. Issar, A. K. Mahapatro, and I. Roy, “Cobalt ferrite nanoparticles for bimodal hyperthermia and their mechanistic interactions with lysozyme,” *J. Mol. Liq.*, vol. 310, no. 113194, p. 113194, 2020. DOI: 10.1016/j.molliq.2020.113194.

[51] P. B. Balakrishnan *et al.*, “Exploiting unique alignment of cobalt ferrite nanoparticles, mild hyperthermia, and controlled intrinsic cobalt toxicity for cancer therapy,” *Adv. Mater.*, vol. 32, no. 45, p. e2003712, 2020. DOI: 10.1002/adma.202003712.

[52] Z. Nemati *et al.*, “Enhanced magnetic hyperthermia in iron oxide nano-octopods: Size and anisotropy effects,” *J. Phys. Chem. C Nanomater. Interfaces*, vol. 120, no. 15, pp. 8370–8379, 2016. DOI: 10.1021/acs.jpcc.6b01426.

[53] S. Zhao, N. Hao, J. X. J. Zhang, P. J. Hoopes, F. Shubitidze, and Z. Chen, “Fabrication of monodisperse magnetic nanorods for improving hyperthermia efficacy,” *J. Nanobiotechnology*, vol. 19, no. 1, p. 63, 2021. DOI: 10.1186/s12951-021-00794-8.

[54] P. Hugounenq *et al.*, “Iron oxide monocrystalline nanoflowers for highly efficient magnetic hyperthermia,” *J. Phys. Chem. C Nanomater. Interfaces*, vol. 116, no. 29, pp. 15702–15712, 2012. DOI: 10.1021/jp3025478.

[55] *Nanomaterials for Magnetic and Optical Hyperthermia Applications*. Elsevier, 2019. DOI: 10.1016/C2017-0-00855-8.

[56] W. J. Atkinson, I. A. Brezovich, and D. P. Chakraborty, “Usable frequencies in hyperthermia with thermal seeds,” *IEEE Trans. Biomed. Eng.*, vol. 31, no. 1, pp. 70–75, 1984. DOI: 10.1109/TBME.1984.325372.

[57] R. Hergt and S. Dutz, “Magnetic particle hyperthermia—biophysical limitations of a visionary tumour therapy,” *J. Magn. Magn. Mater.*, vol. 311, no. 1, pp. 187–192, 2007. DOI: 10.1016/j.jmmm.2006.10.1156.

[58] S. Kossatz *et al.*, “Efficient treatment of breast cancer xenografts with multifunctionalized iron oxide nanoparticles combining magnetic hyperthermia and anti-cancer drug delivery,” *Breast Cancer Res.*, vol. 17, no. 1, p. 66, 2015. DOI: 10.1186/s13058-015-0576-1.

[59] S. Piehler *et al.*, “Iron oxide nanoparticles as carriers for DOX and magnetic hyperthermia after intratumoral application into breast cancer in mice: Impact and future perspectives,” *Nanomaterials (Basel)*, vol. 10, no. 6, p. 1016, 2020. DOI: 10.3390/nano10061016.

[60] A. Espinosa *et al.*, “Magnetic (hyper)thermia or photothermia? Progressive comparison of iron oxide and gold nanoparticles heating in water, in cells, and in vivo,” *Adv. Funct. Mater.*, vol. 28, no. 37, p. 1803660, 2018. DOI: 10.1002/adfm.201803660.

[61] A. Plan Sangnier *et al.*, “Targeted thermal therapy with genetically engineered magnetite magnetosomes@RGD: Photothermia is far more efficient than magnetic hyperthermia,” *J. Control. Release*, vol. 279, pp. 271–281, 2018. DOI: 10.1016/j.jconrel.2018.04.036.

[62] A. Curcio *et al.*, “Iron oxide nanoflowers @ CuS hybrids for cancer Tri-therapy: Interplay of photothermal therapy, magnetic hyperthermia and photodynamic therapy,” *Theranostics*, vol. 9, no. 5, pp. 1288–1302, 2019. DOI: 10.7150/thno.30238.

[63] Z.-Q. Zhang and S.-C. Song, “Thermosensitive/superparamagnetic iron oxide nanoparticle-loaded nanocapsule hydrogels for multiple cancer hyperthermia,” *Biomaterials*, vol. 106, pp. 13–23, 2016. DOI: 10.1016/j.biomaterials.2016.08.015.

[64] O. Sandre, C. Genevois, E. Garaio, L. Adumeau, S. Mornet, and F. Couillaud, “In vivo imaging of local gene expression induced by magnetic hyperthermia,” *Genes (Basel)*, vol. 8, no. 2, p. 61, 2017. DOI: 10.3390/genes8020061.

[65] N. A. Brusentsov *et al.*, “Magnetic fluid hyperthermia of the mouse experimental tumor,” *J. Magn. Magn. Mater.*, vol. 252, pp. 378–380, 2002. DOI: 10.1016/S0304-8853(02)00634-0.

[66] C. L. Dennis *et al.*, “Nearly complete regression of tumors via collective behavior of magnetic nanoparticles in hyperthermia,” *Nanotechnology*, vol. 20, no. 39, p. 395103, 2009. DOI: 10.1088/0957-4484/20/39/395103.

[67] X. Ma *et al.*, “Fe3O4–Pd Janus nanoparticles with amplified dual-mode hyperthermia and enhanced ROS generation for breast cancer treatment,” *Nanoscale Horiz*, vol. 4, no. 6, pp. 1450–1459, 2019. DOI: 10.1039/C9NH00233B.

[68] H. A. Albarqi *et al.*, “Systemically delivered magnetic hyperthermia for prostate cancer treatment,” *Pharmaceutics*, vol. 12, no. 11, p. 1020, 2020. DOI: 10.3390/pharmaceutics12111020.

[69] X. L. Liu *et al.*, “Synthesis of ferromagnetic Fe0.6Mn0.4O nanoflowers as a new class of magnetic theranostic platform for in vivo T1-T2Dual-mode magnetic resonance imaging and magnetic hyperthermia therapy,” *Adv. Healthc. Mater.*, vol. 5, no. 16, pp. 2092–2104, 2016. DOI: 10.1002/adhm.201600357.

[70] J.-H. Lee *et al.*, “Exchange-coupled magnetic nanoparticles for efficient heat induction,” *Nat. Nanotechnol.*, vol. 6, no. 7, pp. 418–422, 2011. DOI: 10.1038/nnano.2011.95.

[71] O. K. Arriortua *et al.*, “Antitumor magnetic hyperthermia induced by RGD-functionalized Fe3O4 nanoparticles, in an experimental model of colorectal liver metastases,” *Beilstein J. Nanotechnol.*, vol. 7, pp. 1532–1542, 2016. DOI: 10.3762/bjnano.7.147.

[72] International Commission on Non-Ionizing Radiation Protection (ICNIRP), "Guidelines for limiting exposure to electromagnetic fields (100 kHz to 300 GHz)," *Health Phys.*, vol. 118, no. 5, pp. 483–524, 2020. DOI: 10.1097/HP.0000000000001210.

[73] F. Adibzadeh, M. M. Paulides, and G. C. van Rhoon, "SAR thresholds for electromagnetic exposure using functional thermal dose limits," *Int. J. Hyperthermia*, vol. 34, no. 8, pp. 1248–1254, 2018. DOI: 10.1080/02656736.2018.1424945.

[74] R. Scorretti, N. Burais, L. Nicolas, and A. Nicolas, "Modeling of induced current into the human body by low-frequency magnetic field from experimental data," *IEEE Trans. Magn.*, vol. 41, no. 5, pp. 1992–1995, 2005. DOI: 10.1109/TMAG.2005.846276.

[75] https://www.nbnanoscale.com.

[76] M. Ohtake *et al.*, "Hyperthermia and chemotherapy using Fe(Salen) nanoparticles might impact glioblastoma treatment," *Sci. Rep.*, vol. 7, p. 42783, 2017. DOI: 10.1038/srep42783.

[77] H. F. Rodrigues, G. Capistrano, and A. F. Bakuzis, "In vivo magnetic nanoparticle hyperthermia: a review on preclinical studies, low-field nano-heaters, noninvasive thermometry and computer simulations for treatment planning," *Int. J. Hyperthermia*, vol. 37, no. 3, pp. 76–99, 2020. DOI: 10.1080/02656736.2020.1800831.

[78] H. F. Rodrigues, F. M. Mello, L. C. Branquinho, N. Zufelato, E. P. Silveira-Lacerda, and A. F. Bakuzis, "Real-time infrared thermography detection of magnetic nanoparticle hyperthermia in a murine model under a non-uniform field configuration," *Int. J. Hyperthermia*, vol. 29, no. 8, pp. 752–767, 2013. DOI: 10.3109/02656736.2013.839056.

[79] T. Araya *et al.*, "Antitumor effects of inductive hyperthermia using magnetic ferucarbotran nanoparticles on human lung cancer xenografts in nude mice," *Onco. Targets. Ther.*, vol. 6, pp. 237–242, 2013. DOI: 10.2147/OTT.S42815.

[80] A. Ademaj *et al.*, "Clinical evidence for thermometric parameters to guide hyperthermia treatment," *Cancers (Basel)*, vol. 14, no. 3, p. 625, 2022. DOI: 10.3390/cancers14030625.

[81] C. M. van Leeuwen *et al.*, "A short time interval between radiotherapy and hyperthermia reduces in-field recurrence and mortality in women with advanced cervical cancer," *Radiat. Oncol.*, vol. 12, no. 1, 2017. DOI: 10.1186/s13014-017-0813-0.

[82] R. S. Cox and D. S. Kapp, "Correlation of thermal parameters with outcome in combined radiation therapy-hyperthermia trials," *Int. J. Hyperthermia*, vol. 8, no. 6, pp. 719–732, 1992. DOI: 10.3109/02656739209005020.

[83] K. A. Leopold *et al.*, "Relationships among tumor temperature, treatment time, and histopathological outcome using preoperative hyperthermia with radiation in soft tissue sarcomas," *Int. J. Radiat. Oncol. Biol. Phys.*, vol. 22, no. 5, pp. 989–998, 1992. DOI: 10.1016/0360-3016(92)90798-m.

[84] H. H. Pennes, "Analysis of tissue and arterial blood temperatures in the resting human forearm," *J. Appl. Physiol.*, vol. 1, no. 2, pp. 93–122, 1948. DOI: 10.1152/jappl.1948.1.2.93.

[85] M. Nakayama, "Macrophage recognition of crystals and nanoparticles," *Front. Immunol.*, vol. 9, p. 103, 2018. DOI: 10.3389/fimmu.2018.00103.

[86] K. M. Tsoi *et al.*, "Mechanism of hard-nanomaterial clearance by the liver," *Nat. Mater.*, vol. 15, no. 11, pp. 1212–1221, 2016. DOI: 10.1038/nmat4718.

[87] L. Arms *et al.*, "Advantages and limitations of current techniques for analyzing the biodistribution of nanoparticles," *Front. Pharmacol.*, vol. 9, p. 802, 2018. DOI: 10.3389/fphar.2018.00802.

[88] L. C. Wu *et al.*, "A review of magnetic particle imaging and perspectives on neuroimaging," *AJNR Am. J. Neuroradiol.*, vol. 40, no. 2, pp. 206–212, 2019. DOI: 10.3174/ajnr.A5896.

[89] H. Kee, H. Lee, and S. Park, "Optimized Halbach array for focused magnetic drug targeting," *J. Magn. Magn. Mater.*, vol. 514, no. 167180, p. 167180, 2020. DOI: 10.1016/j.jmmm.2020.167180.

[90] A. Nacev, C. Beni, O. Bruno, and B. Shapiro, "The behaviors of Ferro-magnetic nano-particles in and around blood vessels under applied magnetic fields," *J. Magn. Magn. Mater.*, vol. 323, no. 6, pp. 651–668, 2011. DOI: 10.1016/j.jmmm.2010.09.008.

[91] E. P. Furlani, “Magnetic Biotransport: Analysis and Applications,” *Materials (Basel)*, vol. 3, no. 4, pp. 2412–2446, 2010. DOI: 10.3390/ma3042412.

Chapter 2

Numerical integration of low-frequency electromagnetic field problem

Part of the material presented in this Chapter is published in Computer Methods and Programs in Biomedicine 223: 106975, August 2022

In this Chapter, we present the quasi-static potential-based formulation of the low-frequency electromagnetic (EM) field problem for the evaluation of eddy currents in biological media, under the application of an alternating current (AC) magnetic field. First, we introduce the equations that govern the phenomenon, then we describe how we apply the Finite Element Method (FEM) for the numerical solution, from the weak formulation of the problem to the assembly of the linear system. Finally, we validate the in-house developed 3D solver by comparing the obtained results, in simplified geometries, to analytical solutions and the results evaluated with the software Sim4Life®.

2.1 Low-frequency EM field problem

Let Ω the region defined by the human/animal body or sample under investigation (tissue portion, test tube, etc.), and $\partial\Omega$ its boundary. Let consider Ω_S

the magnetic field source that is external to the domain Ω (see schematic in Figure 2.1), and σ the electrical conductivity of the tissues/materials. As in this Thesis we are focusing on EM fields with frequencies typical of magnetic hyperthermia, i.e. in the range 50 kHz to 1 MHz, the EM field wavelength is much larger than the size of the domain under analysis Ω, which represents the region occupied by the body. For this reason, we consider a quasi-static approximation of Maxwell's equations neglecting the displacement of currents, i.e. $\partial \mathbf{D}/\partial t = 0$.

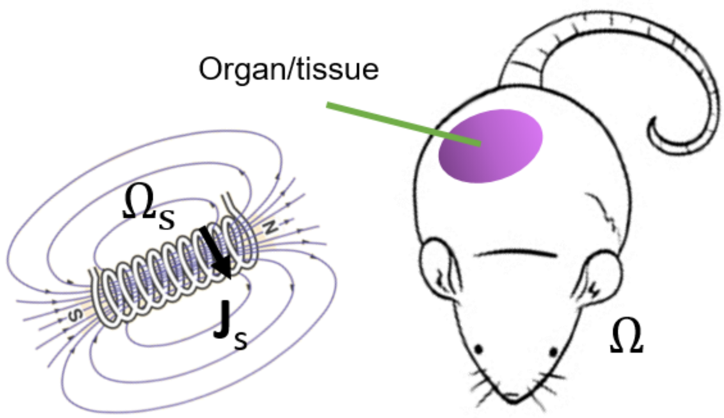

Figure 2.1: Schematic of the domain under investigation Ω and the magnetic field source Ω_S. In this reported case, Ω is defined by all the tissues and organs that compose the animal body, and Ω_S is represented by a solenoid with current density J_S.

Considering to be in the frequency domain, with the convention $\partial/\partial t = j\omega$ where j is the complex unit and ω is the angular frequency, the Maxwell's equations are written as

$$\nabla \times \mathbf{E} = -j\omega\mathbf{B} \tag{2.1}$$

$$\nabla \times \mathbf{H} = \mathbf{J} \tag{2.2}$$

$$\nabla \cdot \mathbf{B} = 0 \tag{2.3}$$

where $\mathbf{E} = \mathbf{E}(x,y,z,\omega)$ is the electric field vector, $\mathbf{B} = \mathbf{B}(x,y,z,\omega)$ is the magnetic flux density vector, $\mathbf{H} = \mathbf{H}(x,y,z,\omega)$ is the magnetic field vector and $\mathbf{J} = \mathbf{J}(x,y,z,\omega)$ is the current density vector. **E**, **B**, **H** and **J** are linked via the following constitutive relationships:

$$\mathbf{B} = \mu(\mathbf{r})\mathbf{H} \tag{2.4}$$

$$\mathbf{J} = \sigma(\mathbf{r})\mathbf{E} \tag{2.5}$$

where μ and σ are the magnetic permeability and the electrical conductivity of the medium, respectively, and $\mathbf{r}$ is the position vector, $\mathbf{r} = \mathbf{r}(x,y,z)$. The magnetic flux density $\mathbf{B}$ can be defined in terms of the magnetic vector potential, $\mathbf{A}$, as

$$\nabla \times \mathbf{A} = \mathbf{B} \tag{2.6}$$

Then, the electric field can be expressed by the following relationship:

$$\mathbf{E} = -\nabla\phi - j\omega\mathbf{A} \tag{2.7}$$

where ϕ is the electric scalar potential. With this last formulation of the electric field, substituting (2.7) in (2.5), the current density vector can be rewritten as

$$\mathbf{J} = -\sigma(j\omega\mathbf{A} + \nabla\phi). \tag{2.8}$$

By considering the continuity condition of the charge conservation equation, $\nabla \cdot \mathbf{J} = 0$, Eq. (2.8) gives the following expression in Ω:

$$\nabla \cdot (\sigma\nabla\phi) = -j\omega\nabla \cdot (\sigma\mathbf{A}). \tag{2.9}$$

Assuming that the vector potential **A,** due to the magnetic field source, is known, the current density can be obtained by computing the scalar potential from the last equation. To guarantee the uniqueness of the solution of Eq. (2.9), a proper boundary condition on the domain boundary, $\delta\Omega$, is imposed. Considering that the current density is zero outside the domain, the boundary condition is defined by the Neumann condition that expresses the normal derivative of the scalar potential over $\delta\Omega$:

$$\frac{\partial\phi}{\partial n} = -j\omega\mathbf{A} \cdot \mathbf{n} \tag{2.10}$$

where $\mathbf{n}$ is the outward unit normal vector with respect to the surface of the boundary.

In addition, we have to take into account the continuity condition at the interface between regions of the domain consisting of materials with different electrical conductivities. At the interface between two different materials, this can be expressed by the following relationship:

$$(\mathbf{J}_2 - \mathbf{J}_1)\cdot\mathbf{n} = 0$$

where $\mathbf{J}_1$ and $\mathbf{J}_2$ are the current densities in the two different regions, with the respective electrical conductivities values σ_1 and σ_2.

Equations (2.9) and (2.10) represent the low-frequency EM field problem in explicit form, with ϕ the unknown quantity. The advantage of this formulation is that we can compute separately the magnetic field source, represented by **A**, and the induced eddy currents into the body. However, it is very restrictive to find a solution to the problem in this formulation (Equations 2.9 and 2.10), as it requires a solution that is two times derivable and with the second derivative continuous in the closed domain, i.e. the solution should belong to the space $C^2(\overline{\Omega})$. The difficulty of the explicit form, also called the strong formulation of the differential problem, is that in general a classical solution of the problem does not exist, but there is a physical solution of the problem that exists but does not pointwise satisfy all the differentiability conditions imposed by the problem and thus it does not belong to $C^2(\overline{\Omega})$ [1]. For this reason, a different formulation of the problem is needed to reduce the order of derivative. In this so-called weak form of the problem, the derivatives are considered in the sense of distributions and the solution of the problem has to belong to a suitable subspace of the Sobolev space $H_0^1(\Omega)$ [1,2] (see Appendix A.1). This weak problem allows us to find a solution regular enough to solve the problem also in the strong formulation, although in the sense of distributions. Thus the weak form is a formulation that is convenient for applying approximation methods, such as FEM. Moreover, this type of solution is also called a weak solution of the problem.

2.1.1 Vector potential

When the magnetic vector potential **A** cannot be calculated through analytical expression, numerical simulations are needed. For example, when the magnetic source is a conductor with complex geometry, **A** can be calculated by the following expression

$$\mathbf{A}(\mathbf{r}) = \frac{\mu_0}{4\pi}\int_{\Omega}\frac{\mathbf{J}_S(\mathbf{r}_S)}{|\mathbf{r}-\mathbf{r}_S|}dv_S \qquad (2.11)$$

where $\mathbf{J}_s$ is the current density vector inside the source conductor (considered to be defined by the domain Ω_s and its boundary by $\partial\Omega_s$), **r** is the position vector referred to the domain Ω and $\mathbf{r}_s$ is the position vector referred to the domain Ω_s. For simplicity in the cases studied in this Thesis, to evaluate the current density vector produced by a conductor, we assume that electromagnetic induction effects within the conductor can be neglected, considering a static condition. Thus, the expression for the current density vector inside the source conductor is the following

$$\mathbf{J}_S = -\sigma \nabla \phi_S .$$

By considering the charge conservation equation, the current density vector inside the source conductor can be obtained numerically through FEM evaluation of the scalar potential ϕ_s expressed by

$$\nabla \cdot \left(\sigma \nabla \phi_S \right) = 0 .$$

Once $\mathbf{J}_s$ is evaluated, the magnetic vector potential can be calculated by solving Eq. (2.11).

2.2 Numerical solution

To numerically solve the low-frequency EM field problem, the FEM is applied with the Galerkin Ansatz. For this purpose, first the equation is rewritten into its weak formulation, then the discretization of the continuum problem can be performed to solve an algebraic system of equations that gives the approximated solution of the problem. In this section, we introduce the main concepts of the FEM, in particular illustrating how the method is adopted for the problem of interest.

2.2.1 Weak formulation

Eq. (2.9) can be rewritten in its weak formulation integrating over the domain and multiplying by an arbitrary function w, $w = w(\mathbf{r})$ called test function, obtaining

$$\int_\Omega \nabla \cdot (\sigma \nabla \phi) w dV = \int_\Omega -j\omega \nabla \cdot (\sigma \mathbf{A}) w dV \tag{2.12}$$

where w and ϕ belong to the same functional space $U \in H_0^1(\Omega)$. Applying the Green's formula (Appendix A.2) to the left-hand side of Eq. (2.12) and the corollary of the divergence theorem (Appendix A.2) to the right-hand side, we find

$$-\int_{\Omega} \sigma\nabla\phi\cdot\nabla w dV + \int_{\partial\Omega} \sigma(\nabla\phi\cdot\mathbf{n}) w ds = \int_{\Omega} j\omega\sigma\mathbf{A}\cdot\nabla w dV - \int_{\partial\Omega} j\omega\sigma\mathbf{A}\cdot\mathbf{n} w ds \tag{2.13}$$

and applying the boundary condition (2.10), we can eliminate the surface integrals on δΩ, and finally we have

$$\int_{\Omega} \sigma\nabla\phi\cdot\nabla w dV = -\int_{\Omega} j\omega\sigma\mathbf{A}\cdot\nabla w dV\,. \tag{2.14}$$

Eq. (2.14) with the boundary condition (2.10) represents the weak formulation of the low-frequency problem. The continuum problem in the weak formulation cannot be solved exactly for the majority of realistic domains, except for very simple geometries. Especially in complex domains, the analytical solution cannot be obtained. For this reason, an approximated solution is calculated by discretizing the geometry and reducing the problem into a system of algebraic equations of simple functions that depend on a finite number of parameters.

2.2.2 FEM discretization

Let now consider that the domain is discretized in M interconnected elements with N the total number of nodes, which are the vertices of the elements, and let $U_h \subset U$ a subspace of finite dimension of order N. We can introduce the approximated form of (2.14) in the subspace U_h,

$$\text{find } \phi_h \in V_h : \int_{\Omega} \sigma\nabla\phi_h\cdot\nabla w dV = -\int_{\Omega} j\omega\sigma\mathbf{A}\cdot\nabla w dV,\ \forall\omega\in V_h \tag{2.15}$$

which, with Eq. (2.10), is the Galerkin formulation of the low-frequency problem, where the solution ϕ_h is the approximation of the solution ϕ of (2.14).

Let us consider $\{\varphi_i,\ i = 1, 2, \ldots, N\}$ a base for the subspace U_h, then ϕ_h can be expressed as a linear combination of φ_i, i.e.

$$\phi_{\mathrm{h}} = \sum_{k}^{N} \hat{\phi}_k \varphi_k ,$$

with $\hat{\phi}_k$, k =1, 2, …, N unknown coefficients and φ_k are called shape functions (Appendix B). Substituting ϕ_h with this linear combination in (2.15) and the test function w with a shape function φ_i, as $w \in U_h$, then, to find the approximate solution, it is sufficient that the following expression is satisfied for each function of the base,

$$\sum_{k=1}^{N} \hat{\phi}_k \int_{\Omega} \sigma \nabla \varphi_k \cdot \nabla \varphi_i dV = -\int_{\Omega} j\omega\sigma \mathbf{A} \cdot \nabla \varphi_i dV,\ i = 1,2,...,\mathrm{N}\,. \tag{2.16}$$

Denoting now $\hat{\phi}$ as the vector of the unknown coefficients $\hat{\phi}_k$ and $\mathbf{S}$ is the $N \times N$ matrix defined by the elements

$$s_{ik} = \int_{\Omega} \sigma \nabla \varphi_i \cdot \nabla \varphi_k dV,\ i,k = 1,2,...,\mathrm{N}$$

where i indicates the row and k the column of the matrix. Finally, (2.16) can be written as the linear system

$$\mathbf{S}\hat{\phi} = \mathbf{f} \tag{2.17}$$

where $\mathbf{f}$ is the vector of elements

$$f_i = -\int_{\Omega} j\omega\sigma \mathbf{A} \cdot \nabla \varphi_i dV\,. \tag{2.18}$$

S takes the name of stiffness matrix and is a symmetric and positive definite matrix, thus it is not-singular. The non-singularity of **S** guarantees the existence and the uniqueness of the approximated solution ϕ_h. In addition, the stiffness matrix is sparse and it could be a very large square matrix, as its dimension depends on the number of nodes that compose the domain discretization. For this reason, a suitable numerical method that takes into account the structure of **S** is needed to solve system (2.17), in order to optimize the computational cost and the accuracy of the solution. When there are large matrices, iterative methods are preferred. In our simulations, the system solution is obtained through the

MATLAB®'s function "*mldivide*", which chooses the system solver on the basis of the sparse matrix structure (e.g. permuted triangular solver, LU solver, or Cholesky solver) [3], in combination with the MATLAB®'s Parallel Computing Toolbox™ to run in parallel the solution, using distributed arrays, and accelerate the solution time [4].

For the calculation of the magnetic vector potential **A**, the FEM is applied to solve the current-field equation described in Section 2.1.1, in the same way as illustrated in this section. In this case, the current vector is evaluated on the region that represents the source conductor Ω_s, which is appropriately discretized in a finite number of elements. Once the current density vector inside the source is evaluated, the vector potential is calculated on the domain Ω with the expression of **A** defined by Eq. (2.11).

Once the calculation of the shape functions and their derivatives is completed, the assembly of the stiffness matrix **S** and the computing of vector **f** are performed and system (2.17) can be solved.

2.3 Validation of the numerical solver

The EM solver, developed within the MATLAB® environment, is validated by comparison to an analytical solution and to a numerical solution evaluated by means of the computation platform Sim4Life®, considering two different simplified geometries.

2.3.1 Comparison to analytical solution

The numerical model is tested through comparison with the analytical solution of the magnetically induced electric field in an inhomogeneous domain composed of two non-concentric cylinders [5]. The schematic of the domain is illustrated in Figure 2.2 that shows a transversal section of the geometry. The section is composed of two circular regions, R_1 defined by the external cylinder and R_2 by the internal one. Moreover, a and b are the radii of R_2 and R_1 respectively, and c is the distance between the centers of the two cylinders. With the assumptions that the AC magnetic field is applied parallel to the longitudinal axis of the domain, i.e. it is perpendicular to the 2D section of Fig. 2.2, and is uniform within the space, the induced electric field can be approximated with a closed form solution. If we let B_0 denote the magnitude of the magnetic-flux

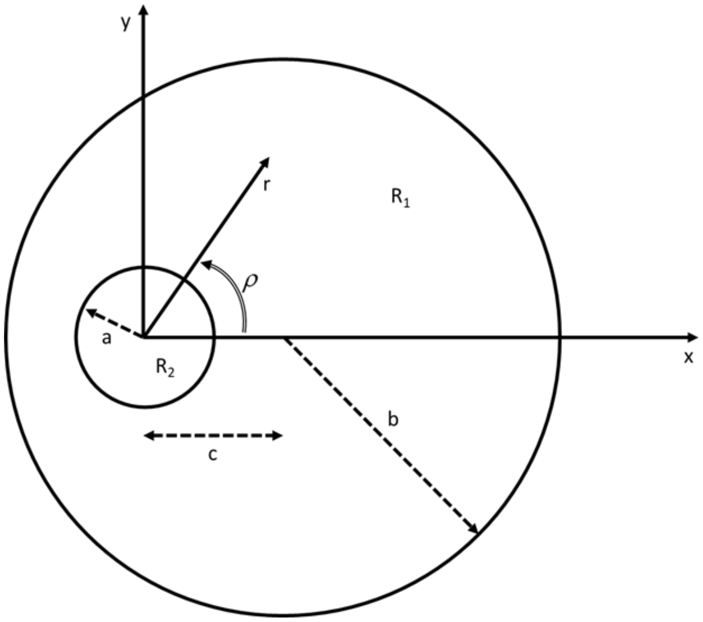

Figure 2.2. Schematic of two non-concentric cylinders. The inner cylinder with radius a is defined by region R_2. The external cylinder has a radius equal to b and it represents a region named R_1. The distance between the centers of the cylinders is indicated by c.

density, the analytical solution of the electric scalar potential on the transverse plane is expressed in cylindrical coordinates (r,ρ) as follows [5]:

$$\phi_1 = \frac{A_1}{r}\sin\rho + D_1 r\sin\rho$$
$$\phi_2 = D_2 r\sin\rho$$

where ϕ_1 and ϕ_2 are the scalar potential in R_1 and R_2 respectively, and r is the distance from the center of the region R_2. Whereas A_1 and D_i, for i =1, 2, are coefficients defined by

$$A_1 = \frac{\left(b^2 - c^2\right)}{1 - \frac{\left(\sigma_1 + \sigma_2\right)\left(b^2 - c^2\right)}{\left(\sigma_1 - \sigma_2\right)a^2}} \frac{j\omega B_0 c}{2}$$
$$D_1 = \frac{\left(\sigma_1 + \sigma_2\right)A_1}{\left(\sigma_1 - \sigma_2\right)a^2}$$
$$D_2 = \frac{A_1}{a^2} + D_1$$

where σ_1 and σ_2 are the electrical conductivities in regions R_1 and R_2 respectively. As the magnetic field is uniform and it is applied along the longitudinal axis of the cylinder, the vector potential is along the ρ-direction only and is equal to the product between B_0 and $r/2$. Therefore, substituting this value of the vector potential and the scalar potential ϕ_1 and ϕ_2 into Eq. (2.7), it follows that the electric field vector is given by

$$\mathbf{E}_1 = \hat{r}\left(\frac{A_1}{r^2} - D_1\right)\sin\rho - \hat{\rho}\left[\left(\frac{A_1}{r^2} - D_1\right)\cos\rho + \frac{j\omega B_0 r}{2}\right]$$

$$\mathbf{E}_2 = -\hat{r}D_2 \sin\rho - \hat{\rho}\left[D_2 \cos\rho + \frac{j\omega B_0 r}{2}\right]$$

where $\mathbf{E}_1$ and $\mathbf{E}_2$ are the induced electric fields.

For the comparison with our numerical model, we consider that region R_2, i.e. the internal cylinder, consists of bone with electrical conductivity equal to 0.0035 S/m [6] and the region R_1 is the surrounding muscle with electrical conductivity 0.355 S/m [6]. The parameters reported in Fig. 2.2 are assigned as follows: a = 0.75 cm, b = 3 cm and c = 1 cm [5]. The magnetic field B_0 is set at 41.9 mT and the field frequency at 150 kHz (the angular frequency is given by $\omega = 2\pi f$, with f the frequency). The numerical solution is obtained by considering a 3D domain constituted by the two cylinders discretized into a tetrahedral mesh. In order to analyze the effects of the discretization of the mesh on the accuracy of the solution, we consider three different meshes, respectively with elements of average size equal to 2.51 mm, 1.27 mm, and 0.64 mm. For simplicity of notation, we denote the first mesh as Mesh 1, the intermediate as Mesh 2 and the finest as Mesh 3. All the meshes are generated with the open-source mesh generator GMSH [6]. The first comparison with the analytical solution is evaluated on a 2D section of the domain, then the solutions are compared along a line that crosses transversally the cylinders.

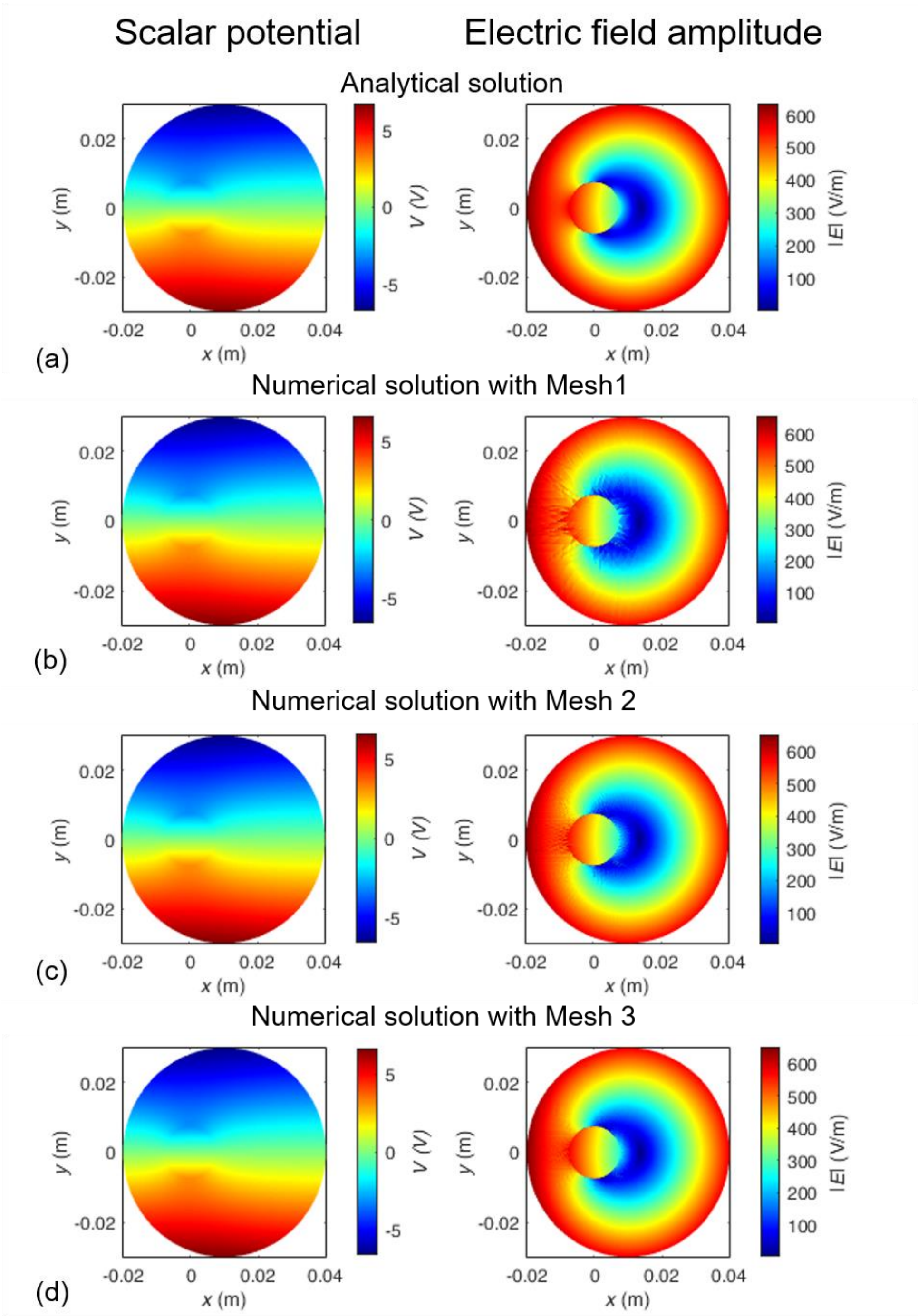

Figure 2.3. Comparison between analytical solution and our numerical solutions. On the left the scalar potential, on the right the electric field amplitude. (a) analytical solution, (b) numerical solution for the mesh with average size of elements equals to 2.51 mm, (c) numerical solution for the mesh with element size 1.27 mm, (c) numerical solution for the mesh with element size 0.64 mm.

For the comparison on a 2D section of the domain, the scalar potential and the electric field are evaluated on a 2D grid, specifically a transversal section of the cylinders, at half of their height. The results of the 2D section are shown in Figure 2.3, where the solutions computed for the scalar potential are reported on the left and those for the electric field amplitude on the right. Fig. 2.3a displays the analytical solutions, whereas Figs. 2.3 b-d show the numerical results for Mesh 1, Mesh 2, and Mesh 3 respectively. The numerical solutions of the scalar potential show a good agreement with the analytical solution, whereas for the electric field amplitude we can observe that a good level of accuracy, with respect to the analytical solution, is only obtained for the finest mesh, i.e. Mesh 3. The other two meshes show worse evaluations of the electric field, especially at the interface between the two regions and on the left side of the map, in the area defined between the boundaries of the internal cylinder and the external one. To compare the results for the electric field, we evaluate the average of the relative errors RE_{avg} defined as a percentage by the following expression

$$\mathrm{RE}_{\mathrm{avg}} = \frac{1}{G}\sum_{i=1}^{G}\left|\frac{S_{\mathrm{an},i} - S_{\mathrm{num},i}}{S_{\mathrm{an},i}}\right| \times 100$$

where G is the total number of the grid points, $S_{\mathrm{num,i}}$ is the numerical solution at point i and $S_{\mathrm{an,i}}$ is the analytical solution at the same point. We find that the largest value of the average relative error is reached for Mesh 1, with RE_{avg} = 2.7%, whereas Mesh 3 has the lowest value, RE_{avg} = 1.5%.

To further analyze the obtained results of the scalar potential and electric field amplitude, the solutions are also evaluated on a line that crosses the 3D structure at half of its height across the y-axis, passing through the center of the internal cylinder. Figure 2.4 displays the numerical results obtained for all three meshes in comparison with the analytical solution. In analogy to the results in the 2D section, no significant differences can be observed for the scalar potential, with RE_{avg} less than 1% for all meshes. Whereas for the electric field amplitude, the same level of accuracy is not observed. The largest value of RE_{avg} is reached for Mesh 1, with a value equal to 3.7%, whereas Mesh 3 has the lowest percentage, with RE_{avg} = 2%. Therefore, also here we can observe that the finest mesh provides the best results, and that the numerical solutions are less accurate in the proximity of the interface between the two regions of different tissue.

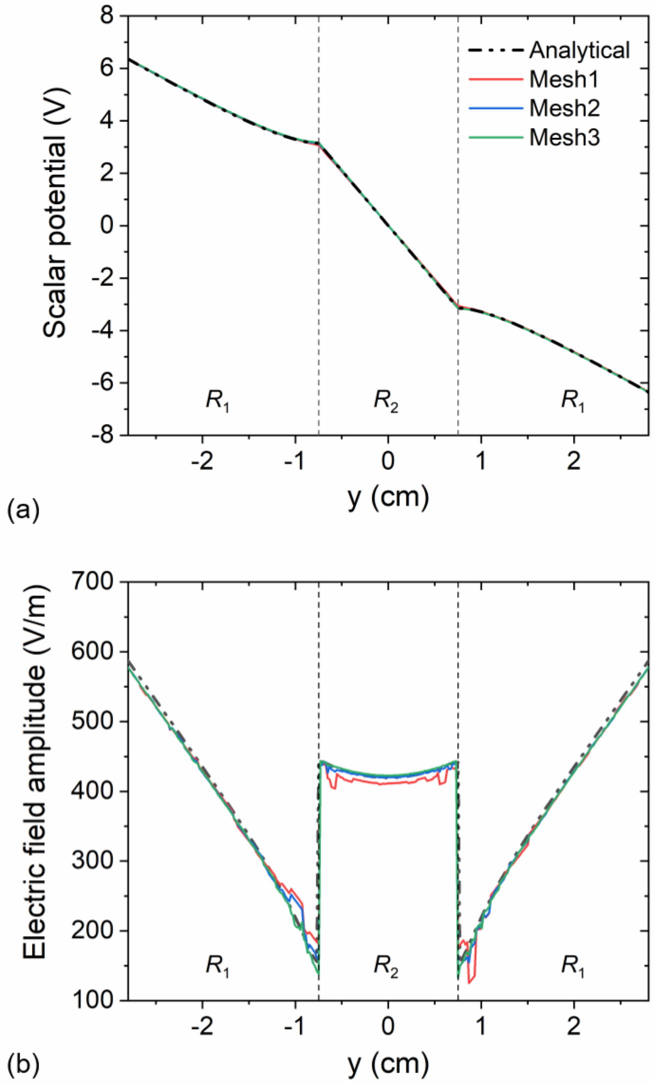

Figure 2.4. Comparison between numerical and analytical solutions of (a) the scalar potential and (b) the amplitude of the electric field evaluated across a line that passes through the center of the internal cylinder. R_1 and R_2 specify if the solutions are in the external cylinder or in the internal one, respectively. The vertical dash lines indicate the interface between the two regions of the domain.

2.3.2 Comparison to numerical solution

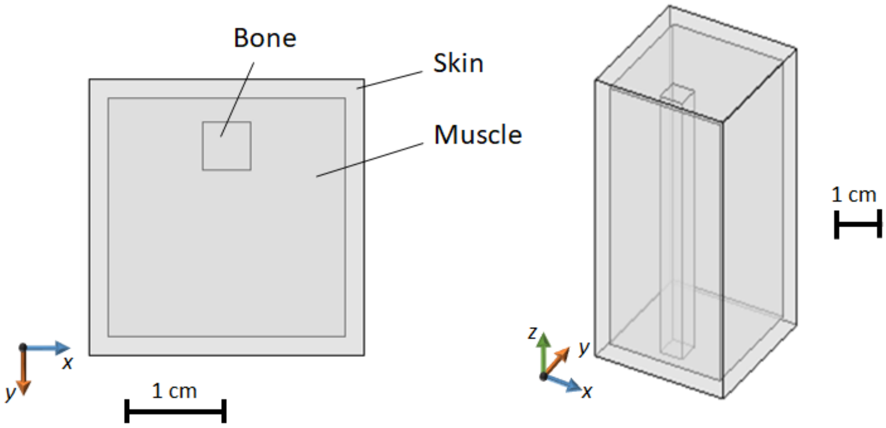

Figure 2.5. Schematic of domain structure. On the left: 2D section where the region materials are indicated. On the right: 3D view of the domain.

We compare the numerical solutions obtained with the implemented EM solver with the ones obtained with the commercial software Sim4Life® (v6.2, ZMT, Zurich, Switzerland) [7]. The solutions obtained with Sim4Life® are evaluated by Ioannis Androulakis, doctoral candidate at Erasmus MC Cancer Institute (Rotterdam, The Netherlands), employing the structured-grid solver for the EM problem based on FEM [8]. For this comparison, we evaluate the values of the induced electric field and of the specific adsorption rate (SAR) within a simplified 3D geometry, schematized in Figure 2.5, consisting of a parallelepiped with a size of 2.9×2.9×5.4 cm^3 composed of three regions:

1) an external layer of 2 mm of thickness that has skin electric properties (σ = 0.17 S/m),
2) an inner parallelepiped of size 0.5×0.5×5 cm^3 with bone properties (σ = 0.0035 S/m),
3) an intermediate region with muscle properties (σ = 0.355 S/m).

The geometry is composed of a uniform mesh of about 1 million voxels, with a size of 0.6 mm, each one split into six tetrahedral to apply our FEM solvers. The low-frequency EM solvers are tested considering a uniform field within the whole volume along the longitudinal axis with a frequency set at 100 kHz and a field amplitude at 80 kA/m.

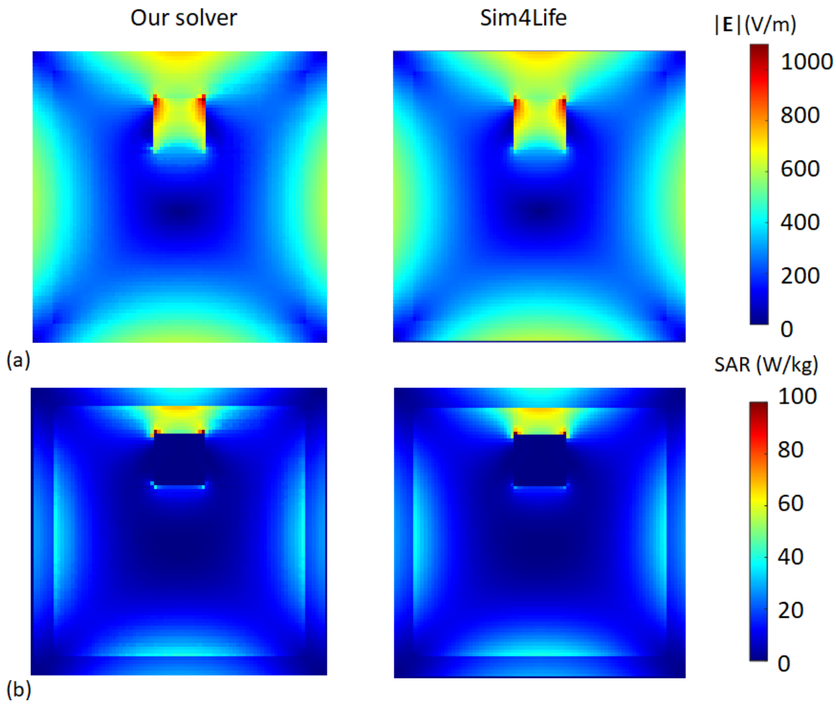

Figure 2.6. Comparison between the implemented EM solver and the Sim4Life solutions on a 2D section of the domain. (a) Maps of the induced electric field. (b) Maps of the SAR.

In Figure 2.6 we report the maps of the induced electric field amplitude and of the SAR evaluated on a transversal section of the domain, located at half of its height. The results show a good agreement between our numerical solution and the Sim4life® solution. For these maps, we evaluate the average discrepancies, expressed as percentage, between the solutions as

$$\mathrm{D}_{\mathrm{avg}} = \frac{1}{G}\sum_{i=1}^{G}\left(\left|\frac{S_{\mathrm{S4L},i} - S_{\mathrm{OS},i}}{S_{\mathrm{S4L},i}}\right|\right)\times 100$$

where $\mathrm{D}_{\mathrm{avg}}$ is evaluated on all the G points that compose the 2D section, S_{S4L} defines the solution calculated with Sim4life S_{S4L}, and S_{OS} the solution with our solver, In the sections reported in Fig. 2.6, $\mathrm{D}_{\mathrm{avg}}$ is equal to 1.2% for the electric field and 2.3% for the SAR.

The numerical solutions are also compared evaluating the electric field amplitude and the SAR on a line that crosses the 3D domain at half of its height and that passes through the central axes of the muscle and bone regions. Figure 2.7 illustrates the results and show again the good agreement between the two solvers, as the curves overlap almost everywhere. Here, D_{avg} has a value of 1% and 2% for the field amplitude and the SAR respectively.

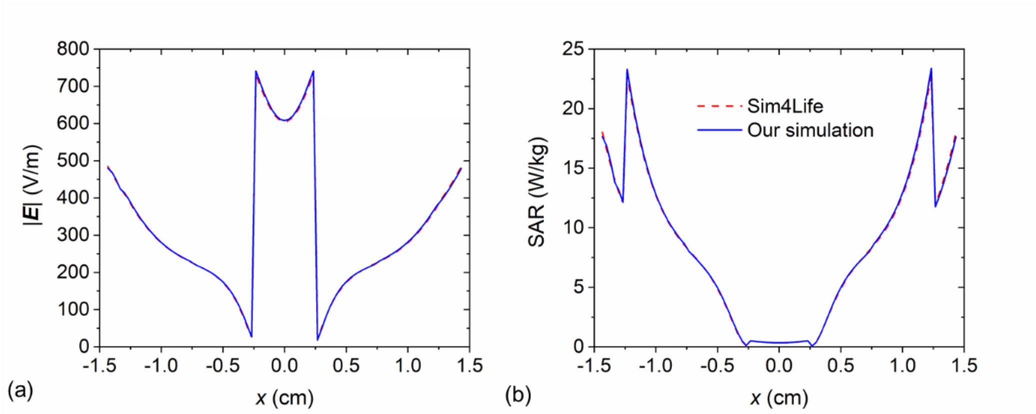

Figure 2.7. Comparison of (a) the electric field amplitude and (b) the SAR, calculated on the median cross-section that passes through the center of the bone region with Sim4Life (dotted red line) and our solver (blue line).

2.4 Tissue parameter acquisition

To evaluate the electric scalar potential, the unique physical property of the tissues or media to know is their electrical conductivity σ. Apart from the tumor tissues, whose value of σ is fixed to 0.8 S/m and is taken from [9], for all the simulations in this Thesis, the electrical conductivity of the different tissues is taken from the database of the IT'IS Foundation [10], which is based on data found in literature. This database also comprises other physical parameters, such as density, thermal properties (i.e. heat capacity and thermal conductivity), and acoustic properties. At the present, the IT'IS database represents the most complete collection of tissue physical parameters. For each tissue property, the database provides the number of scientific papers from which the data is taken, the average value of the data, the maximum, the minimum, and the standard deviation. The literature values are collected from *in vivo* experiments on humans and animals. In particular, the IT'IS dataset divides the electric conductivity values into two sets on the basis of the field frequency, one set is for low frequencies (up to 1 MHz) and the other one for higher frequencies. In the first set, which is the one that we consider, the electrical conductivity is obtained from impedance measurements and most of the data is taken from the exhaustive works of Gabriel *et al.* [11,12].

2.5 References

[1] A. Quarteroni, Numerical models for differential problems. Milano: Springer Milan, 2014.

[2] H. Brezis, Functional analysis, Sobolev spaces and partial differential equations. New York, NY: Springer New York, 2011.

[3] https://it.mathworks.com/help/matlab/ref/mldivide.html.

[4] https://it.mathworks.com/help/parallel-computing/Use-Distributed-Arrays-to-Solve-Systems-of-Linear-Equations-with-Direct-Methods.html.

[5] C. Polk and J. H. Song, "Electric fields induced by low frequency magnetic fields in inhomogeneous biological structures that are surrounded by an electric insulator," *Bioelectromagnetics*, vol. 11, no. 3, pp. 235–249, 1990. DOI: 10.1002/bem.2250110305.

[6] https://gmsh.info.

[7] https://zmt.swiss/sim4life/.

[8] M. Vicentini, M. Vassallo, R. Ferrero, I. Androulakis, and A. Manzin, "In silico evaluation of adverse eddy current effects in preclinical tests of magnetic hyperthermia," *Comput. Methods Programs Biomed.*, vol. 223, no. 106975, 2022. DOI: 10.1016/j.cmpb.2022.106975.

[9] A. Trakic, F. Liu, and S. Crozier, "Transient temperature rise in a mouse due to low-frequency regional hyperthermia," *Phys. Med. Biol.*, vol. 51, no. 7, pp. 1673–1691, 2006. DOI: 10.1088/0031-9155/51/7/003.

[10] https://itis.swiss/virtual-population/tissue-properties/overview.

[11] C. Gabriel, A. Peyman, and E. H. Grant, "Electrical conductivity of tissue at frequencies below 1 MHz," *Phys. Med. Biol.*, vol. 54, no. 16, pp. 4863–4878, 2009. DOI: 10.1088/0031-9155/54/16/002.

[12] http://niremf.ifac.cnr.it/docs/DIELECTRIC/AppendixC.html.

Chapter 3

Numerical integration of heat transfer problem

To support thermometric measurements performed to characterize the heating efficiency of magnetic nanoparticles (MNPs), we developed an in-house 3D solver for the simulation of the spatial distribution and time evolution of temperature within ferrofluids excited by AC magnetic fields. The solver implements a transient thermal model based on the heat transfer equation.

In this Chapter, we present the numerical integration of the heat transfer equation; first, the weak formulation of the equation is derived for the FEM application in the spatial domain, then we illustrate how time integration is performed for the calculation of the thermal transients. Finally, we compare the results obtained with our solver to the simulation results obtained with the MATLAB®'s Partial Differential Equation Toolbox.

3.1 Thermometric measurements

Enhancing the capacity of MNPs as heating agents to convert magnetic energy into heat is fundamental to maximize heat deposition and minimize administered dose. As introduced in Sub-section 1.1.1, the heating efficiency of MNPs and, generally, magnetic nanomaterials is usually characterized by means of calorimetric or thermometric measurements of magnetic suspensions in water or gels.

Typically, in magnetic hyperthermia thermometric measurements are conducted using non-adiabatic custom-built setups, consisting of a water-cooled radiofrequency (RF) coil that generates an electromagnetic (EM) field. Setups that operate under adiabatic conditions require complex isolating systems and long measurement times are needed [1], therefore setups that do not provide adiabatic conditions are mainly used, needing the characterization of the heat exchange of the setup with the external environment.

As an example, Figure 3.1 shows the experimental setup that has been custom-built at INRiM by the research group of Dr. Paola Tiberto [2]. During the measurements, the vial containing the MNP suspension is placed inside the coil and a thermometer, e.g. a fibre optic one, is inserted to measure and record the temperature of the suspension during the heating time, i.e. when the field is applied, and the following cooling time, i.e. when the field is switched off. The magnetic field is usually turned off once the temperature equilibrium is achieved within the sample. After the acquisition of the thermal curve along the heating-cooling transients, the SLP of the MNPs can be estimated [1,3]. As an example, in the thermodynamics model proposed in [3], the heating-cooling obtained from the experimental data is reproduced by leaving the power released by the MNPs as the only free parameter of the equations solved by the model, with the rest of the physical quantities being determined through a calibration procedure.

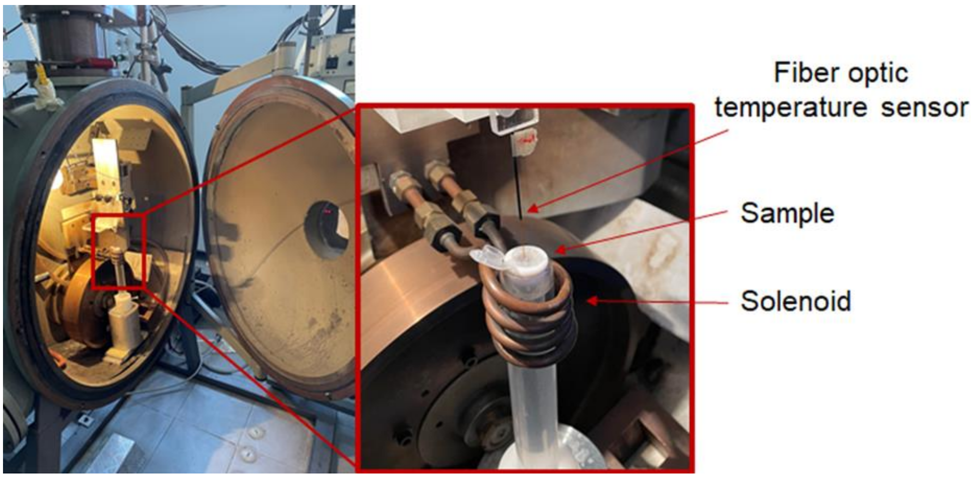

Figure 3.1. Custom-built experimental setup for thermometric measurements developed at INRiM, Torino (Italy).

3.2 The heat transfer equation

Let consider $\Omega \subset \mathbb{R}^3$ the domain under analysis, which can comprise the only vial or test tube with the ferrofluid but also the sample holder and all the surrounding components of interest, and $\partial\Omega$ its boundary. We focus on the heat transfer equation under the hypothesis of negligible convection phenomena. This results in:

$$\rho(\mathbf{r})C_{\mathrm{p}}(\mathbf{r})\frac{\partial T(\mathbf{r},t)}{\partial t}=\nabla\cdot k\nabla T(\mathbf{r},t)+\Gamma Q_{\mathrm{MNPs}}(\mathbf{r},t)+Q_{\mathrm{EM}}(\mathbf{r},t) \quad (3.1)$$

where T is the temperature and unknown quantity, ρ the material density, C_{p} the material heat capacity, k the material thermal conductivity, Q_{MNPs} the heating power per unit volume produced by the MNPs in the suspension, and Q_{EM} is the heating power per unit volume due to external EM field sources. The latter can be associated with the generation of eddy current heating, as described in Chapter 2. Γ is a piecewise function equal to 1 in the suspension region containing MNPs and zero elsewhere. Moreover, t is the time variable, and $\boldsymbol{r}$ the position vector, $\boldsymbol{r} = \boldsymbol{r}(x,y,z)$. Equation (3.1) is completed by the following Neumann boundary condition on $\partial\Omega$:

$$q=-k\frac{\partial T}{\partial n}=-h\left(T_{\mathrm{ext}}-T\right) \quad (3.2)$$

where q is the outward heat flux, T_{ext} the external temperature, and h the heat transfer rate coefficient, which takes into account the convection exchange with the environment neglecting the effects of evaporation and irradiation. In particular, h is null when we are assuming that the thermometric measurement is performed under adiabatic conditions.

3.3 Numerical solution

To numerically solve the thermal problem defined by Eq. (3.1) and Eq. (3.2), a numerical code has been implemented within the MATLAB® environment, applying FEM for spatial integration. Whereas the time integration is performed by including in the code a finite difference method (the θ-method) for the time domain.

3.3.1 Weak formulation

Let consider U a suitable functional space and $U \subset H_0^1(\Omega)$. As seen in Chapter 2, in order to apply FEM, first we write Eq. (3.1) in its weak formulation introducing the test function $w \in H_0^1(\Omega)$, $w = w(\boldsymbol{r})$, and obtaining

$$\int_\Omega \rho C_p \frac{\partial T}{\partial t} w dV = -\int_\Omega k \nabla T \cdot \nabla w dV + \int_{\partial\Omega} k \frac{\partial T}{\partial n} w ds + \int_\Omega Q w dV \qquad (3.3)$$

where here, for simplicity, $Q = Q(\boldsymbol{r},t)$ defines the heating contribution of both field exposure and MNPs, i.e. $Q = Q_{EM} + Q_{MNPs}$.

In Eq. (3.3) we can observe that the surface integral contains the information on the boundary expressed by Eq. (3.2), then we can rewrite Eq. (3.3) as

$$\int_\Omega \rho C_p \frac{\partial T}{\partial t} w dV + \int_\Omega k \nabla T \cdot \nabla w dV + \int_{\partial\Omega} hTw ds = \int_{\partial\Omega} hT_{ext} w ds + \int_\Omega Q w dV \ . \qquad (3.4)$$

If T is such that (3.4) holds for all w belonging to U, then T is the weak solution of Eq. (3.1) with boundary condition (3.2), and Eq. (3.4) is named the weak formulation of Eq. (3.1).

3.3.2 FEM discretization

Let $U_h \subset U$ denote a subspace of finite dimension of order M. With FEM, the aim is to find the approximation of the unknown value of temperature, T, in U_h through the discretization

$$T \cong \sum_{i=1}^{N} \varphi_i \alpha_i = \mathbf{\Phi T} \qquad (3.5)$$

where φ_i are given shape functions and α_k the unknown coefficient for $i = 1, 2, \ldots, N$, where N is the number of nodes in which the domain is discretized. Substituting the test function with φ_i, a basis function of U_h, and T with the discrete expression (3.5) in Eq. (3.4), we obtain the FEM discretization of the problem,

$$\sum_i \int_\Omega \rho C_\mathrm{p} \frac{\partial \alpha_i}{\partial t} \varphi_i \varphi_j dV + \sum_i \int_\Omega k\alpha_i \nabla\varphi_i \cdot \nabla\varphi_j dV + \sum_i \int_{\partial\Omega} h\alpha_i \varphi_i \varphi_j ds = \\ = \int_{\partial\Omega} hT_\mathrm{ext} \varphi_j ds + \int_\Omega Q\varphi_j dV \qquad \text{for } j = 1, ..., N \tag{3.6}$$

The system of Eq. (3.6) can be rewritten in matrix notation as follows:

$$\mathbf{A}\dot{\mathbf{T}} + \mathbf{B}\mathbf{T} = \mathbf{C} + \mathbf{D} \tag{3.7}$$

where

$$\mathbf{A} \in \mathbb{R}^{N\times N},\ a_{ij} = \int_\Omega \rho C_\mathrm{p} \varphi_i \varphi_j dV \quad \text{for } i, j = 1, 2, \ldots, N.$$

$$\dot{\mathbf{T}} \in \mathbb{R}^{N},\ \dot{T}_i = \frac{\partial \alpha_i}{\partial t} \text{ for } i = 1, 2, \ldots, N.$$

$$\mathbf{B} \in \mathbb{R}^{N\times N},\ b_{ij} = \int_\Omega k\nabla\varphi_i \cdot \nabla\varphi_j dV + \int_{\partial\Omega} h\varphi_i \varphi_j ds \quad \text{for } i, j = 1, 2, \ldots, N.$$

$$\mathbf{C} \in \mathbb{R}^{N},\ c_j = \int_\Omega hT_\mathrm{ext} \varphi_j ds \quad \text{for } j = 1, 2, \ldots, N.$$

$$\mathbf{D} \in \mathbb{R}^{N},\ d_j = \int_\Omega Q\varphi_j dV \quad \text{for } j = 1, 2, \ldots, N.$$

$$\mathbf{T} \in \mathbb{R}^{N},\ \alpha_i \quad \text{for } i = 1, 2, \ldots, N.$$

T is the vector of the unknown coefficients α_i of Eq. (3.5) and $\dot{\mathbf{T}}$ is the vector of the respective time derivatives. **A** is the symmetric stiffness matrix and **B** is often named the mass matrix.

3.3.3 Time integration

Once we obtain the system of equations (3.7), the time integration can be performed. It is worth noting that, under the hypothesis of negligible variation of thermal properties with temperature, matrices **A** and **B** and vector **C** are time-independent and they are calculated only one time before starting the time integration, whereas vector **D** is time-dependent and has to be evaluated at each time instant of the simulation.

Let now consider system (3.7) a well-posed problem with the time variable t belonging to a closed time interval of integration, i.e. $t \in I_T = \left[t_0, t_f\right] \subset \mathbb{R}^+$. The numerical method that we have chosen for the time integration of system (3.7) is the θ-method that is a numerically stable implicit finite difference method, where the numerical solution is related to an arbitrary parameter θ in the interval [0,1]. With this method, the numerical solution of the time derivative vector $\dot{\mathbf{T}}$ is obtained approximating its exact solution in successive time instants t_i, for i =1, 2, …, L, which discretize the time interval I_T. The subintervals of I_T can have a variable size, but here we consider an equal decomposition in L subintervals, i.e.

$$\Delta t = \frac{t_f - t_0}{L}.$$

To apply the method, first the system (3.7) is rewritten as,

$$\dot{\mathbf{T}} = -\mathbf{A}^{-1}\mathbf{B}\mathbf{T} + \mathbf{A}^{-1}\mathbf{C} + \mathbf{A}^{-1}\mathbf{D} \tag{3.8}$$

Then, considering for simplicity $\mathbf{F} = -\mathbf{A}^{-1}\mathbf{B}\mathbf{T} + \mathbf{A}^{-1}\mathbf{C} + \mathbf{A}^{-1}\mathbf{D}$, and assuming that $\mathbf{T}_i = \mathbf{T}(\mathbf{r}, t_i)$, $\mathbf{F}_i = \mathbf{F}(\mathbf{r}, t_i)$ and $\mathbf{T}_0 = \mathbf{T}(\mathbf{r}, t_0)$ as the initial condition, the scheme of the θ-method is

$$\begin{cases} \dfrac{\mathbf{T}_i - \mathbf{T}_{i-1}}{\Delta t} = \theta \mathbf{F}_i + (1-\theta)\mathbf{F}_{i-1} \\ \mathbf{T}(t_0) = \mathbf{T}_0 \end{cases} \text{, for } i = 1, 2, \dots, L \tag{3.9}$$

Now, substituting **F** with $-\mathbf{A}^{-1}\mathbf{B}\mathbf{T} + \mathbf{A}^{-1}\mathbf{C} + \mathbf{A}^{-1}\mathbf{D}$, the first equation of system (3.9) becomes

$$\frac{\mathbf{T}_i - \mathbf{T}_{i-1}}{\Delta t} = \theta\left(-\mathbf{A}^{-1}\mathbf{B}\mathbf{T}_i + \mathbf{A}^{-1}\mathbf{C} + \mathbf{A}^{-1}\mathbf{D}_i\right) + (1-\theta)\left(-\mathbf{A}^{-1}\mathbf{B}\mathbf{T}_{i-1} + \mathbf{A}^{-1}\mathbf{C} + \mathbf{A}^{-1}\mathbf{D}_{i-1}\right)$$

Multiplying each term of this last equation by Δt and moving all variables $\mathbf{T}_i$ on the left side, we have

$$\mathbf{T}_i + \Delta t\theta\mathbf{A}^{-1}\mathbf{B}\mathbf{T}_i = \mathbf{T}_{i-1} + \Delta t\theta\mathbf{A}^{-1}\mathbf{D}_i + \Delta t(1-\theta)\left(-\mathbf{A}^{-1}\mathbf{B}\mathbf{T}_{i-1} + \mathbf{A}^{-1}\mathbf{D}_{i-1}\right) + \Delta t\mathbf{A}^{-1}\mathbf{C}$$

that, factoring out common values, becomes

$$\left(\mathbf{I} + \Delta t\theta\mathbf{A}^{-1}\mathbf{B}\right)\mathbf{T}_i = \left[\mathbf{I} - \Delta t(1-\theta)\mathbf{A}^{-1}\mathbf{B}\right]\mathbf{T}_{i-1} + \Delta t\mathbf{A}^{-1}\left[\mathbf{C} + \theta\mathbf{D}_i + (1-\theta)\mathbf{D}_{i-1}\right]$$

with **I** the identity matrix.

Then, multiplying by **A**, we have

$$\left(\mathbf{A} + \Delta t\theta\mathbf{B}\right)\mathbf{T}_i = \left[\mathbf{A} - \Delta t(1-\theta)\mathbf{B}\right]\mathbf{T}_{i-1} + \Delta t\left[\mathbf{C} + \theta\mathbf{D}_i + (1-\theta)\mathbf{D}_{i-1}\right] \quad (3.10)$$

Finally, considering the following expressions

$$\mathbf{P} = \mathbf{A} + \Delta t\theta\mathbf{B}$$

$$\mathbf{R} = \mathbf{A} - \Delta t(1-\theta)\mathbf{B}$$

$$\mathbf{E}_i = \mathbf{R}\mathbf{T}_{i-1} + \Delta t\left[\mathbf{C} + \theta\mathbf{D}_i + (1-\theta)\mathbf{D}_{i-1}\right]$$

and substituting them in Eq. (3.10), we obtain

$$\mathbf{P}\mathbf{T}_i = \mathbf{R}\mathbf{E}_i \quad (3.11)$$

that is the system to solve for each time instant.

As **D** is associated with the heating power deposition due to the MNP excitation and field exposure, it appears in $\mathbf{E}_i$ only when the field is switched on, otherwise it is considered null.

For the selection of the parameter θ, varying its value we can obtain several well-known methods; in fact, for θ = 0 it corresponds to the explicit Euler method (forward difference formula), θ = 1/2 to the Crank-Nicolson method and θ = 1 to the implicit Euler method (backward difference formula). To solve the current problem, expressed by Eq. (3.11) with the initial condition $\mathbf{T}_0 = \mathbf{T}(r, t_0)$, we choose θ = 2/3, as the oscillation errors are reduced with respect to the other values of the parameter [4]. Moreover, for θ ≥ 1/2 the method is unconditionally stable.

3.4 Validation of the solver

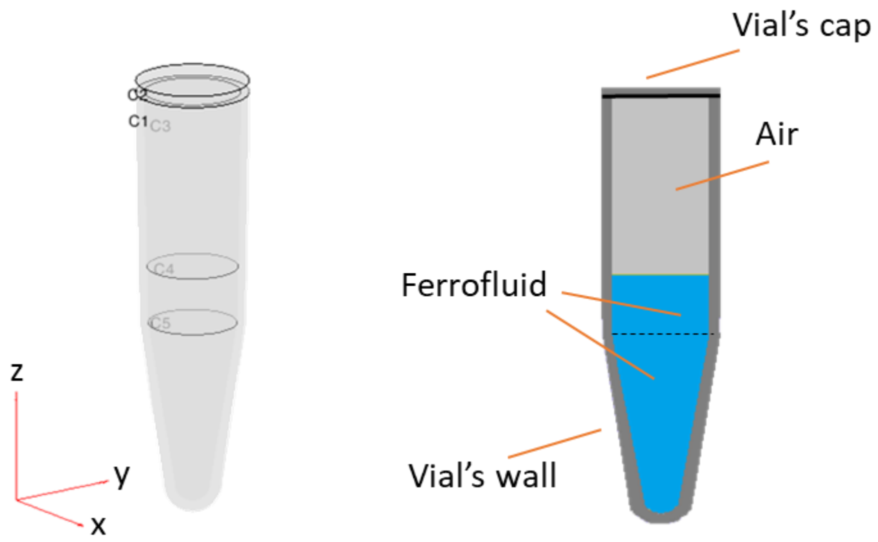

Figure 3.2. Schematics of vial's structure. Left: a 3D view of the vial with the five regions labeled C1 for the vial's wall, C2 for the vial's cap, C3 for the air, C4 and C5 for the liquid containing MNPs. Right: 2D map of the vial with each material colored with different colors: dark grey for propylene, light grey for air and light blue for liquid.

To validate our code, we compare our numerical results with the ones obtained with the MATLAB®'s Partial Differential Equation Toolbox [5]. The MATLAB®'s toolbox provides functions for solving the most common partial differential equations (e.g. wave equation, heat transfer equation, linear elasticity equation, etc.) using FEM-based analysis. Direct time integration solvers are also provided in the toolbox for the transient-state problems.

For this comparison, we evaluate the temperature within a 3D reconstruction of a vial. The geometry is designed and then discretized into a tetrahedral mesh by means of the software COMSOL®. The vial has a maximum diameter of 0.78 cm, with a wall thickness of 0.6 mm, and a height of 3.08 cm. The mesh is composed of about 32 thousand tetrahedra with an average size of 0.39 mm. In addition, the geometry is subdivided into 5 regions (see schematics in Figure 3.2): vial's cap and vial's wall considered to be made in polypropylene, an internal region of air, and two volumes that correspond to the suspension. For the simulations here presented, we consider a water-based suspension, and the material parameters are set as follows:

- polypropylene: ρ = 905 kg/m^3, C_p = 1900 J/(kg·K), k = 0.185 W/(m·K).
- Water: ρ = 997.05 kg/m^3, C_p = 4183 J/(kg·K), k = 0.6 W/(m·K).
- Air: ρ = 1.16 kg/m^3, C_p = 1007 J/(kg·K), k = 0.026 W/(m·K).

The heat transfer rate is set at 20 W/(m^2·K), the heating power Q_{MNPs} is considered to be fixed to 88 kW/m^3 in the whole suspension, Q_{EM} is assumed to be negligible, i.e. equal to zero, and we consider an initial temperature of 25 °C. The MNPs here considered are permalloy nanodisks whose SLP value, in water-based suspension, is estimated through micromagnetic modelling analysis [6].

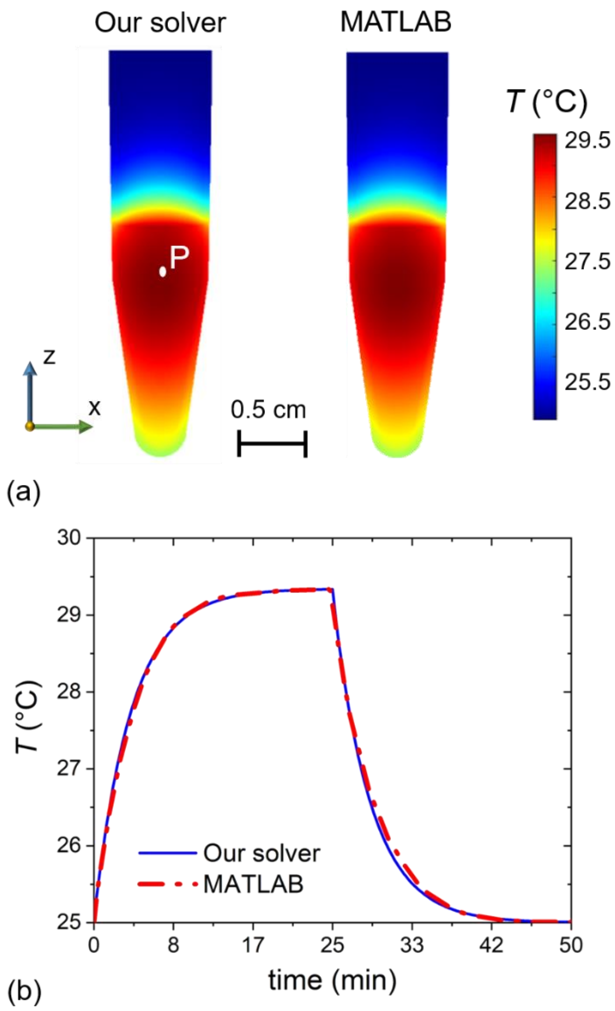

Figure 3.3. Comparison between the results obtained with our solver and the MATLAB® PDE Toolbox. (a) Maps of the temperature spatial distribution at thermal equilibrium calculated over the central longitudinal section of the vial, with P indicating the point that reaches the maximum temperature. (b) The heating-cooling transients evaluated at point P.

Specifically, the value of Q_{MNPs} is obtained considering an SLP equal to 440 W/g multiplied by a MNP concentration of 0.2 mg/ml in the whole suspension. For the time interval, we consider 25 min of heating and successive 25 min of cooling.

We evaluate the solution with our solver with a fixed time step of 10 s, whereas the solution with the MATLAB's toolbox has a shorter time step of 3 s, because we assume it as our reference solution. In Figure 3.3 we report the results obtained with the two methods. Specifically, Fig. 3.3a shows the 2D temperature maps on the central longitudinal section of the vial at the end of the heating time (i.e. at 25 min), when the ferrofluid reaches its temperature equilibrium. The maps show that the temperatures calculated with our solver are in good agreement with the MATLAB's solution; in fact, the discrepancy between the solutions has a maximum value of 0.6% and an average of 0.3%. Whereas Figure 3.3b illustrates the heating-cooling transients for a fixed point, which is located in the central area of the vial, where the suspension reaches the maximum temperature, and is displayed in Fig. 3.3a by point P. The curves are not coincident, but they have very similar temperature values during the whole time interval. Thus, the implemented θ-method enables us to obtain accurate results, comparable to the ones obtained with the MATLAB's toolbox.

3.5 References

[1] P. Lemal, C. Geers, B. Rothen-Rutishauser, M. Lattuada, and A. Petri-Fink, "Measuring the heating power of magnetic nanoparticles: an overview of currently used methods," *Mater. Today*, vol. 4, pp. S107–S117, 2017. DOI: 10.1016/j.matpr.2017.09.175.

[2] M. Coïsson et al., "Specific loss power measurements by calorimetric and thermal methods on γ-Fe2O3 nanoparticles for magnetic hyperthermia," *J. Magn. Magn. Mater.*, vol. 473, pp. 403–409, 2019. DOI: 10.1016/j.jmmm.2018.10.107.

[3] M. Coïsson et al., "Hysteresis losses and specific absorption rate measurements in magnetic nanoparticles for hyperthermia applications," *Biochim. Biophys. Acta Gen. Subj.*, vol. 1861, no. 6, pp. 1545–1558, 2017. DOI: 10.1016/j.bbagen.2016.12.006.

[4] O. C. Zienkiewicz, R. L. Taylor, and J. Z. Zhu, The finite element method: Its basis and fundamentals, 7th ed. Oxford, England: Butterworth-Heinemann, 2013.

[5] https://it.mathworks.com/products/pde.html.

[6] A. Manzin, R. Ferrero, and M. Vicentini, "From micromagnetic to in silico modeling of magnetic nanodisks for hyperthermia applications," *Adv. Theory Simul.*, p. 2100013, 2021. DOI: 10.1002/adts.202100013.

Chapter 4

Numerical integration of thermal problem in living tissues

Part of the material presented in this chapter is published in Computer Methods and Programs in Biomedicine 223: 106975, August 2022

In this Chapter, we introduce the numerical model developed to simulate the thermal effects induced by the AC magnetic field exposure and MNP excitation in living tissues. First, we introduce the Pennes' bioheat equation, which is the equation that governs the phenomenon. Second, in analogy with the previous chapters, we describe how we obtain the numerical solution of this equation, from the application of the FEM for the spatial discretization to the implementation of the θ-method for the time discretization. Third, we validate the developed numerical model by comparing the results obtained in a simplified geometry to the solution evaluated with the software Sim4Life®. Finally, we introduce the computational anatomical phantoms in which the studies presented in this Thesis are performed.

4.1 The Pennes' bioheat transfer equation

The Pennes' bioheat transfer equation is considered a standard model for predicting temperature distributions within living tissues. Pennes proposed the equation in 1948 after the conduction of a sequence of experiments where temperatures of tissue and arterial blood were measured in resting human forearms. The equation is an energy balance equation between the conductive heat transfer, the heat generated by the metabolism, and the heat exchange between blood flow and solid tissues [1-4]. Additional terms can be added to represent the heat deposition into tissues due to possible external heating sources. The main limitations of the Pennes' equation are the assumption that the arterial blood temperature is assumed to be constant, from the heart to capillaries; moreover, it does not consider the direction of blood flow and it supposes a uniform perfusion rate [5]. However, the equation is widely used thanks to its simplicity, in terms of mathematical formulation, and the reasonable agreements obtained with experimental data in a wide class of problems [1,6].

4.2 The bioheat equation in magnetic hyperthermia

Let Ω the region occupied by the human/animal body under study, and ∂Ω its boundary. The hyperthermia effects induced in the living tissues of Ω, are described by the Pennes' equation as follows:

$$\begin{aligned}\rho(\mathbf{r})C_\mathrm{p}(\mathbf{r})\frac{\partial T(\mathbf{r},t)}{\partial t} &= \nabla\cdot k\nabla T(\mathbf{r},t)+Q_\mathrm{m}+\\ &-WC_\mathrm{blood}\left(T(\mathbf{r},t)-T_\mathrm{blood}\right)+\Gamma Q_\mathrm{MNPs}(\mathbf{r},t)+Q_\mathrm{EM}(\mathbf{r},t)\end{aligned} \tag{4.1}$$

where ρ is the tissue density, C_p the tissue heat capacity, k the tissue thermal conductivity, T and T_blood are the tissue temperature and the arterial blood temperature respectively, Q_m is the metabolic heat produced per unit volume, W is the tissue-blood perfusion rate, and C_blood is the blood heat capacity. Moreover, the external heating power deposition is split into two terms [5]: one is due to the heat released by the MNP excitation, Q_MNPs, and the other one is produced by the applied AC magnetic field, Q_EM. The term $W\mathrm{C}_\mathrm{blood}(T\text{-}T_\mathrm{blood})$ describes the effects of blood perfusion, which can be the physiological dominant form of energy transfer in heating processes [4,7]. Γ is the piecewise function equal to 1 in the tissue regions where MNPs are distributed and zero elsewhere, see schematic in Figure 4.1.

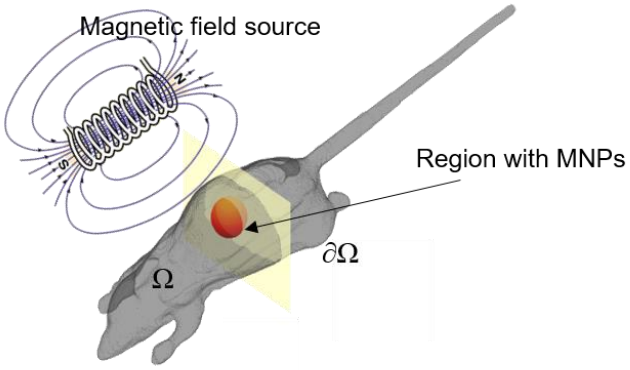

Figure 4.1. Schematic of the domain Ω represented by the mouse body, with ∂Ω the interface between the skin and the surrounding air. The red sphere indicates the inner region where MNPs are injected and the magnetic field source is defined by the external solenoid.

The boundary condition describes the heat exchange at the interface $\partial\Omega$ between the skin and the surrounding air and is defined by

$$q = -k\frac{\partial T}{\partial n} = -h\left(T_{\mathrm{air}} - T_{\mathrm{skin}}\right) \tag{4.2}$$

where q is the outward heat flux, T_{air} is the temperature of the air, T_{skin} is the skin temperature and h is the convection heat transfer coefficient at the interface. The initial condition, i.e. at $t = 0$, corresponds to the steady-state temperature distribution before the heating due to MNPs and EM field exposure, which is governed by the metabolic heat only.

In Eq. (4.1) we do not take into account the thermoregulatory response, i.e. disregarding the fact that the blood perfusion is temperature dependent. This decision is based on the fact that animals are generally anesthetized during hyperthermia experiments, resulting in the inactivation of the thermoregulatory response, as well as a reduction in blood flow and basal metabolism [8,9]. The eddy current effects are more severe under these conditions, with a high risk of tissue damage. A lesser increase in temperature is expected if thermoregulatory systems are present (without anesthesia). As a result, when we exclude this dependence, we get higher precautionary levels.

4.3 Numerical solution

As done in Chapter 3, to numerically solve the thermal problem defined by Eq. (4.1) and Eq. (4.2), first the weak formulation of the Pennes' equation is derived, then the matrix notation for the resulting system obtained from the application of FEM is formulated; finally, the time integration is described. All the mathematical passages are not expounded in detail in this chapter, as they are analogous to the ones illustrated in Chapters 2 and 3.

4.3.1 Weak formulation

Let w, $w = w(\mathbf{r})$, denote the test function and U the functional space, with $T \in U$ and $U \subset \mathrm{H}_0^1(\Omega)$. Applying the weak formulation to Eq. (4.1), we have

$$\begin{aligned}\int_\Omega \rho C_\mathrm{p} \frac{\partial T}{\partial t} w dV = & -\int_\Omega k \nabla T \cdot \nabla w dV + \int_{\partial\Omega} k \frac{\partial T}{\partial n} w ds + \int_\Omega Q_\mathrm{m} w dV + \\ & -\int_\Omega W C_\mathrm{blood} T w dV + \int_\Omega W C_\mathrm{blood} T_\mathrm{blood} w dV + \int_\Omega \Gamma Q_\mathrm{MNPs} w dV + \int_\Omega Q_\mathrm{EM} w dV\end{aligned} \tag{4.3}$$

We can rewrite the surface integral of Eq. (4.3) considering the boundary condition (4.2), and we obtain the following weak form of the problem

$$\begin{aligned}\int_\Omega \rho C_\mathrm{p} \frac{\partial T}{\partial t} w dV = & -\int_\Omega k \nabla T \cdot \nabla w dV + \int_{\partial\Omega} h\left(T_\mathrm{air} - T_\mathrm{skin}\right) w ds + \int_\Omega Q_\mathrm{m} w dV + \\ & -\int_\Omega W C_\mathrm{blood} T w dV + \int_\Omega W C_\mathrm{blood} T_\mathrm{blood} w dV + \int_\Omega \Gamma Q_\mathrm{MNPs} w dV + \int_\Omega Q_\mathrm{EM} w dV\end{aligned} \tag{4.4}$$

for all w belonging to U.

4.3.2 FEM discretization

Let consider $\{\varphi_1, \ldots, \varphi_N\}$ the set of basis linear functions for the FEM discretization and $\{\alpha_1, \ldots, \alpha_N\}$ the corresponding set of unknown coefficients. The approximation of the temperature T can be described by the following discretization

$$T \cong \sum_{i=1}^{N} \varphi_i \alpha_i = \mathbf{\Phi T} \cdot \tag{4.5}$$

Substituting the test function with the basis function φ_j and T with the discrete expression (4.5) in Eq. (4.4), we obtain

$$\begin{aligned}
&\sum_i \int_\Omega \rho C_\text{p} \frac{\partial \alpha_i}{\partial t} \varphi_i \varphi_j dV + \sum_i \int_\Omega k \alpha_i \nabla \varphi_i \cdot \nabla \varphi_j dV + \sum_i \int_\Omega W C_\text{blood} \alpha_i \varphi_i \varphi_j dV + \\
&\quad + \sum_i \int_{\partial\Omega} h \alpha_i \varphi_i \varphi_j ds = \int_{\partial\Omega} h T_\text{air} \varphi_j ds + \int_\Omega W C_\text{blood} T_\text{blood} \varphi_j dV + \\
&\quad + \int_\Omega \Gamma Q_\text{MNPs} \varphi_j dV + \int_\Omega Q_\text{EM} \varphi_j dV + \int_\Omega Q_\text{m} \varphi_j dV
\end{aligned} \tag{4.6}$$

for $j = 1, 2, \ldots, N$. Then, the system of Eq.s (4.6) in its matrix notation is

$$\mathbf{A\dot{T}} + \mathbf{BT} = \mathbf{C} + \mathbf{D} \tag{4.7}$$

where

$\mathbf{T} \in \mathbb{R}^N$, α_i for i =1, 2, …, N, is the vector of unknown coefficients of Eq. (4.5).

$\dot{\mathbf{T}} \in \mathbb{R}^N$, $\dot{T}_i = \dfrac{\partial \alpha_i}{\partial t}$ for i =1, 2, …, N is the vector of time derivatives related to the unknown coefficients α_i.

$\mathbf{A} \in \mathbb{R}^{N\times N}$, $a_{ij} = \int_\Omega \rho C_\text{p} \varphi_i \varphi_j dV$ for i, j =1, 2, …, N.

$\mathbf{B} \in \mathbb{R}^{N\times N}$, $b_{ij} = \int_\Omega k \nabla \varphi_i \cdot \nabla \varphi_j dV + \int_\Omega W C_\text{blood} \varphi_i \varphi_j dV + \int_{\partial\Omega} h \varphi_i \varphi_j ds$ for i, j = 1, 2, …, N.

$\mathbf{C} \in \mathbb{R}^N$, $c_j = \int_\Omega h T_\text{air} \varphi_j ds + \int_\Omega W C_\text{blood} T_\text{blood} \varphi_j dV + \int_\Omega Q_\text{m} \varphi_j dV$ for j =1, 2, …, N.

$\mathbf{D} \in \mathbb{R}^N$, $d_j = \int_\Omega \Gamma Q_\text{MNPs} \varphi_j dV + \int_\Omega Q_\text{EM} \varphi_j dV$ for j =1, 2, …, N.

4.3.3 Time integration

For the time integration of the system (4.7), the θ-method is applied with θ set at 2/3. System (4.7) is written to have the same type of matrices as in the system

(3.7) of Chapter 3, with **A**, **B**, and **C** the time-independent matrices that are calculated only one time before the time integration, and **D** the time-dependent matrix to compute at each time instant of the simulation.

The time variable t ranges over a fixed closed interval, $I_T = \left[t_0, t_f\right] \subset \mathbb{R}^+$ discretized into L subintervals, and the time steps are considered to be equal to each other and are specified by

$$\Delta t = \frac{t_f - t_0}{L} .$$

Applying the θ-method as seen in Chapter 3, we finally have to solve for each time instant the following system of equations

$$\mathbf{P}\mathbf{T}_i = \mathbf{R}\mathbf{E}_i \tag{4.8}$$

with

$$\mathbf{P} = \mathbf{A} + \Delta t \theta \mathbf{B},$$

$$\mathbf{R} = \mathbf{A} - \Delta t \left(1-\theta\right)\mathbf{B},$$

$$\mathbf{E}_i = \mathbf{R}\mathbf{T}_{i-1} + \Delta t\left[\mathbf{C} + \theta \mathbf{D}_i + \left(1-\theta\right)\mathbf{D}_{i-1}\right].$$

4.4 Validation

We compare the numerical solutions obtained through the custom-build thermal solver, implemented within the MATLAB® environment, with the numerical results obtained with the commercial software Sim4Life® [10]. We evaluate the solutions on the same 3D prism-shaped geometry used for the low-frequency EM field solver in Sub-section 2.3.2. For this comparison, the solutions obtained with Sim4Life® are evaluated employing the finite-difference time-domain (FDTD) method, and are performed by Ioannis Androulakis (Erasmus MC Cancer Institute). The heat transfer coefficient h is set at 3.5 W/(m^2·K) on the external surface of the skin mimicking layer. The external heating power deposition defined by Q_{EM} is determined by the scalar potential evaluated with the solution reported in Sub-section 2.3.2, whereas Q_{MNPs} is assumed to be null, as it is considered for simplicity that no MNPs are distributed within the domain and only eddy current effects are present.

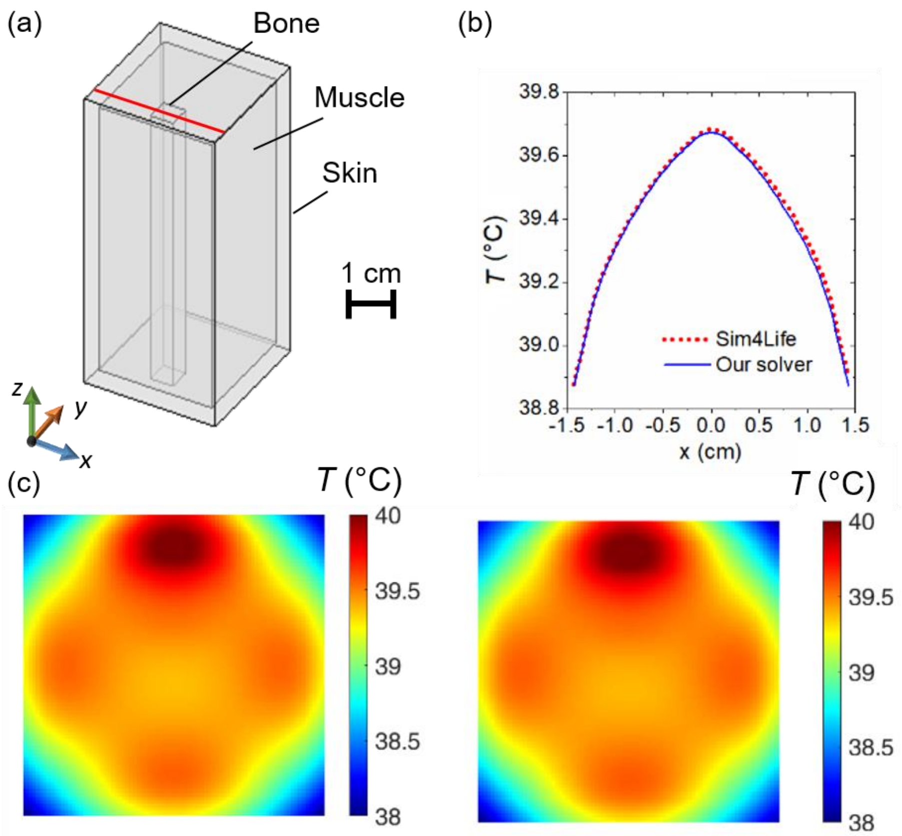

Figure 4.2. (a) Schematic of the calculation domain. (b) Temperature spatial variation at thermal equilibrium, evaluated along a line at half height of the domain and parallel to the red line depicted in the schematic in (a). (d) Comparison of the temperature maps at equilibrium evaluated on the median cross-section, with on the left the results obtained with our solver and on the right with Sim4Life®. Adaptation of the graphs reported in [9].

As a first comparison, we evaluate the temperature in the stationary case, i.e. assuming the time derivative of temperature is equal to zero. The results are compared in Figure 4.2, where we report the spatial distribution of the temperature at the equilibrium calculated along a line parallel to the x-axis that intersects the bone mimicking region (i.e. parallel to the red line in Fig. 4.2a) and on a 2D median section of the domain (the same considered in Fig. 2.6). The results obtained with the two solvers show a very good agreement, in fact the average and the maximum discrepancies are equal to 0.008% and 0.3% respectively.

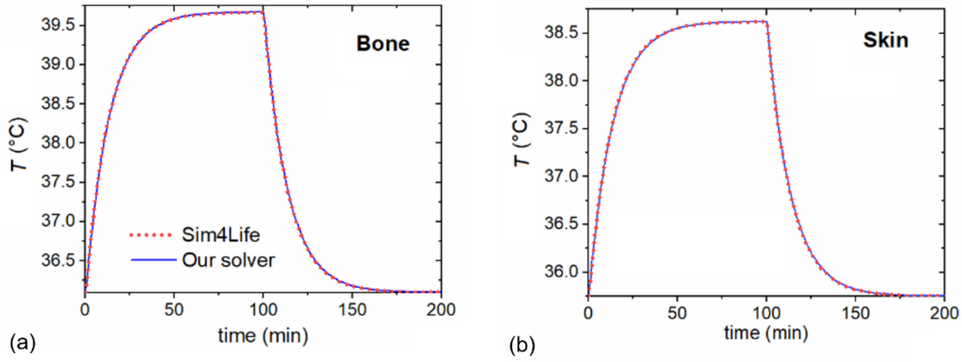

Figure 4.3. Comparison between the time evolutions of the temperature evaluated with our solver (blue line) and with Sim4Life®(red dotted line). Two different points of calculation are considered: (a) one inside the bone region, and (b) one inside the skin region. Adaptation of the graphs reported in [9].

Then, we evaluate the temperature in the transient case, considering a heating time of 100 min and a following cooling time with the same duration. For both solvers, the time-step is constant and fixed to 1 min, and for the initial temperature, we consider the spatial distribution of the temperature evaluated in the absence of the EM field (i.e., due to the only metabolic heat). Figure 4.3 shows the time evolutions of the temperature evaluated at two different point locations, one in the bone mimicking region (Fig. 4.3a) and one in the skin mimicking region (Fig. 4.3b). The discrepancies averaged throughout the entire time interval are in the order of 0.2%, which confirms the good agreement between the solution obtained with our solver and the one with Sim4Life® also for the transient case.

4.5 Computational murine models

The models described in this Chapter and in Chapter 2 are developed to be applied to computational anatomical phantoms of living beings. In particular, in this Thesis these models are applied to murine models, as the focus is on preclinical tests. The computational anatomical phantoms considered in this Thesis are voxel-based models of mice and rats. These types of phantoms arise in pre-clinical dosimetry studies in the 1980s from the need to have models to estimate radiation dose in biological media from non-ionizing and ionizing radiation exposures [11,12]. Models of humans and several types of animals are currently available, especially mice and rats, but also monkeys, pigs, and rabbits [13-16]. In particular, computational voxel-based phantoms describe the anatomy by matrices of voxels (three-dimensional volume elements with cubic shape), specifying the tissue or organ to which they belong. The voxel discretization is extracted from cross-sectional images, typically computed tomography, magnetic resonance, or cryosection images.

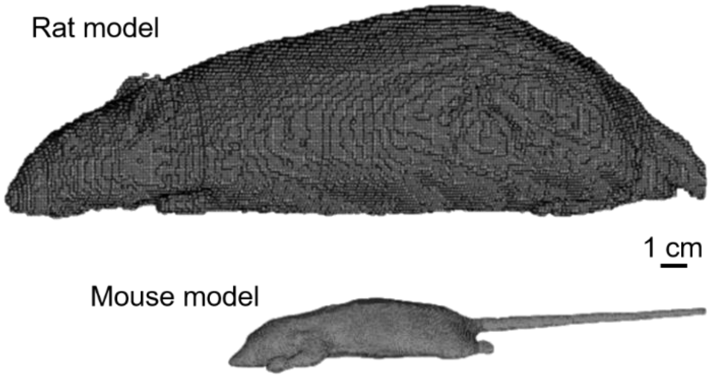

Figure 4.4. Voxel structure of the two murine models considered: (top) Sprague Dawley rat, (down) male nude normal mouse.

The computational phantoms considered in this Thesis are two murine models of different sizes with high detailed resolution quality, both provided by the IT'IS Foundation [13]. The animal models, illustrated in Figure 4.4, are:

- "Diggy" male nude normal mouse, which is an adaptation from the "Digimouse" model [15]. Specifically, it corresponds to a mouse with a weight of 28 g and a length of 8.6 cm, tail excluded. It is composed of voxels with an average size of 0.25 mm.
- Sprague Dawley rat, with a weight of 503 g and a body length of 22.5 cm, tail excluded. The model corresponds to a female rat with three tumors inside and it is discretized in voxels with a size equal to 1 mm.

Both the models are composed of more than forty tissues and the rat model is the most detailed one, as tissues such as tongue, nails, teeth, nerves, tendons, and blood vessels are included in the phantom. Figure 4.5 displays the mouse model cut in half to show the internal structure. To apply FEM, each voxel of the phantoms is split into six tetrahedral elements.

4.6 Parameter acquisition

In the Pennes' bioheat equation the physical properties of the tissues involved are the density, heat capacity, thermal conductivity, metabolic heat, and tissue-blood perfusion rate. The density is derived from mass and volume measurements on tissue samples [17] or estimated *in vivo* from computed tomography scan data [18]. Heat capacity can be measured through a calorimeter or by means of hot-

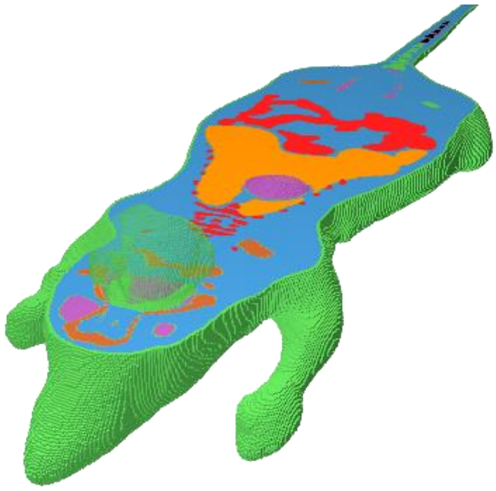

Figure 4.5. Mouse model details. Tissues are represented by different colors, such as light blue for fat, green for skin and brain, and orange for lung.

water bath and it is in general obtained with *in vitro* measurements of excised tissues. The thermal conductivity is measured by applying a thermal gradient on a given tissue volume, recording the equilibrium temperature of the sample. The tissue-blood perfusion rate is calculated as the product between the blood density, the tissue density, and the heat transfer rate, which is measured by clearance and microsphere trapping methods based on the use of radioactive tracers [19]. Finally, the metabolic heat is calculated as the product between the tissue density and the heat generation rate of the tissue, which is related to the heat transfer rate [19].

For all the simulations of the temperature in living tissues, apart from the parameters of the rat tumors, the values of tissue density, heat capacity, thermal conductivity, heat transfer rate, and heat generation rate are taken from the IT'IS database [13]. Most of the measured thermal properties included in the database are taken from the works of McIntosh, Anderson, and Duck, [19,20]. Whereas, the values of the heat generation rate reported in the database are calculated from the formula reported in [21]. For the thermal properties of the tumors present in the rat model, we consider the values reported in [22]; specifically, $\rho = 1045$ kg/m^3, $C_\mathrm{p} = 3760$ J/(K·kg), $k = 0.51$ W/(K·m), $Q_\mathrm{m} = 31872.5$ W/m^3, and $W = 9.97$ kg/(s·m^3).

4.7 References

[1] H. H. Pennes, "Analysis of tissue and arterial blood temperature in the resting human forearm," *J. Appl. Physiol.*, vol. 1, no. 2, pp. 93–122, 1948. DOI: 10.1152/jappl.1948.1.2.93.

[2] D. Poljak and M. Cvetković, "Biomedical Applications of Electromagnetic Fields in Human interaction with electromagnetic fields computational models in dosimetry", 1st ed. St. Louis, Missouri: Elsevier Ltd. :Academic Press, 2019, pp. 199-239.

[3] S. Ahmed, B. L. Rajak, M. Gogoi, and H. D. Sarma, "Magnetic nanoparticles mediated cancer hyperthermia," in *Smart Healthcare for Disease Diagnosis and Prevention*, Elsevier, 2020, pp. 153–173. DOI: 10.1016/B978-0-12-817913-0.00016-X.

[4] H.-W. Huang and T.-L. Horng, "Bioheat transfer and thermal heating for tumor treatment," in *Heat Transfer and Fluid Flow in Biological Processes*, Elsevier, 2015, pp. 1–42. DOI: 10.1016/B978-0-12-408077-5.00001-8.

[5] C. Tucci, M. Trujillo, E. Berjano, M. Iasiello, A. Andreozzi, and G. P. Vanoli, "Pennes' bioheat equation vs. porous media approach in computer modeling of radiofrequency tumor ablation," *Sci. Rep.*, vol. 11, no. 1, p. 5272, 2021. DOI: 10.1038/s41598-021-84546-6.

[6] Y. Zhang, "Generalized dual-phase lag bioheat equations based on nonequilibrium heat transfer in living biological tissues," *Int. J. Heat Mass Transf.*, vol. 52, no. 21–22, pp. 4829–4834, 2009. DOI: 10.1016/j.ijheatmasstransfer.2009.06.007.

[7] A. Manzin, R. Ferrero, and M. Vicentini, "From micromagnetic to in silico modeling of magnetic nanodisks for hyperthermia applications," *Adv. Theory Simul.*, p. 2100013, 2021.

[8] S. Kodera, J. Gomez-Tames, A. Hirata, H. Masuda, T. Arima, and S. Watanabe, "Multiphysics and thermal response models to improve accuracy of local temperature estimation in rat cortex under microwave exposure," *Int. J. Environ. Res. Public Health*, vol. 14, no. 4, p. 358, 2017. DOI: 10.3390/ijerph14040358.

[9] A. Hirata *et al.*, “Computational verification of anesthesia effect on temperature variations in rabbit eyes exposed to 2.45 GHz microwave energy,” *Bioelectromagnetics*, vol. 27, no. 8, pp. 602–612, 2006. DOI: 10.1002/bem.20251.

[10] M. Vicentini, M. Vassallo, R. Ferrero, I. Androulakis, and A. Manzin, “In silico evaluation of adverse eddy current effects in preclinical tests of magnetic hyperthermia,” *Comput. Methods Programs Biomed.*, vol. 223, no. 106975, 2022. DOI: 10.1016/j.cmpb.2022.106975.

[11] M. Zankl, J. Becker, C. Lee, W. E. Bolch, Y. S. Yeom, and C. H. Kim, “Computational phantoms, ICRP/ICRU, and further developments,” *Ann. ICRP*, vol. 47, no. 3–4, pp. 35–44, 2018. DOI: 10.1177/0146645318756229.

[12] T. Xie and H. Zaidi, “Development of computational small animal models and their applications in preclinical imaging and therapy research: Computational small animal models,” *Med. Phys.*, vol. 43, no. 1, p. 111, 2016. DOI: 10.1118/1.4937598.

[13] https://itis.swiss/.

[14] https://www.nitrc.org/frs/?group_id=1081.

[15] https://neuroimage.usc.edu/neuro/Digimouse.

[16] M. Mitrovic *et al.*, “Voxel model of a rabbit: assessment of absorbed doses in organs after CT examination performed by two different protocols,” *Radiat. Environ. Biophys.*, vol. 60, no. 4, pp. 631–638, 2021. DOI: 10.1007/s00411-021-00941-7.

[17] W. S. Erdmann and T. Gos, “Density of trunk tissues of young and medium age people,” *J. Biomech.*, vol. 23, no. 9, pp. 945–947, 1990. DOI: 10.1016/0021-9290(90)90360-f.

[18] H. K. Huang and S. C. Wu, “The evaluation of mass densities of human body in vivo from CT scans,” *Comput. Biol. Med.*, vol. 6, no. 4, pp. 337–343, 1976. DOI: 10.1016/0010-4825(76)90070-6.

[19] R. L. Mcintosh and V. Anderson, “A comprehensive tissue properties database provided for the thermal assessment of a human at rest,” *Biophys. Rev. Lett.*, vol. 05, no. 03, pp. 129–151, 2010. DOI: 10.1142/S1793048010001184.

[20] F. A. Duck, “Physical properties of tissue: a comprehensive reference book”, London : Academic Press, 1990.

[21] R. G. Gordon, R. B. Roemer, and S. M. Horvath, “A mathematical model of the human temperature regulatory system - transient cold exposure response,” *IEEE Trans. Biomed. Eng.*, vol. BME-23, no. 6, pp. 434–444, 1976. DOI: 10.1109/TBME.1976.324601.

[22] A. Attaluri *et al.*, “Magnetic nanoparticle hyperthermia enhances radiation therapy: A study in mouse models of human prostate cancer,” *Int. J. Hyperthermia*, vol. 31, no. 4, pp. 359–374, 2015. DOI: 10.3109/02656736.2015.1005178.

Chapter 5

Numerical simulations to support thermometric characterization of magnetic nanoparticles

The material presented in this chapter is published in Advanced Theory and Simulations 4 (5): 2100013, May 2021 and Nanomaterials 11 (9): 2179, August 2021

The search for new strategies to obtain magnetic nanoparticles (MNPs) with high values of specific loss power (SLP) has led to the study of new magnetic nanostructures as an alternative to superparamagnetic iron oxide nanoparticles (SPIONs), which are typically employed for clinical uses. A new generation of promising nanostructures for magnetic hyperthermia is represented by magnetic nanodisks, nanorings, nanocubes and nanoflowers made of different materials [1-5]. Here we focus on permalloy ($Ni_{80}Fe_{20}$) nanodisks and iron oxide (Fe_3O_4) nanocubes. Magnetic nanodisks present the advantage that can be characterized by vortex state at remanence, which leads to low probabilities of aggregation due to small magnetostatic interactions, making them particularly suitable for biomedical applications. Moreover, several studies proved that magnetic nanodisks show higher values of SLP, with respect to SPIONs [2,6,7,8], and present a good biocompatibility, especially when coated with a gold layer [9].

Good heating efficiency was also observed for Fe_3O_4 nanocubes, in both *in vitro* and *in vivo* studies for the treatment of tumors [10,11]. In addition, calorimetric and thermometric measurements documented an enhancement of SLP in comparison to spherical Fe_3O_4 NPs of certain sizes, due to the introduction of shape anisotropy [12,13].

In this Chapter, we present the numerical simulations of the thermal problem described in Chapter 3. The simulations are performed to support thermometric measurements for testing the heating properties of MNPs. In particular, we analyze the role of non-adiabatic conditions and the duration of the heating-cooling transients during measurements, as well as the influence of MNP concentration in the magnetic suspension and dispersing medium (water or gel). For a better understanding of the MNP heating efficiency, in the first section of this Chapter we briefly investigate the influence of ferrofluid parameters (effective density, heat capacity and thermal conductivity) on the thermal response of the ferrofluid itself. In the second part of the Chapter, we provide a brief introduction to micromagnetic numerical modelling, which is a fundamental tool for the modeling and the study of MNP magnetization dynamics and hysteresis losses, at the basis of the heating process. In the third part of the Chapter, we report the results obtained for the analysis of permalloy nanodisks [14], where we study their heating properties in two different dispersion media, i.e. water and gel. Finally, in the last part of the Chapter, we report the study of the heating efficiency of Fe_3O_4 nanocubes and the comparison between experimental data and the numerical results evaluated with our thermal solver [15].

5.1 Influence of ferrofluid parameters on the thermal response

The ferrofluid can be approximated as a two-phase system including a solid phase (MNPs) and a liquid phase (fluid medium). MNP material defines density, heat capacity and thermal conductivity of the solid phase contributing to ferrofluid properties in proportion to the volume concentration of MNPs. For the thermal simulations, the density, the heat capacity, and the thermal conductivity of the sample must be known. Since the ferrofluid is mainly composed of a fluid that is usually water or gel, and the MNPs represent only a certain percentage of the sample, its physical properties have values that can be slightly different from those of the only fluid. To better understand the impact of these parameter variations, we perform thermal simulations with sample parameters set to ferrofluid parameters estimated as a function of MNP concentration [16].

The effective mass density ρ_{eff} of the ferrofluid is evaluated by the following expression,

$$\rho_{eff} = (1-\phi)\rho_{fluid} + \phi\rho_{MNPs} ,$$

where ϕ is the volume concentration of particles, ρ_{fluid} is the density of the fluid and ρ_{MNPs} is the density of the MNPs.

The heat capacity $C_{p,eff}$ is calculated as

$$C_{p,eff} = \frac{(1-\phi)\rho_{fluid}C_{p,fluid} + \phi\rho_{MNPs}C_{p,MNps}}{(1-\phi)\rho_{fluid} + \phi\rho_{MNPs}} ,$$

where $C_{p,fluid}$ and $C_{p,MNPs}$ are the heat capacities of the fluid and of the MNPs respectively.

The thermal conductivity is defined by

$$k_{eff} = k_{fluid}\left[\frac{k_{MNPs} + 2k_{fluid} + 2(k_{MNPs} - k_{fluid})\phi}{k_{MNPs} + 2k_{fluid} - (k_{MNPs} - k_{fluid})\phi}\right] ,$$

where k_{fluid} is the thermal conductivity of the fluid and k_{MNPs} of the MNPs.

The simulations are performed on the vial geometry considered in Chapter 3, where the sample volume is 0.2 ml. We consider that the sample is composed of water (ρ = 997.05 kg/m^3, $C_{p,fluid}$ = 4183 J/(kg·K), k_{fluid} = 0.6 W/(m·K)) and iron oxide MNPs (ρ_{MNPs} = 5200 kg/m^3, $C_{p,MNPs}$ = 670 J/(kg·K), k_{MNPs} = 6 W/(m·K) [17]) with an SLP value of 10.9 W/g [18]. We evaluate the temperature for two different MNP concentrations: 0.1 mg/cm^3 and 60 mg/cm^3, considering a heating time of 1 hour with a successive cooling time of 1 hour, an initial temperature of 24.85 °C, and the application of an AC magnetic field of frequency 150 kHz and amplitude 8 kA/m along the longitudinal axis of the vial. Considering the equations above, the resulting values of the ferrofluid parameters are:

- for the concentration of 0.1 mg/cm^3: ρ_{eff} = 997.13 kg/m3, $C_{p,eff}$ = 4182.6 J/(kg·K), k_{eff} = 0.6 W/(m·K);

- for the concentration of 60 mg/cm^3: ρ_{eff} = 1045.4 kg/m3, $C_{p,eff}$ = 3982 J/(kg·K), k_{eff} = 0.6157 W/(m·K).

We can already observe that there are no large differences between the water parameters and the ones evaluated for the ferrofluid, with consequent slight differences between the results of the thermal simulations performed on the sample with water parameters and on the two samples with ferrofluid properties, dependent on MNP concentration.

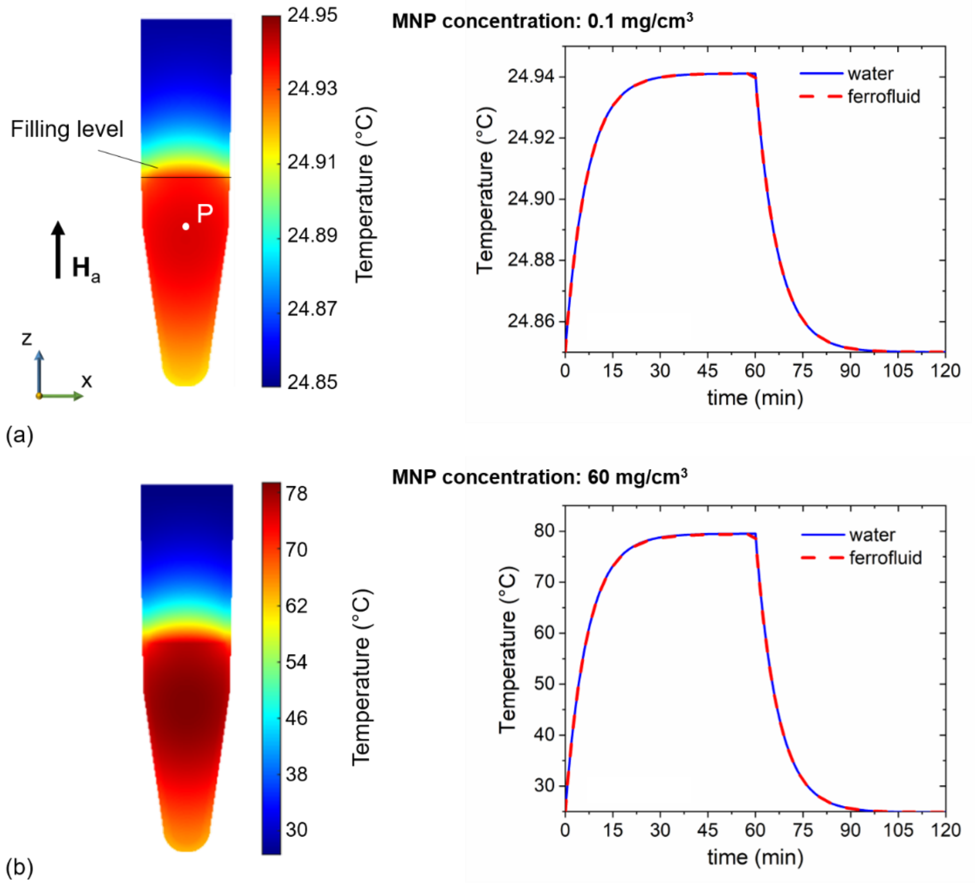

Figure 5.1. Effects of ferrofluid parameters on thermal response on two samples with concentration equal to (a) 0.1 mg/cm^3 and (b) 60 mg/cm^3, after the excitation of the MNPs with an AC magnetic field of frequency 150 kHz and amplitude 8 kA/m, along the longitudinal axis of the vial. On the left the maps of the temperature distribution at the end of the heating transient for the samples with parameters of water. On the right the comparison of the heating-cooling transients evaluated at point P, which reaches the maximum temperature and is indicated on the map in (a), for the samples with water parameters (blue line) and ferrofluid parameters (red dotted line).

As an example, in Figure 5.1 we report the results obtained with the two concentrations, where on the left the maps display the temperature distribution at the end of the heating transient for the samples with parameters of water, whereas on the right the graphs illustrate the heating-cooling transients evaluated at the point inside the sample that reaches the maximum temperature value at the end of the heating time (about 25 °C for the lowest concentration and 79 °C for the highest one). The discrepancy with the simulations obtained with the ferrofluid parameters has a maximum value of 0.00002% and 0.2% for a concentration of 0.1 mg/cm^3 and 60 mg/cm^3, respectively. Because the MNP concentrations examined in all the simulations described in this Thesis are always less than 60 mg/cm^3, if the ferrofluid parameters are set identical to the characteristics of the fluid in which MNPs are dispersed, there is no substantial impact on the thermal simulation results.

In addition, in order to investigate how the ferrofluid parameters impact on the thermal response, we simulate the time-spatial temperature evolution of the ferrofluid with a concentration of the MNPs equal to 60 mg/cm^3, varying the parameters of all the materials by 10%. First, we assume that the sample has the ferrofluid parameters and not the ones of the water. Then, we consider a scenario of maximum temperature increment, with a 10% increase in density and heat capacity, and a 10% decrease in thermal conductivity. Finally, we consider the opposite scenario, i.e. density and heat capacity with a 10% decrease and thermal conductivity with a 10% increase. With these two scenarios, we obtain a maximum temperature of 80.6 °C for the first one, and of 78.3 °C for the second one, with a difference of about 1 °C with respect to the simulation without the parameter variation.

5.2 Micromagnetic modeling analysis

To find the optimal geometrical properties of MNPs and AC magnetic field parameters (peak amplitude and frequency) that maximize the SLP of the considered nanodisks and nanocubes, a parametric analysis is performed. The SLP values derive from hysteresis losses, which correspond to the main heating contribution for the examined magnetic nanostructures. The analysis of the hysteresis loops presented in this Chapter was conducted at INRiM (Torino, Italy) by Dr. Alessandra Manzin and Dr. Riccardo Ferrero, and was performed by means of in-house micromagnetic solvers, exploiting parallel computing on graphics processing units (GPUs) [19-21]. In this Chapter, we report the main results of the micromagnetic analysis for both nanoparticles for a complete understanding of their magnetic behaviours. In particular, the SLP values of the nanodisks are estimated thanks to the micromagnetic simulations.

The micromagnetic numerical model is based on the spatial and time integration of the Landau-Lifshitz-Gilbert equation, see Appendix C,

$$\frac{\partial \mathbf{M}}{\partial t} = -\frac{\gamma}{\left(1+\alpha^2\right)} \mathbf{M} \times \left[\mathbf{H}_{\mathrm{eff}} + \frac{\alpha}{M_{\mathrm{S}}} \left(\mathbf{M} \times \mathbf{H}_{\mathrm{eff}} \right) \right] \tag{5.1}$$

where **M** is the magnetization vector, α is the damping coefficient, γ is the gyromagnetic ratio and $\mathbf{H}_{\mathrm{eff}}$ is the effective field, which is the sum of the applied external field, the exchange field, the magnetostatic field, the magnetocrystalline anisotropy field and the thermal field. The micromagnetic modeling analyses are described in detail in [14] and [15] for the nanodisks and nanocubes respectively. The simulations are first carried out on single MNPs with variable size to optimize MNP dimensions. Then, simulations are performed on MNP assemblies to study the influence of magnetostatic interactions on hysteresis loops (in terms of coercivity, remanence, and specific energy losses), for different MNP local concentration, aggregation state, and MNP-field relative orientation. Moreover, for the nanocubes, the micromagnetic model is also used to support the experimental magnetic and thermometric characterizations. The parametric analysis is performed considering the biophysical constraint imposed by the Hergt-Dutz limit [22] for the proper selection of field frequency, f, and amplitude, $\hat{H}_{\mathrm{a}}$.

5.3 Characterization of permalloy nanodisks

In this section, we present the results obtained with the analyses conducted on permalloy nanodisks. First, we present the micromagnetic analysis performed to optimize the hyperthermia properties and the selection of f and $\hat{H}_{\mathrm{a}}$, in accordance with the Hergt-Dutz limit. Then, the heating efficiency of the permalloy nanodisksis tested through the thermal solver, evaluating the temperature increment within a vial filled with ferrofluids that contain the nanodisks. The thermal analysis is focused on the optimized hyperthermia properties addressed by the micromagnetic study.

5.3.1 Optimization of heating efficiency via micromagnetic modelling

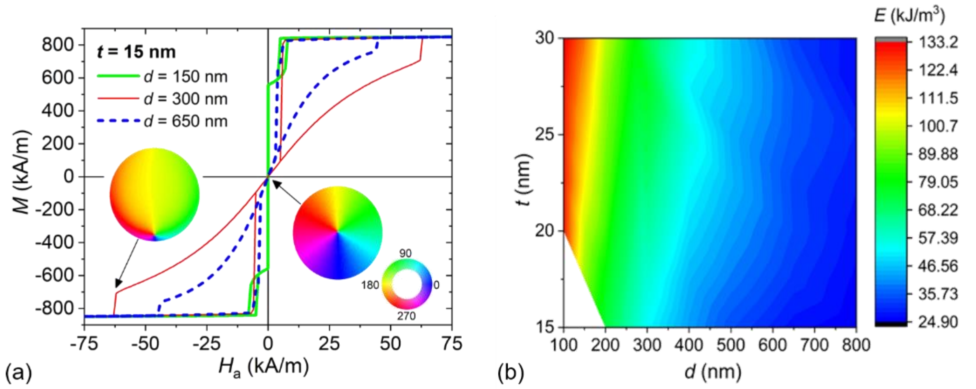

Figure 5.2. Influence of geometrical properties (thickness and diameter). (a) Comparison hysteresis loops evaluated for a fixed value of the thickness, i.e. t = 15 nm, and variable diameter (d = 150 nm, 300 nm, and 650 nm). The magnetization configurations at remanence are illustrated in the maps at the equilibrium state, immediately before the vortex expulsion, where the angle, in degrees, between the x-asis and the magnetization vector is represented with the colour wheel. (c) The specific energy losses estimated as a function of the diameter (d in the range of 100-800 nm) and thickness (t in the range of 15-30 nm), without considering the effects of thermal noise. The white area refers to conditions of no vortex nucleation.

Regarding the geometrical properties, in the micromagnetic analysis the disk diameter, *d*, is varied between 100 nm and 800 nm, and the thickness, *t*, between 15 nm and 30 nm. The analysis has proven that an optimal heating efficiency is achieved when the permalloy nanodisks have diameters in the range of 100-200 nm and thicknesses in the range of 20-30 nm. For all the considered dimensions of the nanodisks a vortex state at remanence is exhibited. The role of the geometrical properties on the shape of the hysteresis loops is illustrated in Figure 5.2a, which displays the loops evaluated for different diameters (*d* = 150, 300, and 650 nm) and for *t* fixed to 15 nm. Apart from the case with *d* equal to 150 nm, each loop is characterized by two irreversible jumps, which correspond to the vortex nucleation and expulsion and are connected through a part that is reversible and dominated by vortex translation in the plane of the disk. A negligible average magnetization is found at remanence, with the vortex that is pinned at the nanodisk center. As reported in [14] the "*evolution of magnetic state is clearly illustrated by the magnetization maps reported*" in Figure 5.2a, "*calculated for d = 300 nm and t = 15 nm. When d = 150 nm and t = 15 nm, the magnetization reversal occurs at zero applied field with an irreversible jump between two C-*

states, leading to a negligible loop area". Moreover, Fig. 5.2a well demonstrates "*that, in the case of vortex formation, wider hysteresis loops can be obtained by reducing nanodisk diameter*". Considering $\mathbf{H}_a$ the external magnetic field and $\mathbf{M}$ the magnetization, the diagram in Figure 5.2b displays the specific energy losses $E = \mu_0 \oint \mathbf{H}_a \cdot d\mathbf{M}$ for the major loops as a function of t and d, and illustrates how these conditions result in larger heating capabilities. The plotted data are only for the cases with vortex nucleation.

The role of temperature on hysteresis loops is also analyzed and is reported in Figure 5.3, for all the ranges of thickness and diameter considered. Fig. 5.3a compares the vortex repulsion field H_{exp} values calculated with and without taking thermal effects into account. We can observe that the thermal effects promote the vortex expulsion, enabling saturation with lower fields. However, there is only a small impact on the hysteresis losses, since the decrease is in the order of 24-30%. In addition, when the applied field is in the order of the vortex expulsion field and the Hergt-Dutz limit [22] is taken into account, the maximum permissible frequency, f_{max}, should range between 55 and 160 kHz, as illustrated at the top of Figure 5.3b. For the excitation of nanodisks with a small diameter and thickness of 20–30 nm, the lowest frequencies have to be chosen. These nanodisks end up being the most efficient in terms of heat generation, as shown by the diagram at the bottom of Figure 5.3c, which reports the maximum values that are obtainable for the specific loss power (SLP_{max}) as a function of d and t, calculated by fixing the frequency to f_{max}. This is true even though the frequency is reduced due to the fulfillment of the biophysical constraint. The mass density of permalloy is

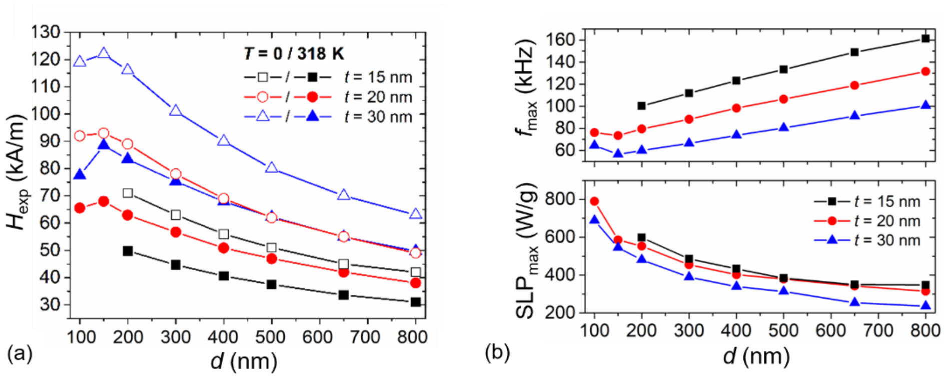

Figure 5.3. Influence of temperature. (a) Effect of the thermal noise on the vortex expulsion field H_{exp} for variable diameter (d between 100 and 800 nm) and thickness (t from 15 nm to 30 nm). (c) At the top the maximum frequency, f_{max}, and at the bottom the specific loss power, SLP_{max}, as a function of diameter and thickness, when thermal noise is included and the Hergt-Dutz limit is considered.

adjusted to 8.72 g/cm^3 to carry out the SLP estimation. In instance, when an external field is applied, SLP_{max} ranges from 790 W/g (for t = 20 nm and d = 100 nm) to 235 W/g (for t = 30 nm and d = 800 nm).

From the modelling of permalloy nanodisk ensembles, the study has also displayed a reduction in the SLP value of about 40-50% for a very high local concentration of nanodisks, due to magnetostatic interactions that strongly modify the shape of the global hysteresis loops. This is well illustrated in Figure 5.4, where we report in Fig. 5.4a the SLP as a function of the local volume concentration, calculated for 55 random-distributed nanodisks with d = 150 nm and t = 25 nm, and a field frequency of 50 kHz. Whereas, Fig. 5.4b shows an example of how the hysteresis loop can be influenced by the MNP concentration, with a reduction in the loop area and thus of hysteresis loesses with the increase of the volume concentration.

In addition, we have investigated mechanical phenomena, like the possible rotation of nanodisks within suspensions with low viscosity. In particular, we have found that the alignment of the nanodisks with the applied field is very rapid in water-based dispersions in comparison to more viscous media, such as gel or cell cultures, where the alignment is obstructed and the nanodisks can be assumed to be immobilized. Thus, in water-based dispersions we can observe a larger value of the magnetic nanodisk SLP.

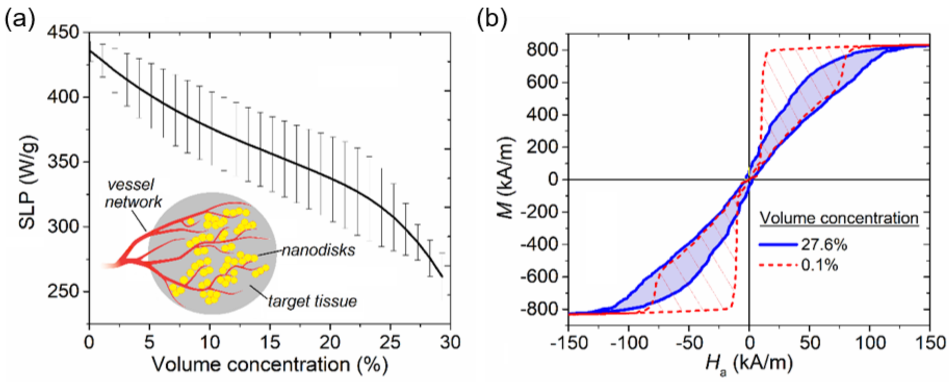

Figure 5.4. Effects of MNP local concentration and magnetostatic interactions. (a) SLP values as a function of volume concentration of 55 permalloy nanodisks with a diameter of 150 nm and a thickness of 25 nm, calculated at 50 kHz. (b) Comparison between hysteresis loops evaluated at a temperature of 45 °C for two different volume concentrations, i.e. 0.1% and 27.6%. Graphs reported in [14].

5.3.2 Thermal simulations

Thanks to the micromagnetic modeling analysis outcomes, the study of the permalloy nanodisk heating efficiency is carried out for the nanodisks with optimized hyperthermia properties. Specifically, we investigate the thermal response of nanodisks with d = 150 nm and t = 25 nm. The field frequency is fixed to 50 kHz and the magnetic field is uniformly applied along the longitudinal axis of the vial. The simulations are carried out on the vial geometry used for the validation of the thermal solver in Chapter 3. Moreover, we assume that the thermal effects due to field exposure are negligible within the vials, i.e. Q_{EM} in Eq. 3.1 is null. The temperature increase is evaluated by varying

- the nanodisk concentration in the range 0.01-0.3 mg/ml;
- the heat transfer coefficient h between 0 and 50 W/(K·m^2), to simulate both non-adiabatic and adiabatic conditions;
- the dispersion medium, i.e. water or gel.

The heating power due to MNP excitation, Q_{MNPs}, is calculated as the product between the MNP concentration and the SLP evaluated with the micromagnetic analysis. For the nanodisks dispersed in water, the SLP value is set at 440 W/g (see Fig. 5.4a), which is the value obtained assuming an optimal dispersion of disks in water (infinite dilution) and therefore negligible magnetostatic interactions between the MNPs. Whereas, a lower value of SLP, equal to 225 W/g, is considered for the gel-based dispersion fluid, obtained considering a random orientation of nanodisks with respect to the field. For this last medium, we consider the properties of gellan gum (ρ = 1010 kg/m^3, C_p = 4160 J/(kg·K), k = 0.53 W/(m·K)). Whereas, for the other material properties (water, polypropylene, and air) we consider the values used in Chapter 3, section 3.4. In addition, in all the simulations, MNPs are assumed to be uniformly distributed in the whole ferrofluid and the initial temperature is assumed to be equal to the temperature of the air T_{ext}, i.e. T_0 = 25 °C.

To simulate different cooling conditions of free convection in air, we simulate the thermal effects produced in the partially filled vial varying the heat transfer rate coefficient h from 0 W/(K·m^2), for an ideal adiabatic condition, to 50 W/(K·m^2), for different non-adiabatic conditions. For these simulations the concentration of nanodisks is fixed to 0.2 mg/ml, both media are considered, and the results are reported in Figure 5.5 for the water suspension and Figure 5.6 for the gel suspension. At the top left of the figures, the 2D sections of the vial illustrate the spatial distribution of temperature calculated for h = 10 W/(K·m^2) at the heating equilibrium (reached after ~30 min). The temperature maps show how a temperature gradient is present in the ferrofluid, even if the equilibrium is reached, and we can observe a variation of about 2 °C and 1 °C within the water- and gel-based fluids respectively, between the peak (in the proximity of the vial filling level) and the minimum (at the vial bottom) values. The graphs at the bottom of the figures report the heating-cooling transients evaluated in a point of

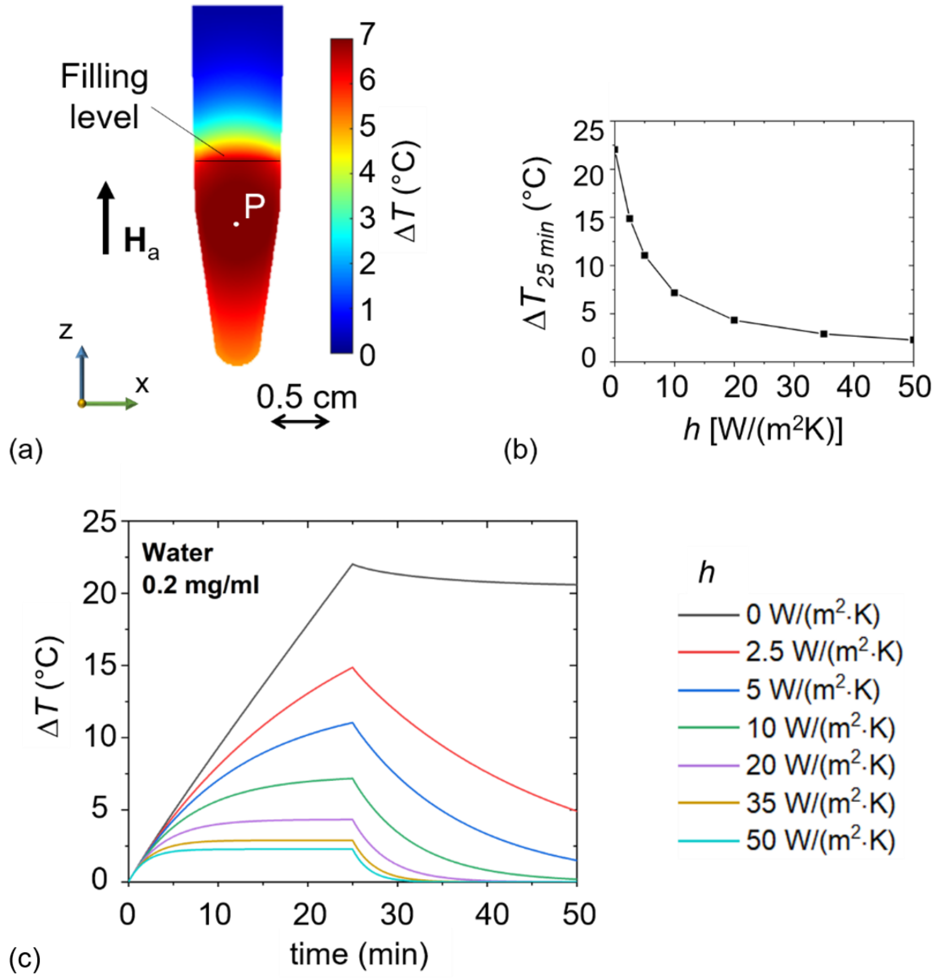

Figure 5.5. Thermal effects in a water-based suspension containing a nanodisk concentration of 0.2 mg/ml. (a) Map of the temperature increment ΔT evaluated on the central longitudinal section of the vial at the end of the heating interval, for a heat transfer rate h = 10 W/(K·m^2). The black line defines the filling level of the sample. (b) Graph of ΔT evaluated in point P after 25 min for different values of h, from 2.5 W/(K·m^2) to 22.5 W/(K·m^2). (c) Comparison of the heating-cooling transients evaluated in P for a variable value of h from zero to 50 W/(K·m^2). Graphs adapted from [14].

the sample, labelled as P in the reported 2D sections, for different values of h, considering a 25 min of AC field application and a consequent 25 min of cooling. The graphs put in evidence how the temperature increment at 25 min decreases with the increase in h. In fact, at the end of the heating time, the temperature increase varies from 2.3 °C, for h = 50 W/(K·m^2), to 22 °C, for h = 0 W/(K·m^2), in water and from 1.2 °C to 11 °C in gel. Furthermore, for not all the values of the heat transfer coefficient the temperature equilibrium is reached during the heating

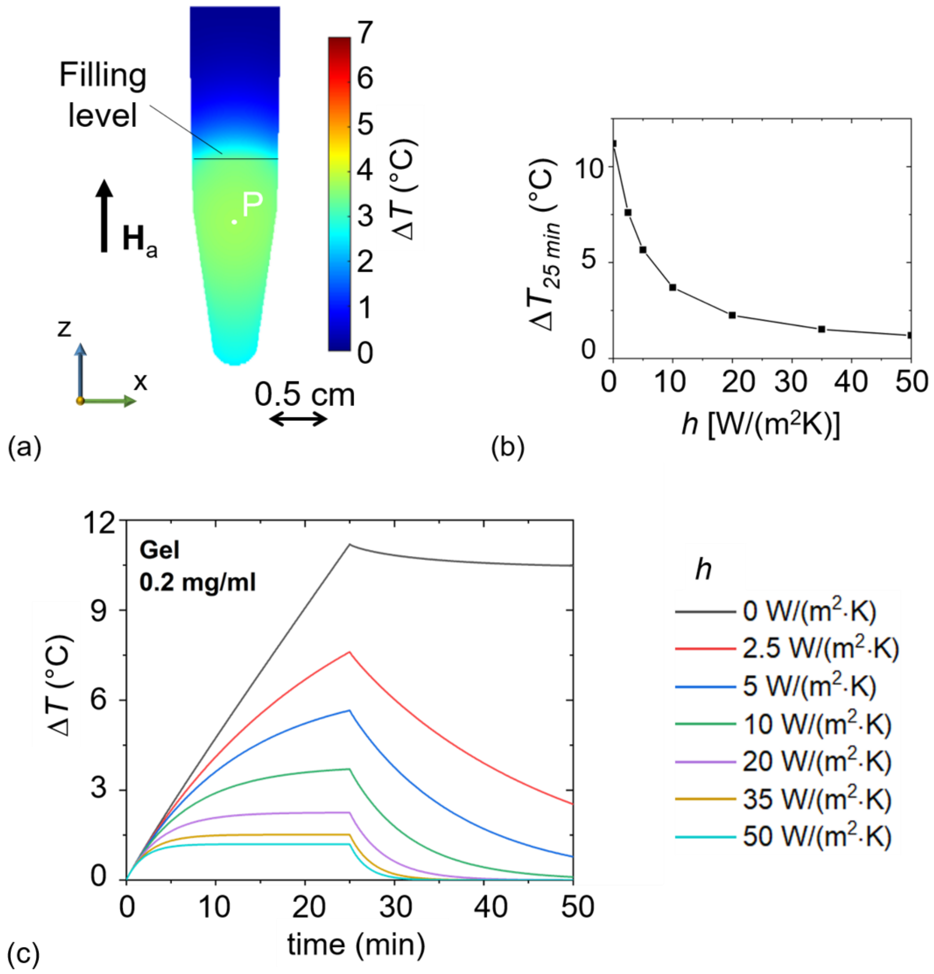

Figure 5.6. Thermal effects in a gel-based suspension containing a nanodisk concentration of 0.2 mg/ml. (a) Map of the temperature increment ΔT evaluated on the central longitudinal section of the vial at the end of the heating interval, for a heat transfer rate h = 10 W/(K·m^2). The black line defines the filling level of the sample. (b) Graph of ΔT evaluated in point P after 25 min for different values of h, from 2.5 W/(K·m^2) to 22.5 W/(K·m^2). (c) Comparison of the heating-cooling transients evaluated in P for a variable value of h from zero to 50 W/(K·m^2). Graphs adapted from [14].

time, and consequently a complete cooling-down of the sample does not occur. In particular, the heating regime condition is not achieved for values of *h* lower than 10 W/(K·m^2), giving the possibility of a higher temperature increase for a longer duration of field application.

To elucidate the impact of nanodisk concentration, we compare the time-evolution of temperature at the same point P of Fig. 5.6 and Fig. 5.7 for different values of

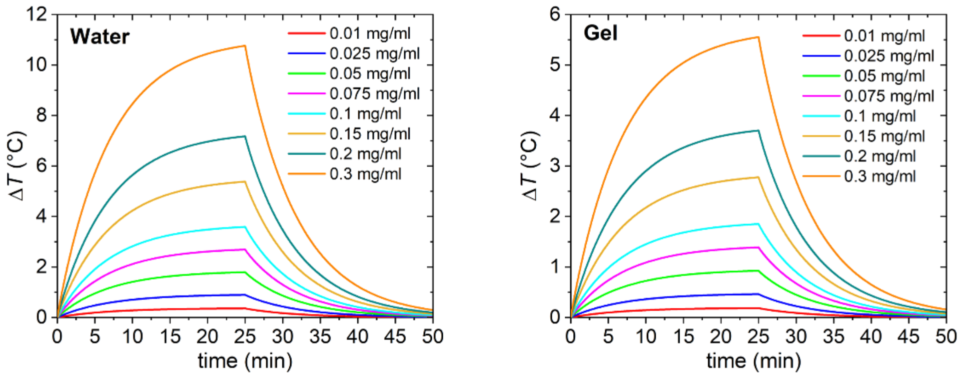

Figure 5.7. Effects of nanodisk concentration. Comparison of heating-cooling transients, evaluated in water (left) and gel (right) for a fixed value of h equal to 10 W/(K·m^2) and a variable nanodisk concentration in the range of 0.01-0.3 mg/ml. Graphs adapted from [14].

concentrations, from 0.01 to 0.3 mg/ml, considering a fixed heat transfer coefficient, *h* = 10 W/(K·m^2). The results are reported in Figure 5.7. In both media, a temperature increase lower than 0.5 °C is found after 25 min for the lowest value of MNP concentration (0.01 mg/ml), whereas for the highest concentration (0.3 mg/ml) a temperature elevation of 10.8 °C is found in water and of 5.5 °C in gel. As the previous figures, also these graphs illustrate how the reduction of the SLP value, due to the viscosity of the medium, impacts on the heating efficiency of MNPs, putting in evidence the importance of performing thermometric measurements in different media, especially in fluids with properties similar to blood and biological tissues. In our simulations, we can observe that in water MNPs are responsible for maximum temperature increments that are about twice the increments calculated in the gel medium, which has an almost halved SLP value.

5.4 Characterization of iron oxide nanocubes

In this section, we present the results obtained with our thermal solver to analyze the heating efficiency of iron oxide nanocubes and support their thermometric characterization. Specifically, the considered samples are two and are composed of Fe_3O_4 nanocubes synthesized by hydrothermal method at TÜBİTAK Ulusal Metroloji Enstitüsü (Turkey), thanks to the collaboration with Dr. Hüseyin Sözeri, considering different autoclave temperatures (in the range 150-200 °C) and reaction times (12 hours and 24 hours). Via TEM imaging, see Figure 5.8a, the analysis of nanocubes morphology and size distribution has shown that the average size of the particles is 22 nm for one sample, which here we name sample A, and 165 nm for the other one, named sample B. Whereas, the magnetometric measurements, combined and supported with the micromagnetic modeling, have analyzed the nanocube hysteresis loops and found that the MNPs show primarily a single-domain ferromagnetic behavior. Figure 5.8 reports also the hysteresis loops of the two samples evaluated via VSM measurements.

In this context, the micromagnetic simulations are fundamental for the comprehensive understanding of MNP magnetic behavior, as many parameters influence the generation of hysteresis losses. In fact, as reported in [15], with the micromagnetic simulations "*the overall properties of the analyzed samples can be numerically reconstructed by introducing an average of the different behaviors obtained by varying size, orientation of the MNPs with respect to the applied magnetic field and state of MNP aggregation (e.g., cluster, chain)*". In this way, the "*experimental results were successfully supported by micromagnetic simulations, which have clarified the role of several factors in the generation of hysteresis losses, like MNP size, effective anisotropy (shape and crystalline contributions) and state of aggregation*". Moreover, the analysis has shown how, depending on the size of the nanocubes, the specific energy losses vary. In particular, "*the specific energy losses, calculated with the magnetic field applied along the cubic MNP edge, reflect the non-monotonic behavior of the coercivity, with a peak at 105 nm, i.e., after the transition from single-domain to multi-domain configuration, which occurs at 80 nm"*, as reported in Figure 5.9. *"Moreover, micromagnetic simulations allowed us to shed light on the magnetization reversal process, revealing a vortex-like configuration for the multi-domain MNPs*".

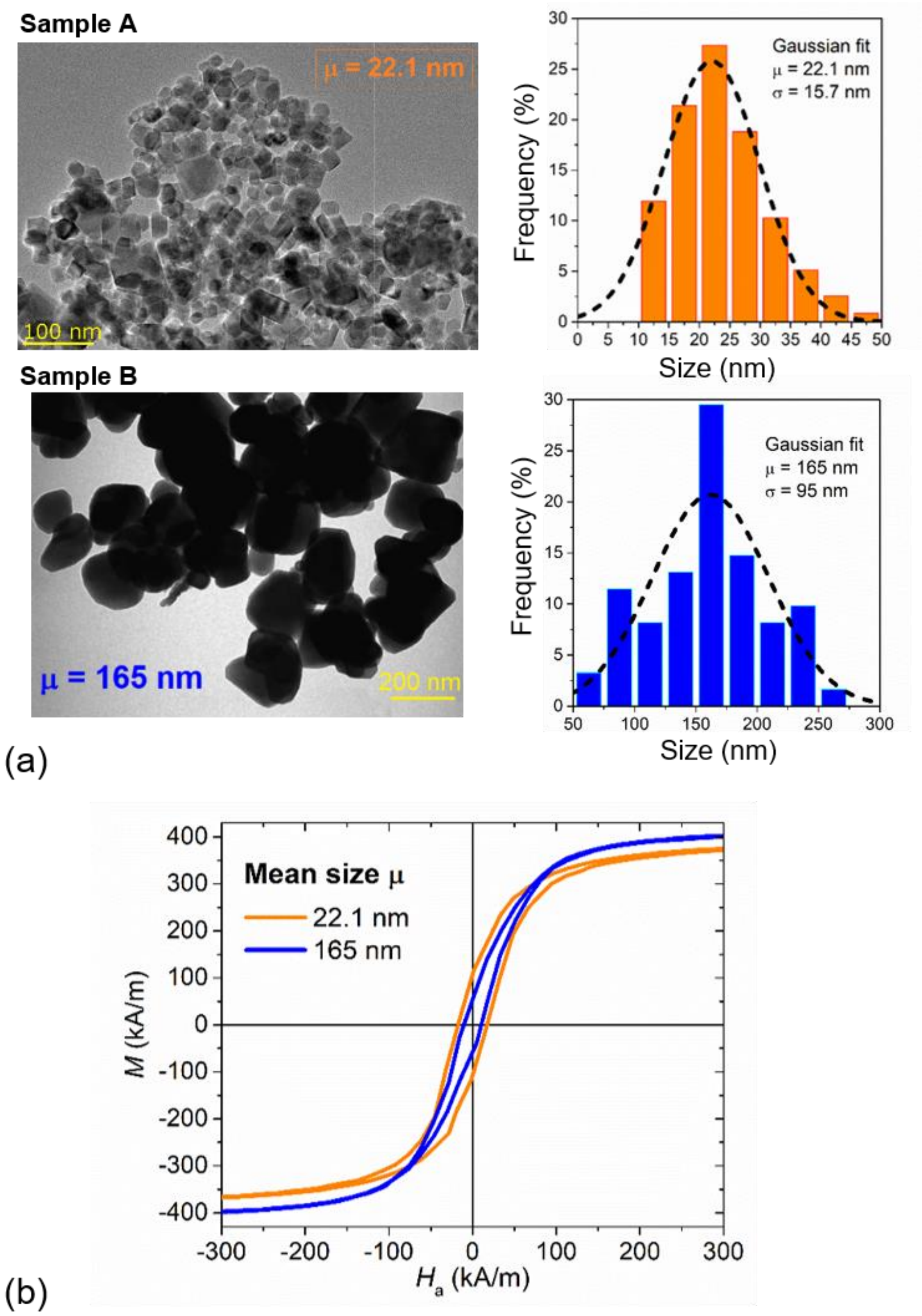

Figure 5.8. (a) Transmission Electron Microscopy (TEM) images of the two samples of Fe_3O_4 NPs (left) executed at TÜBİTAK, with the correspondent size histograms fitted by a Gaussian function where μ is the mean value and σ the standard deviation (right). (b) Static hysteresis loops measured by means of the Vibrating Sample Magnetometry (VSM) for the samples of iron oxide nanocubes. Graphs reported in [15].

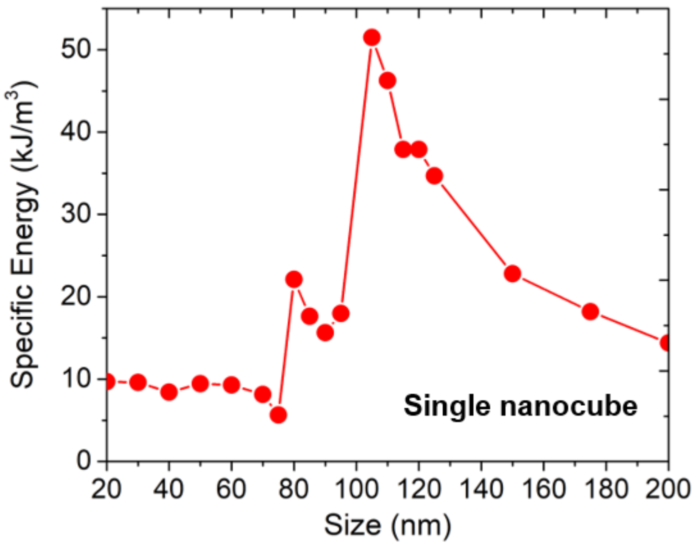

Figure 5.9. Influence of size on the specific energy losses E for Fe3O4 nanocubes. The data, fitted with basis spline functions, are extracted from the static hysteresis loops evaluated by considering the application of the magnetic field along the cubic MNP edge.

5.4.1 Thermal simulations and comparison to experimental data

During the characterization of the samples, thermometric measurements were also performed. The measurements were made at INRiM with a custom-built setup, described in detail in [23]. The heating capacity of the samples was tested by applying an AC magnetic field with a peak amplitude equal to 48 kA/m and a frequency of 100 kHz. A fiber optic thermometer, placed in the center of the water-based suspension contained in the vial, was used to record the temperature of the sample for successive time instants. The temperature was measured for a total time interval of 150 min, where in the first 65 min the field was turned on and was turned off for the successive 65 minutes. Then, the measured data were fitted to reproduce the entire heating-cooling transient curve, by means of a thermodynamic analytical model [16] used to estimate the SLP.

To confirm the thermometric characterization and verify the thermodynamic analytical model, the spatial-temporal evolution of temperature within the samples was simulated, considering the same field parameters of the thermometric measurements (frequency equal to 100 kHz and peak amplitude to 48 kA/m). Here we report the results obtained for the two samples A and B which contain an

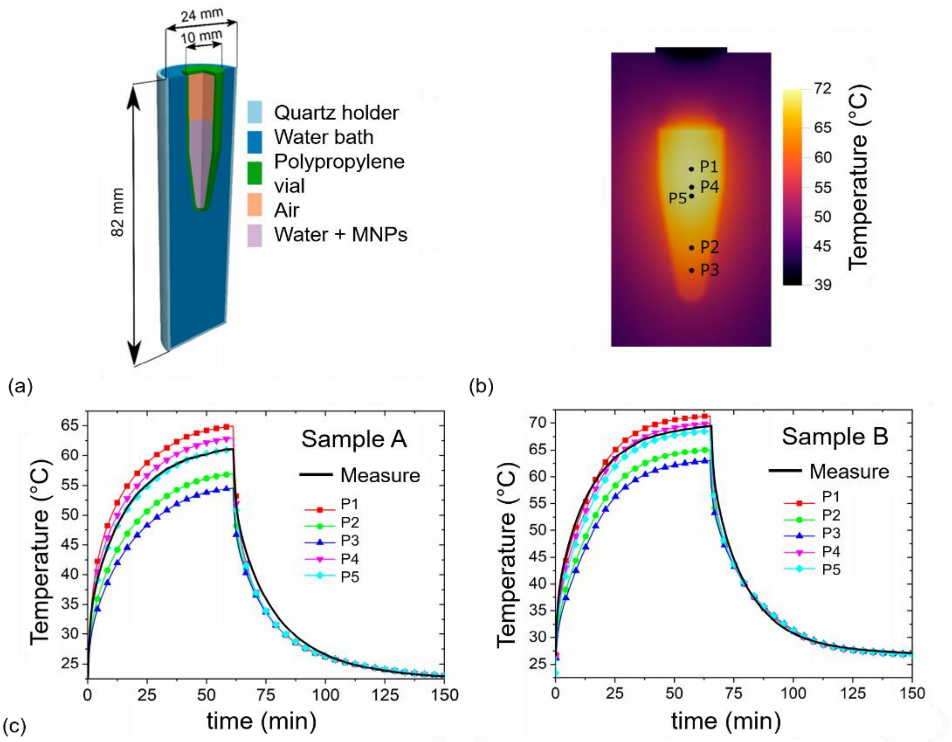

Figure 5.10. (a) Schematic of the calculation domain for the thermal solver. (b) 2D map of the temperature distribution within the vial at the end of the heating interval for the sample B. (c) The heating-cooling transients evaluated for the point locations specified in the 2D map of temperature, where on the left the results of sample A are reported and on the right those for sample B. Graphs adapted from [15].

MNP mass equal to 5.43 mg and 9.82 mg, respectively. For these simulations, the temperature was evaluated within the vial (maximum diameter of 1 cm and height of about 4 cm) and also in the surrounding water bath and quartz holder (the solution domain is schematized in Figure 5.10a). The values of Q_{MNPs} for the two samples are evaluated from the values of the MNP mass and the SLP (of about 150 W/g for sample A and 90 W/g for sample B) estimated by the thermodynamic model, and set to 825 kW/m^3 and 894 kW/m^3 for samples A and B, respectively. The thermal properties used for the quartz and the samples are the followings

- quartz: ρ = 2600 kg/m^3, C_p = 820 J/(kg·K), k = 3 W/(m·K);
- sample A: ρ = 1019.8 kg/m^3, C_p = 4086 J/(kg·K), k = 0.61 W/(m·K);
- sample B: ρ = 1038.1 kg/m^3, C_p = 4011 J/(kg·K), k = 0.62 W/(m·K);

Whereas, the thermal properties of water, air, and polypropylene are the same used in Chapter 3. The heat transfer coefficient h at the interface between the holder and the external air is fixed to 25 W/(K·m^2). In addition, the initial temperature of the whole domain is assumed to be equal to the external temperature of the air, i.e. 25 °C. In Figure 5.10b the temperature distribution at the time instant of 25 min (i.e. at the end of the heating interval) is displayed for sample B. The heating transients are reported in Figure 5.10c for the two samples evaluated for different points within the vial, whose position is indicated in Fig. 5.10b. The curves evaluated at the point labeled as P5 present a good agreement with the experimental data and the point is actually placed in a position close to the thermometer extremity, i.e. in proximity to the position where the temperature is measured during the thermometric measurements.

5.5 Conclusions

In this Chapter, we have illustrated the importance of numerical simulations to support the experimental measurements for the MNP characterization. In particular, we have reported the results obtained with the micromagnetic modeling as they are essential for a comprehensive understanding of MNP magnetic behavior, and also because they enable us to select the optimal size and SLP values of MNPs for the thermometric measurement simulations. A first analysis was carried out on permalloy nanodisks, where the numerical simulations of the temperature distribution of ferrofluids within a vial enabled us to investigate the role of non-adiabatic conditions that could occur during measurements. As an example, for the magnetic suspension we have predicted a wide range of temperature increments that range from a value of 2.3 °C for a heat transfer rate of 50 W/(K·m^2) to a value of 22 °C for an ideal adiabatic system. Moreover, with the thermal simulations we have studied the heating efficiency of the permalloy nanodisks for different concentrations, durations of field application, and types of medium where they are dispersed in order to test their suitability for hyperthermia applications. High temperature increments have been obtained, as in the water-based suspension significant increases of more than 2 °C occur after 25 min of heating also for low concentrations, such as 0.075 mg/ml and 0.01 mg/ml. This analysis has also put in evidence how the reduction of the SLP value in high viscosity media impacts on the heating efficiency. In fact, in the gel-based suspension, for the same MNP concentrations, the temperature increases are reduced to half.

Finally, we presented the results obtained with our thermal model in comparison with experimental data. The simulations showed good agreements with the thermometric measurements, confirming the validity of the thermodynamic model [23] used to estimate the values of SLP, and the suitability of the thermal solver as a tool to test the MNP heating efficiency.

5.6 References

[1] H. F. Rodrigues, G. Capistrano, and A. F. Bakuzis, "In vivo magnetic nanoparticle hyperthermia: a review on preclinical studies, low-field nano-heaters, noninvasive thermometry and computer simulations for treatment planning," *Int. J. Hyperthermia*, vol. 37, no. 3, 76-99, 2020. DOI: 10.1080/02656736.2020.1800831.

[2] Y. Yang *et al.*, "Orientation mediated enhancement on magnetic hyperthermia of Fe3O4Nanodisc," *Adv. Funct. Mater.*, vol. 25, no. 5, pp. 812–820, 2015. DOI: 10.1002/adfm.201402764.

[3] X. L. Liu *et al.*, "Magnetic vortex nanorings: a new class of hyperthermia agent for highly efficient in vivo regression of tumors," *Adv. Mater.*, vol. 27, no. 11, pp. 1939–1944, 2015. DOI: 10.1002/adma.201405036.

[4] B. T. Mai *et al.*, "Thermoresponsive iron oxide nanocubes for an effective clinical translation of magnetic hyperthermia and heat-mediated chemotherapy," *ACS Appl. Mater. Interfaces*, vol. 11, no. 6, pp. 5727–5739, 2019. DOI: 10.1021/acsami.8b16226.

[5] P. Hugounenq *et al.*, "Iron oxide monocrystalline nanoflowers for highly efficient magnetic hyperthermia," *J. Phys. Chem. C Nanomater. Interfaces*, vol. 116, no. 29, pp. 15702–15712, 2012. DOI: 10.1021/jp3025478.

[6] X. Liu *et al.*, "Comprehensive understanding of magnetic hyperthermia for improving antitumor therapeutic efficacy," *Theranostics*, vol. 10, no. 8, pp. 3793–3815, 2020. DOI: 10.7150/thno.40805.

[7] H. Gavilán *et al.*, "How size, shape and assembly of magnetic nanoparticles give rise to different hyperthermia scenarios," *Nanoscale*, vol. 13, no. 37, pp. 15631–15646, 2021. DOI: 10.1039/D1NR03484G.

[8] R. Ferrero, A. Manzin, G. Barrera, F. Celegato, M. Coïsson, and P. Tiberto, "Influence of shape, size and magnetostatic interactions on the hyperthermia properties of permalloy nanostructures," *Sci. Rep.*, vol. 9, no. 1, p. 6591, 2019. DOI: 10.1038/s41598-019-43197-4.

[9] G. Barrera *et al.*, “Surface modification and cellular uptake evaluation of Au-coated Ni80Fe20 nanodiscs for biomedical applications,” *Interface Focus*, vol. 6, no. 6, p. 20160052, 2016. DOI: 10.1098/rsfs.2016.0052.

[10] P. Guardia *et al.*, “Water-soluble iron oxide nanocubes with high values of specific absorption rate for cancer cell hyperthermia treatment,” *ACS Nano*, vol. 6, no. 4, pp. 3080–3091, 2012. DOI: 10.1021/nn2048137.

[11] J. Kolosnjaj-Tabi *et al.*, “Heat-generating iron oxide nanocubes: subtle ‘destructurators’ of the tumoral microenvironment,” *ACS Nano*, vol. 8, no. 5, pp. 4268–4283, 2014. DOI: 10.1021/nn405356r.

[12] Z. Nemati, R. Das, J. Alonso, E. Clements, M. H. Phan, and H. Srikanth, “Iron oxide nanospheres and nanocubes for magnetic hyperthermia therapy: A comparative study,” *J. Electron. Mater.*, vol. 46, no. 6, pp. 3764–3769, 2017. DOI: 10.1007/s11664-017-5347-6.

[13] H. Khurshid *et al.*, “Anisotropy effects in magnetic hyperthermia: A comparison between spherical and cubic exchange-coupled FeO/Fe3O4 nanoparticles,” *J. Appl. Phys.*, vol. 117, no. 17, p. 17A337, 2015. DOI: 10.1063/1.4919250.

[14] A. Manzin, R. Ferrero, and M. Vicentini, “From micromagnetic to in silico modeling of magnetic nanodisks for hyperthermia applications,” *Adv. Theory Simul.*, p. 2100013, 2021. DOI: 10.1002/adts.202100013.

[15] R. Ferrero *et al.*, “Experimental and modelling analysis of the hyperthermia properties of iron oxide nanocubes,” *Nanomaterials (Basel)*, vol. 11, no. 9, 2021. DOI: 10.3390/nano11092179.

[16] E. V. Timofeeva, W. Yu, D. M. France, D. Singh, and J. L. Routbort, “Nanofluids for heat transfer: an engineering approach,” *Nanoscale Res. Lett.*, vol. 6, no. 1, p. 182, 2011. DOI: 10.1186/1556-276X-6-182.

[17] M. Sheikholeslami and D. D. Ganji, “Ferrofluid convective heat transfer under the influence of external magnetic source,” *Alex. Eng. J.*, vol. 57, no. 1, pp. 49–60, 2018. DOI: 10.1016/j.aej.2016.11.007.

[18] F. Soetaert, S. K. Kandala, A. Bakuzis, and R. Ivkov, “Experimental estimation and analysis of variance of the measured loss power of magnetic nanoparticles,” *Sci. Rep.*, vol. 7, no. 1, 2017. DOI: 10.1038/s41598-017-07088-w.

[19] R. Ferrero and A. Manzin, “Adaptive geometric integration applied to a 3D micromagnetic solver,” *J. Magn. Magn. Mater.*, vol. 518, no. 167409, p. 167409, 2021. DOI: 10.1016/j.jmmm.2020.167409.

[20] A. Manzin and R. Ferrero, “A 2.5D micromagnetic solver for randomly distributed magnetic thin objects,” *J. Magn. Magn. Mater.*, vol. 492, no. 165649, p. 165649, 2019. DOI: 10.1016/j.jmmm.2019.165649.

[21] O. Bottauscio and A. Manzin, “Parallelized micromagnetic solver for the efficient simulation of large patterned magnetic nanostructures,” *J. Appl. Phys.*, vol. 115, no. 17, p. 17D122, 2014. DOI: 10.1063/1.4862379.

[22] R. Hergt and S. Dutz, “Magnetic particle hyperthermia—biophysical limitations of a visionary tumour therapy,” *J. Magn. Magn. Mater.*, vol. 311, no. 1, pp. 187–192, 2007. DOI: 10.1016/j.jmmm.2006.10.1156.

[23] M. Coïsson *et al.*, “Hysteresis losses and specific absorption rate measurements in magnetic nanoparticles for hyperthermia applications,” *Biochim. Biophys. Acta Gen. Subj.*, vol. 1861, no. 6, pp. 1545–1558, 2017. DOI: 10.1016/j.bbagen.2016.12.006.

Chapter 6

In silico modelling of eddy current effects in magnetic hyperthermia preclinical tests

The material presented in this is published in Computer Methods and Programs in Biomedicine 223: 106975, August 2022

In the Introduction, we have discussed the importance of biophysical constraints to consider during magnetic hyperthermia sessions, in order to avoid adverse eddy current effects due to electromagnetic (EM) field exposure. The heating efficiency of magnetic nanoparticles (MNPs) is strongly related to the values of field frequency and peak amplitude used during the treatments. In particular, the efficiency rises when increasing the field parameters, reaching a plateau at very large fields and fixed frequency. However, the increase in EM field parameters can also lead to undesirable eddy current effects, with possible heating of healthy tissues and generation of hot spots. For these reasons, a careful selection of EM field frequency and peak amplitude is needed to guarantee proper and safe EM field exposure as well as successful treatments.

In this Chapter, we study eddy current effects caused by the only EM field exposure during preclinical tests of magnetic hyperthermia, calculating the whole-body average specific absorption rate (SAR) and temperature increment in tissues. The simulations are carried out on the two murine models introduced in Chapter 4: the 28 g normal male nude mouse and the 503 g Sprague Dawley rat. The eddy current effects produced in biological tissues during AC magnetic field application are evaluated by solving the low-frequency EM field problem introduced in Chapter 2. Whereas, the thermal response is estimated by evaluating the spatial-temporal distribution of temperature within the animal model by solving the Pennes' bioheat equation, as described in Chapter 4.

The Chapter is divided into three parts, in the first part we study the EM field exposure assuming a uniform field within the exposed body; in the second part we consider non-uniform field distributions, simulating the magnetic field generated by four different EM field applicators; in the third part we elucidate the role of the heat transfer coefficient and of the tissue thermal parameters on eddy current effects. In the analysis of the EM field exposure, different values of field frequency and peak amplitude are considered in order to investigate the EM dosimetry and determine safe conditions of EM field exposure during magnetic hyperthermia preclinical tests. In all the simulations, apart from specific cases, the heat transfer coefficient (the parameter *h* in Eq. (4.2) of Chapter 4), which expresses the heat flux due to convection at the skin-air interface, is set at 3.5 W/(K·m^2).

6.1 Cases with body exposed to uniform fields

As a first approximation, we assume that the applied magnetic field is uniformly distributed over the entire body. This assumption is based on the fact that in the majority of preclinical studies mice with reduced dimensions are placed inside coils that completely surround the animal body. Thus, in these cases the assumption of a uniform field exposure is acceptable. Moreover, in preclinical experiments the animal is accurately positioned inside the coil so that the body region to be treated is where the field is more uniform and with higher amplitude values.

In this section, first we focus on the mouse model and we investigate how the induced eddy current heating is influenced by the AC magnetic field parameters, varying its frequency and peak amplitude. Then, for specific cases of field amplitude and frequency, we compare the thermal response of the mouse model with the rat one, in order to assess the impact of body size on eddy current effects due to EM field exposure. We also change the animal orientation with respect to the field direction. Finally, we simulate different conditions of forced convection to mimic strategies to reduce possible non-negligible thermal effects of EM fields.

6.1.1 Influence of AC magnetic field parameters

We evaluate the eddy current effects induced in the mouse model, varying the field frequency, f, between 50 kHz and 1 MHz, and the field peak amplitude, $\hat{H}_a$, between 5 kA/m and 75 kA/m [1]. With these values, we intentionally exceed the biophysical limits of Atkinson-Brezovich and Hergt-Dutz, to simulate the preclinical tests documented in the literature [2-11] that are reported in Table 1.1 of Chapter 1, where large products of f and $\hat{H}_a$ are considered. The field is assumed to be uniform and applied along the animal longitudinal axis.

After calculating the electric field within the mouse animal body, using the EM numerical model, we evaluate the SAR locally through Eq. (1.3), the SAR averaged over the whole body and the spatial distribution of temperature, by solving the bio-heat equation. The results of the whole-body average SAR are reported in Figure 6.1, where for some of the field frequency and peak amplitude values listed in Table 1.1 and reported in the table of Fig. 6.1, we have evaluated

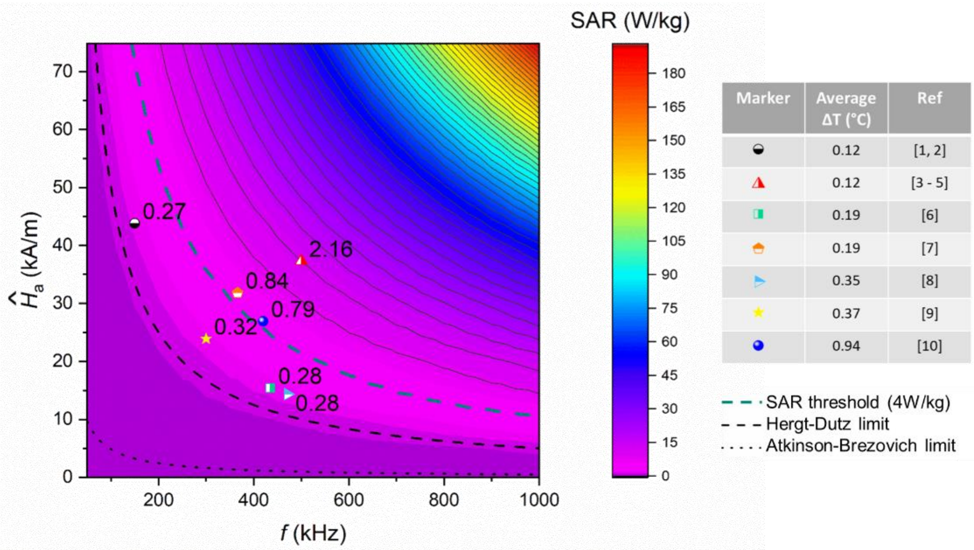

Figure 6.1. Whole-body average SAR as a function of field frequency f and peak amplitude $\hat{H}_a$. Evaluations on the 28 g mouse, considering the AC magnetic field uniformly applied along the body longitudinal axis. The markers specify the maximum temperature increases (in °C) evaluated with the field parameters used in the preclinical tests reported in the table on the right, together with the correspondent estimations of the average temperature increments. Graph reported in [1].

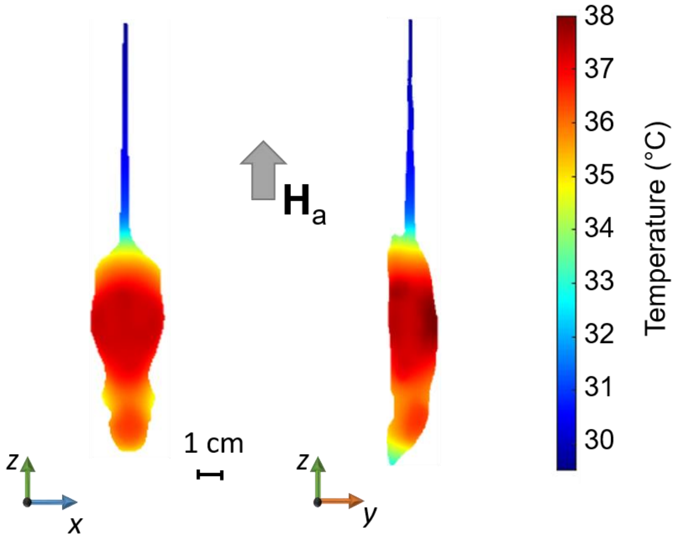

Figure 6.2. Spatial distribution of the temperature evaluated at the thermal equilibrium over the longitudinal sections of the mouse, considering the AC magnetic field applied uniformly along the longitudinal axis of the animal body with a frequency of 500 kHz and a peak amplitude of 37.3 kA/m.

the maximum and the average temperature increments by means of the bio-heat model. Specifically, the maximum increment ΔT_{max} is calculated as the maximum difference of the temperature at thermal equilibrium (during EM field exposure) and the temperature before the application of the field, that is the result of only metabolic processes and blood-tissues heat exchanges. The obtained results demonstrate that in small animals the maximum temperature increase is negligible if the Hergt-Dutz limit is fulfil. In fact, for field values that do not exceed this limit, the whole-body average SAR is below 1 W/kg and the maximum temperature increment is less than 0.3 °C. Moreover, the simulations show that with a value of whole-body average SAR lower than 4 W/kg, which is obtained when $\hat{H}_a \times f$ is approximately $12 \cdot 10^9$ A/(m·s), the maximum temperature increment does not exceed 1 °C. In these cases, the maximum increments are reached in areas deep within the body, e.g. in the head and the abdomen, that are in general the warmest parts also in the absence of fields. Moreover, a variation of the core temperature of about 1 °C is considered acceptable as it is the variation of body core temperature during the day, typical of mice and humans [12]. When the Hergt-Dutz limit is strongly exceeded, the temperature increments become non-negligible, e.g. a maximum temperature increment of more than 2 °C is estimated for a field frequency of 500 kHz and a field amplitude of 37.3 kA/m (field parameters used in [11]). In this simulation, the maximum temperature increment is found on the skin of the back and reached in about 50 min after the field is turned on. When the field is turned off, the initial temperature is reestablished in 40 min. Even if we choose a 10-minute heating duration, as in [11], the highest temperature increase is in the order of 2 °C. The temperature distribution at the equilibrium is reported in Figure 6.2, where it is evaluated on two 2D longitudinal sections. In particular, we can observe that the warmest areas are in proximity of the back, where the maximum temperature is reached. For all the cases where the temperature distribution is evaluated, the temperature increment averaged on the whole body does not exceed 1 °C. For these cases, we also calculate the peak spatial SAR, averaged over 5 mg of mass [13], that reaches a minimum value of 5.9 W/kg, when $\hat{H}_a \times f = 6.7 \cdot 10^9$ A/(m·s) and $\Delta T_{max} = 0.28$ °C, and a maximum value of 46 W/kg, when $\hat{H}_a \times f = 18.7 \cdot 10^9$ A/(m·s) and $\Delta T_{max} = 2.16$ °C.

6.1.2 Influence of body size

As discussed in Chapter 1, the heating power due to EM field exposure, roughly expressed by Eq. (1.2), is also influenced by the radial distance, i.e. with fixed field conditions the greater the transversal section of a body, the greater the heating power. To elucidate this, we evaluate the whole-body average SAR and the thermal response in the 503 g rat model, for some of the field conditions considered with the mouse model in the previous section. Figure 6.3 shows the results obtained in the rat, varying the field product $\hat{H}_a \times f$ from $0.48 \cdot 10^9$ A/(m·s) to $8.5 \cdot 10^9$ A/(m·s), in order to consider field exposures complying with or exceeding biophysical limitations, such as in [14], where an AC magnetic field with $\hat{H}_a = 14$ kA/m and $f = 606$ kHz ($\hat{H}_a \times f = 8.48 \cdot 10^9$ A/(m·s)) has been applied to a 250-270 g rat, generating a temperature increase of about 2 °C. Figure 6.3a displays the whole-body average SAR, the maximum and the average temperature increments achieved at the heating equilibrium within the rat for the different field conditions. In comparison to the mouse model, in the rat there are significant temperature increases even when the Hergt-Dutz limit is not exceeded. In correspondence to this limit ($\hat{H}_a \times f = 5 \cdot 10^9$ A/(m·s)), the whole-body SAR is equal to 4.78 W/kg and the maximum and average temperature increments are 2.6 °C and 0.88 °C, respectively. In comparison, for the same field parameters, the mouse model presents a maximum temperature increment much lower than 1 °C. Only with a field exposure where the product $\hat{H}_a \times f$ is close to the Atkinson-Brezovich limit, there is a negligible thermal response in the rat model. In fact, when the average SAR does not exceed 2 W/kg and the value of $\hat{H}_a \times f$ is lower than $2{\cdot}10^9$ A/(m·s), the maximum temperature increases are below 1 °C.

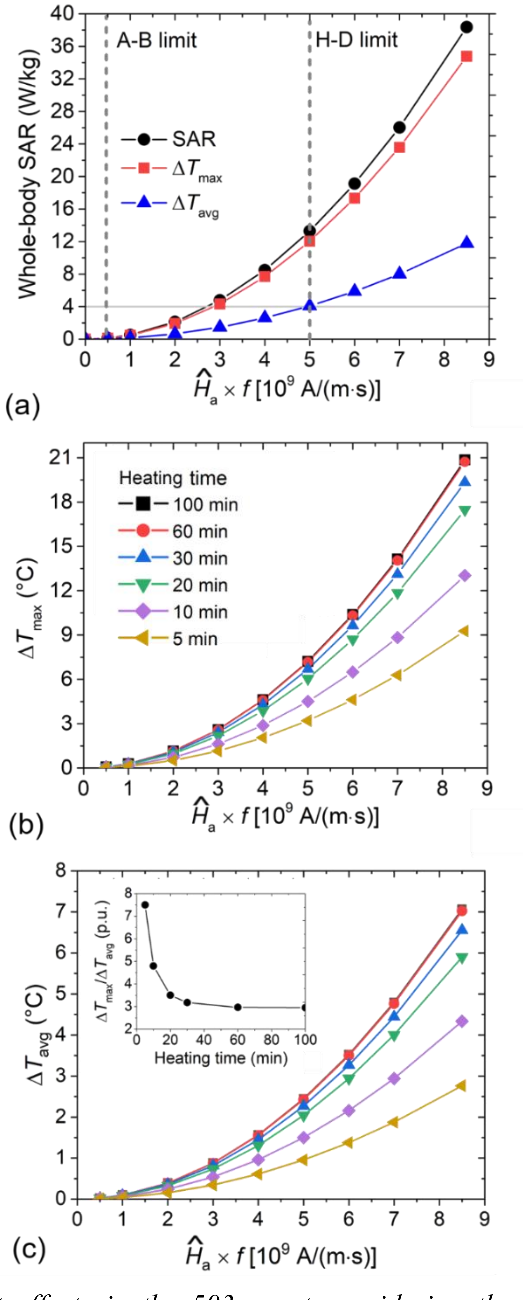

Figure 6.3. Eddy current effects in the 503 g rat considering the AC magnetic field uniformly applied along the body longitudinal axis. (a) Maximum and average temperature increments (right), and the whole-body average SAR (left) as a function of the product between the field frequency and peak amplitude. (b) Corresponding maximum temperature increments for different values of heating time. (c) Corresponding average

temperature increases, where the inset shows the ratio of the maximum to the average increment as a function of the heating time. Graphs reported in [1].

In particular, for a field exposure with $\hat{H}_a \times f$ equal to the Atkinson-Brezovich limit (i.e. $4.8 \cdot 10^8$ A/(m·s)) the maximum temperature increment is lower than 0.1 °C.

However, a mitigation of the heating effects can be obtained by reducing the heating time. For this reason, we have calculated the maximum and average temperature increments for the same field conditions of Fig. 6.3a, varying the heating time (from 5 min to 100 min). The results are illustrated in Figure 6.3b and Figure 6.3c, where it can be observed that a significant reduction in the temperature increments is obtained only when the heating time intervals are rather short, e.g. less than 10 min. For example, when $\hat{H}_a \times f = 6 \cdot 10^9$ A/(m·s), the temperature increments have an average of 3.52 °C and a maximum of 10.39 °C for 100 min of AC field application (with the achievement of the thermal equilibrium) and are reduced to 1.38 °C and 4.62 °C, respectively, when the heating time lasts only 5 min, with a corresponding reduction of about 61% and 56%. Moreover, when the heating time raises from 5 min to 60 min, the regions characterized by the highest temperatures extend, i.e. the ratio between the maximum and the average temperature increment decreases from 7.5 to 3, as displayed in the inset of Figure 6.3c.

The different thermal responses of the two murine models are clearly illustrated in Figure 6.4a, where we have reported the temperature distribution at the equilibrium on 2D longitudinal sections, for the same field condition, i.e. field amplitude equal to 50 kA/m and frequency equal to 100 kHz. The rat presents non-negligible peaks of temperature in body areas close to the skin, especially where the body transversal section is wider because the heating due to EM field exposure prevails on the metabolic heat contribution. Whereas in the mouse the temperature distribution presents no significant temperature increments and is similar to the distribution that can be observed when the field is not applied, i.e. the warmest areas are the brain and the abdomen and the coldest region is the tail, as a result of the dominance of metabolic heat.

Figure 6.4b shows the corresponding heating-cooling transients evaluated in the two models, which report the time evolution of both maximum and average increments. For these simulations, we consider a heating time interval of 100 min to guarantee that the thermal equilibrium is reached. The mouse maintains a temperature within the body that is nearly stable during the heating and cooling intervals; in fact, it has a maximum temperature increment of only 0.16 °C, for an average increase of 0.07 °C and an associated whole-body SAR of 0.9 W/kg. On the contrary, the rat reaches a significant maximum temperature increment of 7.22 °C, corresponding to an average temperature increase of 2.45 °C and whole-body SAR of 13.28 W/kg. During the cooling time, the initial temperature is reestablished after about 80 min and 50 min in the rat and in the mouse, respectively.

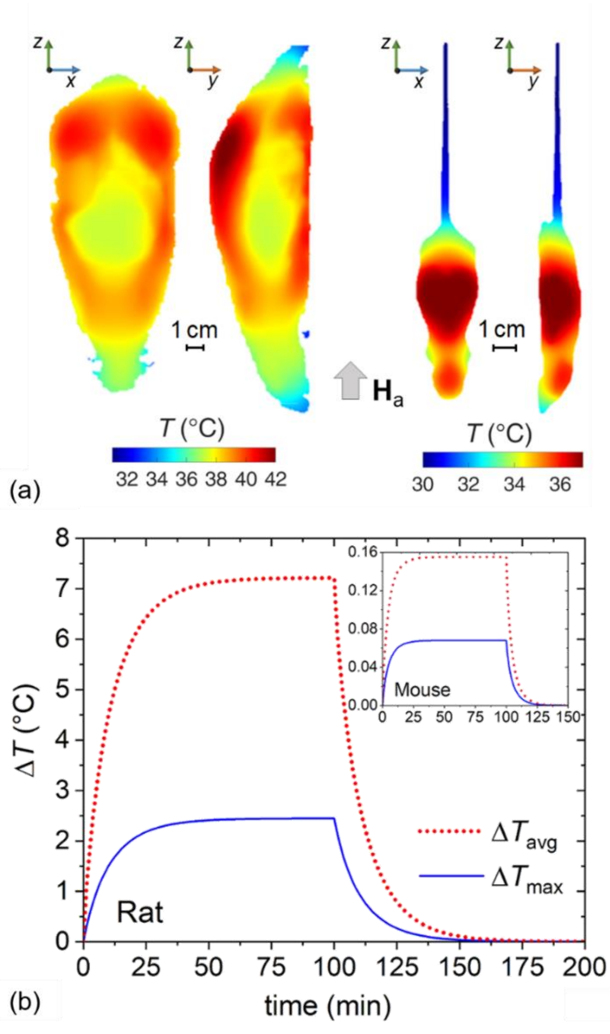

Figure 6.4. Influence of body size. (a) Spatial distribution of the temperature evaluated at the thermal equilibrium over the longitudinal sections of the rat (left) and the mouse (right), considering the AC magnetic field applied uniformly along the longitudinal axis of the animal body with a frequency of 100 kHz and a peak amplitude of 50 kA/m. (b) Corresponding evolution over time of the average and maximum temperature increments during the heating-cooling transient, evaluated for the rat. The inset displays the corresponding temperature increase time evolution for the mouse with the same measure units of the main graph. Graphs reported in [1].

6.1.3 Influence of body-field relative orientation

In the majority of preclinical trials, the animals, which are totally positioned inside the coils, have their longitudinal axis that is oriented parallel to the vertical axis of the coil. However, animals can be also positioned perpendicularly [15], with the magnetic field lines from the applicator orthogonal to the body longitudinal axis. The different orientations can highly impact on the thermal response; we indeed expect that stronger eddy current effects occur when the body is orthogonal to the field direction, as the body section exposed to the field becomes wider.

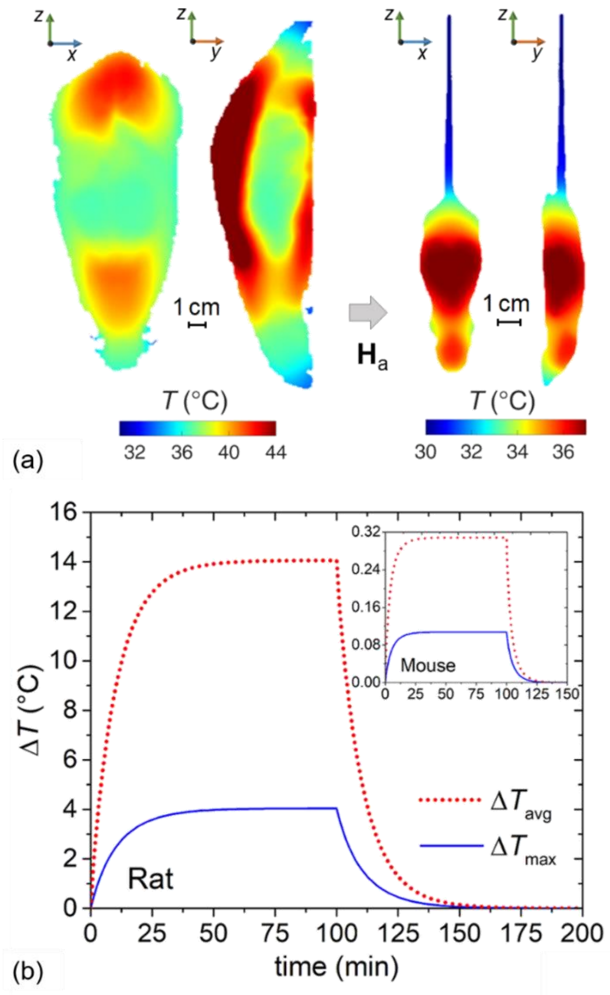

Figure 6.5. Influence of body size. (a) Spatial distribution of the temperature evaluated at the thermal equilibrium over the longitudinal sections of the rat (left) and the mouse (right), considering the AC magnetic field applied uniformly and transversally the

longitudinal axis of the animal body, with a frequency of 100 kHz and a peak amplitude of 50 kA/m. (b) Corresponding evolution over time of the average and maximum temperature increments during the heating-cooling transient, evaluated for the rat. The inset displays the corresponding temperature increase evolution for the mouse with the same measure units of the main graph. Graphs reported in [1].

Figure 6.5a displays the temperature distribution at thermal equilibrium on 2D sections of the two animal models, with the same field parameters considered in Figure 6.3 ($\hat{H}_a$ = 50 kA/m and f = 100 kHz), but with the field applied transversally. With this field orientation, the mouse presents a non-significant variation in the temperature distribution, which is similar to the case when the field is absent. In fact, the maximum and the average temperature increments are equal to 0.31 °C and 0.11 °C respectively, corresponding to a whole-body SAR of 1.24 W/kg. In comparison to the scenario with the field applied longitudinally, the values of these increments are enhanced by nearly twice as much, even though the increases remain negligible. The rat, on the other hand, clearly shows the influence of field orientation and the relative eddy current effects. In this case, the maximum temperature increment is equal to 14.1 °C and the average increase is equal to 4 °C, with a whole-body average SAR of 21.2 W/kg and a peak spatial SAR (averaged over 50 mg of tissue) equal to 132 W/kg. The temperature peaks are mostly localized at the body surface, specifically in the skin, connective tissue, and muscles. Figure 6.5b shows the evolution of the maximum and average temperature increments over 100 min of heating and subsequent 100 min of cooling. The cooling time needed to restore the initial temperature is similar to the case when the field is applied longitudinally. Furthermore, with these heating transients, we can observe how in both animal models the temperature increases have values that are almost double the values reported for the cases of Figure 6.4b.

6.1.4 Influence of forced convection

Even when the Hergt-Dutz limit is not exceeded, the rat model shows excessive temperature increments that can have a significant influence on the mechanisms of thermoregulation. The temperature distributions within the rat, which are reported in Figure 6.4b and 6.5b, put in evidence how the thermal response is stronger on the body surface. Possible strategies to mitigate these excessive temperature increases are the displacement of the coil or the intermittent application of the magnetic field [16,17]. Another possibility is the use of water boluses [18], which are systems specifically designed to prevent excessively high temperatures on the skin.

The introduction of cooling systems, such as water boluses, determines a forced convection between skin and air, which corresponds to an increase in the outward heat flux. This is described in Eq. (4.2) with an increment of the convection heat transfer coefficient *h*, which depends on several properties of the water bolus, such as the thermal conductivity of the bag material and its thickness [19]. To take into account different conditions of forced convection, we evaluate the maximum temperature increment in the rat model varying *h* in the range from 3.5 W/(K·m^2) to 150 W/(K·m^2) [20] and assuming that the temperature of the water circulating in the bolus is constantly equal to 25 °C, i.e. equal to the temperature of the environment.

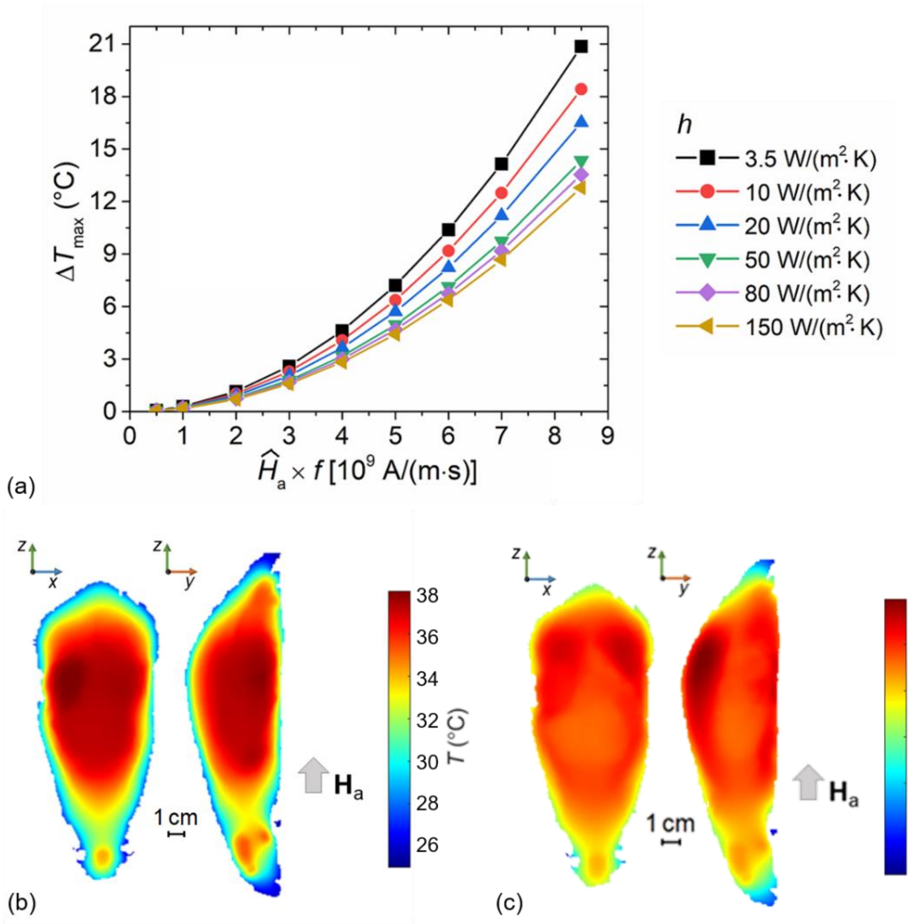

Figure 6.6. Influence of forced convection. Maximum temperature increments evaluated for the 503 g rat as a function of the product of the magnetic field peak amplitude and frequency and heat transfer coefficient h, with the AC magnetic field uniformly applied along the longitudinal axis of the body. Corresponding maps of the spatial distribution of the temperature at the equilibrium evaluated on two 2D longitudinal sections of the

animal, considering an AC magnetic field with $\hat{H}_a \times f = 5 \cdot 10^9$ A/(m·s), for (b) h = 80 W/(m^2·K) and (c) h = 10 W/(m^2·K). Graphs reported in [1].

The field is assumed to be applied along the longitudinal body axis ($\hat{H}_a \times f$ in the range $0.48 \cdot 10^9$ - $8.5 \cdot 10^9$ A/(m·s)) and we consider a heating time interval of 100 min. Moreover, as a first approximation we consider that the heat transfer coefficient is modified over the entire body surface. The results are reported on the graphs of Figure 6.6, where in Fig. 6.6a the maximum and average temperature increments are plotted as a function of the product $\hat{H}_a \times f$. The graphs show how the difference between the increments evaluated for different values of *h* becomes more significant with the increase of $\hat{H}_a \times f$. In particular, for a field with $\hat{H}_a \times f = 8.5 \cdot 10^9$ A/(m·s), the maximum increments vary between 12.79 °C and 20.86 °C, reducing *h* from 150 W/(K·m^2) to 3.5 W/(K·m^2). In addition, comparing the temperature increments calculated for *h* equal to 3.5 W/(K·m^2) with the ones obtained for 150 W/(K·m^2), we can observe a reduction in the average and maximum increments of 56% and 39% respectively. Fig. 6.6a displays an asymptotic behavior of the temperature increase as a function of *h*, since the eddy currents are significantly mitigated for large values of *h*. The influence of *h* on the temperature mitigation can be clearly observed in Figures 6.6b and 6.6c, where the temperature spatial distributions at the thermal equilibrium, evaluated on a longitudinal section of the rat body, are illustrated for *h* = 80 W/(K·m^2) and *h* = 10 W/(K·m^2) respectively, for the same field conditions, i.e. $\hat{H}_a \times f = 5 \cdot 10^9$ A/(m·s). The temperature distribution obtained with *h* = 10 W/(K·m^2) is similar to the case with *h* = 3.5 W/(K·m^2) illustrated in Fig. 6.3, where maximum values of temperature are mostly localized in more external areas. Whereas, for *h* = 80 W/(K·m^2), temperature peaks are no more concentrated on the skin or on peripheral tissues but are localized on more internal areas.

6.2 Cases with body exposed to non-uniform fields

In many preclinical studies, the AC magnetic fields are mainly focused on a small portion of the body, where the target region is localized, in order to not expose the surrounding healthy tissues to high magnetic field amplitudes. In some circumstances, the coils are placed in such a way to surround only specific portions of the body (e.g. limbs [21]), otherwise they do not surround any part of the body, but they are placed very close to the region to be treated. This ensures safer exposure conditions, reducing the appearance of hot spots in healthy tissues. For this reason, before applying an AC magnetic field, the analysis of its spatial distribution is essential to permit the displacement of the treated region where the field reaches larger values and has a more uniform distribution, leaving the surrounding healthy tissues exposed to magnetic fields with negligible field amplitudes.

In this section, we first compare the magnetic field generated by four applicators with different geometrical configurations typically used in preclinical tests: an 8-turn helical coil [22,23], a pancake coil [24], a Helmholtz type coil [25], and a 2-turn helical coil [26]. Then, for the first two types, we analyze the impact of the applicator's coil size, comparing the AC magnetic fields generated for different outer diameters. Finally, we simulate the thermal effects due to the magnetic field generated by some of the applicators analyzed.

The study of magnetic field distribution is finalized to analyze how non-uniform fields, which guarantee a more localized exposure of the target area, could mitigate eddy current effects. The analysis is performed on the rat model, which is the only one of the two considered animal models in which tumors are present, and we consider the largest tumor region, positioned in the flank of the animal (approximate size: 2.4×3.7×3.8 cm^3), to be the target region.

6.2.1 Magnetic field calculation

The current density vector inside the conductors is evaluated with the finite element method (FEM) solution of the current-field equation introduced in Section 2.1.1. To apply the FEM, the geometry of the coils is computationally reconstructed and discretized into tetrahedral elements. Afterward, the magnetic field within the body is numerically calculated by solving the Biot-Savart law

$$\mathbf{B}(\mathbf{r}) = \frac{\mu_0}{4\pi} \int_{\Omega_s} \frac{\mathbf{J}(\mathbf{r}_s) \times (\mathbf{r} - \mathbf{r}_s)}{|\mathbf{r} - \mathbf{r}_s|^3} dV_s$$

where $\mathbf{J}$ is the current density vector evaluated in the conductor (domain Ω_s) with the current-field equation, $\mathbf{r}$ is the position vector in the calculation domain Ω (i.e. the animal body), and $\mathbf{r}_s$ is the position vector in the conductor.

6.2.2 Influence of applicator geometry on magnetic field spatial distribution

For a first analysis, we consider the four types of coil geometry introduced above, where the 8-turn, the pancake, and the Helmholtz coils have an outer diameter of 5 cm; whereas, the 2-turn coil has an outer diameter of 20 cm.

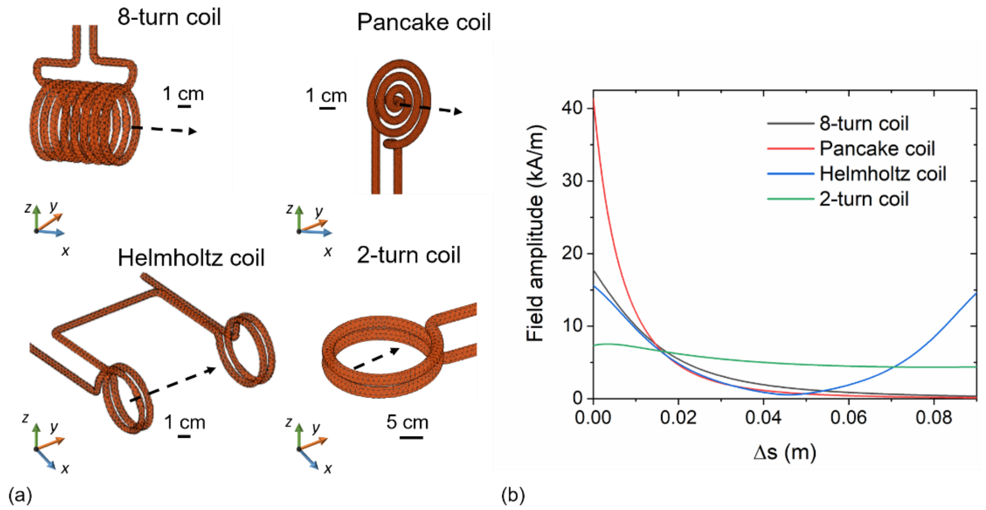

Figure 6.7. (a) Schematics of the coils. (b) Corresponding magnetic field evaluated over the black line indicated in (a).

Furthermore, each side of the Helmholtz coil is made up of two turns of wire. Figure 6.7a depicts the geometrical structure of the coils. Due to their size, only the Helmholtz and the 2-turn coils are assumed to partially surround the animal, whereas the other two coils are considered to be placed totally external to the body, as schematized in Figure 6.8. Here we evaluate the magnetic field along a line at half the turn height (the dash black line in Figure 6.7a) and up to 9 cm of distance from the outermost turn (or the most internal for the Helmholtz and 2-turn coils) because the rat model's transversal section is 8 cm wide. For the calculation, we have considered that the 8-turn and the pancake coil are supplied with a current of 300 A, whereas the other two coils with a current of 400 A. The evaluated magnetic field amplitude is reported in Figure 6.7b for each coil. The pancake and the 8-turn coils have similar behaviors, their field amplitude decreases as the distance from the applicator increases, starting with a peak amplitude of about 41.3 kA/m and 17.8 kA/m respectively, and tending to zero when the distance Δs is larger than 6 cm. The Helmholtz presents a u-shaped curve, where the field peaks are reached in the proximity of the turns with a value of about 15.6 kA/m, and the minimum, located at the center between the coils of

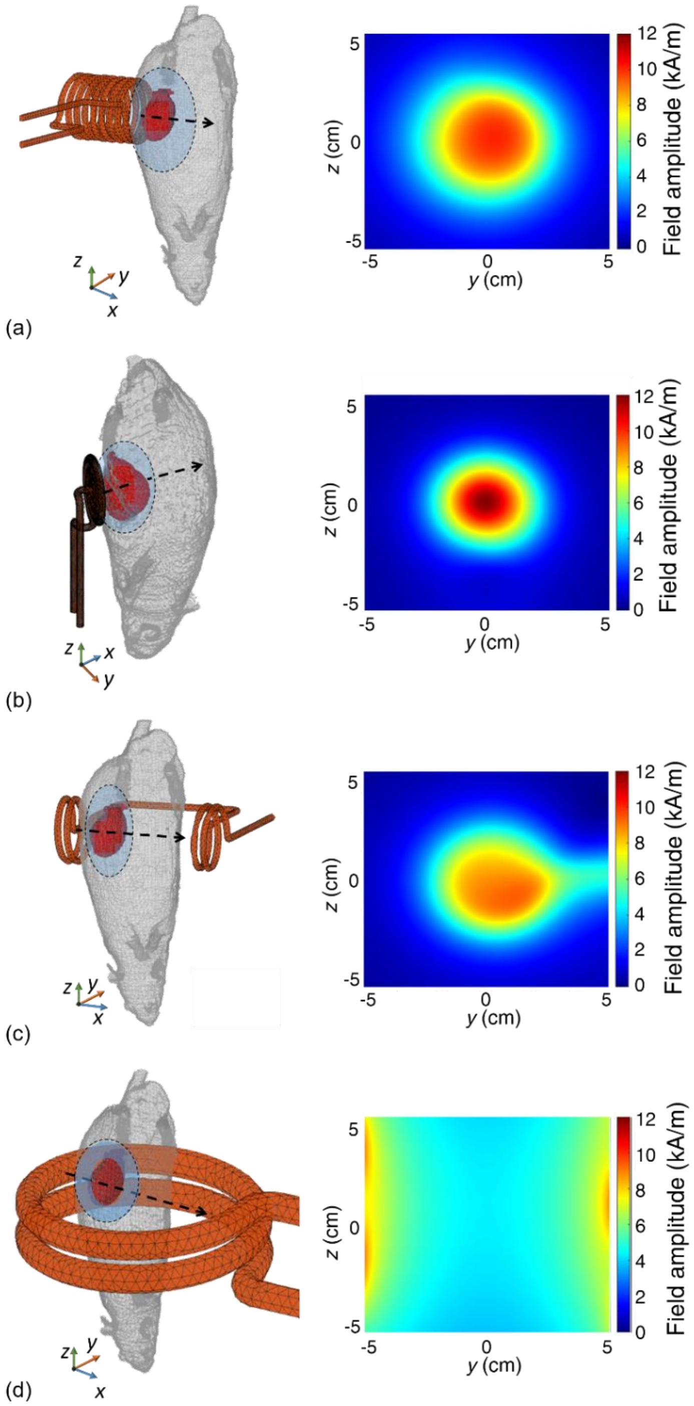

Figure 6.8. Figure 6.8. 2D maps of the magnetic field evaluated on the yz-plane for (a) the 8-turn coil supplied with a 300 A current, (b) the pancake coil supplied with a 300 A current, (c) the Helmholtz coil supplied with a 400 A current, and (d) the 2-turn coil supplied with a 400 A current.

the applicator, has a value of 0.55 kA/m. In the 2-turn coil, the magnetic field is quite uniform along the whole line of calculation, since it is calculated inside the applicator. It has a maximum field value of 7.5 kA/m, which is the lowest reached by the applicators considered, a minimum value of 4.4 kA/m, and an average value of 5.2 kA/m.

In addition, for each coil configuration, we calculate the field amplitude on 2D maps of the same size, whose position is schematized with the light blue oval at the left of Figure 6.8. For the 8-turn and pancake coils, the map is calculated on a plane parallel to the coil turns, i.e. orthogonal to and centered on the calculation line of Figure 6.7b, at a distance of 1 cm. The results are displayed in Figure 6.8a and Figure 6.8b, where we can observe a similar distribution of the field amplitude, with maximum values in correspondence with the central area. The pancake coil shows a field amplitude that decreases faster with respect to the 8-turn coil, with the increase in the radial distance from the center of the map. Whereas, Figure 6.8c shows the field map of the Helmholtz coil calculated on a 2D section parallel to its two coils, and at a distance of 1 cm from one of the internal turns. In comparison to the other two maps, the Helmholtz presents a more asymmetric field, which is however focused at the center of the turns. Finally, Figure 6.8d reports the 2D map of the field generated by the 2-turn coil and is evaluated on a plane perpendicular to the coil turns, orthogonal to the black line of Fig. 6.7a, and at a distance of 1 cm from the internal part of the turns. In this case, the map shows larger values of field amplitude in the most external areas that are in proximity to the turns, whereas the central area has the lowest field values. However, comparing these maps as well, the 2-turn coil is characterized by the most uniform field distribution.

Since the pancake coil and the 8-turn coil show a magnetic field that rapidly decreases, as displayed in Figure 6.7b, we have evaluated the magnetic field for the same applicator types, but varying the outer diameter of the coils and/or adding turns. Specifically, for the 8-turn coil first we change the outer diameter, varying it from 4 cm to 10 cm, then we also add turns to the applicators, but only for the applicators with the largest diameters, i.e. 7.5 cm and 10 cm. Adding turns, the solenoid changes its length from 6.1 cm, for the 8-turn coil, to a length of 7.5 cm, for the 10-turn coil. Whereas, for the pancake coil, we only enlarge the diameter, considering a coil with an outer diameter of 7.6 cm and one of 9 cm. We compare the magnetic field generated by these applicators along the same line of Figure 6.7b, considering a current supply of 300 A, and the results are reported in Figure 6.9a for the solenoid, and in Figure 6.9b for the pancake. We can observe a

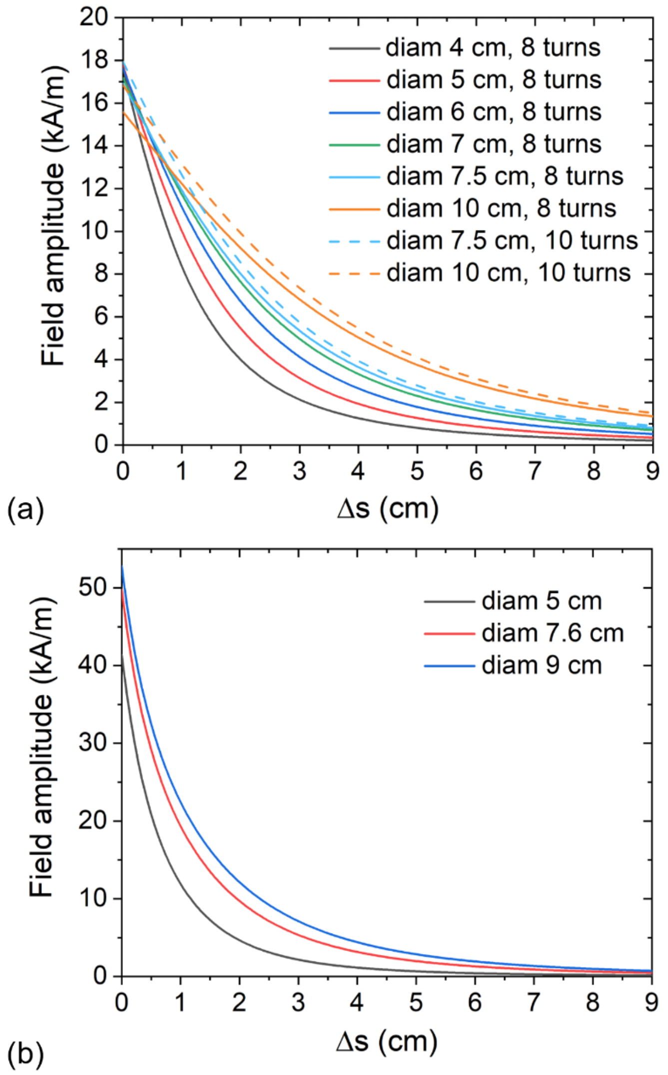

Figure 6.9. (a) Magnetic field amplitude evaluated along the black line reported in Fig. 6.6a, for (a) the 8-turn coil by varying the outer diameter from 4 cm to 10 cm and adding 2 turns for the coils with diameter equal to 7.5 cm and 10 cm; (b) the pancake coil by varying the diameter from 5 cm to 9 cm.

rise in magnetic field amplitude for both coil types as the outer diameter increases. For example, at Δs = 1 cm the 8-turn coil has a field amplitude that varies between 8.2 kA/m, for the smallest diameter (4 cm), and 12.2 kA/m, for the largest one (10 cm), with an increment of 48.8%. The addition of turns leads to a slight increase in the field amplitude, but this is not very relevant, in comparison to the coils with the same outer diameter. As an example, at Δs = 2 cm, the 8-turn coil with an outer diameter of 10 cm generates a field with amplitude of 9.2 kA/m, whereas the corresponding coil with 10 turns and the same diameter provides a field equal to 9.9 kA/m. Moreover, at Δs = 8.5 cm, only the applicators with an outer diameter larger than 7.5 cm reach a value higher than 1 kA/m. Similar observations can be made for the pancake coil, where the configurations with a larger outer diameter present higher field peaks. For example, at Δs = 1 cm the field varies from 12 kA/m for the coil with an outer diameter of 5 cm to 22.6 kA/m for the coil with a diameter equal to 9 cm, with an increase of 88%. Comparing the two types of coils, the field amplitude decreases rapidly for all the configurations, but the pancake coils present a faster decrease along the displacement than the 8-turn coils.

6.2.3 Influence of applicator geometry on thermal effects

The position of the coils with respect to the animal body has been selected in such a way that a side of their wires is very close to the target region, in order to expose mainly the tumor to a magnetic field sufficiently large and uniform to permit a proper activation of MNPs. The positions of the coils are schematized on the left of Figure 6.10, where the tumor to be treated is colored in red. The 8-turn coil and the pancake coil are placed entirely outside the rat body, whereas the Helmholtz coil and the 2-turn coils surround the flanks of the animal. Apart from the 2-turn coil and the Helmholtz coil, which in our simulations have a fixed outer diameter of 20 cm and 5 cm respectively, we consider in these first simulations that the 8-turn and the pancake coils have a turn diameter equal to 5 cm. Moreover, the 8-turn and the pancake coil are supplied with a current of 300 A, whereas the other two coils with 400 A, as previously considered.

Regarding the magnetic field distribution inside the target region, the maximum, the minimum, and the average values of the field generated by the four coils are reported in Table 6.1. The pancake coil shows the highest difference between the maximum and the minimum values of the field amplitude, whereas the 2-turn coil presents the most uniform field distribution inside the tumor. In the central graphs of Figure 6.10, we report the maps of the field amplitude along a 2D section of the animal body that crosses the barycenter of the tumor, whose boundary is indicated by the gray line, and the graphs on the right are the temperature maps on the same section, obtained with a field frequency of 300 kHz, as a consequence of eddy current effects. Even if the three smallest coils have different field distributions within the rat body, as it is displayed by the field maps, the temperature distributions do not show significant differences between the four field sources. All the thermal simulations result in a temperature spatial distribution that is very similar to the case when the field applicator is turned off and the temperature distribution is only due to metabolic processes. In fact, the warmest areas in the rat are the brain, tumors, intestine, and heart, as found in the absence of an applied field. Moreover, the maximum temperature increments evaluated in the whole body are 0.36 °C, 0.18 °C, and 0.17 °C, in correspondence with a whole-body average SAR of 0.3 W/kg, 0.2 W/kg, and 0.2 W/kg, for the 8-turn, the pancake, and the Helmholtz coil respectively. Thus, the eddy current effects are limited and the increments are negligible, concentrated on peripheral tissues in the areas closest to the coils. Only with the 2-turn coil there is a slight variation in the temperature distribution, especially within the tumor and the surrounding areas that are closer to the coil turns. The impact is moderate along the whole 2D section, as illustrated on the temperature map, due to the more uniform field distribution along the body section that is surrounded by the EM field applicator. In particular, the maximum temperature increment within the whole body is equal to 1.28 °C and it is localized on the muscle of the flank on the side where the target region is located, near the skin, at a point outside the 2D map.

Since with a field frequency of 300 kHz part of the target region exceeds the Herg-Dutz limit, we perform the same simulations by varying only the field frequency that we fix to 150 kHz. For this field frequency, the maximum temperature increase is 0.32 °C and is reached with the 2-turn coil, in correspondence with a whole-body average SAR of 0.8 W/kg. The other applicators lead to a temperature increase of 0.08 °C, 0.05 °C, and 0.04 °C, and SAR values of 0.09 W/kg, 0.05 W/kg, and 0.04 W/kg for the 8-turn, the pancake, and the Helmholtz coil respectively. Thus, with a field frequency of 150 kHz, no significant temperature increments are observed for all the applicators.

Table 6.1. Magnetic field amplitude within the target region.

Coil	Magnetic field amplitude (kA/m)		
	Maximum	Minimum	Average
8-turn	17.5	3.8	8.5
Pancake	28.2	2	7.2
Helmholtz	10.1	1.5	4.1
2-turn	8	4.9	6.2

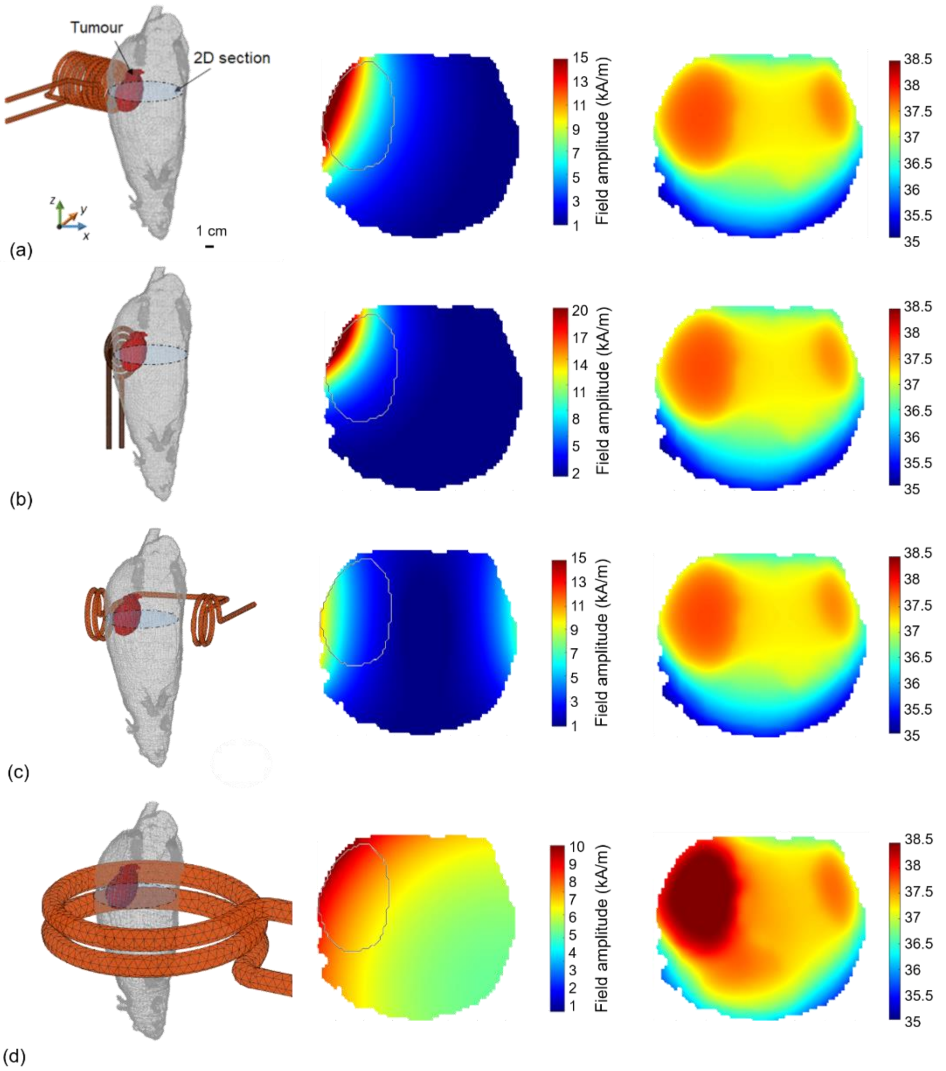

Figure 6.10. Exposure to the AC magnetic fields produced by four EM field applicators: (a) an 8-turn coil with outer diameter of 5 cm, (b) a pancake coil with outer diameter of 5 cm, (c) Helmholtz coil with a turn diameter of 5 cm, and (d) a 2-turn coil with outer diameter of 20 cm. On the left, schematics of the applicator position with respect to the animal body, with the tumor colored in red. At the center, the magnetic field maps, and on the right the corresponding maps of the temperature distribution are evaluated over the same 2D transversal section depicted in the schematics. (a), (b), and (c) have a supply current of 300 A, whereas (d) of 400 A with frequency of 300 kHz. The boundary of the tumor is indicated with a gray line.

Because there is no significant temperature increase for both frequencies with the 8-turn and pancake coils with an outer diameter of 5 cm, we repeat the thermal simulations with the 8-turn coil with an outer diameter of 10 cm and the pancake coil with a diameter of 9 cm to investigate how coil size affects the thermal

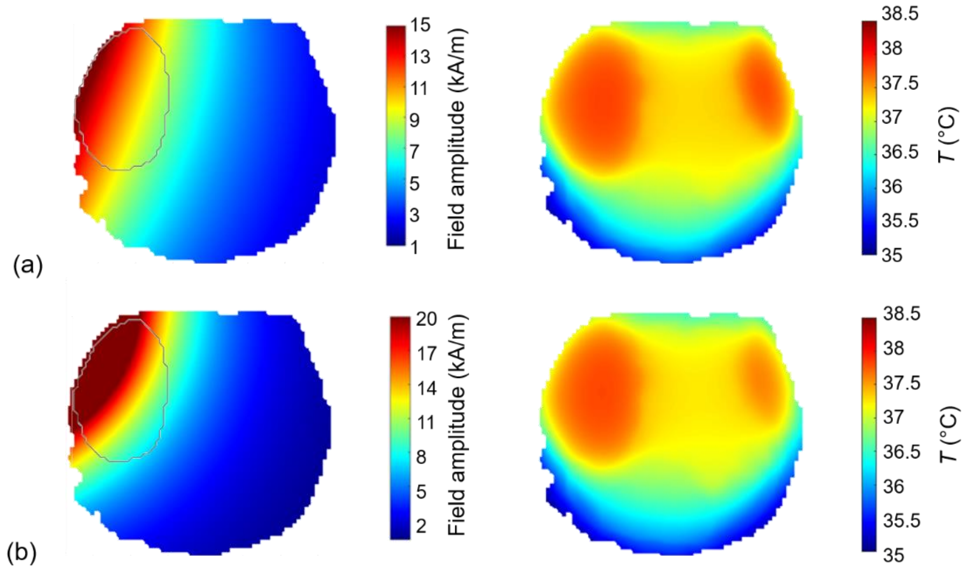

Figure 6.11. On the left, the maps of the magnetic field amplitude evaluated over the same 2D section of Fig. 6.9, and on the right the correspondent spatial distribution of the temperature, for (a) the 8-turn coil with an outer diameter of 10 cm, (b) the pancake coil with an outer diameter of 9 cm. The magnetic fields have a fixed frequency of 150 kHz, and both coils have a supply current of 300 A. The tumor boundary is indicated with the grey line on the maps on the left.

response. The simulations are performed considering that the coils are supplied with a current of 300 A and we consider a field frequency fixed to 150 kHz. The coils are positioned in the same way as schematized on the left graphs of Figure 6.10a. In particular, Figure 6.11a and 6.11b show the results for the 8-turn coil and the pancake coil respectively, where on the left the 2D field map of the transversal section of the animal's body is reported, and the map on the right is the temperature spatial distribution in the same body section. Inside the tumor, for the 8-turn coil the maximum field amplitude reached is 15.5 kA/m (the minimum field value is 7.7 kA/m and the average value is 11.5 kA/m), whereas the pancake coil provides a larger maximum field amplitude equal to 47.3 kA/m (minimum value of 7.6 kA/m and average value of 17.9 kA/m). In comparison to the field maps reported in Figure 6.10a and 6.10b, there are larger portions of the body outside the tumor that are exposed to high field values. However, considering only the temperature maps, the temperature values are very similar to the ones reported in Figure 6.10. Whereas the maximum increments within the whole body are larger, i.e. 0.86 °C and 0.77 °C (in correspondence with a whole-body average

SAR of 1.8 W/kg and 0.4 W/kg) for the 8-turn coil and the pancake coil respectively. The maximum temperature increases are localized within the skin of the flank of the target region and they are not in the nearest proximity to the tumor, as the distance between the point with the highest temperature increment and the tumor's barycenter is about 3.5 cm (3.8 cm for the 8-turn coil and 3.3 for the pancake coil).

6.3 Effects of parameter uncertainties

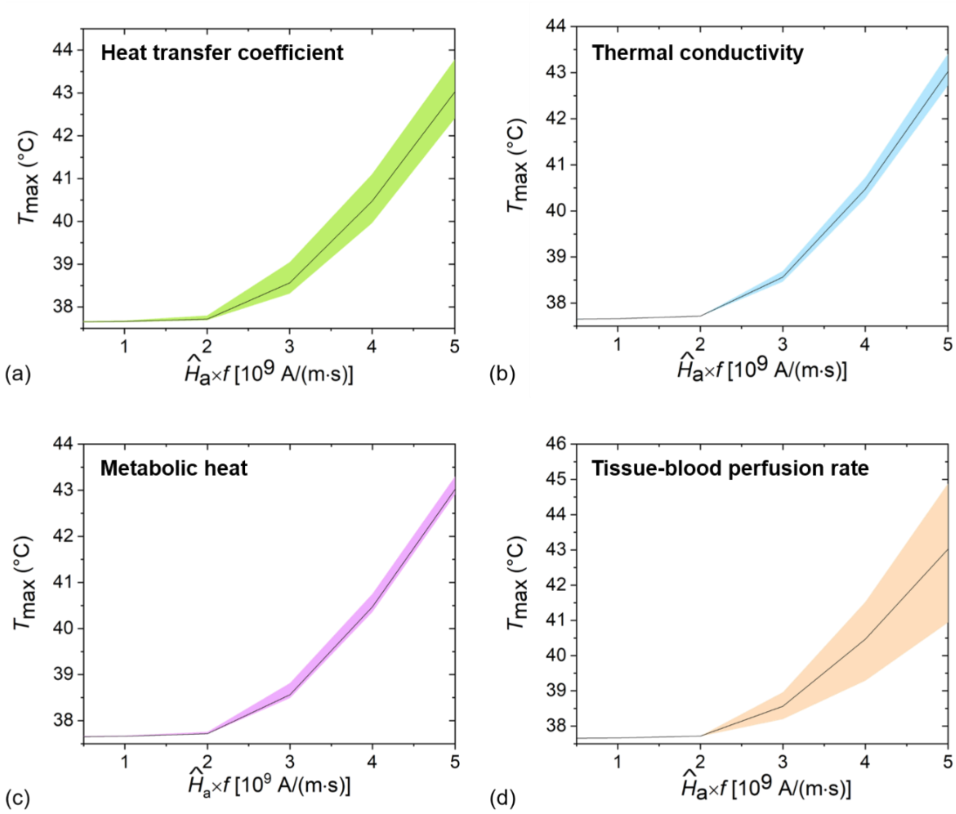

Figure 6.12. Effects of parameter selection on the maximum temperature within the rat model. Values of the maximum temperature as a function of the product between the field amplitude and frequency, varying: (a) the heat transfer coefficient between 2 W/(K·m^2) and 5 W/(K·m^2), and (b) the thermal conductivity, (c) the metabolic heat, and (d) the tissue-blood perfusion rate in their interval of variation.

The bio-heat simulations require several input parameters, which comprise the tissue thermal properties, the tissue density, and the heat transfer coefficient at the skin-air interface. The tissue parameters are derived from measurements with a certain degree of uncertainty, whereas the heat transfer coefficient depends on conditions that are difficult to evaluate (e.g. environment characteristics, animal type, etc. [27]). Thus, the parameters present variability that could significantly impact on the temperature evaluation, and for this reason, the selection of the parameters becomes crucial to guarantee realistic simulations.

In this Chapter, all the thermal simulations are performed setting the heat transfer coefficient h at 3.5 W/(K·m^2), in accordance to [28], and for the tissue properties we consider the mean value of each parameter reported in the IT'IS Foundation database [29] (apart from the tumor properties that are taken from [30], as specified in Section 4.6). To investigate the impact of the variation of h, we evaluate the maximum temperature in the rat model, considering a uniform field along the body axis and varying the values of $\hat{H}_a \times f$ in the range of $0.5 \cdot 10^9$ - $5 \cdot 10^9$ A/(m·s), and the values of h from 2 W/(K·m^2) to 5 W/(K·m^2), in order to consider a wide range of variation for this last parameter that comprises the values reported in the literature [25,31,32,33]. The results are displayed in Figure 6.12a, where we can observe a difference between the case with h = 2 W/(K·m^2) and h = 5 W/(K·m^2) that increases with the increment of $\hat{H}_a \times f$ and reaches a maximum difference of 1.38 °C for $\hat{H}_a \times f$ = $5 \cdot 10^9$ A/(m·s). A similar, but limited, trend can be observed in the evaluation of the average temperature, where the maximum difference is equal to 1.03 °C, for $\hat{H}_a \times f$ = $5 \cdot 10^9$ A/(m·s).

To analyze the impact of the tissue thermal parameters, we evaluate the maximum temperature at equilibrium within the rat body with the same field conditions considered above, h fixed to 3.5 W/(K·m^2), and varying the values of thermal conductivity k (Fig. 6.12b), metabolic heat Q_m (Fig. 6.12c), and tissue-blood perfusion rate W (Fig. 6.12d) one at a time. For the variation of these parameters, we consider the minimum and the maximum values reported in the IT'IS Foundation database for each tissue. It is worth noting that for each tissue and for each parameter the number of measurements is different and varies a lot. As an example, for the thermal conductivity the data are derived from 9 measurements for the liver and from only one for the hypophysis. The parameters of the tumor and of the tissues derived from only one measurement in the database are not changed in the simulations. In figures 6.12b-d we can observe that the variation of T_{max} rises with the increment of $\hat{H}_a \times f$, and that only the tissue-blood perfusion rate has a significant impact on the temperature evaluation, with a maximum difference between T_{max} obtained with the lowest values of W and the one with the largest values of W equal to 3.95 °C, in correspondence of a maximum difference of 1.48 °C for the average temperature. Whereas k and Q_m have a maximum variation of T_{max} equal to 0.42 °C and 0.4 °C, respectively.

6.4 Conclusions

In this Chapter, we have analyzed how the only field exposure can influence the thermal response of tissues, taking into account the biophysical limits discussed in section 1.2.1. In particular, we have investigated the possible occurrence of non-negligible effects of eddy currents in preclinical studies. Through the simulations on two murine models, we have shown that the thermal effects caused by AC magnetic fields are quite low for animals of small sizes, e.g. mice of 25-30 g, even when the Hergt-Dutz limit is slightly exceeded. Only for very large values of the product $\hat{H}_a \times f$ significant thermal effects can be obtained. As an example, for $\hat{H}_a$ = 40 kA/m and f = 500 kHz, a maximum temperature increment of more than 2 °C is observed on the skin. On the contrary, in larger animals, such as rats, eddy current effects are no longer negligible. For example, in the case of the 503 g rat model exposed to a uniform magnetic field along the body longitudinal axis, we have demonstrated that a maximum temperature increment of less than 1 °C occurs only when $\hat{H}_a \times f < 2 \cdot 10^9$ A/(m·s). Moreover, when the field is applied transversally, higher temperature increases are observed, due to the increment of the section of the animal body orthogonal to the field direction. The simulation results have shown that the Hergt-Dutz limit could not be assumed as a condition that ensures a safe level of AC magnetic field exposure for animals like rats or larger ones, which has clear implications for its applicability to humans. However, a significant reduction in eddy current effects can be achieved with the introduction of water boluses, due to the forced heat convection at the skin-environment interface. Another strategy is the use of suitable EM field applicators that focus the field only on the diseased region to be treated. With the analysis of four applicators with different geometry, we have found a strong reduction in the SAR values, and consequently in the temperature increments. In particular, the 8-turn, the pancake, and the Helmholtz coils with an outer diameter of 5 cm showed a negligible temperature increment lower than 0.4 °C, for both frequency values considered. In these simulations, the largest effects due to eddy currents are found only on peripheral areas in close proximity to the coils, i.e. where the field parameter product, $\hat{H}_a \times f$ is close to or slightly exceeds the Hergt-Dutz limit. Nevertheless, the focus of the field within the diseased area becomes more difficult with the largest applicators, for which we have found higher temperature increments, of about 1 °C, but not within the tumor. As an example, with a field frequency of 300 kHz and with the 2-turn coil (outer diameter of 20 cm) a maximum temperature increment of 1.28 °C was found on the muscle between the treated tumor and the nearest paw. Finally, we have briefly analyzed the influence of the parameter selection (heat transfer coefficient, thermal conductivity, tissue-blood perfusion rate, and metabolic heat) on the thermal response. Specifically, we have observed that, for the simulated cases, the thermal conductivity and the metabolic heat variations weakly affect the maximum temperature, whereas the tissue-blood perfusion rate variation leads to a maximum difference of about 4 °C. Thus, the uncertainty due to the tissue property measurement could have a significant impact on the thermal simulations and their outcomes to support *in vivo* tests. Luckily, the IT'IS Foundation database is continuously updated because a careful selection of the physical input parameters of the model is crucial to perform reliable simulations.

6.5 References

[1] M. Vicentini, M. Vassallo, R. Ferrero, I. Androulakis, and A. Manzin, "In silico evaluation of adverse eddy current effects in preclinical tests of magnetic hyperthermia," *Comput. Methods Programs Biomed.*, vol. 223, no. 106975, 2022. DOI: 10.1016/j.cmpb.2022.106975.

[2] S. Kossatz *et al.*, "Efficient treatment of breast cancer xenografts with multifunctionalized iron oxide nanoparticles combining magnetic hyperthermia and anti-cancer drug delivery," *Breast Cancer Res.*, vol. 17, no. 1, p. 66, 2015. DOI: 10.1186/s13058-015-0576-1.

[3] S. Piehler *et al.*, "Iron oxide nanoparticles as carriers for DOX and magnetic hyperthermia after intratumoral application into breast cancer in mice: Impact and future perspectives," *Nanomaterials (Basel)*, vol. 10, no. 6, p. 1016, 2020. DOI: 10.3390/nano10061016.

[4] A. Espinosa *et al.*, "Magnetic (hyper)thermia or photothermia? Progressive comparison of iron oxide and gold nanoparticles heating in water, in cells, and in vivo," *Adv. Funct. Mater.*, vol. 28, no. 37, p. 1803660, 2018. DOI: 10.1002/adfm.201803660.

[5] A. Plan Sangnier *et al.*, "Targeted thermal therapy with genetically engineered magnetite magnetosomes@RGD: Photothermia is far more efficient than

magnetic hyperthermia," *J. Control. Release*, vol. 279, pp. 271–281, 2018. DOI: 10.1016/j.jconrel.2018.04.036.

[6] A. Curcio *et al.*, "Iron oxide nanoflowers @ CuS hybrids for cancer Tri-therapy: Interplay of photothermal therapy, magnetic hyperthermia and photodynamic therapy," *Theranostics*, vol. 9, no. 5, pp. 1288–1302, 2019. DOI: 10.7150/thno.30238.

[7] C. L. Dennis *et al.*, "Nearly complete regression of tumors via collective behavior of magnetic nanoparticles in hyperthermia," *Nanotechnology*, vol. 20, no. 39, p. 395103, 2009. DOI: 10.1088/0957-4484/20/39/395103.

[8] X. Ma *et al.*, "Fe3O4–Pd Janus nanoparticles with amplified dual-mode hyperthermia and enhanced ROS generation for breast cancer treatment," *Nanoscale Horiz*, vol. 4, no. 6, pp. 1450–1459, 2019. DOI: 10.1039/C9NH00233B.

[9] H. A. Albarqi *et al.*, "Systemically delivered magnetic hyperthermia for prostate cancer treatment," *Pharmaceutics*, vol. 12, no. 11, p. 1020, 2020. DOI: 10.3390/pharmaceutics12111020.

[10] X. L. Liu *et al.*, "Synthesis of ferromagnetic Fe0.6Mn0.4O nanoflowers as a new class of magnetic theranostic platform for in vivo T1-T2Dual-mode magnetic resonance imaging and magnetic hyperthermia therapy," *Adv. Healthc. Mater.*, vol. 5, no. 16, pp. 2092–2104, 2016. DOI: 10.1002/adhm.201600357.

[11] J.-H. Lee *et al.*, "Exchange-coupled magnetic nanoparticles for efficient heat induction," *Nat. Nanotechnol.*, vol. 6, no. 7, pp. 418–422, 2011. DOI: 10.1038/nnano.2011.95.

[12] M. L. Reitman, "Of mice and men - environmental temperature, body temperature, and treatment of obesity," *FEBS Lett.*, vol. 592, no. 12, pp. 2098–2107, 2018. DOI: 10.1002/1873-3468.13070.

[13] W. Lin *et al.*, "Thermosensitive magnetic liposomes with doxorubicin cell-penetrating peptides conjugate for enhanced and targeted cancer therapy," *Drug Deliv.*, vol. 23, no. 9, pp. 3436–3443, 2016. DOI: 10.1080/10717544.2016.1189983.

[14] O. K. Arriortua *et al.*, "Antitumor magnetic hyperthermia induced by RGD-functionalized Fe3O4 nanoparticles, in an experimental model of colorectal liver metastases," *Beilstein J. Nanotechnol.*, vol. 7, pp. 1532–1542, 2016. DOI: 10.3762/bjnano.7.147.

[15] S.-W. Ding *et al.*, "Magnetic hydrogel with long in situ retention time for self-regulating temperature hyperthermia," *Int. J. Hyperthermia*, vol. 38, no. 1, pp. 13–21, 2021. DOI: 10.1080/02656736.2020.1863479.

[16] G. Pefanis, N. Maniotis, A.-R. Tsiapla, A. Makridis, T. Samaras, and M. Angelakeris, "Numerical simulation of temperature variations during the application of safety protocols in magnetic particle hyperthermia," *Nanomaterials (Basel)*, vol. 12, no. 3, p. 554, 2022. DOI: 10.3390/nano12030554.

[17] A. Balousis, N. Maniotis, and T. Samaras, "Improvement of magnetic particle hyperthermia: Healthy tissues sparing by reduction in eddy currents," *Nanomaterials (Basel)*, vol. 11, no. 2, p. 556, 2021. DOI: 10.3390/nano11020556.

[18] K. Arunachalam, P. F. Maccarini, J. L. Schlorff, Y. Birkelund, S. Jacobsen, and P. R. Stauffer, "Design of a water coupling bolus with improved flow distribution for multi-element superficial hyperthermia applicators," *Int. J. Hyperthermia*, vol. 25, no. 7, pp. 554–565, 2009. DOI: 10.3109/02656730903124506.

[19] A. Bakker *et al.*, "Clinical feasibility of a high-resolution thermal monitoring sheet for superficial hyperthermia in breast cancer patients," *Cancers (Basel)*, vol. 12, no. 12, p. 3644, 2020. DOI: 10.3390/cancers12123644.

[20] M. L. Van der Gaag, M. De Bruijne, T. Samaras, J. Van der Zee, and G. C. Van Rhoon, "Development of a guideline for the water bolus temperature in superficial hyperthermia," *Int. J. Hyperthermia*, vol. 22, no. 8, pp. 637–656, 2006. DOI: 10.1080/02656730601074409.

[21] L. Bubnovskaya *et al.*, "Magnetic fluid hyperthermia of rodent tumors using manganese perovskite nanoparticles," *J. Nanoparticles*, vol. 2014, pp. 1–9, 2014. DOI: 10.1155/2014/278761.

[22] M. Ohtake *et al.*, "Hyperthermia and chemotherapy using Fe(Salen) nanoparticles might impact glioblastoma treatment," *Sci. Rep.*, vol. 7, p. 42783, 2017. DOI: 10.1038/srep42783.

[23] H. F. Rodrigues, F. M. Mello, L. C. Branquinho, N. Zufelato, E. P. Silveira-Lacerda, and A. F. Bakuzis, "Real-time infrared thermography detection of magnetic nanoparticle hyperthermia in a murine model under a non-uniform field configuration," *Int. J. Hyperthermia*, vol. 29, no. 8, pp. 752–767, 2013. DOI: 10.3109/02656736.2013.839056.

[24] T. Araya *et al.*, "Antitumor effects of inductive hyperthermia using magnetic ferucarbotran nanoparticles on human lung cancer xenografts in nude mice," *Onco. Targets. Ther.*, vol. 6, pp. 237–242, 2013. DOI: 10.2147/OTT.S42815.

[25] H. F. Rodrigues, G. Capistrano, F. M. Mello, N. Zufelato, E. Silveira-Lacerda, and A. F. Bakuzis, "Precise determination of the heat delivery during in vivo magnetic nanoparticle hyperthermia with infrared thermography," *Phys. Med. Biol.*, vol. 62, no. 10, pp. 4062–4082, 2017. DOI: 10.1088/1361-6560/aa6793.

[26] A. Attaluri, R. Ma, Y. Qiu, W. Li, and L. Zhu, "Nanoparticle distribution and temperature elevations in prostatic tumours in mice during magnetic nanoparticle hyperthermia," *Int. J. Hyperthermia*, vol. 27, no. 5, pp. 491–502, 2011. DOI: 10.3109/02656736.2011.584856.

[27] K. M. Wooden and G. E. Walsberg, "Effect of wind and solar radiation on metabolic heat production in a small desert rodent, Spermophilus tereticaudus," *J. Exp. Biol.*, vol. 203, no. Pt 5, pp. 879–888, 2000. DOI: 10.1242/jeb.203.5.879.

[28] A. Trakic, F. Liu, and S. Crozier, "Transient temperature rise in a mouse due to low-frequency regional hyperthermia," *Phys. Med. Biol.*, vol. 51, no. 7, pp. 1673–1691, 2006. DOI: 10.1088/0031-9155/51/7/003.

[29] https://itis.swiss/virtual-population/tissue-properties/overview/.

[30] A. Attaluri *et al.*, "Magnetic nanoparticle hyperthermia enhances radiation therapy: A study in mouse models of human prostate cancer," *Int. J. Hyperthermia*, vol. 31, no. 4, pp. 359–374, 2015. DOI: 10.3109/02656736.2015.1005178.

[31] A. Hirata *et al.*, "Computational verification of anesthesia effect on temperature variations in rabbit eyes exposed to 2.45 GHz microwave energy," *Bioelectromagnetics*, vol. 27, no. 8, pp. 602–612, 2006. DOI: 10.1002/bem.20251.

[32] M. Singh, Q. Gu, R. Ma, and L. Zhu, "Heating protocol design affected by nanoparticle redistribution and thermal damage model in magnetic nanoparticle hyperthermia for cancer treatment," *J. Heat Transfer*, vol. 142, no. 7, 2020. DOI: 10.1115/1.4046967.

[33] E. H. Ooi, V. Popov, M. Alfano, and J. K. K. Cheong, "Influence of natural convection on gold nanorods-assisted photothermal treatment of bladder cancer in mice," *Int. J. Hyperthermia*, vol. 37, no. 1, pp. 634–650, 2020. DOI: 10.1080/02656736.2020.1771437.

Chapter 7

In silico modelling of heating effects due to magnetic nanoparticles activation

Part of the material presented in this chapter is published in Advanced Theory and Simulations 4 (5): 2100013, May 2021

In this Chapter, we describe the results obtained by mimicking *in vivo* experiments of magnetic hyperthermia on animals. The study is carried out on the computational anatomical models of a mouse and a rat, and the heating efficiencies of different types of MNPs are compared. The aim is to establish the optimal conditions to reach the therapeutic temperature range (40-45 °C) inside the target region to be treated (generally a tumor region), as a function of the administered dose and spatial distribution of MNPs, and of AC magnetic field parameters (frequency and peak amplitude), starting from the results discussed in Chapter 6 for the safe levels of EM field exposure. Specifically, the heating efficiency of MNPs is analyzed in relation to the main factors that influence tissue thermal response. These comprise the size and the location of the tumor region where the MNPs are administered, the thermal properties of such region and of its surrounding tissues, as well as the MNP and magnetic field spatial distribution within it.

The thermal response is calculated by solving the Pennes' bio-heat equation as described in Chapter 4, where the MNP heating contribution is taken into account by the term Q_{MNPs} of Eq. 4.1, which is the product between the SLP (W/g) and the dose (g/m^3) of MNPs.

The *in silico* analysis of MNP heating efficiency is first carried out on the mouse model, varying the location of the target region where the MNPs are administered, to elucidate the role of tissue thermal properties on the thermal response. The heating agents here considered are the permalloy nanodisks analyzed in Chapter 5. Then, the analysis is moved to the rat model, where the MNPs are assumed to be distributed within one of the three tumors present in the animal body, i.e. the largest one. With this animal model, the heating efficiency of four different types of MNPs [1] is investigated, varying the MNP dose and the AC magnetic field parameters (peak amplitude and frequency). As a first assumption, the MNPs and magnetic field spatial distributions are considered to be uniform within the tumor region.

In the last part of the Chapter, the influence of MNPs and magnetic field distribution are investigated with the rat model, first considering non-uniform MNP distributions within the tumor (assuming that the MNPs are injected in multiple sites), then simulating the thermal response for non-uniform field distributions evaluated with the four EM field applicators analyzed in Chapter 6.

7.1 Analysis of the heating effects of magnetic nanodisks in a mouse model

This Section evaluates the heating effects in the 28 g mouse model of the permalloy nanodisks analyzed in Chapter 5. As a first approximation, we assume that the nanodisks are uniformly distributed within spherical regions of diameter δ with values of 4 mm, 6 mm, 8 mm, and 10 mm, and with different doses (from 0.1 mg/cm^3 to 5 mg/cm^3). We test the nanodisk heating efficiency by varying the location of the region containing them: intestine, lung, liver, and brain. Since the nanodisks are located inside tissues that have a higher viscosity than liquid samples, the SLP value is set at 225 W/g as done in Chapter 5 for the simulations mimicking thermometric measurements in gel. The AC magnetic field is oriented along the longitudinal body axis and is assumed to be uniform with a frequency value of 50 kHz. As seen in Chapter 6, if the Hergt-Dutz limit is fulfilled the EM field is responsible for negligible eddy current effects in mice, thus the heating power due to the field is considered to be null in the Pennes' bio-heat equation. The simulations are performed considering a value for the heat transfer coefficient h equal to 0.5 W/(m^2·K) [2], the temperature of the environment, i.e. T_{air} in Equation 4.2, is assumed to be 25 °C and the initial skin temperature is fixed to 33 °C [3].

7.1.1 Influence of tissue thermal properties

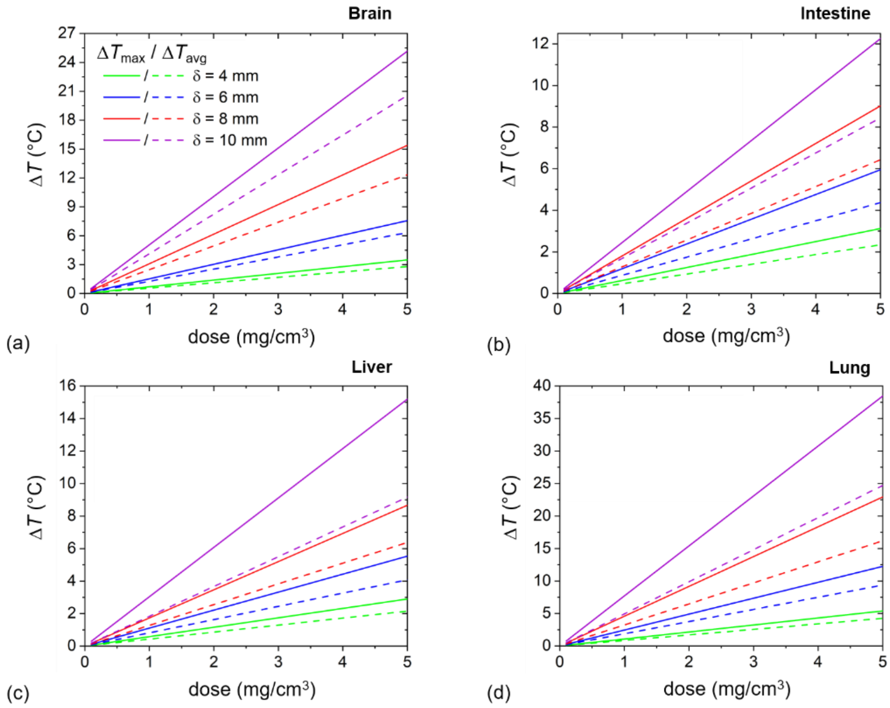

Figure 7.1. Maximum and average temperature increments reached in the 28 g mouse at the heating equilibrium, by varying the size of the target region δ and the dose of magnetic nanodisks. Comparison of organs where the target region is placed: (a) brain, (b) intestine, (c) liver, (d) lung. Adaptation from the graphs reported in [4].

Figure 7.1 shows the maximum temperature increment evaluated at the thermal equilibrium as a function of the magnetic nanodisk dose, for the different region diameters δ. The figure is made up of four graphs, one for each tissue where the tumor region is placed: brain, intestine, liver, and lung. The temperature increase is calculated as the difference with the temperature evaluated when the heating contribution is due to metabolic processes only. The values of the average increment within the target region are also reported in Figure 7.1. As discussed in [4], it is important to note that "for the lowest nanodisk dose (0.1 mg/cm^3), due to the dominance of blood perfusion effects, the temperature increase is practically negligible, regardless of δ and the target organ, while for the same concentration in water or in a viscous gel this results to be 3.6 °C and 1.9 °C, respectively" (see Chapter 5, Figure 5.4). Moreover, according to previous findings [5-8], larger amounts of magnetic material are required to see a substantial rise in temperature in the perfused biological tissues. As an example, to obtain a maximum temperature increment of some degrees for a region size fixed to 4 mm, a nanodisk dose of at least 5 mg/cm^3 is necessary. With these conditions, we find a maximum increase of 2.9 °C in the liver, 3.5 °C in the brain, 3.1 °C in the intestine, and 5.4 °C in the lung. Whereas, when the size of the target region is duplicated, the maximum temperature increment shows a significant increase, as it ranges from a minimum value of 8.7 °C in the liver to a maximum of 22.9 °C in the lung, with temperatures comparable with the ones required for thermal ablation [5]. This finding illustrates the possibility of lowering the magnetic nanomaterial dose when large portions of tissues are treated, hence limiting potential toxicity effects [9]. In comparison to the other organs, the lung experiences the greatest temperature increase due to its lower blood perfusion rate and reduced thermal conductivity (see Table 7.1 that summarizes the thermal

Table 7.1 Density and thermal properties of some of the tissues (Source: IT'IS Foundation database [10]). From the table reported in [4].

Tissue	Density ρ [kg/m^3]	Thermal conductivity k [W/(m·K)]	Heat capacity C_p [J/(kg·K)]	Perfusion rate W [kg/(s·m^3]	Metabolic heat rate Q_m [W/m^3]
Lung	394	0.387	3886	2.764	2446
Brain	1045	0.547	3696	13.956	16231
Liver	1079	0.519	3540	16.24	10713
Intestine	1030	0.493	3595	18.494	16370
Heart	1081	0.558	3686	19.403	42640
Fat	911	0.212	2348	0.521	462
Bones	1908	0.32	1313	0.334	296
Skin	1109	0.372	3391	2.064	1827

properties of tissues). The thermal gradient from the treated region center to its periphery causes a 20-30% difference between the maximum and average temperature rises.

Another noteworthy aspect is the relatively rapid heating transient because the thermal equilibrium is reached within 20 min at most, independently of the organ in which the target region is located, its size δ, or the magnetic nanodisk dose. The transient is longer in the lung for fixed values of δ and nanodisk concentrations, as displayed in Figure 7.2, due to the lower blood perfusion rate and the increased heat capacity.

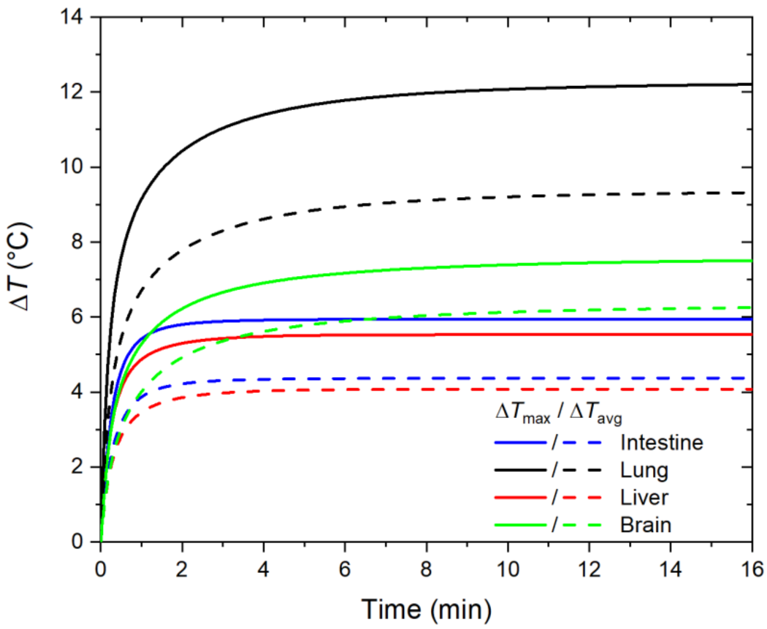

Figure 7.2. Analysis of thermal effects in the 28 g mouse model. Time evolutions of maximum and average temperature increments for four different organs (intestine, lung, liver, brain), fixing the tumor region size δ to 6 mm and the nanodisk dose to 5 mg/cm^3. Adaptation from the graphs reported in [4].

In addition, when the target region extends to other tissues or organs that have considerably different thermal properties, the temperature increase can have a non-spherical distribution. This can result in enhanced adverse effects and a shift in the point at which the maximum increment of temperature is obtained, moving from the region center to tissues with poorer blood perfusion rate and thermal conductivity. These effects are visible in Figure 7.3 that shows the temperature increase maps evaluated on transverse sections of the animal body placed in correspondence to the different target regions (see schematic in Figure 7.3c), with the region size fixed to 6 mm and the magnetic nanodisk dose set at 5 mg/cm^3. For example, when the target region is primarily inside the lung, the maximum temperature increase transfers to the thorax and surrounding fat, while the temperature increase near the heart is more limited. The liver and intestine also present temperature amplification effects due to their proximity to fat, while the brain has a considerable temperature increase towards the skull.

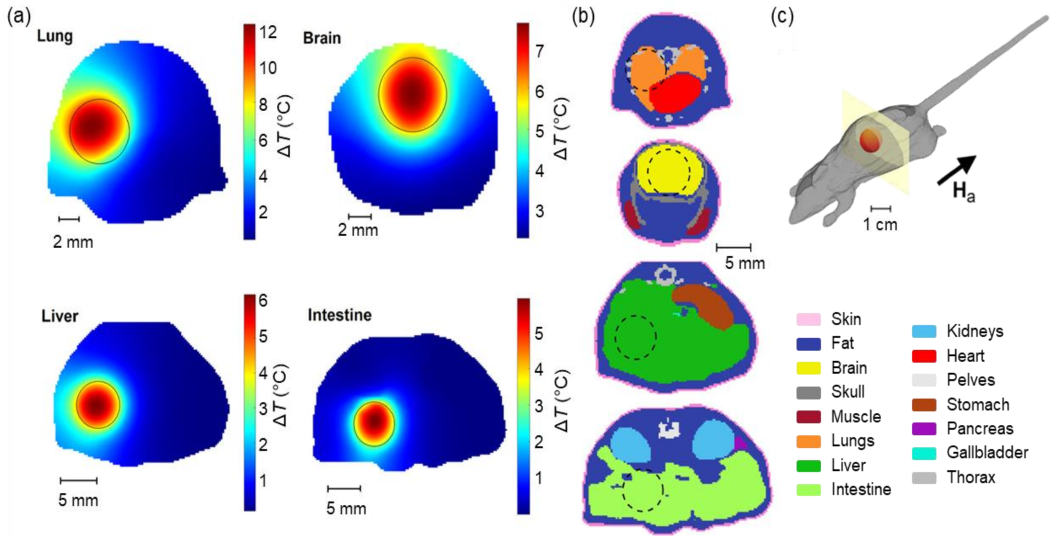

Figure 7.3. Analysis of thermal effects in the 28 g mouse model. (a) Maps of the temperature increment calculated on a transverse section of the animal body in correspondence to the target organs; the target region is indicated with a black circle line and has a fixed size of 6 mm, and the nanodisk dose is set at 5 mg/cm^3. (b) Maps showing the tissues and organs crossed by the sections considered. (c) Schematic of the mouse body, with the indication of the variable region containing the nanodisks and the transversal section for the calculation of the temperature increment map. Adaptation from the graphs reported in [4].

7.2 Analysis of the heating efficiency of magnetic nanoparticles in a rat model

In this section, we evaluate the heating efficiency of different types of MNPs assumed to be distributed within the largest tumor of the rat model. Four types of MNPs are considered [1,11], varying the MNP dose and the AC magnetic field parameters (i.e. peak amplitude and frequency). These MNPs have a hydrodynamic radius of about 100 nm. Specifically, they are:

- FeO@dextran NPs consisting of a core of parallelepiped iron oxide crystallites coated with dextran (BNF-Dextran from Micromod Partikeltechnologie GmbH [12]);
- FeO@citrate NPs composed of a core of spherical iron oxide crystallites and citrate-stabilized with a citric acid coating (JHU from NanoMaterials Technology [13]);
- Superparamagnetic iron oxide NPs (SPIONs) with a core of spherical iron oxide crystallites dispersed in a matrix of dextran (Nanomag®-D-spio from Micromod Partikeltechnologie GmbH [12]);
- $MnFe_2O_4$@citrate NPs consisting of manganese-ferrite NPs coated with citric acid (custom-made for [1]).

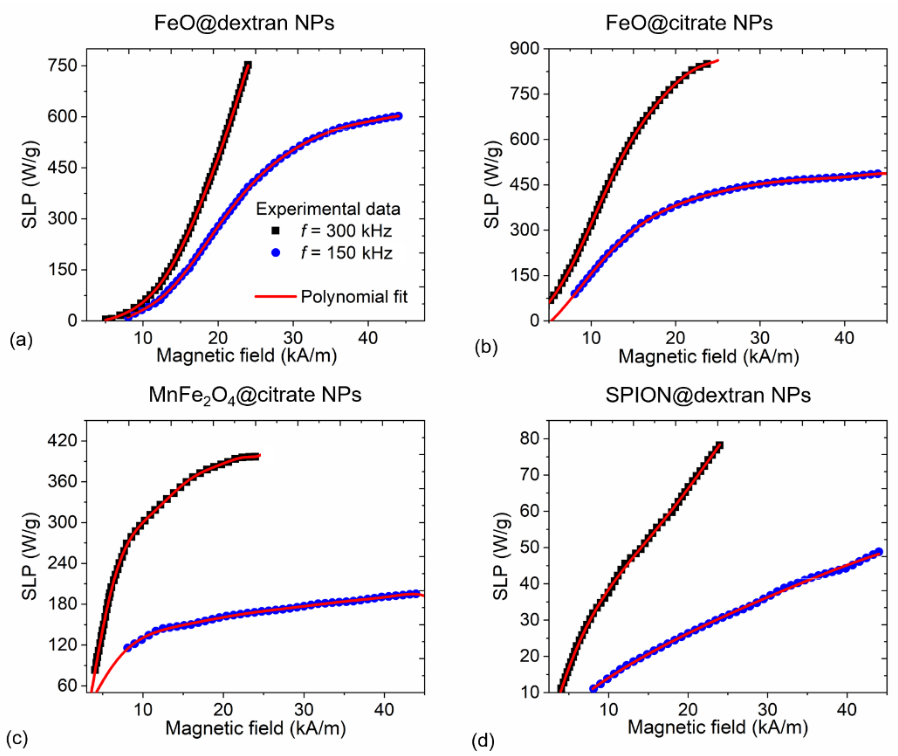

Figure 7.4. Specific loss power (SLP) vs magnetic field amplitude at two different field frequency, i.e. 150 kHz and 300 kHz. Four different MNPs considered: (a) FeO@dextran, (b) FeO@citrate NPs, (c) $MnFe_2O_4$@citrate NPs, and (d) SPION@dextran NPs. The blue and black markers are the data extrapolated from the mean SLP values reported in [1], whereas the red line is our curve-fitting obtained by means of polynomial interpolation.

In the study of F. Soetaert *et al*. [1], the SLP of the MNPs was estimated from calorimetric measurements of aqueous MNP solutions stored in vials, considering different AC magnetic field frequencies (from 150 kHz to 375 kHz) and peak amplitudes (from 4 kA/m to 44 kA/m). The measurements were performed to *“identify data ranges that conform to (quasi)-adiabatic conditions. Each time interval of measurement that met a predetermined criterion was used to generate a value of SLP, and the mean from all estimates was selected as the estimated SLP”* [1]. From this analysis, we extrapolate only the SLP values for two frequencies, i.e. 150 kHz and 300 kHz, whereas the magnetic field amplitude is in the same range considered above.

Figure 7.4 shows the SLP curves that we have reconstructed from the extrapolated data by means of polynomial interpolation. From Figure 7.4, we can observe that SPIONs have the lowest SLP values for both frequencies, whereas FeO@citrate NPs have the largest values for a frequency of 300 kHz (SLP ≈ 800 W/g when $\hat{H}_a$ = 25 kA/m), and the FeO@dextran NPs have the largest values for a frequency of 150 kHz (SLP ≈ 600 W/g when $\hat{H}_a$ = 44 kA/m).

To estimate the MNP heating efficiency, we simulate the thermal response in the rat model, and we evaluate the maximum and the average temperature at the thermal equilibrium within the tumor, i.e. where the MNPs are assumed to be injected. Other aspects we focus on are the temperature spatial distribution within the target region and its degree of uniformity, as a parameter that should be controlled to achieve good therapeutic outcomes. To analyze the temperature uniformity within the target region, we define the following heterogeneity coefficient,

$$HC = \frac{T_5 - T_{95}}{T_{95}}$$

where T_5 and T_{95} are the temperatures reached within at least 5% and 95% of tumor volume respectively. *HC* is a dimensionless coefficient, whose value decreases with the increase in the temperature uniformity within the tumor. For each selected combination of field peak amplitude and frequency, we consider different values of the MNP dose, from a minimum of 0.1 mg/cm^3 to a maximum of 20 mg/cm^3 in relation to the type of MNPs. Apart from Subsection 7.2.4, where the MNPs are non-uniformly distributed within the tumor, the MNPs are assumed to be uniformly distributed inside the tumor.

In Subsection 7.2.3, the rat model is resized by a factor 2.6, in an analogous way as done in [14], in order to study how the heating efficiency of MNPs changes in an animal model that has tumors inside and has a size similar to the mouse model. In all the other subsections the rat model is not resized.

In the following simulations, we disregard the contribution due to EM field exposure, thus neglecting eddy current effects. With this assumption, the heating contribution in the Pennes' equation is defined by the only MNPs, and Q_{EM} is null in Eq. 4.1.

7.2.1 Influence of MNP type

To estimate the heating efficiency of the four different MNPs, we calculate by solving the bio-heat equation the spatial distribution of the temperature within the whole rat model, assuming that the MNPs are uniformly distributed within the tumor located in the right flank. For each value of magnetic field frequency (i.e. 150 kHz or 300 kHz) and for each MNP type, we vary the field amplitude and the MNP dose. For the frequency of 150 kHz, the magnetic field amplitude is varied between 8 kA/m and 40 kA/m, whereas for 300 kHz it is varied in the range of 5-20 kA/m, in accordance with the SLP values reported in Figure 7.4 and in order to consider reasonable field parameters for *in vivo* treatments, fulfilling or slightly exceeding the Hergt-Dutz limit. For the SPIONs the dose is varied between 0.25 mg/cm^3 and 20 mg/cm^3 because high concentrations are needed due to their lower heating performance, and taking into account that doses up to 30 mg/cm^3 were employed during *in vivo* pilot studies [15]. Since the other MNPs show larger values of SLP, we use lower concentrations, i.e. doses in the range of 0.1-5 mg/cm^3, as the upper limit is considered a moderate dose for clinical magnetic hyperthermia [16].

The values of T_{avg}, T_{max}, and *HC* within the target region are reported in Figure 7.5 for the frequency set at 150 kHz, and in Figure 7.6 for 300 kHz. The yellow dotted lines define the therapeutic temperature range, which corresponds to a temperature increment of about 3-8 °C in the rat's tumor, as the average temperature within the tumor in the absence of MNP activation is about 37 °C. The values reported in the graphs are not evaluated numerically for all the combinations of dose and magnetic field peak amplitude, but only for some of them. The results obtained with our numerical solver are then used to train regression models that predict T_{avg}, T_{max}, and *HC* for the remaining combinations. As T_{avg} and T_{max} have a linear dependence on the product between the SLP values and the doses, i.e. on Q_{MNPs} of Eq. 4.1, the missing values can be predicted through linear regression models with SLP and dose as predictors. The models are obtained with the Matlab® function *fitlm* [17], specifying the relationship between variables 'T_{avg} ~ SLP * Dose' and 'T_{max} ~ SLP * Dose' for each model. The models are trained on a dataset that collects the MNP doses and the SLP values used for the evaluation with the thermal solver, and the values of T_{avg} and T_{max} obtained with the simulations. The resulting dataset is a matrix composed of four columns (SLP, MNP dose, T_{avg}, and T_{max}) and 117 rows, 64 related to the SLP

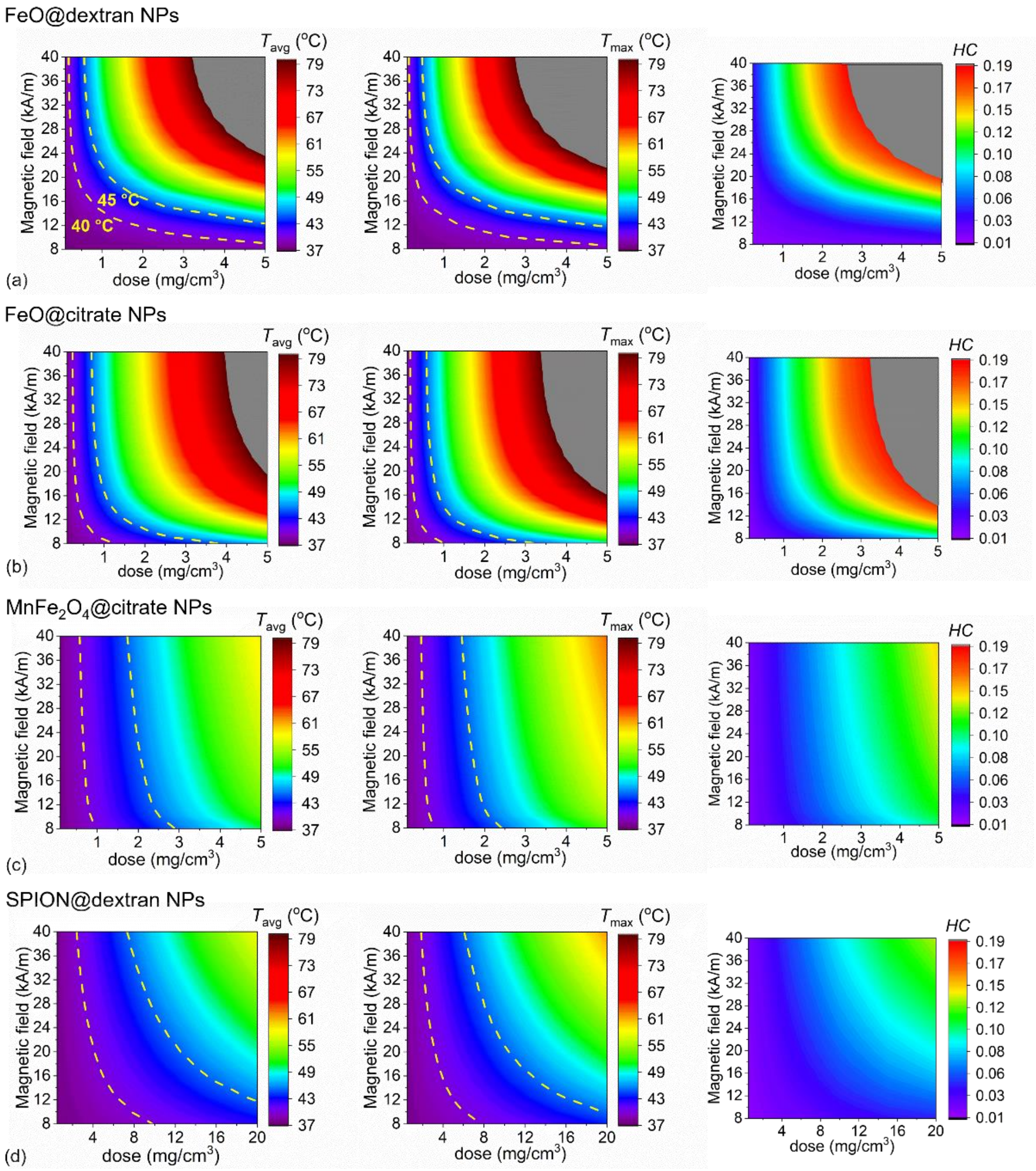

Figure 7.5. Maps of the average temperature, the maximum temperature and the heterogeneity coefficient within the tumor of the rat model as a function of MNP dose and magnetic field peak amplitude, for different types of MNPs: (a) FeO@dextran NPs, (b) FeO@citrate NPs, (c) $MnFe_2O_4$@citrate NPs, and (d) SPION@dextran NPs. The field frequency is fixed to 150 kHz.

values taken from the SLP-field curve of the FeO@citrate NPs with the frequency fixed at 150 kHz, and the other 64 from the curve with the frequency at 300 kHz, for the same MNP type. The models trained on this set have a root mean squared error (RMSE) of 0.009 and of 0.006 for T_{avg} and T_{max} respectively, and an R-squared of 1 for both. The reliability of the model is assessed by comparing

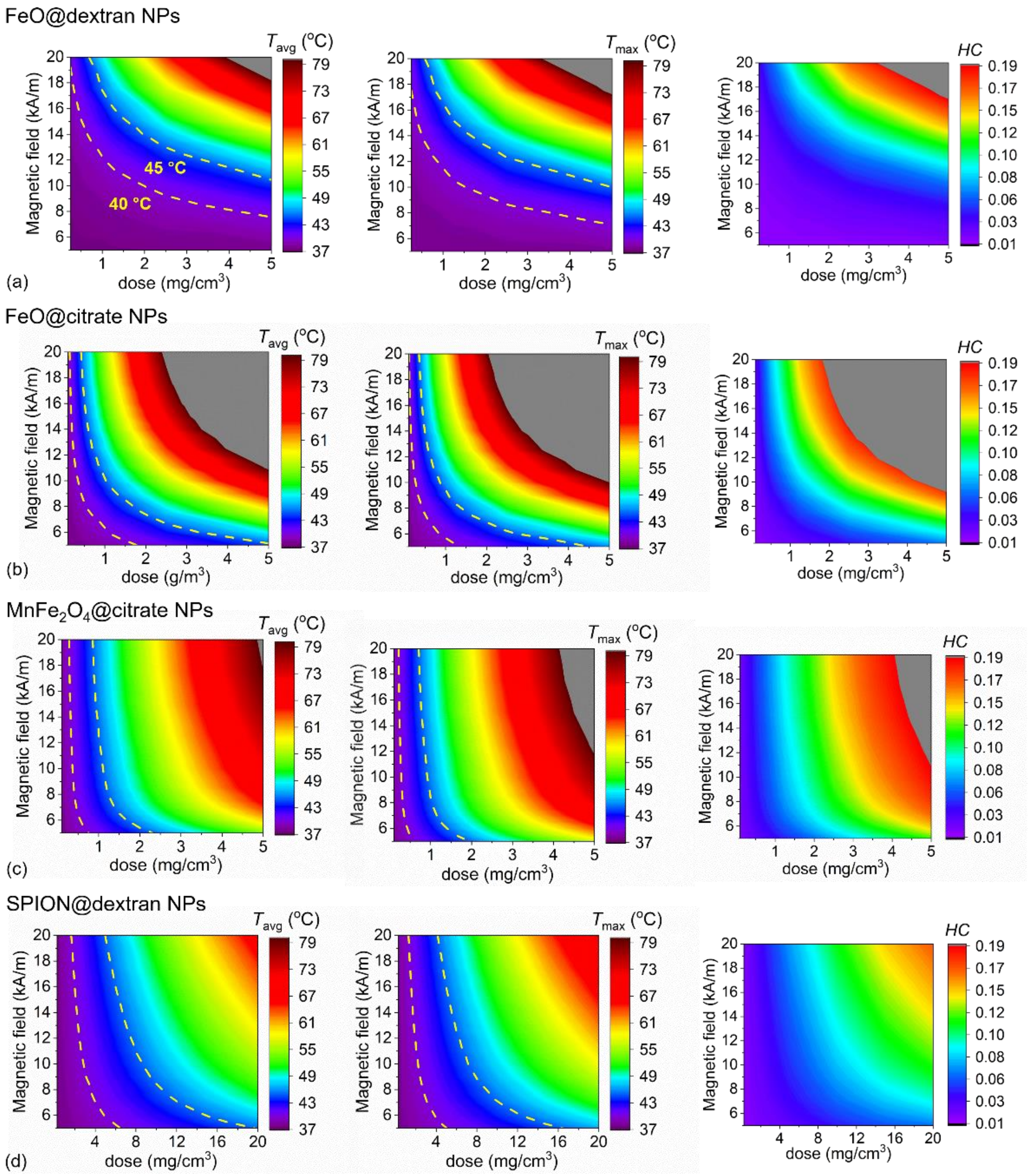

Figure 7.6. Maps of the average temperature, the maximum temperature and the heterogeneity coefficient within the tumor of the rat model as a function of MNP dose and magnetic field peak amplitude, for different types of MNPs: (a) FeO@dextran NPs, (b) FeO@citrate NPs, (c) $MnFe_2O_4$@citrate NPs, and (d) SPION@dextran NPs. The field frequency is fixed to 300 kHz.

the values of T_{avg} and T_{max} obtained with our thermal solver with the values predicted by the regression models for some combinations of SLP and MNP dose not utilized in the training. For the FeO@dextran NPs, for example, we have done 21 new simulations and, comparing the values calculated with the solver and the regression model, we have found an average discrepancy of 0.003% and 0.01%, and a maximum discrepancy of 0.007% and 0.03% for the evaluation of T_{avg} and T_{max}, respectively.

In Figures 7.5 and 7.6 we report only the values of T_{avg} and T_{max} that do not exceed 80 °C, as larger temperatures are not typically reached in *in vivo* tests of magnetic hyperthermia (for example in [20] maximum temperatures of about 70 °C are obtained). Thus, the graphs of *HC* illustrate only the values that correspond to a T_{max} lower than 80 °C. We can observe that T_{avg}, T_{max}, and *HC* show a similar trend depending on the MNP type.

The FeO@citrate and $MnFe_2O_4$@citrate NPs permit to reach the therapeutic temperature range with the lowest values of MNP dose, for all the field amplitudes considered and for both field frequencies. Moreover, for a frequency of 150 kHz, $MnFe_2O_4$@citrate NPs enable to achieve the therapeutic temperature interval for a wider field amplitude range than the FeO@citrate NPs, employing almost the same MNP dose range (1-3 mg/cm^3). As a result, with $MnFe_2O_4$@citrate NPs, there is more flexibility in selecting the magnetic field amplitude and MNP dose that ensure the achievement of temperatures in the therapeutic range. With the FeO@dextran NPs larger MNP doses should be used, with only limited values of the magnetic field (up to about 15 kA/m). SPIONs, on the other hand, demand higher doses, demonstrating that their lower SLP values make them the MNPs with the lowest heating efficiency when compared to the others. With a field frequency of 300 kHz, the possibility of selecting optimized magnetic field amplitude and MNP dose is reduced for all MNP types.

Table 7.2. Average temperature, maximum temperature, and heterogeneity coefficient within the target region evaluated for the rat model considering a uniform distribution of the MNPs within the whole target region. Values obtained for fixed dose of MNPs (0.5 mg/cm^3), fixed peak amplitude of the magnetic field (15 kA/m), and the two considered field frequencies (150 and 300 kHz).

MNP type	Frequency = 150 kHz			Frequency = 300 kHz		
	T_{avg} (°C)	T_{max} (°C)	*HC*	T_{avg} (°C)	T_{max} (°C)	*HC*
FeO@dextran	39	39.4	0.025	39.9	40.5	0.032
FeO@citrate	40.9	41.7	0.039	44.4	45.8	0.064
$MnFe_2O_4$	39.2	39.8	0.027	41.6	42.5	0.044

With regard to the heterogeneity coefficient, the largest values do not exceed 0.2, and the lowest values are reached where T_{avg} and T_{max} have the lowest values, i.e. when the heating due to the activation of the MNPs is not very significant. To better understand the differences between the MNPs, in Table 7.2 we report the values of T_{avg}, T_{max} and *HC* for the following case: dose = 0.5 mg/cm^3 and $\hat{H}_a$ = 15 kA/m. The FeO@citrate NPs present the highest temperatures, for example T_{max} is equal to 41.7 °C and 45.8 °C with a field frequency of 150 kHz and 300 kHz, respectively, and lead to the highest values of the heterogeneity coefficient, i.e. 0.039 for f = 150 kHz and 0.064 for f = 300 kHz. Whereas the FeO@dextran NPs are the least efficient in terms of heating, with T_{max} of 40.5 °C when the field frequency is equal to 300 kHz. SPIONs are not reported, as the temperatures are almost the same as when the MNPs are not activated, i.e. T_{avg} and T_{max} with similar values of about 37 °C (i.e. the magnetic hyperthermia effects are negligible).

7.2.2 Influence of animal size

For the rat model resized by a factor of 2.6, the same analysis as in the preceding subsection is done. For random values of MNP dose and field amplitude, the temperature distribution is evaluated with our thermal model, and the rest of the data is fitted with the same regression models described above but trained with the values evaluated for the resized geometry. Figure 7.7 and Figure 7.8 show the values of T_{avg} and T_{max} obtained with the different MNPs for a field frequency of 150 kHz and 300 kHz, respectively. These temperatures are lower with respect to the ones obtained with the original model of the rat. Specifically, we have a minimum reduction of 2% for the cases where MNP dose and field amplitude are the lowest (i.e. dose equal to 0.1 mg/cm^3 and $\hat{H}_a$ = 8 kA/m) and a

Table 7.3. Average temperature, maximum temperature, and heterogeneity coefficient within the target region evaluated for the rat model resized with a scale factor of 2.6, considering a uniform distribution of the MNPs within the whole target region. Values obtained for fixed dose of MNPs (0.5 mg/cm^3), fixed peak amplitude of the magnetic field (15 kA/m), and the two considered field frequencies (150 and 300 kHz).

MNP type	Frequency = 150 kHz			Frequency = 300 kHz		
	T_{avg} (°C)	T_{max} (°C)	*HC*	T_{avg} (°C)	T_{max} (°C)	*HC*
FeO@dextran	37.7	38.15	0.022	38.4	38.9	0.027
FeO@citrate	39	39.7	0.032	41.3	42.5	0.051
$MnFe_2O_4$	37.9	38.4	0.024	39.4	40.2	0.029

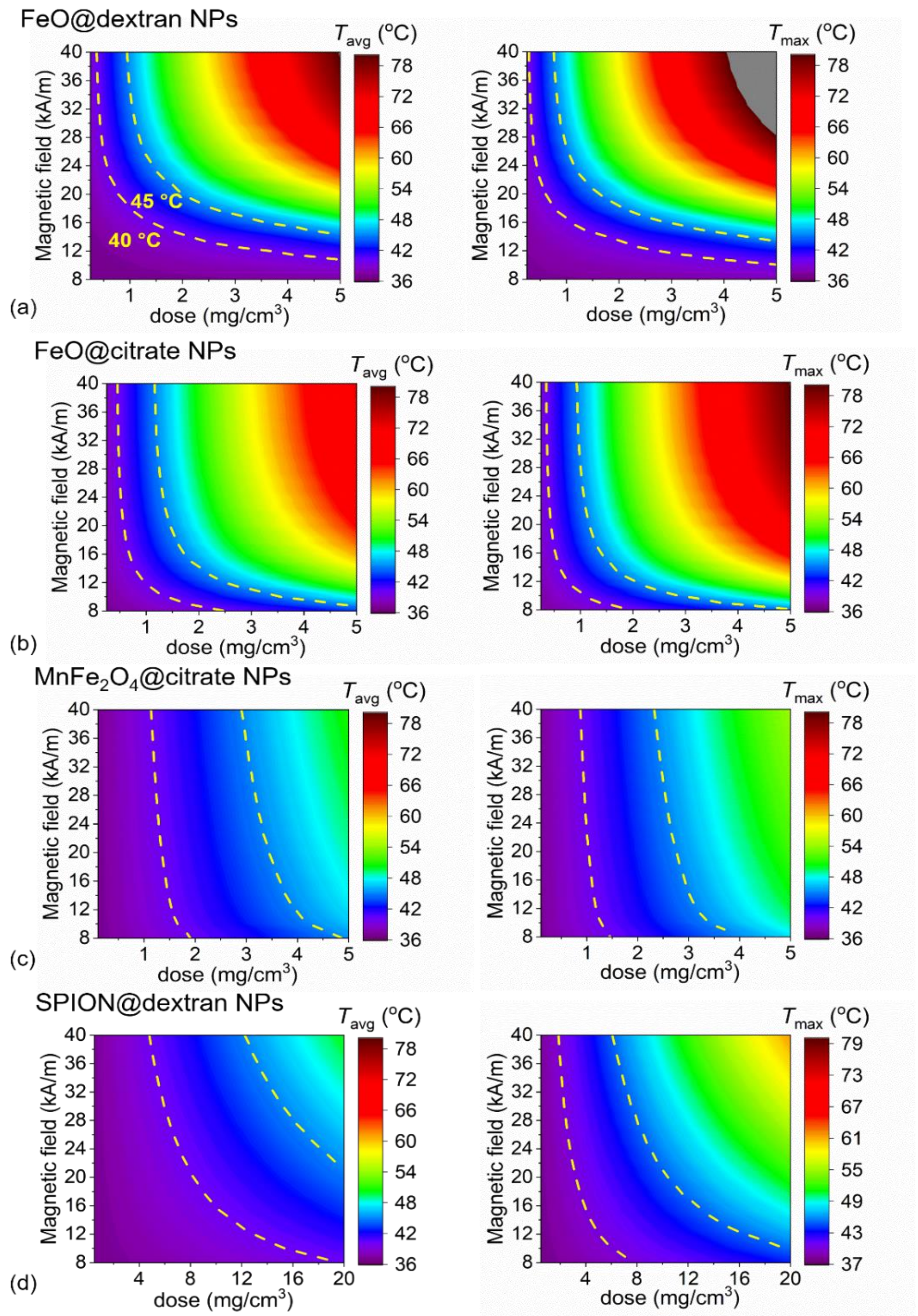

Figure 7.7. Maps of the average temperature and the maximum temperature reached within the tumor of the rat model resized with a scale factor of 2.6, as a function of MNP dose and magnetic field peak amplitude, for different types of MNPs: (a) FeO@dextran NPs, (b) FeO@citrate NPs, (c) $MnFe_2O_4$@citrate NPs, and (d) SPION@dextran NPs. The field frequency is fixed to 150 kHz.

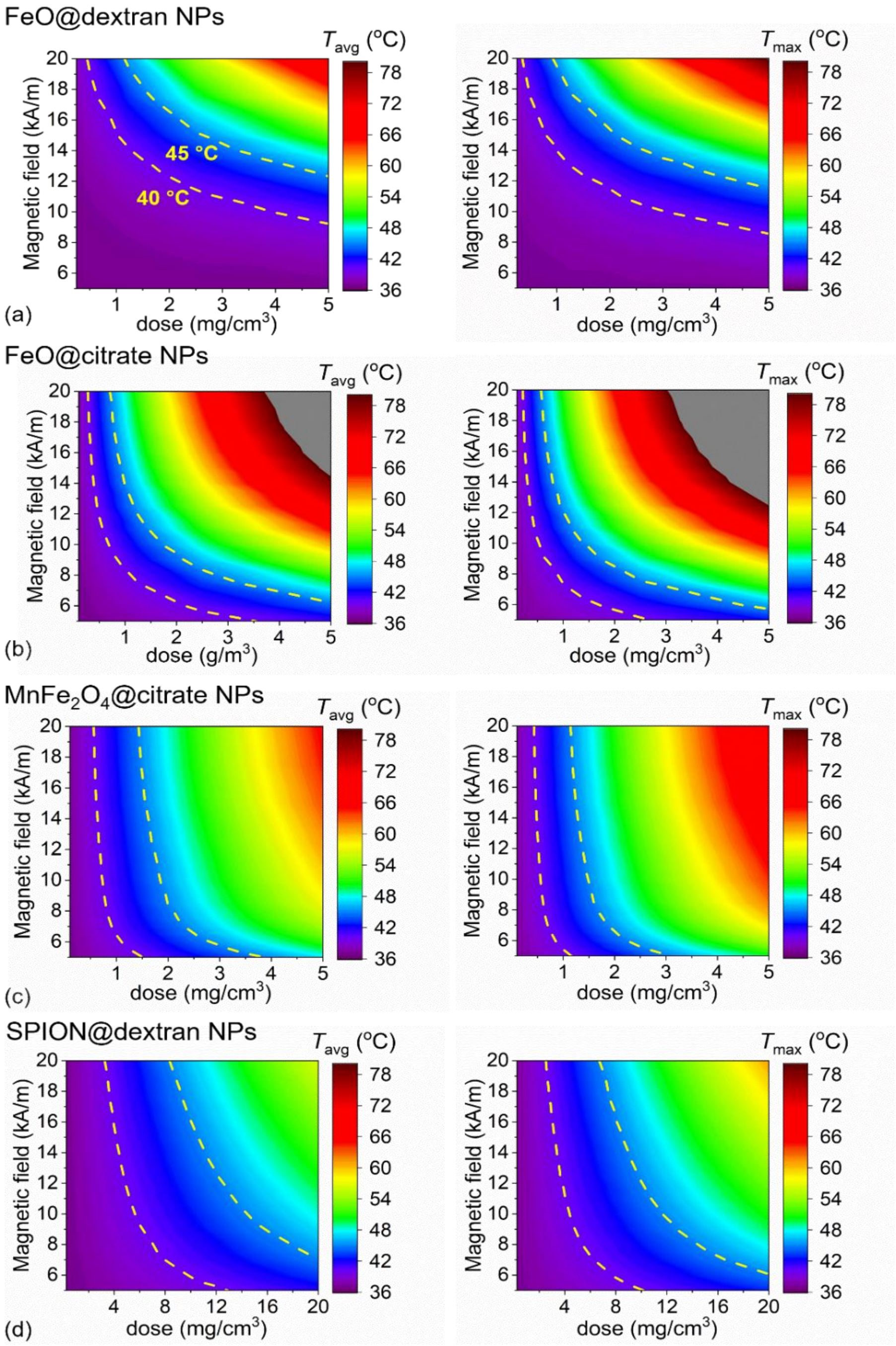

Figure 7.8. Maps of the average temperature and the maximum temperature reached within the tumor of the rat model resized with a scale factor of 2.6, as a function of MNP dose and magnetic field peak amplitude, for different types of MNPs: (a) FeO@dextran NPs, (b) FeO@citrate NPs, (c) $MnFe_2O_4$@citrate NPs, and (d) SPION@dextran NPs. The field frequency is fixed to 300 kHz.

maximum reduction of about 25% for the largest values (i.e. dose equal to 5 mg/cm^3 and $\hat{H}_a$ = 40 kA/m). For a field frequency of 150 kHz, the MNPs that permit the use of minor doses are the FeO@citrate and the FeO@dextran NPs, whereas for 300 kHz are the FeO@citrate and the $MnFe_2O_4$@citrate NPs, as for the not-resized rat. In Table 7.3, we have reported the values of T_{avg}, T_{max} and HC for the same case of Table 7.2, i.e. MNP dose = 0.5 mg/cm^3 and $\hat{H}_a$ = 15 kA/m. We can observe that the values for the resized animal model are reduced not just in temperature but also in *HC* levels. Moreover, as seen in Table 7.2, also here the highest temperature and *HC* values are reached with the FeO@citrate NPs. For the field frequency equal to 300 kHz, FeO@citrate NPs are the unique type of MNPs in the resized digital phantom that lead to temperatures belonging to the therapeutic range with T_{avg} = 41.3 °C and T_{max} = 42.5 °C. The temperatures reached in the tumor and reported in the graphs of Fig. 7.7 and Fig. 7.8 show a trend very similar to the one illustrated in Fig. 7.5 and Fig. 7.6 for the not-resized animal model, but with lower values.

7.2.3 Influence of non-uniform distribution of MNPs

To test the influence of non-uniform spatial distributions of MNPs, we assume that the MNPs are uniformly distributed inside spherical regions collocated in different places within the tumor, assuming that multi injections in situ are done. We consider three different scenarios: one with three injection sites, another one with four sites, and the last one with five sites. For each case, we vary the size of the spherical region where MNPs are distributed: 5 mm, 10 mm, and 15 mm. In Figure 7.9 we schematize the spatial collocation of the spherical regions inside the tumor.

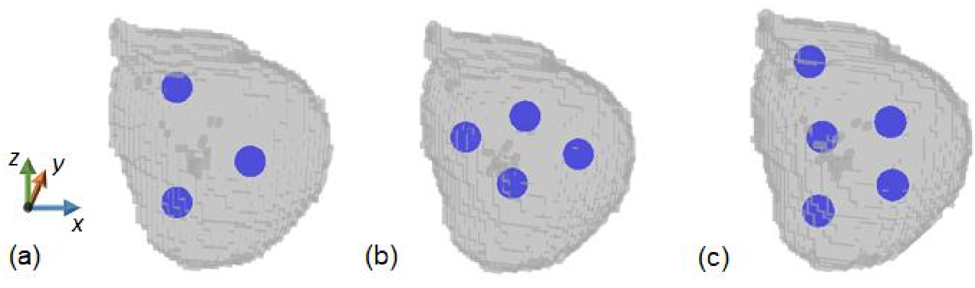

Figure 7.9. Schematic of tumor (in grey) with the regions containing the MNPs (in blue) that represent the scenario with: (a) three injection sites, (b) four injection sites, (c) five injection sites. The regions have a radius of 2.5 mm.

Table 7.4. Features of the linear regression models used for the prediction of the average temperature within the rat's tumor. LM = linear regression model. Stepwise LM = stepwise regression.

Injections	Region size (mm)	Model (training set size/ test set size)	Predictors	RMSE	Mean discrepancy (%)	Max discrepancy (%)
3	5	LM (27/8)	Field amplitude, dose, SLP	$3.77 \cdot 10^{-5}$	$0.35 \cdot 10^{-3}$	0.39
3	10	LM (28/8)	Field amplitude, dose, SLP	0.18	$5.67 \cdot 10^{-5}$	$0.18 \cdot 10^{-3}$
3	15	LM (13/13)	Dose, SLP	$5.23 \cdot 10^{-5}$	$3.46 \cdot 10^{-5}$	$9.43 \cdot 10^{-5}$
4	5	LM (19/8)	Dose, SLP	$4.37 \cdot 10^{-4}$	$5.59 \cdot 10^{-5}$	$7.98 \cdot 10^{-5}$
4	10	LM (20/9)	Dose, SLP	$0.38 \cdot 10^{-2}$	$4.55 \cdot 10^{-5}$	$0.11 \cdot 10^{-3}$
4	15	LM (23/9)	Dose, SLP	$0.30 \cdot 10^{-1}$	$3.75 \cdot 10^{-5}$	$7.86 \cdot 10^{-5}$
5	5	Stepwise LM (22/9)	Dose, SLP	$1.32 \cdot 10^{-4}$	$4.69 \cdot 10^{-5}$	$7.98 \cdot 10^{-5}$
5	10	LM (21/9)	Dose, SLP	$0.54 \cdot 10^{-2}$	$0.57 \cdot 10^{-2}$	0.05
5	15	LM (19/9)	Dose, SLP	$0.24 \cdot 10^{-2}$	$4.4 \cdot 10^{-5}$	$0.1 \cdot 10^{-3}$

Table 7.5. Features of the linear regression models used for the prediction of the maximum temperature within the rat's tumor. LM = linear regression model. Stepwise LM = stepwise regression.

Injections	Region size (mm)	Model (training set size / test set size)	Predictors	RMSE	Mean discrepancy (%)	Max discrepancy (%)
3	5	LM (27/8)	Field amplitude, dose, SLP, T_{avg}	$1.49 \cdot 10^{-2}$	0.28	2.88
3	10	Stepwise LM (28/8)	Field amplitude, dose, SLP, T_{avg}	$0.24 \cdot 10^{-1}$	$0.37 \cdot 10^{-1}$	0.15
3	15	LM (13/13)	Dose, SLP	$0.33 \cdot 10^{-1}$	$0.22 \cdot 10^{-1}$	$0.37 \cdot 10^{-1}$
4	5	LM (19/8)	Dose, SLP	$0.21 \cdot 10^{-1}$	$0.33 \cdot 10^{-1}$	$0.79 \cdot 10^{-1}$
4	10	Stepwise LM (20/9)	Field amplitude, dose, SLP, T_{avg}	0.18	$0.33 \cdot 10^{-1}$	0.23
4	15	Stepwise LM (23/9)	Field amplitude, dose, SLP, T_{avg}	$0.97 \cdot 10^{-2}$	$0.41 \cdot 10^{-2}$	$0.18 \cdot 10^{-1}$
5	5	LM (22/9)	Dose, SLP	$0.18 \cdot 10^{-1}$	$0.77 \cdot 10^{-2}$	$0.25 \cdot 10^{-1}$
5	10	LM (21/9)	Dose, SLP	$0.43 \cdot 10^{-1}$	$0.69 \cdot 10^{-1}$	0.33
5	15	LM (19/9)	Dose, SLP	$0.87 \cdot 10^{-1}$	$0.12 \cdot 10^{-2}$	$0.69 \cdot 10^{-2}$

As done in the previous subsections, we evaluate the values of T_{max} and T_{avg} in the tumor, but only for two types of MNPs, the FeO@citrate NPs and the FeO@dextran NPs, and for a field frequency fixed to 150 kHz. Analogously to the previous subsections, at first T_{max} and T_{avg} are calculated from the body temperature obtained with our thermal solver, using some SLP values taken from the SLP vs field amplitude curve of the FeO@citrate NPs reported in Figure 7.4. Then, to reduce the time necessary to obtain the results from the solver, the rest of the data are calculated using linear regression models. The type of models used (linear model or stepwise regression), the root mean square error of the model, and the discrepancy between the values obtained from the temperatures evaluated by means of the thermal solver and the predicted values are reported in Table 7.4 for T_{avg} and Table 7.5 for T_{max}. For each row of the table we have also specified the number of elements that compose the dataset for the training of the model (named training set) and the dataset used for the evaluation of the discrepancy (named test set). All the models are linear and have always in common the SLP and the MNP dose as predictors. Some models for T_{avg} have better results when the field amplitude is added as a predictor, such as in the case with 3 injection sites and region size of 5 mm. The models that predict T_{avg} have more accurate results and present values of RMSE that vary between $5.23 \cdot 10^5$ and 0.18, whereas for the T_{max} the models have RMSEs between $1.49 \cdot 10^2$ and 0.18. The maximum discrepancy is 2.88% and is reached in the prediction of T_{max} for three injection sites and region size equal to 5 mm.

Figure 7.10, Figure 7.11, and Figure 7.12 display the values of T_{avg} and T_{max} for the case of three injection sites, four sites, and five sites respectively. The graphs at the top of the figures are the results obtained with the region size equal to 5 mm, the central graphs to 10 mm, and the graphs at the bottom to 15 mm. As seen in the previous subsections, each MNP type has a specific trend of T_{max} and T_{avg}, as a function of MNP dose and magnetic field amplitude. Comparing the results for the different number of injections and region size, T_{max} and T_{avg} values increase with the increment of the number of injections and of the region size. For the same region size, T_{avg} is larger when there are more injection sites, but this is not always valid for T_{max}. In fact, an exception is the case in which the MNP-containing regions have a size of 15 mm, where the largest values of T_{max} are obtained when the number of injections is four and not five. For example, for the magnetic field fixed to 10 kA/m and the MNP dose to 5 mg/cm^3, T_{avg} is larger when the number of injections is higher (46.3 °C for four injections, 48.1 °C for five injections), whereas T_{max} has the largest value when the injections are four and has a value equal to 60.6 °C (58.7 °C for five injections). This comes from the fact that the four injections are closer to each other with respect to the configuration with five injections, and when the spheres containing the MNPs have the largest size, most of their volumes overlap and generate a sort of unique

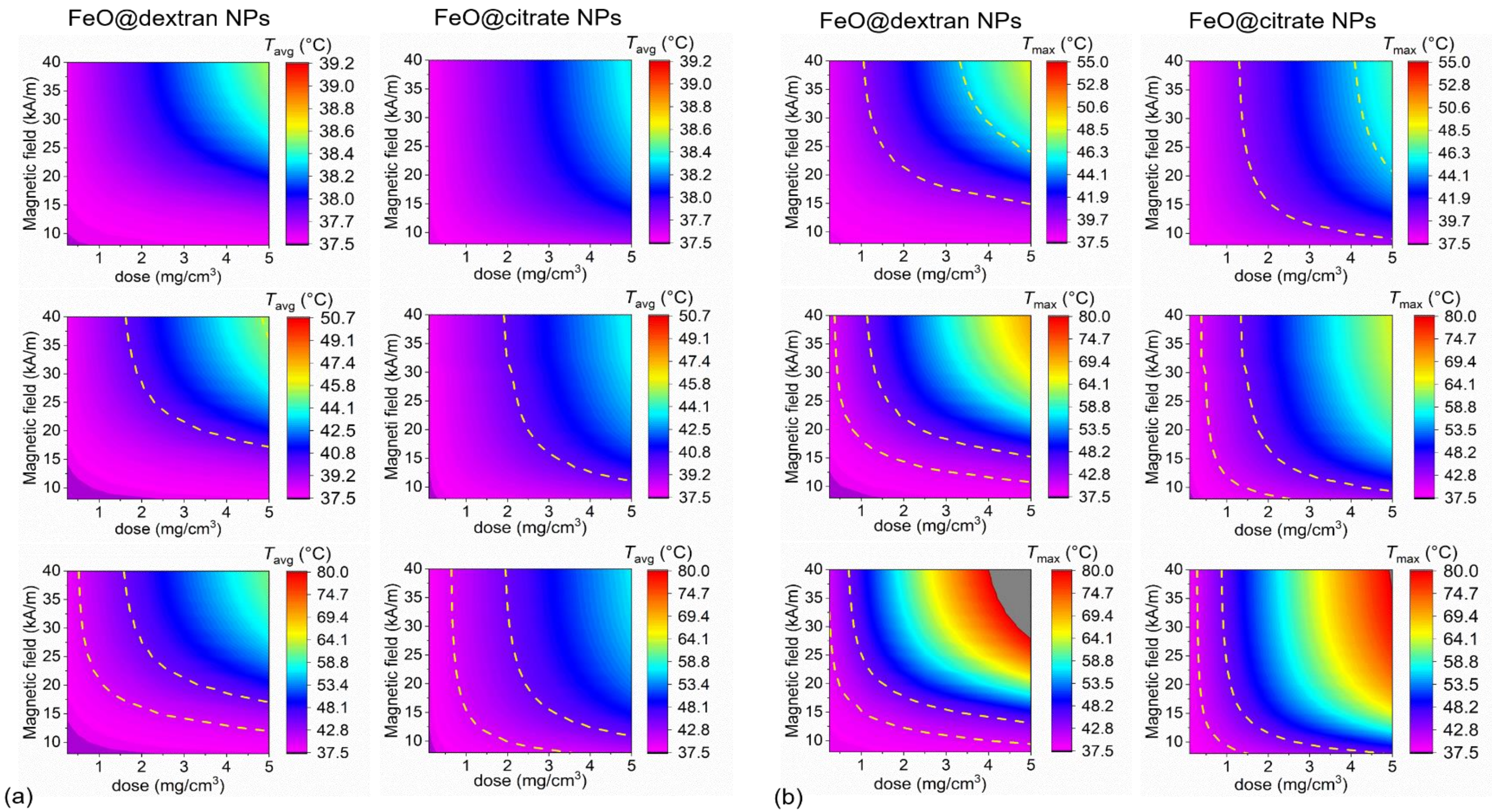

Figure 7.10: Thermal effects for three injection sites. Maps of the (a) average and (b) maximum temperatures reached within the rat's tumor as a function of MNP dose and magnetic field, for two types of MNPs: FeO@dextran NPs on the left and FeO@citrate NPs on the right. Results with injection region size equal to 5 mm (graphs at the top), 10 mm (central graphs), 15 mm (graphs at the bottom).

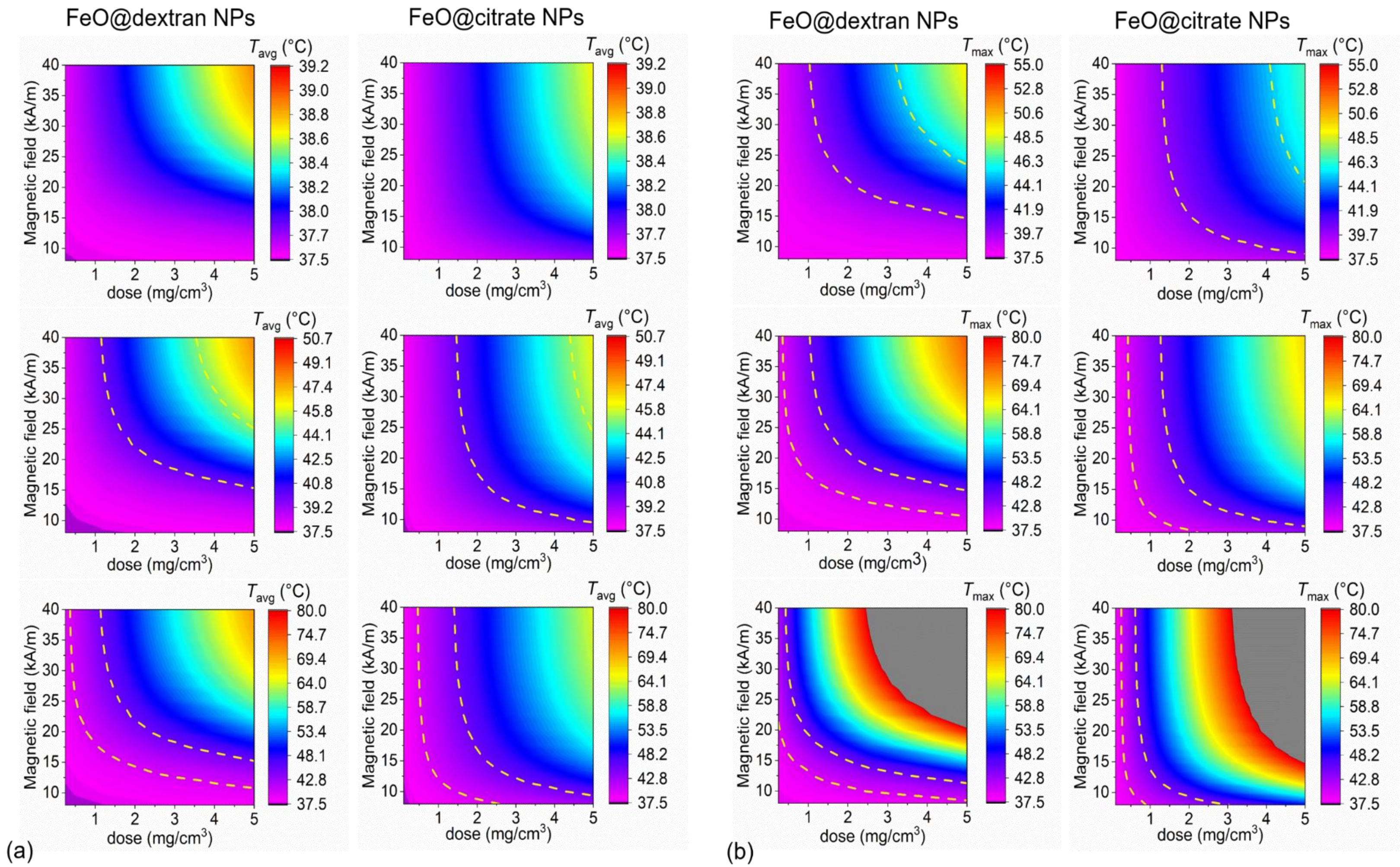

Figure 7.11: Thermal effects for four injection sites. Maps of the (a) average and (b) maximum temperatures reached within the rat's tumor as a function of MNP dose and magnetic field, for two types of MNPs: FeO@dextran NPs on the left and FeO@citrate NPs on the right. Results with injection region size equal to 5 mm (graphs at the top), 10 mm (central graphs), 15 mm (graphs at the bottom).

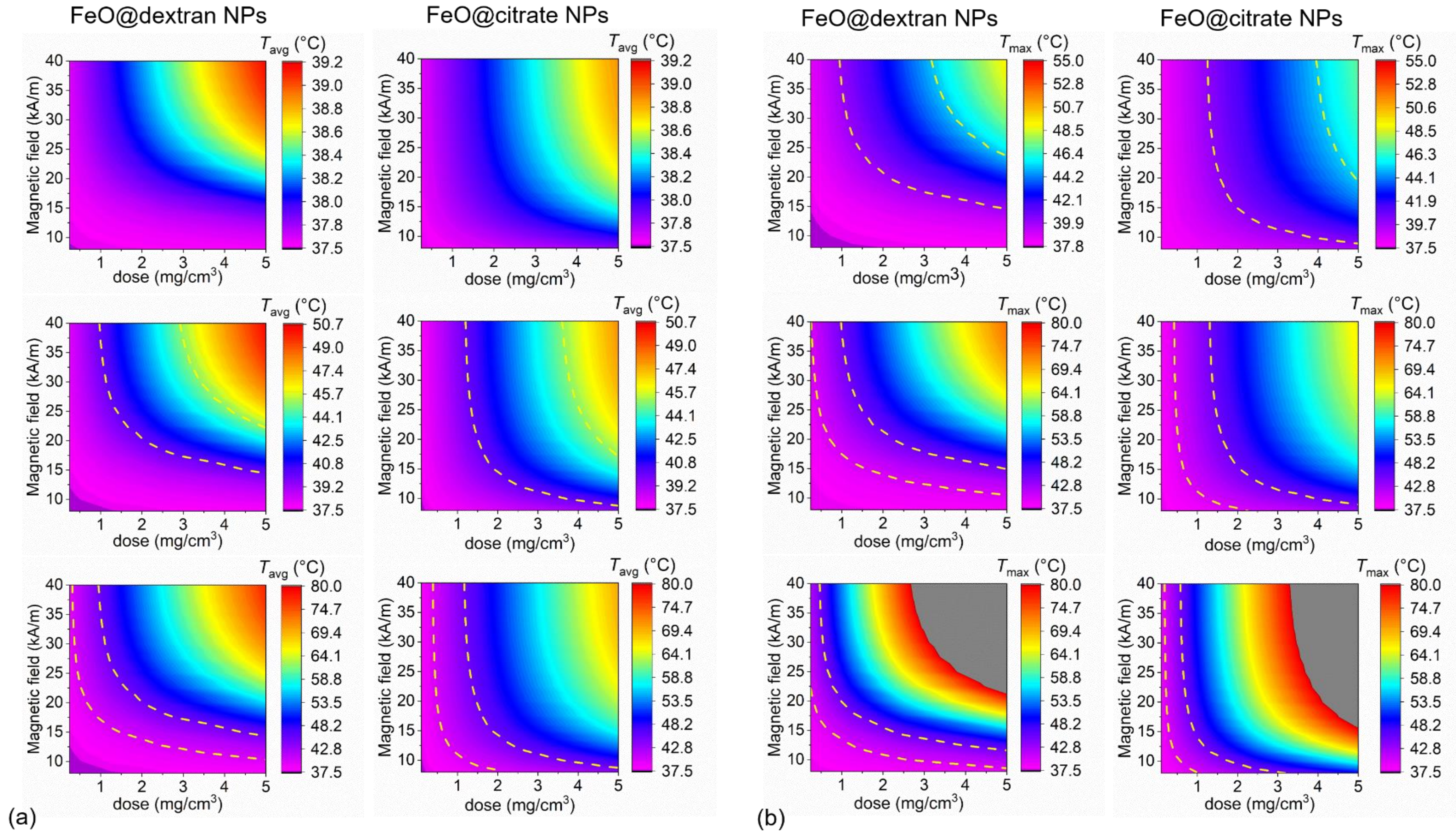

Figure 7.12: Thermal effects for five injection sites. Maps of the (a) average and (b) maximum temperature reached within the rat's tumor as a function of MNP dose and magnetic field, for two types of MNPs: FeO@dextran NPs on the left and FeO@citrate NPs on the right. Results with injection region size equal to 5 mm (graphs at the top), 10 mm (central graphs), 15 mm (graphs at the bottom).

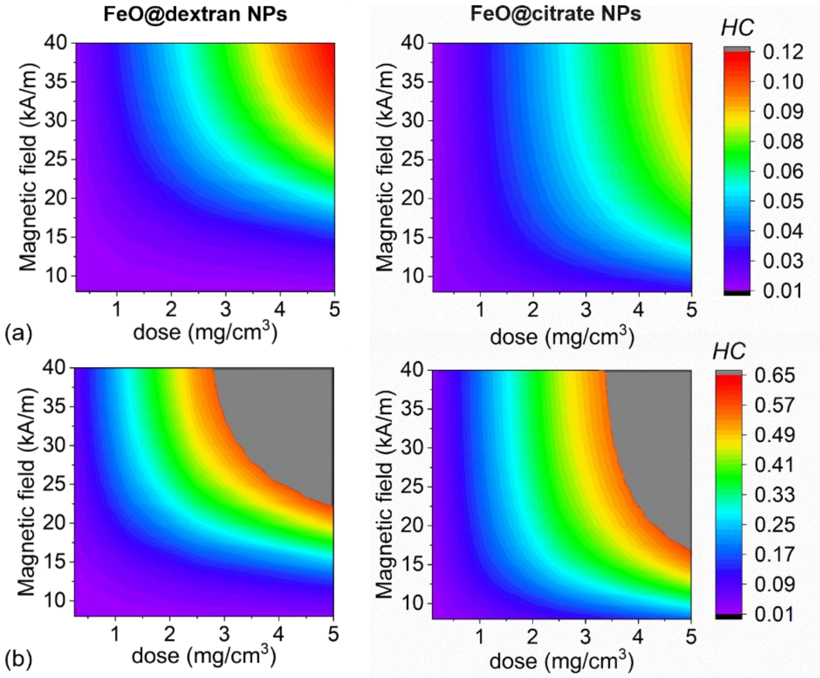

Figure 7.13. Maps of the heterogeneity coefficient for five injection sites and region size of (a) 5 mm and (b) 15 mm. The results are reported for the FeO@dextran NPs (left), and the FeO@citrate NPs (right).

region that is more concentrated with respect to the case of five injections that are distributed more uniformly within the tumor. Moreover, in this example, also the value of the heterogeneity coefficient *HC* is larger when there are four injection sites and is equal to 0.4, whereas it is 0.3 for the case with five injection sites.

In Figure 7.13 the values of *HC* are reported for the cases with five injection sites and region size of 5 mm and 15 mm. The *HC* trend is similar to the ones shown by T_{max} and T_{avg}, depending on the MNP type. With respect to the FeO@dextran NPs, for low field amplitudes the FeO@citrate NPs have larger values of *HC* with increasing MNP dose; whereas *HC* values are larger for the FeO@dextran NPs when the field amplitudes are greater than 15 kA/m. For example, considering an injection site with size of 15 mm and a fixed MNP dose of 2.5 mg/cm^3, for a field amplitude of 12.5 kA/m *HC* is 0.08 and 0.16 for the FeO@dextran NPs and the FeO@citrate NPs respectively, whereas for $\hat{H}_a$ = 30 kA/m *HC* is equal to 0.46 for the FeO@dextran NPs and 0.42 for the FeO@citrate NPs.

In comparison to the MNP uniformly distributed inside the whole tumor, the cases studied with multi injections lead to lower temperatures and need larger values of MNP dose and magnetic field amplitude to reach the therapeutic temperature range of 40-45 °C. Furthermore, T_{avg} does not overcome 40 °C for three sites of injection, and region size equal to 5 mm, for both FeO@dextran and FeO@citrate NPs, and there are no significant temperature increases in comparison to the solution with the only metabolic heat. With the multiple injections, the MNPs indeed occupy only a portion of the tumor, from 13.6% for the case with three injection sites and a region size of 5 mm, to 54% for the scenario with five injection sites and a region size of 15 mm. In addition, with respect to the case where MNPs are uniformly distributed within the whole tumor, the heterogeneity of the temperature distribution inside the tumor is very low when the regions containing the MNPs are smaller (i.e. *HC* does not exceed 0.12), whereas *HC* has larger values for the regions with the largest size, reaching values up to 0.6 (in the uniform case *HC* does not exceed 0.2).

7.2.4 Influence of non-uniform magnetic field distribution

To investigate the influence of non-uniform magnetic field distribution within the animal body, we simulate the thermal response in the rat model with the magnetic field evaluated with the four EM field applicators introduced in Chapter 6. In particular, here we consider that the magnetic field is generated from the following applicators:

- the solenoid with 8 turns and an outer diameter of 5 cm (supply current = 300 A);
- the pancake coil with an external diameter equal to 5 cm (supply current = 300 A);
- the Helmholtz coil (supply current = 400 A);
- the solenoid with 2 turns and an outer diameter of 20 cm (supply current = 400 A).

The results are displayed in Figure 7.14 and show the temperature distribution within the animal body at the thermal equilibrium. For each applicator considered we report the schematic of the applicator position with respect to the animal body, The field frequency is fixed to 150 kHz and the MNPs are assumed to be uniformly distributed within the whole tumor with a dose equal to 5 mg/cm^3. Because the pancake coil achieves the largest magnetic field amplitude of roughly 28 kA/m within the tumor, we have that the maximum value of $\hat{H}_a \times f$ is $4.2 \cdot 10^9$ A/(m·s), reached locally; thus, the Hergt-Dutz limit is fulfilled for all the applicators. For the evaluation of the temperature, the heating power due to the exposure to the only magnetic field is considered null, in accordance with the results reported in Chapter 6.

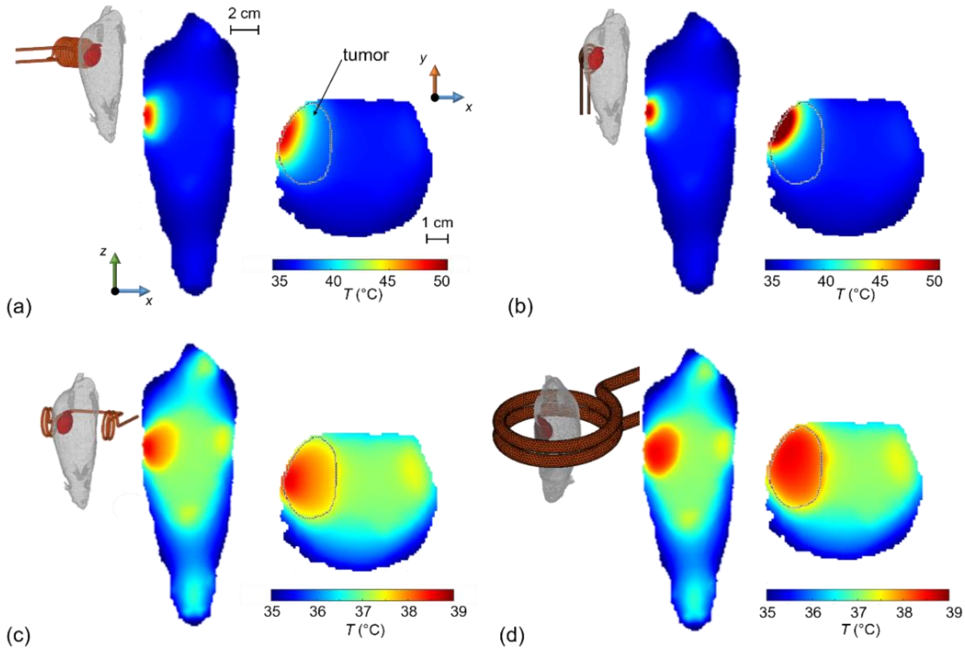

Figure 7.14. Temperature maps calculated on two transverse sections of the rat body that crosses the tumor barycenter. The magnetic field is generated by four different applicators whose position with respect to the animal model is schematized on the top left: (a) coil with 8 turns, (b) pancake coil, (c) Helmholtz coil, (d) coil with 2 turns.

and two maps that show the temperature distribution within two sections of the body that cross the body passing through the barycenter of the tumor. The 8-turn solenoid and the pancake coils permit to obtain a significant temperature increase focused inside the tumor and the tissues in its proximity, with the highest values concentrated in the peripheral area of the tumor and the part of the skin closer to the applicator, and no significant thermal effects in the rest of the body. For both applicators, the average temperature within the tumor is similar (40.6 °C for the solenoid and 40.5 °C for the pancake coil), whereas the temperature peak is much higher for the pancake coil, with a maximum temperature equal to 57.3 °C, which corresponds to a temperature increment of 20 °C, reaching values characteristic of thermal ablation. In fact, as evaluated in Chapter 6, the pancake coil generates a magnetic field that inside the tumor reaches a maximum field amplitude that is larger than the peak amplitude of the 8-turn coil, see Table 6.1. The simulation obtained with the field generated from the 8-turn coil show temperatures more consistent with the therapeutic temperature range of 40-45 °C, as the maximum temperature within the tumor is 48.7 °C, with a corresponding temperature increment of 11.6 °C. Moreover, from the temperature maps we can see a high heterogeneity in the temperature distribution within the tumor that is larger for the pancake coil, where the magnetic field decays faster and there is a larger difference between T_{max} and T_{avg} (about 17 °C). In fact, the heterogeneity coefficient *HC* is larger for the pancake coil and is equal to 0.29, whereas for the 8-turn coil is equal to 0.21. Similar significant heating does not take place with the other two types of coil, which have not a magnetic field as intense as generated by the previous coils, and no significant temperature increments are evaluated. We can indeed observe that the temperature maps related to the simulation with the Helmholtz coil and reported in Figure 7.14c are very similar to the temperature distribution obtained without the application of any magnetic fields. Whereas, the maps obtained with the application of the field applied by the largest coil with two turns show a temperature distribution more uniform within the tumor but without high increments; in fact, T_{avg} is equal to 38.1 °C and T_{max} to 38.6 °C. In addition, the heterogeneity coefficient has its lowest value with the 2-turn coil with HC = 0.022, but it remains low also with the Helmholtz coil (HC = 0.026).

As with the field and MNP configuration considered above, the pancake coil leads to an excessive temperature increase within the tumor, we have successively evaluated the temperature distribution for the same field configuration but considering a reduced MNP dose, i.e. 2.5 mg/cm^3. With this dosage, the maximum temperature in the target region is drastically reduced and has a value of 47.3 °C (with a maximum temperature increment of 10.2 °C). Because the temperature is now more uniform within the tumor (T_{avg} = 38.9 °C), the heterogeneity coefficient is smaller, HC = 0.15.

Focusing on the Helmholtz coil, we have also calculated the temperature distribution for a field frequency of 300 kHz and an MNP dose of 5 mg/cm^3, because the thermal effects due to the only field exposure are still negligible with this frequency, as seen in Chapter 6. The obtained temperatures are larger than the ones found for the case with the field frequency fixed to 150 kHz, but T_{max} and T_{avg} have values that are still below the therapeutic temperature range. In fact, the maximum temperature reached within the tumor is 39.6 °C, which corresponds to a temperature increase of 2.7 °C.

7.3 Conclusions

In this Chapter, we have presented an extensive analysis of the heating efficiency of several types of MNPs, mimicking *in vivo* experiments in murine models. The first analysis, which was carried out in the mouse digital phantom has put in evidence that to achieve temperature increments of a few degrees centigrade in a target region with size of 4 mm, a dose of at least 5 mg/cm^3 is necessary. Moreover, when the target zone is doubled in size, the maximum increment increases significantly, reaching levels suitable for thermal ablation (e.g. an increment of 22.9 °C is reached when the treated region is positioned in the lung). This allows us to reduce the MNP dose when the tissue portion that contains the MNPs is large, limiting potential toxicity consequences. Another crucial consideration is the presence of side effects near the target region's periphery, with a large temperature increase in tissues with reduced blood perfusion rate and thermal conductivity, e.g. fat.

The second analysis, which was performed with the rat models, has tested the heating efficiency of different MNPs. The analysis has indicated that when MNPs are uniformly distributed throughout the tumor, doses lower than 5 mg/cm^3 can be used to induce considerable temperature rises, reaching tumor temperatures exceeding 40 °C in both the rat model and the resized rat model. In particular, FeO@citrate NPs and $MnFe_2O_4$@citrate NPs can reach temperatures in the therapeutic range with lower doses and smaller field amplitudes than the other two MNP types. Whereas, when more injections are done and MNPs occupy only a portion of the tumor volume, the possibility of selecting field amplitudes and doses to achieve values of T_{avg} and T_{max} between 40 and 45 °C is in general much greater, but it necessitates the use of higher doses and field amplitudes. Furthermore, increasing the number of injections does not always guarantee the achievement of greater temperature uniformity in the tumor. In particular, for MNP-containing regions with the smallest diameter (5 mm), heterogeneity is reduced compared to uniformly distributed MNPs, although only the maximum temperature T_{max} achieves therapeutic values. T_{max} and T_{avg}, on the other hand, reach values ranging from 40 to 45 °C for regions with a larger diameter, but the temperature heterogeneity is much larger, and the choice of MNP dose and field amplitude is limited.

Finally, simulations with magnetic fields generated by various applicators have shown that an initial study of magnetic field distribution is required for focusing the field within the tumor to avoid the formation of hotspots in the surrounding healthy tissues. Another important consideration is the selection of the MNP dose in relation to the spatial distribution of the field generated by the applicator; for example, with the pancake coil the maximum temperature reached within the tumor containing a concentration of MNPs equal to 5 mg/cm^3 is 57.3 °C, and it can be drastically reduced to 47.3 °C by halving the MNP dose.

All the obtained results highlight the reliability of *in silico* models in assisting *in vivo* experiments by predicting the heating caused by the MNPs activation, and the possible adverse thermal effects that in this way can be avoided *in vivo*.

7.4 References

[1] F. Soetaert, S. K. Kandala, A. Bakuzis, and R. Ivkov, "Experimental estimation and analysis of variance of the measured loss power of magnetic nanoparticles," *Sci. Rep.*, vol. 7, no. 1, p. 6661, 2017. DOI: 10.1038/s41598-017-07088-w.

[2] S. Kodera and A. Hirata, "Comparison of thermal response for RF exposure in human and rat models," *Int. J. Environ. Res. Public Health*, vol. 15, no. 10, p. 2320, 2018. DOI: 10.3390/ijerph15102320.

[3] C. J. Gordon, "The mouse thermoregulatory system: Its impact on translating biomedical data to humans," *Physiol. Behav.*, vol. 179, pp. 55–66, 2017. DOI: 10.1016/j.physbeh.2017.05.026.

[4] A. Manzin, R. Ferrero, and M. Vicentini, "From micromagnetic to in silico modeling of magnetic nanodisks for hyperthermia applications," *Adv. Theory Simul.*, p. 2100013, 2021. DOI: 10.1002/adts.202100013.

[5] S. Dutz, M. Kettering, I. Hilger, R. Müller, and M. Zeisberger, "Magnetic multicore nanoparticles for hyperthermia--influence of particle immobilization in tumour tissue on magnetic properties," *Nanotechnology*, vol. 22, no. 26, p. 265102, 2011. DOI: 10.1088/0957-4484/22/26/265102.

[6] S. Kossatz *et al.*, "High therapeutic efficiency of magnetic hyperthermia in xenograft models achieved with moderate temperature dosages in the tumor area," *Pharm. Res.*, vol. 31, no. 12, pp. 3274–3288, 2014. DOI: 10.1007/s11095-014-1417-0.

[7] A. Attaluri, R. Ma, Y. Qiu, W. Li, and L. Zhu, “Nanoparticle distribution and temperature elevations in prostatic tumours in mice during magnetic nanoparticle hyperthermia,” *Int. J. Hyperthermia*, vol. 27, no. 5, pp. 491–502, 2011. DOI: 10.3109/02656736.2011.584856.

[8] F. Oltolina *et al.*, “Biomimetic magnetite nanoparticles as targeted drug nanocarriers and mediators of hyperthermia in an experimental cancer model,” *Cancers (Basel)*, vol. 12, no. 9, p. 2564, 2020. DOI: 10.3390/cancers12092564.

[9] B. Kozissnik, A. C. Bohorquez, J. Dobson, and C. Rinaldi, “Magnetic fluid hyperthermia: advances, challenges, and opportunity,” *Int. J. Hyperthermia*, vol. 29, no. 8, pp. 706–714, 2013. DOI: 10.3109/02656736.2013.837200.

[10] https://itis.swiss/virtual-population/tissueproperties/downloads/database-v4-0/.

[11] M. Wabler *et al.*, “Magnetic resonance imaging contrast of iron oxide nanoparticles developed for hyperthermia is dominated by iron content,” *Int. J. Hyperthermia*, vol. 30, no. 3, pp. 192–200, 2014. DOI: 10.3109/02656736.2014.913321.

[12] https://micromod.de/.

[13] https://nanomt.com/.

[14] Y. Gong *et al.*, “Life-time dosimetric assessment for mice and rats exposed in reverberation chambers for the two-year NTP cancer bioassay study on cell phone radiation,” *IEEE Trans. Electromagn. Compat.*, vol. 59, no. 6, pp. 1798–1808, 2017. DOI: 10.1109/TEMC.2017.2665039.

[15] M. Johannsen *et al.*, “Clinical hyperthermia of prostate cancer using magnetic nanoparticles: presentation of a new interstitial technique,” *Int. J. Hyperthermia*, vol. 21, no. 7, pp. 637–647, 2005. DOI: 10.1080/02656730500158360.

[16] A. Jordan, P. Wust, H. Fähling, W. John, A. Hinz, and R. Felix, “Inductive heating of ferrimagnetic particles and magnetic fluids: physical evaluation of their potential for hyperthermia,” *Int. J. Hyperthermia*, vol. 25, no. 7, pp. 499–511, 2009.DOI: 10.3109/02656730903287790.

[17] https://it.mathworks.com/help/stats/fitlm.html.

[18] https://it.mathworks.com/help/stats/gaussian-process-regression-models.html.

[19] https://it.mathworks.com/help/stats/regression-learner-app.html.

[20] M. Johannsen *et al.*, “Magnetic fluid hyperthermia (MFH)reduces prostate cancer growth in the orthotopic Dunning R3327 rat model,” *Prostate*, vol. 64, no. 3, pp. 283–292, 2005. DOI: 10.1002/pros.20213.

Chapter 8

Numerical model to simulate magnetic particle transport in blood vessels

In this Chapter, the physical model used to analyze the magnetic particle transport in viscous media is described. The model is discrete and based on classical Newtonian dynamics. Its numerical implementation allows us to simulate the motion of an ensemble of spherical micro/nanoparticles circulating in a microvascular network, under the influence of an external magnetic field.

In the following sections, first we introduce the main physical phenomena that govern the transport of magnetic micro/nanoparticles in blood flow. Second, we describe in detail each force term that influences the trajectory. Third, we illustrate how we reconstruct the vessel portion in which simulations are performed. Finally, we discuss the implementation of the numerical solution.

8.1 Physical model

The transport of magnetic micro/nanoparticles within blood vessels is governed by the combination of several factors and phenomena, such as the viscous drag forces due to blood flow, the magnetic force due to the applied magnetic field, gravity, buoyancy, the inter-particle effects (e.g. van der Waals force, magnetic dipole-dipole interactions, interactions between the surface coating layers, etc.), particle-vessel wall interactions, perturbation of blood flow, and Brownian motion [1]. In our simulations, we take into account the main effects, namely:

- the drag force;
- the magnetic force;
- the magnetic dipole-dipole interactions;
- the steric repulsion force.

The adhesion of particles to the vessel walls is approximated as an inelastic collision [2]. We validate this last assumption a priori by applying the contact model described by Decuzzi and Ferrari in [3]. Specifically, we found that when the particles moved in close proximity to the vessel wall, a succession of collisions occurred, but it was characterized by oscillations with an amplitude that rapidly reduced.

Let consider Ω the domain defined by the portion of the vessel taken under study, and let consider a set of magnetic particles with a spherical shape and with the same radius and physical properties (e.g. mass and material composition). Furthermore, we assume that there is a magnet with a cylindrical shape placed outside the body and it manipulates the particle motion with its magnetic field [13]. The trajectory of the *i*-th micro/nanoparticle is described by Newton's second law of motion as follows

$$\begin{aligned} &\chi \frac{d\mathbf{v}_i}{dt} = \mathbf{F}_{\text{drag},i} + \mathbf{F}_{\text{mag},i} + \sum_{\substack{j=1 \\ j \neq i}}^{N} \mathbf{F}_{\text{dip},ij} + \sum_{\substack{j=1 \\ j \neq i}}^{N} \mathbf{F}_{\text{ste},ij} \\ &\frac{d\mathbf{s}_i}{dt} = \mathbf{v}_i \end{aligned} \quad . \qquad (8.1)$$

where N is the number of magnetic particles, χ is the particle mass, $\mathbf{v}_i$ is the velocity of the *i*-th particle, $\mathbf{s}_i$ is its position, $\mathbf{F}_{\text{drag},i}$ is the drag force, $\mathbf{F}_{\text{mag},i}$ is the magnetic force defined by the applied magnetic field, $\mathbf{F}_{\text{dip},ij}$ is the force related to the mutual magnetic dipole-dipole interaction between the *i*-th particle and the *j*-th one, $\mathbf{F}_{\text{ste},ij}$ is the *i*-th and *j*-th particle steric layers overlapping force, which describes the steric repulsive interaction between two particles [5,6].

8.1.1 Drag force

The viscous drag force acting on the *i*-th particle is described by

$$\mathbf{F}_{\text{drag},i} = -6\pi\eta R_{\text{hyd}} \left(\mathbf{v}_i - \mathbf{v}_\text{b} \right) \tag{8.2}$$

where η is the viscosity of blood, R_{hyd} is the hydrodynamic radius, and $\mathbf{v}_\text{b}$ is the blood velocity. For simplicity, the hydrodynamic radius is assumed to be equal to the particle radius R_p, which takes into account that the particle is made of a hard core, which radius R_S, and a uniform surfactant or steric layer (due to surface coating), with thickness δ, thus $R_\text{p} = R_\text{S} + \delta$. Assuming that blood can be simulated as a steady-state laminar incompressible flow, the values of $\mathbf{v}_b$ within the considered vessel network are obtained by solving in Ω the Navier-Stokes equations [7],

$$\begin{cases} \rho\nabla \cdot \left(\mathbf{v}_\text{b} \right) = 0 \\ \rho\mathbf{v}_\text{b} \cdot \nabla\mathbf{v}_\text{b} = -\nabla p + \eta\nabla^2\mathbf{v}_\text{b} \end{cases} \tag{8.3}$$

where ρ is the blood density and p is the blood pressure. Moreover, the boundary condition $\mathbf{v}_\text{b} = 0$ is applied on the vessel surface. The first equation of (8.3) expresses the incompressibility of the fluid, whereas the second one is derived from the balance of the momentum.

8.1.2 Magnetic force

Since micro/nanoparticles are approximated as dipoles, the magnetic force acting on the dipole that represents the *i*-th particles is given by

$$\mathbf{F}_{\text{mag},i} = \mu_0 \left(\mathbf{m}_i \cdot \nabla \right) \mathbf{H}_\text{a} \tag{8.4}$$

where μ_0 is the magnetic permeability of the vacuum ($1.26 \cdot 10^{-6}$ H/m), $\mathbf{m}_i$ is the magnetic dipole moment of the particle, and $\mathbf{H}_\text{a}$ is the applied field at the point dipole. The particles are assumed to have a magnetization curve with negligible remament magnetization and coercivity, and their magnetic moment is expressed in two different ways. When we consider MNPs with a size lower than 20-30 nm (i.e. in the superparamagnetic state), the magnetic moment of the *i*-th particle is expressed as follows

$$\mathbf{m}_i = m_S \mathcal{L}\left(\frac{\mathbf{H}_a}{H_0}\right) \quad (8.5)$$

where m_S and H_0 are the MNP and the characteristic field, respectively, assumed to be the same for all the MNPs and determined by fitting the MNP magnetization curve, and $\mathcal{L}$ is the Langevin function,

$$\mathcal{L}(c) = \coth(c) - \frac{1}{c}.$$

Otherwise, if we are considering nano/microbeads, i.e. larger particles that contain small MNPs embedded in a matrix of inorganic or organic materials, then the magnetic moment is expressed by

$$\mathbf{m}_i = N_{nano}\mu_{nano}\mathcal{L}\left(\frac{\mu_{nano}\mu_0\mathbf{H}_a}{k_B T}\right) \quad (8.6)$$

where N_{nano} is the number of non-interacting MNPs that compose the bead, μ_{nano} is the amplitude of the MNP magnetic moment, k_B is the Boltzmann constant, and T is the absolute temperature [8]. In particular, N_{nano} and μ_{nano} are used as fitting parameters to approximate the magnetization curve of the bead [8,9].

The applied field $\mathbf{H}_a$ is assumed to be generated by an external cylindrical permanent magnet and it is evaluated in an analytical way. Let consider that the magnet has a radius a, a height b, and a remanent magnetization M_r, then, moving to cylindrical coordinates (ρ, φ, z) with the origin of the space centered at the barycenter of the magnet, the field is evaluated as follows [10]

$$H_\rho = M_r\left[\alpha_+ C(k_+,1,1,-1) - \alpha_- C(k_-,1,1,-1)\right]$$
$$H_\varphi = 0$$
$$H_z = M_r \frac{a}{a+\rho}\left[\beta_+ C(k_+,\gamma^2,1,-1) - \beta_- C(k_-,\gamma^2,1,-1)\right]$$

with $z_\pm = z \pm b/2$, $\alpha_\pm = \dfrac{a}{\sqrt{z_\pm^2 + (\rho+a)^2}}$, $\beta_\pm = \dfrac{z_\pm}{\sqrt{z_\pm^2 + (\rho+a)^2}}$, $\gamma = \dfrac{a-\rho}{a+\rho}$,

$k_\pm = \sqrt{\dfrac{z_\pm^2 + (\rho-a)^2}{z_\pm^2 + (\rho+a)^2}}$, and C is the generalized complete elliptic integral.

8.1.3 Magnetic dipole-dipole interaction

The magnetic dipole force of the j-th particle on the i-th one is expressed by [6,11]

$$\mathbf{F}_{\mathrm{dip},ij} = \frac{3\mu_0}{4\pi r_{ij}^4}\left[\left(\mathbf{e}_{ij}\times\mathbf{m}_i\right)\times\mathbf{m}_j + \left(\mathbf{e}_{ij}\times\mathbf{m}_j\right)\times\mathbf{m}_i - 2\mathbf{e}_{ij}\left(\mathbf{m}_i\cdot\mathbf{m}_j\right) + 5\mathbf{e}_{ij}\left(\mathbf{e}_{ij}\times\mathbf{m}_i\right)\cdot\left(\mathbf{e}_{ij}\times\mathbf{m}_j\right)\right] \quad (8.7)$$

where $\mathbf{r}_{ij} = \mathbf{r}_i - \mathbf{r}_j$ defines the vector distance between magnetic particle barycenters, with the corresponding unit vector $\mathbf{e}_{ij}$. When two particles are far enough away from each other (we consider a distance larger than 12 times the particle radius), the contribution of the resulting magnetic dipole force is negligible, so $\mathbf{F}_{\mathrm{dip,ij}}$ is assumed to be zero, otherwise it is evaluated with Eq. (8.7).

8.1.4 Steric repulsion

Magnetic particles are usually coated with a uniform steric or surfactant layer, with the aim of keeping magnetic fluids stable and avoiding agglomeration phenomena between particles. As a result, when particles are too close to each other, a steric repulsive interaction occurs. Here this force is considered as an excluded volume force [12], which increases exponentially when overlapping is approached and it becomes negligible if the distance between particles is more than the particle radius R_p. Specifically, the steric repulsion force on the i-th bead is given by [12]

$$\mathbf{F}_{\mathrm{ste},ij} = \begin{cases} 2\pi k_\mathrm{B} T R_\mathrm{s}^2 \mathbf{e}_{ij} \dfrac{n_\mathrm{s}}{\delta} ln\left(\dfrac{2R_\mathrm{p}}{r_{ij}}\right) & \text{for } R_\mathrm{s} \le r_{ij} \le R_\mathrm{p} \\ 0 & \text{elsewhere} \end{cases} \quad (8.8)$$

where n_S corresponds to the number of surfactant molecules on the surface of the particle per unit area.

8.2 Blood vessel reconstruction

In this Thesis, we consider a blood vessel segment that reconstructs a real human blood vessel that presents several bifurcations. The geometry was reconstructed and processed by Dr. Riccardo Ferrero, research fellow at INRiM.

The vessel segment extends for about 1.8 cm, has a cross-section of about 0.8 mm, and is composed of an entering branch that is divided into four branches, one of which splits into two. The structure is acquired from real computed tomography (CT) scans belonging to the example dataset of 3D Slicer, an open-source software that is specifically used for processing and 3D visualization of medical images [13]. The software includes an anisotropic diffusion filter to smooth image noise while maintaining the light-dark transition. The reconstruction in 3D of the selected vessel segment is carried out with the Vascular Modelling Toolkit (VMTK) software, a collection of libraries and tools for data analysis for image-based modeling of blood networks [14]. With VMTK we can improve the visualization accuracy of the 3D image, obtained by 3D Slicer, using the proper filters, and extract the segmentation of the vessel region. An example of vessel reconstruction is displayed in Figure 8.1. Once the 3D structure is acquired, the geometry is discretized with a mesh composed of tetrahedral elements (average size of 0.9 μm) by means of COMSOL Multiphysics® software.

8.3 Numerical solution

Since blood is considered as a steady-state fluid that is not perturbed by the motion of the particles, the spatial distribution of the blood velocity is evaluated separately before the calculation of the numerical solution of the system (8.1). The blood velocity is obtained by solving Eqs. (8.3) with COMSOL®, which adopts mixed FEM, as the pressure, which is often smoother, is evaluated considering linear basis functions, whereas the velocity is approximated with quadratic basis functions. The resulting algebraic system, obtained with the application of FEM, is then solved by using the generalized minimal residual method (GMRES), which is an iterative method for the numerical solution of non-symmetric systems. The fluid dynamics simulations are obtained by fixing ρ at 1060 kg/m^3 [16] and η at 0.005 $N{\cdot}s/m^2$.

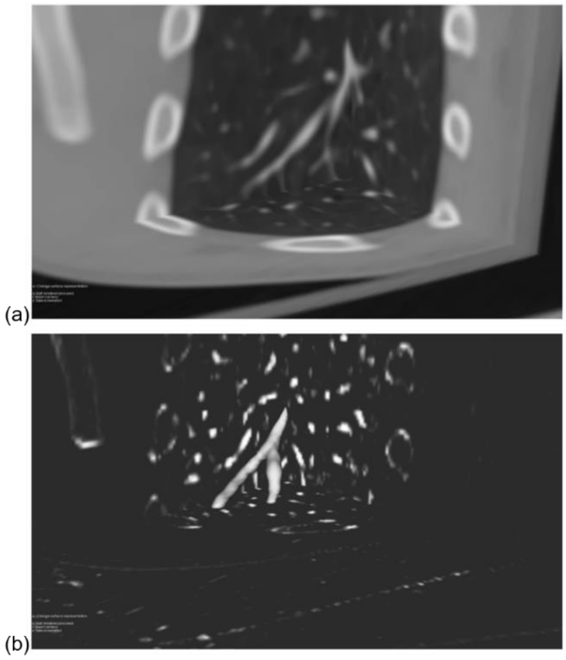

Figure 8.1. Example of reconstruction of a vessel segment with VMTK from computed tomography scans. (a) 3D image before the application of filters. (b) Reconstruction of a selected vessel portion after the application of filters.

After the fluid dynamics simulation, system (8.1) is solved by using the MATLAB® solver ode15s [17], which is an implicit variable-order method with adaptive step and is based on Numerical Differentiation Formulas (NDFs) [18]. The selection of this specific solver comes from the comparison between constant-step methods (e.g. Runge-Kutta of fourth-order, and Crank-Nicolson) and variable step methods (e.g. ode45 that implements the Runge-Kutta-Fehlberg [19]), where the NDFs-based method resulted to be the one to properly handle the stiffness of the system (8.1). The detailed analysis is reported in [20], where the numerical model was validated by comparison to analytical solutions [21] obtained in the case of a simple vessel geometry (i.e. vessel approximated with a cylinder) and the cylindrical magnet assumed to be of infinite length along with one of the axis transversal to the vessel.

8.4 References

[1] E. P. Furlani, "Magnetic Biotransport: Analysis and Applications," *Materials (Basel)*, vol. 3, no. 4, pp. 2412–2446, 2010. DOI: 10.3390/ma3042412.

[2] J. W. Haverkort, S. Kenjeres, and C. R. Kleijn, “Computational simulations of magnetic particle capture in arterial flows,” *Ann. Biomed. Eng.*, vol. 37, no. 12, pp. 2436–2448, 2009. DOI: 10.1007/s10439-009-9786-y.

[3] P. Decuzzi and M. Ferrari, “The adhesive strength of non-spherical particles mediated by specific interactions,” *Biomaterials*, vol. 27, no. 30, pp. 5307–5314, 2006. DOI: 10.1016/j.biomaterials.2006.05.024.

[4] A. K. Hoshiar, S. D. Javan, T. A. Le, M. R. H. Yazdi, and J. Yoon, “Studies on aggregated nanoparticles steering during deep brain membrane crossing,” *Nanomaterials (Basel)*, vol. 11, no. 10, p. 2754, 2021. DOI: 10.3390/nano11102754.

[5] A. Satoh and R. W. Chantrell, “Application of the dissipative particle dynamics method to magnetic colloidal dispersions,” *Mol. Phys.*, vol. 104, no. 20–21, pp. 3287–3302, 2006. DOI: 10.1080/00268970601094437.

[6] W. Li and Q. Li, “Study about the structure and dynamics of magnetic nanofluids using a mesoscopic simulation approach,” *Nonlinear Dyn.*, vol. 91, no. 4, pp. 2141–2155, 2018. DOI: 10.1007/s11071-017-4006-z.

[7] T. Lunnoo and T. Puangmali, “Capture efficiency of biocompatible magnetic nanoparticles in arterial flow: A computer simulation for magnetic drug targeting,” *Nanoscale Res. Lett.*, vol. 10, no. 1, p. 426, 2015. DOI: 10.1186/s11671-015-1127-5

[8] A. Manzin, V. Nabaei, and O. Kazakova, “Modelling and optimization of submicron Hall sensors for the detection of superparamagnetic beads,” *J. Appl. Phys.*, vol. 111, no. 7, p. 07E513, 2012. DOI: 10.1063/1.3678322.

[9] A. Manzin, V. Nabaei, and R. Ferrero, “Quantification of magnetic nanobeads with micrometer hall sensors,” *IEEE Sens. J.*, vol. 18, no. 24, pp. 10058–10065, 2018. DOI: 10.1109/JSEN.2018.2874520.

[10] N. Derby and S. Olbert, “Cylindrical magnets and ideal solenoids,” *Am. J. Phys.*, vol. 78, no. 3, pp. 229–235, 2010. DOI: 10.1119/1.3256157.

[11] K. W. Yung, P. B. Landecker, and D. D. Villani, “An analytic solution for the force between two magnetic dipoles,” *Magn. Electr. Sep.*, vol. 9, no. 1, pp. 39–52, 1998. DOI: 10.1155/1998/79537.

[12] E. J. Furlani and E. P. Furlani, “A model for predicting magnetic targeting of multifunctional particles in the microvasculature,” *J. Magn. Magn. Mater.*, vol. 312, no. 1, pp. 187–193, 2007. DOI: 10.1016/j.jmmm.2006.09.026.

[13] https://www.slicer.org/.

[14] http://www.vmtk.org/.

[15] M. Zamir, "Arterial branching within the confines of fractal L-system formalism," *J. Gen. Physiol.*, vol. 118, no. 3, pp. 267–276, 2001. DOI: 10.1085/jgp.118.3.267.

[16] S. S. Hossain, T. J. R. Hughes, and P. Decuzzi, "Vascular deposition patterns for nanoparticles in an inflamed patient-specific arterial tree," *Biomech. Model. Mechanobiol.*, vol. 13, no. 3, pp. 585–597, 2014. DOI: 10.1007/s10237-013-0520-1.

[17] https://it.mathworks.com/help/matlab/ref/ode15s.html.

[18] A. Pelios and R. W. Klopfenstein, "Minimal error constant numerical differentiation (N.d.) formulas," *Math. Comput.*, vol. 26, no. 118, p. 467, 1972. DOI: 10.2307/2005173.

[19] https://it.mathworks.com/help/matlab/ref/ode45.html.

[20] M. Vicentini, "Numerical modelling of the transport of magnetic nanoystems in blood vessels", Thesis for Master's Degree, Università degli Studi di Torino, 2018, supervisor: M. Semplice, co-supervisor: A. Manzin.

[21] E. P. Furlani and K. C. Ng, "Analytical model of magnetic nanoparticle transport and capture in the microvasculature," *Phys. Rev. E Stat. Nonlin. Soft Matter Phys.*, vol. 73, no. 6 Pt 1, p. 061919, 2006. DOI: 10.1103/PhysRevE.73.061919.

Chapter 9

In silico modelling of magnetic particle transport in blood vessels guided by magnetic fields

Part of the material presented in this chapter is published in Journal of Magnetism and Magnetic Materials 513 (6): 167234, July 2020

In this Chapter, we present the results obtained in the study of particle motion in a 3D domain that reconstructs the structure of a realistic vessel network segment, considering that the magnetic field source is an external magnet. A first analysis is done to study the influence of the magnet size and position with respect to the blood vessel geometry on the magnetic force exerted on the particles. Then, we simulate the motion of the particles to investigate how the percentage of particles adhering to the vessel wall could be enhanced with the optimization of the magnet configuration and in relation to the position of the injection site. The study is performed considering three types of spherical particles of different sizes (from 20 nm to 1 μm) and magnetic moments. All the presented results are compared to those obtained without the magnetic field source in order to highlight the magnet's role in driving particle transport.

9.1 Numerical analysis

Nano/microbeads are considered in addition to MNPs with features typical of magnetic hyperthermia applications. This choice is done to put in evidence the differences in terms of magnetic force exerted by the external magnet, used to drive particle transport and release to a target tissue. In particular, the analysis is performed considering three types of commercial magnetic particles:

- MagSIGNAL beads (AMSBIO [1]), which have an average size of 300 nm and saturation magnetic moment m_s equal to 0.002 pA·m^2;
- Dynabeads MyOne (ThermoFisher Scientific [2]) beads with an average size of 1 μm and m_s = 0.025 pA·m^2;
- SHA-20 NPs [3,4] with an average size of 20 nm and m_s = 1.18·10^{-18} A·m^2.

The first ones are beads composed of ferromagnetic grains, with a diameter of 10-15 nm, dispersed in a silica shell and with a density of 2.5 g/cm^3 [1]; the second ones are beads based on a mixture of iron oxide NPs embedded in a polymeric matrix and have a density of 1.8 g/cm^3 [2]; the third ones are amine-functionalized iron oxide NPs and with a density of about 5 g/cm^3. Figure 9.1 reports the magnetization curves of the particles, where the magnetic behaviors are reconstructed from experimental data by fitting through the formulation (8.6) for the MagSIGNAL beads and the Dynabeads Myone beads, and the formulation (8.5) for the SHA-20 particles. In particular, the approximation of the magnetization curves is obtained considering H_0 = 7.5 kA/m in Eq. (8.5) for SHA-20, whereas for the beads we use the following fitting parameters in Eq. (8.6):

- MagSIGNAL: N_{nano} =10400, μ_{nano}= 20400μ_B
- Dynabead: N_{nano} =145000, μ_{nano}= 18500μ_B

where μ_B is the Bohr magneton (9.274·10^{-24} J/T).

If not otherwise specified, the following simulations are performed considering that the magnetic field source is a cylindrical magnet of NdFeB with a remanent magnetization of 1000 kA/m, a radius a of 1.5 cm, and a height b of 2 cm. The bottom of the magnet is positioned for most of the analyzed cases at a distance of about 1 cm from the nearest part of the vessel wall. As a reference position, the magnet barycenter is placed above the middle of the target region,

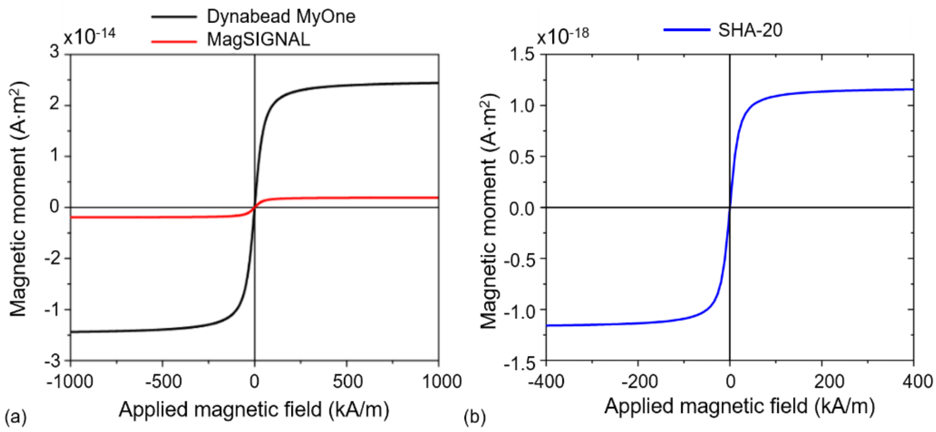

Figure 9.1. Magnetization curve of the considered magnetic particles: (a) Dynabead MyOne (black line) and MagSignal (red line) beads, (b) SHA-20 (blue line) NPs.

which is defined as the top part of the wall in the central area of the vessel bifurcation (see schematic in Figure 9.2a).

For the calculation of the steric force $\mathbf{F}_{ste}$, we consider that the number of surfactant molecules n_s is equal to 10^{15} [5] for all particle types, and the thickness of the surfactant layer δ is set at 15 nm for MagSIGNAL, 40 nm for Dynabeads MyOne, and 5 nm for SHA-20. The fluid dynamics simulation is performed by setting the blood average velocity at 0.75 cm/s; the velocity profile is displayed in Fig. 9.2b. The simulation is performed in order to obtain the blood flux that enters

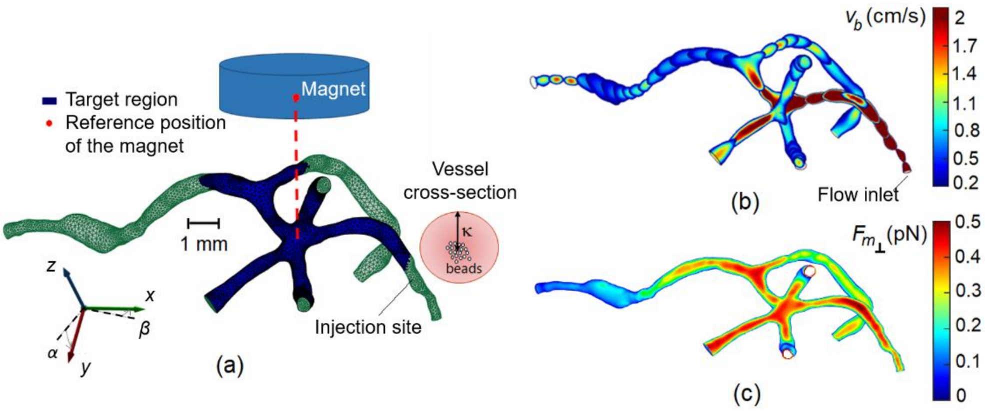

Figure 9.2. (a) Schematic of the selected segment of a blood vessel, with the indication of the reference position of the cylindrical magnet, the target region for particle adhesion, and the injection site. (b) Velocity profile of blood within the vessel portion obtained with the fluid-dynamics simulation. (c) Spatial distribution of the outward component of the magnetic force normal to the vessel wall, obtained for the Dynabeads MyOne beads, considering the magnet with a radius of 1.5 cm and a height of 2 cm in the reference position. The graphs are reported in [6].

from the inlet of the vessel portion that is the closest to the injection site (see Fig. 9.2a)

9.2 Influence of the magnetic source configuration

To investigate the efficiency of the magnet to attract the particles in the target region indicated in Fig. 9.2a, we first calculate the outward normal component $F_{m_\perp}$ of the magnetic force on the surface of the vessel wall. As an example, Fig. 9.2c shows the magnetic force on the surface of the vessel for the magnet positioned in the reference configuration, evaluated for the Dynabeads MyOne, and with a = 1.5 cm and b = 2 cm (force amplitude of about 0.4-0.5 pN). The force map is particularly useful to establish the areas of the vessel where a stronger attraction should be guaranteed. The analysis of the magnetic force is carried out by changing the magnet's size (height and radius), its position, and orientation with respect to the vessel, in order to maximize the magnetic force and consequently increase the percentage of particles adherent to the vessel wall in the target region.

For each considered magnet configuration, we estimate the average $\bar{F}_{m_\perp}$, calculated as the average of $F_{m_\perp}$ over the mesh nodes that compose the vessel surface in the target region. Figure 9.3 reports the maps of $\bar{F}_{m_\perp}$ for the Dynabeads MyOne only, varying the magnet parameters. In particular, Fig. 9.3a shows how $\bar{F}_{m_\perp}$ changes as a function of magnet dimensions (i.e. a and b), where the x and y components of the barycenter of the magnet are fixed to the coordinates of the reference position, whereas the z component is changed to maintain a minimum distance of 1 cm between the vessel wall and the base of the magnet. The largest values of the magnetic force are reached when a = 1.5 cm and b is larger than 1.5 cm. For example, the greatest value, which is in the order of 0.24 pN, is obtained when b is equal to 3.2 cm.

In a successive analysis, the values of the magnet radius and height are fixed to 1.5 cm and 2 cm respectively, and the magnet is shifted on the xy-plane. The results are reported in Figure 9.3b that shows the map of $\bar{F}_{m_\perp}$ with a quasi-circular region that comprises the largest values, up to 0.3 pN for displacements along the x- and y-axes of about 1 cm. The magnetic force becomes practically ineffective in the target region for displacements larger than 2 cm, emphasizing the need of a precise fine-tuning of magnet's position, which can be accomplished with pre-

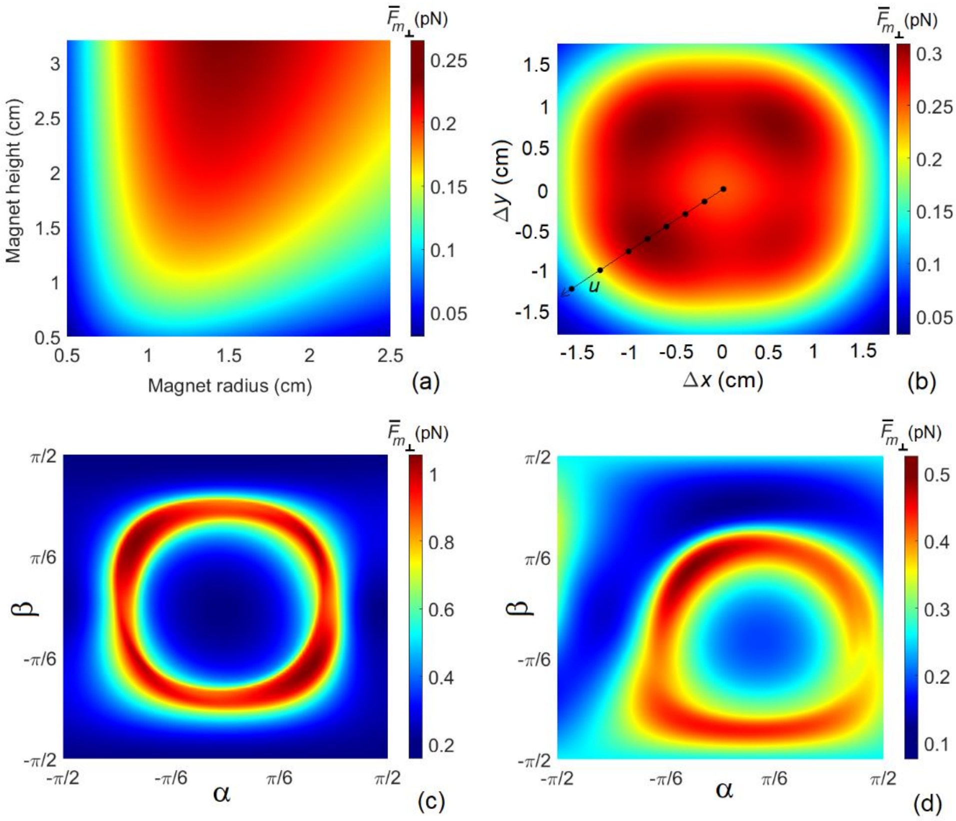

Figure 9.3. Evaluation of the magnetic force for different magnet configurations, evaluated for the Dynabeads MyOne beads. The maps report the average of the magnetic force calculated on the outward normal component with respect to the vessel surface. Variable parameters: (a) height and radius of the magnet; (b) position of the barycenter of the magnet in the xy-plane; inclination of the magnet with respect to the x-axis (defined by angle β) and y-axis (defined by angle α) for the barycenter located (c) at the reference position and (d) shifted (Δx = -8 mm, Δy = -6 mm). Apart from (a), the other maps are evaluated considering the magnet's radius equal to 1.5 cm and its height to 2 cm. Graphs reported in [6].

treatment medical imaging. Modifying the magnet's orientation with respect to the vessel wall might increase its attracting action. Figures 9.3c and 9.3d demonstrate the change in $\bar{F}_{m_\perp}$ achieved for two distinct magnet positions when varying the angles α and β, which specify the orientations with regard to the *y*- and *x*-axes, respectively, as depicted in the reference frame of Fig. 9.2a. In particular, Fig. 9.3c displays the case for $\Delta x = \Delta y = 0$, where a maximum force larger than 1 pN is reached when the magnet is in close proximity to the vessel, limiting the possibility of applications. Whereas Fig. 9.3d reports the results for the position that leads to the greatest value of the average magnetic force, i.e. Δx = -8 mm and Δy = -6 mm. In these two maps, we can notice that the areas where $\bar{F}_{m_\perp}$ is larger have a ring shape. In this case, a maximum value of about 0.5 pN is reached with $\alpha = 4.6^o$ and $\beta = 8^o$.

The reported results are obtained for the Dynabeads MyOne bead type and are qualitatively valid also for the other particles, with the significant difference that for MagSIGNAL beads the magnetic force amplitude is approximately one order of magnitude lower and even lower for SHA-20 NPs.

9.3 Analysis of bead transport and adhesion rate

In this section, we investigate the transport of the magnetic particles and their rate of adhesion in the target region for different positions of the magnet, in accordance with the results of the previous section. The system of equations (9.1) is solved for each particle type, evaluating the trajectories of an ensemble of 300 particles, from the injection site to target areas or to the outlets of the vessel, assuming an initial velocity of the particles equal to zero. We choose an inner volume near the inlet cross-section, where particles are randomly dispersed, as the initial positions of the particles, i.e. it represents an ideal injection site (see the schematic in Fig. 9.2a).

Considering the results reported in Fig. 9.3b, first we simulate the transport of MagSIGNAL and Dynabeads MyOne beads for the eight different magnet's positions along the *xy*-plane, which are defined by the parameter u and are indicated with the marker points in the same map. For all the simulations, the magnet axis is assumed to be parallel to the z-axis, except for u = 1 cm, where we also analyze the case of a non-zero inclination, i.e. $\alpha = 4.6^o$ and $\beta = 8^o$. Once the simulations are performed, we calculate the percentage of beads that adhere to the wall and we report the results in Fig. 9.4 as a function of u, considering the adhesion across the entire vessel wall and in the only target region separately. In comparison to the simulations without the presence of the magnet, the percentage of beads that adhere to the vessel is almost always larger, with a significant increase in the target region, and this demonstrates the magnet's ability to attract beads in the area of interest. The influence of the magnet is particularly evident for Dynabeads MyOne beads, where the larger magnetic force enhances the adhesion percentage in the whole vessel. Whereas, for distances greater than 1.5 cm from the reference position, the magnet efficacy tends to dwindle, necessitating precision control of its location in order to drive the bead trajectories in an optimal manner. Moreover, varying u produces no significant changes in magnet performance for distances lower than 1.2 cm.

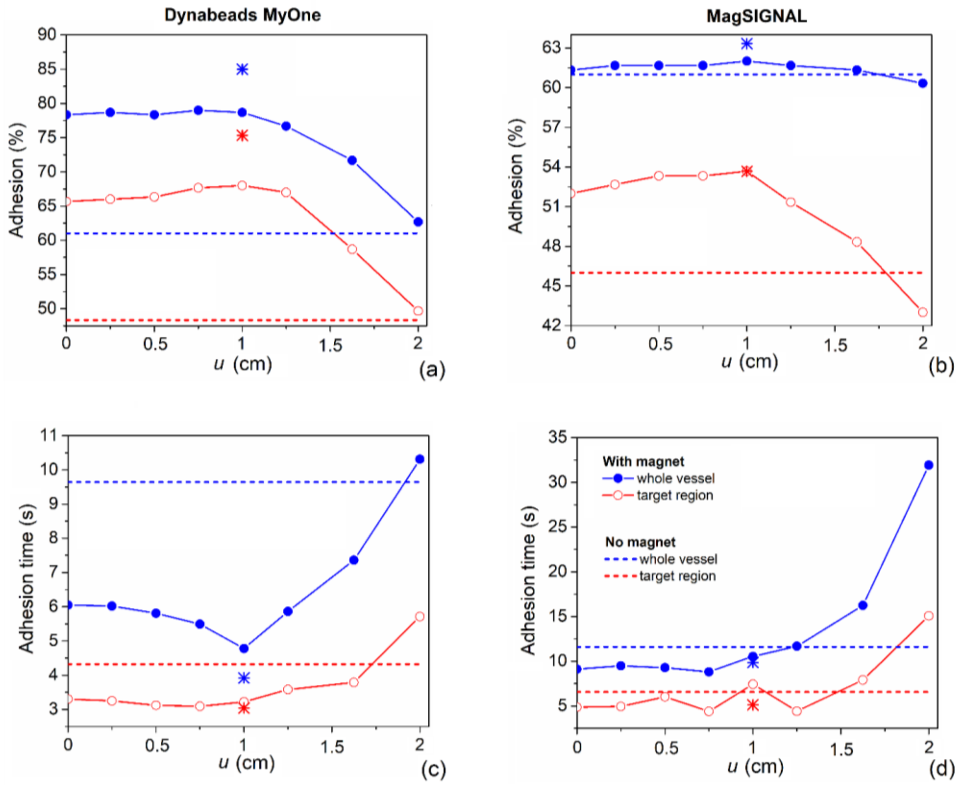

Figure 9.4. Results of particle adhesion as a function of the magnet positions u, indicated in Fig. 9.3, comparing the behavior of an ensemble of 300 Dynabeads MyOne (left) and MagSIGNAL beads (right). The percentage of bead adhesion is reported in (a) and (b). The average adhesion time is illustrated in (c) and (d). For each graph, the contribution from the entire vessel and the target region only is displayed separately, comparing the results obtained with and without the magnet (magnet radius equal to 1.5 cm and height fixed to 2 cm). The markers with a star shape correspond to the magnet at u = 1 cm and with rotation angles α = 4.6º and β = 8º. The results related to the whole vessel are represented in blue and the ones for the target region in red. Graphs reported in [6].

For *u* fixed to 1 cm, we also simulate the trajectory of the SHA-20 NPs and we find that the percentage of particle adhesion in the target region is 46.3% for SHA-20, 54% for MagSIGNAL, and 68% for Dynabeads MyOne. Whereas, without the magnet, the percentage is equal to 46%, 46%, and 49% respectively. This proves the difficulty of driving very small particles, like the ones tipically used in magnetic hyperthermia, since in the simulations with the magnet, in comparison to the correspondent case without it, there is a significant increase in the adhesion percentage only for the beads. Regarding the magnetic beads, the adhesion percentage can be significantly increased by a proper inclination of the magnet, especially for the Dynabeads MyOne; in fact, for α = 4.6º and β = 8º, the

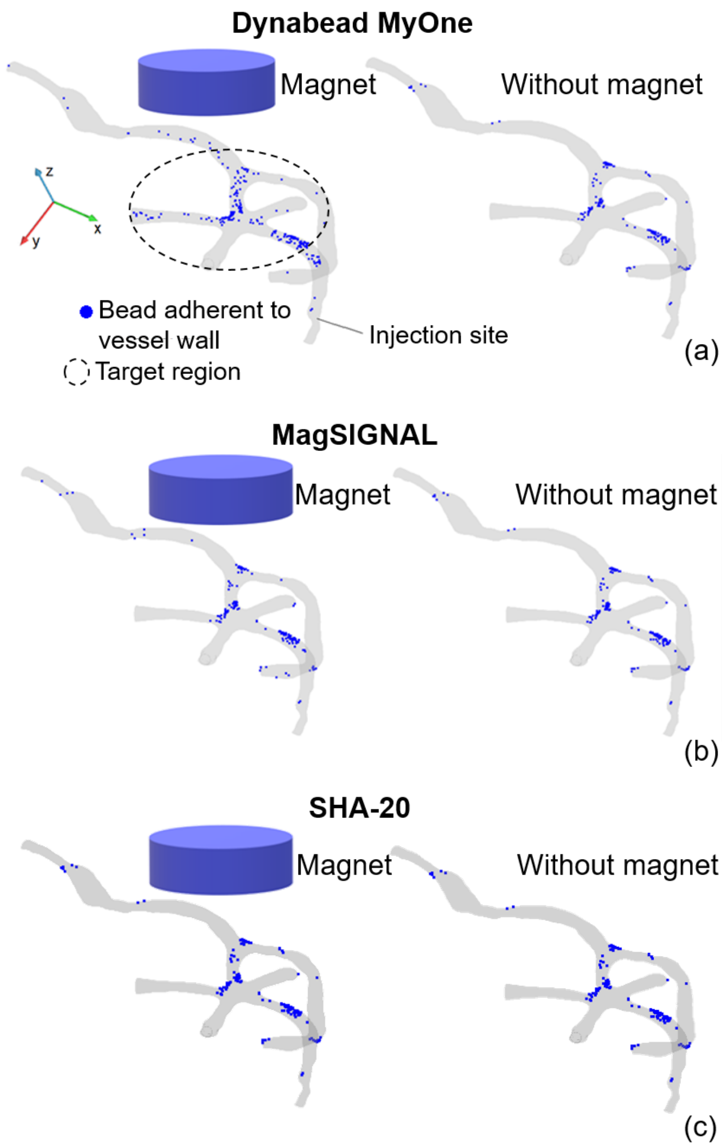

Figure 9.5. Schematic of particles adherent to the vessel wall. Comparison beetween the results obtained for (a) Dynabeads MyOne beads, (b) MagSIGNAL beads, and (c) SHA-20 NPs to the correspondent ones for the case without magnet. Simulations with a magnet of radius equal to 1.5 cm, height to 2 cm, and a position in the xy-plane defined by the parameter u = 1 cm. Adaptation from graphs reported in [6].

percentage in the target region rises to 75% (represented by the red star-shaped marker in Fig. 9.4).

We also calculate the adhesion time, i.e. the period of time between the injection and the collision to the wall, which we consider to be the moment in which particles stop moving, without considering the particles that exit from the vessel outlets. The results of this analysis are reported in Figure 9.4c and 9.4d that show the average time of adhesion as a function of *u*. The adhesion time, similarly to the percentage of adhesion, does not vary significantly for distances lower than 1.2 cm, where the magnet, in most circumstances, speeds the anchorage to the vessel wall, especially for the Dynabeads MyOne beads. However, when *u* is greater than 1.5 cm, a significant increase can be seen, particularly with the MagSIGNAL beads. This is another indication of the magnet efficacy decline within the considered blood vessel, as evidenced by the fact that when $u > 2$ cm the average adhesion time is longer than when the magnet is absent. For large values of *u*, the magnetic force tends to slow down the beads in the blood flow and it is too weak to drive them to the wall in the region of interest. As a result, there is a decrease in the adhesions in the target region and an increase in the peripheral areas. As a consequence, the average adhesion time rises and this is particularly evident in the cases where there is a large difference between the adhesion percentage in the entire vessel and in the region of interest.

Figure 9.5 shows the spatial distribution of the three types of particles adherent to the vessel wall, comparing the results of the simulations obtained with the magnet in its optimal configuration (i.e. *u* equal to 1 cm) to the ones without the magnet. We can observe that with the presence of the magnet, particles tend to have a more uniform distribution, especially in the target region. However, even if the magnet is responsible for an increase in the number of adhesions, this aspect is less evident for MagSIGNAL beads and for SHA-20 NPs, due to a strong reduction of the magnetic force. The distributions of the MagSIGNAL beads and of the SHA-20 particles look very similar but are slightly different, i.e. the particles do not adhere at the same points of the wall, albeit they are rather close.

Finally, we analyze the influence of the spatial distribution of beads at the injection site. To this aim, we fixed the magnet configuration (i.e. the optimal one with $u = 1$ cm), and we introduce a parameter κ that defines the distance of the ensemble of beads from the upper part of the wall, as schematized in Fig. 9.2a. Specifically, κ is evaluated as the average distance of the particles at the initial instant of time to the upper part of the vessel wall. The results are reported in Fig. 9.6 with the adhesion percentage represented as a function of κ (the previous configurations are obtained with $\kappa \cong 0.17$ mm). We can observe that with beads initially closer to the wall and on the same side of the magnet, a larger number of adherent beads is in general obtained, demonstrating the need for suitable injection site selection with respect to the magnet position and the vessel geometry. Due to the decrease in bead velocity in the proximity to the wall, a lower reduction can be noticed in the percentage of adhesion at very low values of κ. These aspects are more evident for MagSIGNAL, where the reaction to the applied field is weaker and the viscous drag force is dominant.

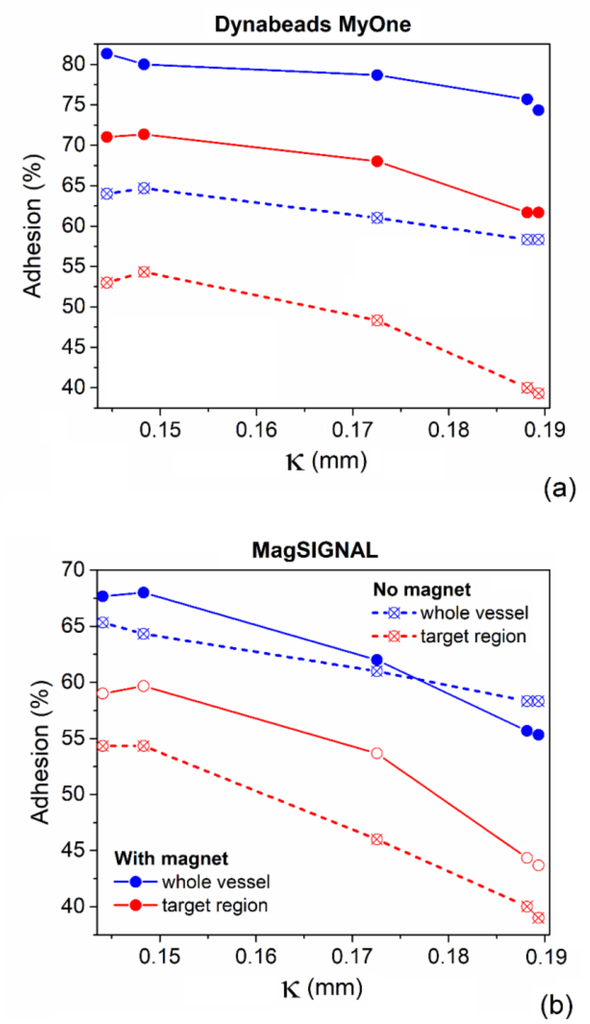

Figure 9.6. Adhesion percentage for different spatial distributions of 300 identical particles at the injection site, achieved by varying parameter k. Comparison between (a) Dynabeads MyOne beads and (b) MagSIGNAL beads, also considering the correspondent cases without the magnet. The adhesion percentages evaluated for the whole vessel and for the target region are reported separately. The magnet considered for the simulations has a height of 2 cm, a radius of 1.5 cm, and the position in the xy-plane is defined by u = 1 cm. Graphs reported in [6].

9.4 Conclusions

In this Chapter, we have analyzed how an external cylindrical magnet could drive particle motion and adhesion to a target region within a realistic 3D reconstruction of a blood vessel segment. In particular, we have investigated the role of magnet position and size with respect to the blood vessel structure. The magnet results to be more effective for particles with large magnetic moment and size since the magnetic force overcomes the viscous drag effects. The simulations with the smallest type of particles (SHA-20) have demonstrated how difficult it is to drive the motion of particles with a size of a few tens of nanometers. In fact, with one of the optimal magnet configurations found in the analysis of section 9.2, the percentage of particles adherent to the vessel wall in the target region is almost the same as without the magnet. A possible strategy to drive small NPs, or particles circulating in not peripheral areas, could be the use of implanted magnet systems within the body in close proximity to the target region, in order to reduce the distance between the magnet and the particles. Moreover, in order to improve the rate of adhesion to a specific target zone, the study has also emphasized the need of a precise fine-tuning of the magnet position as well as of the site of particle injection. Specifically, the analysis has evidenced the relevance of conducting a preliminary study of the spatial distribution of the magnetic force within the whole target region, in order to identify the configurations of the magnet that result in larger magnetic field gradients and, as a result, that enhance the number of particle adhesions while reducing circulation time.

Finally, the presented model can be considered a useful tool for analyzing the targeting and the magnetically driven transport of magnetic particles in blood vessels, as well as for optimizing magnetic source configurations and particle physical properties for biomedical applications, such as drug delivery.

9.5 References

[1] https://www.amsbio.com/magsi-magnetic-beads-immunoassays/.

[2] http://www.thermofisher.com/order/catalog/product/65011?ICID=sproduct.

[3] https://oceannanotech.com/web/products.php?category3=Amine_Iron_Oxide_Nanoparticles.

[4] K. Wu *et al.*, “Investigation of commercial iron oxide nanoparticles: Structural and magnetic property characterization,” *ACS Omega*, vol. 6, no. 9, pp. 6274–6283, 2021. DOI: 10.1021/acsomega.0c05845.

[5] S. S. Hossain, T. J. R. Hughes, and P. Decuzzi, “Vascular deposition patterns for nanoparticles in an inflamed patient-specific arterial tree,” *Biomech. Model. Mechanobiol.*, vol. 13, no. 3, pp. 585–597, 2014. DOI: 10.1007/s10237-013-0520-1.

[6] M. Vicentini, R. Ferrero, and A. Manzin, “Modelling of magnetic bead transport in a microvascular network,” *J. Magn. Magn. Mater.*, vol. 513, no. 167234, p. 167234, 2020. DOI: 10.1016/j.jmmm.2020.167234.

Chapter 10

Conclusions

In this Thesis, the application of MNPs in magnetic hyperthermia experiments has been investigated with a modelling methodology. The analysis has been performed by means of a set of numerical tools for the simulation of the thermometric measurements of MNP-containing samples, the heating process generated by magnetic hyperthermia in living tissues, and the MNP transport in microvascular networks. After the description of the numerical implementation and validation of the developed models, the obtained simulation results were presented and discussed.

First, we have simulated the temporal-spatial distribution of the temperature within samples containing MNPs with nanodisk shape to investigate the role of non-adiabatic conditions, MNP concentration, medium where the MNPs are dispersed, and duration of the AC magnetic field application. The magnetic nanodisks allow to obtain high temperature increments also for low concentrations, and the analysis has put in evidence how the reduction of the SLP value, due to the viscosity of the medium, impacts on the heating efficiency. In fact, in high-viscosity media (e.g. gel), for the same magnetic nanodisk concentrations, the temperature increases are reduced to half in comparison to those obtained with water-based suspensions. In this context, we have also presented the results that have been obtained with our thermal model for iron oxide nanocubes, to show the good agreement with experimental data, confirming the validity of the thermal solver as a tool to test MNP heating efficiency.

A second analysis has been performed on two high-resolution digital phantoms of murine models, a 28 g mouse and a 503 g rat, to investigate the eddy current effects due to the only AC magnetic field exposure, in terms of SAR and temperature increase. Different aspects were taken into accounts, such as the orientation of the animal body with respect to the field direction and the field source configuration. When the magnetic field is assumed to be uniformly distributed along the longitudinal axis of the animal body, the simulations have shown that the thermal effects caused by the field exposure are very weak for the animal with the smallest size, even when the biophysical constraint on the field amplitude and frequency defined by the Hergt-Dutz limit is slightly exceeded. Only for very large values of the product $\hat{H}_a \times f$ significant undesirable thermal effects can occur. On the contrary, in the largest animal model eddy current effects are no longer negligible, even when the Hergt-Dutz limit is not overcome. In the rat, maximum temperature increments of less than 1 °C occur only when $\hat{H}_a \times f < 2 \cdot 10^9$ A/(m·s), i.e. about half between the Atkinson-Brezovich and the Hegt-Dutz limits. Furthermore, when the field is applied transversally, higher temperature increases are observed, due to the increment of the body section when the animal is perpendicular to the field direction. Thus, the thermal simulations have shown that the Hergt-Dutz limit could not be assumed as a condition that ensures a safe level of AC magnetic field exposure for animals like rats or larger ones, with clear implications for the applicability in human treatments. However, a significant reduction in eddy current effects can be achieved with the introduction of water boluses, due to the forced heat convection at the skin-environment interface, as demonstrated by the simulations where the heat transfer coefficient was increased. Another considered strategy is the use of EM field applicators that focus the field on the diseased region to be treated. For this analysis, we have considered four different applicator geometries, i.e. 8-turn, pancake, Helmholtz, and 2-turn coils. With the non-uniform and focused field generated by the coils we have found a strong reduction in the SAR and a consequent decrease in the temperature increments, with respect to the cases with the uniform fields. In these simulations, the largest effects due to eddy currents are concentrated only on peripheral areas in close proximity to the coils, i.e. where the field parameter product, $\hat{H}_a \times f$ is near to or slightly exceeds the Hergt-Dutz limit. Nevertheless, the focus of the field within the diseased area becomes more difficult with the applicators with the largest sizes, since the highest temperatures are achieved in tissues in proximity but outside the tumor-affected region. Moreover, due to the presence of higher magnetic field gradients, achieving a high level of magnetic field uniformity becomes critical throughout extended tumors.

Regarding the thermal response in living tissues due to MNP injection, we have presented an extensive analysis of the heating efficiency of several types of MNPs on both murine models. The first part of the study was conducted by means of simulations on the mouse model to test the heating performance of magnetic nanodisks as a function of their concentration as well as of the size and location of the diseased region. The simulations have put in evidence that temperature increases comparable to those obtained with the simulated thermometric tests (under quasi adiabatic conditions) can only be produced by employing a concentration of nanodisks that is an order of magnitude larger. In addition, when the target zone is doubled in size, the maximum increment increases significantly, reaching levels suitable for thermal ablation, especially in tissues with low blood perfusion rate and thermal conductivity. Thus, the MNP dose could be reduced when the MNP-containing region is large, limiting potential toxicity consequences.

The second study was conducted on the rat model, testing the heating efficiency of four types of MNPs with different doses, and varying the AC magnetic field and MNP distribution within the tumor. With the uniform distribution of the magnetic field, FeO@citrate NPs and $MnFe_2O_4$@citrate NPs have shown the possibility to reach temperatures in the therapeutic range with lower doses and smaller field amplitudes than the other two MNP types. Whereas, when MNPs are not uniformly distributed, i.e. in the case where we have assumed that more injections are done and the MNPs occupy only a limited volume portion of the tumor, the possibility of selecting field amplitudes and doses to achieve values of maximum and average temperature within the tumor between 40 and 45 °C is in general much wider, but it necessitates the use of higher doses and field amplitudes. Furthermore, we have noticed that increasing the number of injections does not always guarantee the achievement of greater temperature uniformity in the tumor. Finally, the simulations with a non-uniform distribution of magnetic fields were performed by evaluating the field generated by the four applicators previously analyzed. The results have highlighted the importance of focusing the field on the only diseased area to reduce the generation of hot spots in healthy tissues, in correspondence with a suitable concentration of MNPs.

In the last part of the Thesis, we have studied how a cylindrical magnet could drive particles toward target regions. The analysis was performed by means of the simulations of particle trajectories through a realistic 3D reconstruction of a blood vessel segment. Three different types of particles were studied and we have found that the attractive action of the magnet is more effective for particles with large magnetic moment and size since the magnetic force overcomes the viscous drag effects. Moreover, we have observed that the optimization of the magnet configuration can significantly increase the number of particles that reach the target region, even if with the smallest nanoparticles the magnetic force of the magnet remains almost negligible.

In conclusion, the results and analyses presented in this Thesis have highlighted the importance of *in silico* models in assisting *in vivo* experiments by providing information to plane and optimize magnetic hyperthermia preclinical tests on animals, especially to prevent the occurrence of excessive temperature increase in healthy tissues, in compliance with the Directive 2010/63/EU on the protection of animals used for scientific purposes. Moreover, *in silico* models have demonstrated their suitability to predict the thermal response in biological tissues of different types of MNPs, as a function of their dose, spatial distribution and AC magnetic field parameters, thus providing important indications for successful treatments. Finally, the numerical simulations have shown the possibility to study the magnetically driven transport of MNPs and magnetic beads in blood vessels, in order to optimize the magnetic source configuration and the particle release to target tissues for drug delivery or further treatment, like magnetic hyperthermia.

Appendix A

A.1 Elements of functional analysis

In this Appendix we describe some basic concepts of the theory of distributions, and of Sobolev spaces.

A.1.1 L^p spaces and Hilbert spaces

Let $L^1(\Omega)$ denote the space of integrable functions from the set Ω to $\mathbb{R}$.

Definition (A.1). Let $p \in \mathbb{R}$, $1<p<\infty$, we define

$$L^p(\Omega)=\left\{f:\Omega\rightarrow\mathbb{R};f \text{ is measurable and } |f|^p\in L^1(\Omega)\right\}$$

with the norm

$$\|f\|_{L^p}=\|f\|_p=\left[\int_\Omega |f(x)|^p d\mu\right]^{1/p}.$$

Definition (A.2). Let u and v denote any elements of the space H. A Hilbert space is a vector space H equipped with a scalar product (u,v) such that H is complete for the norm $\|u\|=(u,u)^{1/2}$.

Observation. The space $L^2(\Omega)$ with the following scalar product

$$(u,v)=\int_{\Omega} u(x)v(x)\,d\mu$$

is a Hilbert space.

A.1.2 Distributions

Definition (A.3). Let f be a function, $f: \Omega \to \mathbb{R}$, with Ω an open set of $\mathbb{R}^n$. The support of f is the closure of the set where the function takes values different from zero, i.e.

$$\text{supp} f = \left\{\overline{\mathbf{x} : f(\mathbf{x}) \neq 0}\right\}.$$

Moreover, if there exists a compact set $J \subset \Omega$ such that the support of f is included in J, we say that f has a compact support in Ω.

Let $\mathfrak{D}(\Omega)$ denote the space of infinitely differentiable functions with compact support in Ω, i.e.

$$\mathfrak{D}(\Omega) = \left\{ f \in C^\infty(\Omega) : \exists K \subset \Omega, \text{ compact: supp} f \subset K \right\}.$$

Let now $\alpha = (\alpha_1, ..., \alpha_n)$ be an n-tuple of non-negative integers and let f a function defined from $\Omega \subset \mathbb{R}^n$ to $\mathbb{R}$, we can now introduce the multi-index notation for the derivatives

$$D^\alpha f(\mathbf{x}) = \frac{\partial^{|\alpha|} f(\mathbf{x})}{\partial x_1^{\alpha_1} \partial x_2^{\alpha_2} ... \partial x_n^{\alpha_n}}$$

where the sum $|\alpha| = \alpha_1 + ... + \alpha_n$ coincides with the differentiation order of f.

In the space $\mathfrak{D}(\Omega)$ the notation of convergence of functions is described by the following definition.

Definition (A.4). Let us consider a sequence of functions $\{\varphi_j, \varphi_j \in \mathfrak{D}(\Omega)\}$. The functions converge in $\mathfrak{D}(\Omega)$ to a function φ, and we denote it by $\varphi_j \xrightarrow[\mathfrak{D}(\Omega)]{} \varphi$, if:

1. we have that $D^{\alpha}\varphi_j \xrightarrow[\mathcal{D}(\Omega)]{} D^{\alpha}\varphi$, $\forall\alpha \in \mathbb{N}^n$;
2. for all the functions φ_j and for a fixed compact set J, we have supp $\varphi_j \subset J$.

Definition (A.5). Let T be a linear transformation, $T : \mathcal{D}(\Omega) \rightarrow \mathbb{R}$, and let us denote by $< T,\varphi >$ the value taken by T on $\varphi \in \mathcal{D}(\Omega)$. Then, T is continuous if $\lim_{k\to\infty}\langle T,\varphi_k\rangle = \langle T,\varphi\rangle$, where $\{\varphi_k\}_{k=1}^{\infty}$ is a sequence, arbitrary chosen, of $\mathcal{D}(\Omega)$ that converges to $\varphi \in \mathcal{D}(\Omega)$. We define a distribution on Ω any continuous and linear transformation $T : \mathcal{D}(\Omega) \rightarrow \mathbb{R}$, where the dual space $\mathcal{D}'(\Omega)$ of $\mathcal{D}(\Omega)$ is called the space of distributions on Ω.

Observation. The norm in $L^2(\Omega)$ is defined by:

$$\|g\|_{L^2(\Omega)} = \sqrt{(f,f)_{L^2(\Omega)}}\,.$$

To each function $g \in L^2(\Omega)$, we can associate a distribution $T_g \in D'(\Omega)$ defined by

$$\langle T_f,\phi\rangle = \int_{\Omega} f(\mathbf{x})\phi(\mathbf{x})d\Omega \qquad \forall\phi\in\mathcal{D}(\Omega).$$

And this leads to the Lemma for which the space $\mathcal{D}(\Omega)$ is dense in $L^2(\Omega)$.

A.1.2 Differentiation in the sense of distributions

The differentiation of distribution is an extension and generalization of the classical differentiation of smooth functions. In particular, the distributions permit obtaining the derivative of functions that does not exist in the classical sense of differentiation.

Let us consider the set $\Omega \subset \mathbb{R}^n$ and the transformation $T \in \mathcal{D}'(\Omega)$.

Definition (A.6). The derivatives of T in the sense of distributions, $\partial T/\partial x_i$, are the distributions defined as follows

$$\left\langle \frac{\partial T}{\partial x_i},\phi \right\rangle = -\left\langle T,\frac{\partial \phi}{\partial x_i} \right\rangle \qquad \forall\phi\in\mathcal{D}(\Omega), \qquad i = 1,\ldots,\mathrm{n}\,.$$

Moreover, we can define the derivatives of any arbitrary order for each multi-index $\alpha = (\alpha_1,...,\alpha_n)$, in the following way

$$\langle D^\alpha T, \phi \rangle = (-1)^{|\alpha|} \langle T, D^\alpha \phi \rangle \qquad \forall \phi \in \mathcal{D}(\Omega)$$

with $D^\alpha T$ as a new distribution.

The derivatives in the sense of distributions have some properties that do not hold for the derivatives in the classical sense. In particular, two main properties are the following.

<u>Property</u> 1. The space of distributions on Ω, $\mathcal{D}'(\Omega)$, is a closed space with respect to the differentiation in the sense of distributions.

<u>Property</u> 2. In $\mathcal{D}'(\Omega)$, the differentiation is a continuous operation, i.e.

$$T_n \xrightarrow[\mathcal{D}'(\Omega)]{n\to\infty} T \ .$$

In addition, for each multi-index $\alpha = (\alpha_1,...,\alpha_n)$ it holds that

$$D^\alpha T_n \xrightarrow[\mathcal{D}'(\Omega)]{n\to\infty} D^\alpha T \ .$$

A.1.3 Sobolev space

Sobolev spaces are particular spaces equipped with a norm that is a combination of L^p norms, and the functions belonging to them possess sufficiently many derivatives for some application domains, which make them key tools in pure and applied mathematics (e.g. in partial differential equations and differential geometry).

<u>Definition</u> (A.7). Consider $\Omega \subset \mathbb{R}^n$ an open set and q a positive integer. A Sobolev space of order q on Ω is the space composed of the totality of functions belonging to $L^2(\Omega)$ whose derivatives, in sense of distributions, up to order q belong to $L^2(\Omega)$, i.e.

$$\mathrm{H}^q(\Omega) = \{ g \in L^2(\Omega) : D^\alpha f \in L^2(\Omega) \qquad \forall \alpha : |\alpha| \le q \} \ .$$

It follows that $H^{q+1}(\Omega) \subset H^q(\Omega)$ for each $q \geq 0$ and this inclusion is continuous.

The Sobolev spaces $H^q(\Omega)$ are Hilbert spaces with respect to the scalar product

$$(g, f)_q = \sum_{|\alpha| \leq q} \int_\Omega \left(D^\alpha g\right)\left(D^\alpha f\right) d\Omega \ ,$$

from which we have the following norm

$$\|g\|_{H^q(\Omega)} = \sqrt{(g, g)_q} = \sqrt{\sum_{|\alpha| \leq q} \int_\Omega \left(D^\alpha g\right)^2 d\Omega}$$

and seminorm

$$|g|_{H^q(\Omega)} = \sqrt{(g, g)_q} = \sqrt{\sum_{|\alpha| = q} \int_\Omega \left(D^\alpha g\right)^2 d\Omega} \, .$$

Observation: The space $L^2(\Omega)$ is usually denoted by $H^0(\Omega)$.

A.1.3 The space $H^1_0(\Omega)$

In $\mathbb{R}^1$ the functions of $H^1(\Omega)$ are continuous, whereas in two or three spatial dimensions the functions of the Sobolev space are not necessarily continuous. On the contrary, the functions of $H^1(\Omega)$ are continuous in $\mathbb{R}^n$ for n =1, 2, and 3. Moreover, if we consider the set Ω as bounded, then the space is not dense in $H^1(\Omega)$. Thus, the following space is introduced.

Definition (A.8). The space $H^1_0(\Omega)$ is the closure of $\mathfrak{D}(\Omega)$ in $H^1(\Omega)$.

The main properties of this space are the following.

Property 3. (Poincaré inequality). Consider $\Omega \subset \mathbb{R}^n$ a bounded set, then

$$\exists c \text{ s. t. } \|v\|_{L^2(\Omega)} \leq c|v|_{H^1(\Omega)} \quad \forall v \in H^1_0(\Omega)$$

with c a constant.

Property 4. The seminorm $|v|_{H1(\Omega)}$ is a norm on the space $H_0^1(\Omega)$ that is equivalent to the norm $||v||_{H1(\Omega)}$.

Similarly, the space $H_0^q(\Omega)$ is defined as the closure of $\mathcal{D}(\Omega)$ in $H^q(\Omega)$.

A.2 Calculus theorems

A.2.1 Divergence theorem

Let consider the compact $\Omega \subset \mathbb{R}^3$ with boundary $\partial\Omega$. If F is a vector field once continuously differentiable on Ω, it holds that

$$\int_{\Omega} \nabla \cdot \mathbf{F} dV = \int_{\partial\Omega} \mathbf{F} \cdot \mathbf{n} dv \ .$$

If $\mathbf{F}$ = g$\mathbf{F}$ with g a scalar function on Ω, we obtain the following corollary

$$\int_{\Omega} \mathbf{F} \cdot (\nabla g) dV + \int_{\Omega} g (\nabla \cdot \mathbf{F}) dV = \int_{\partial\Omega} g (\mathbf{F} \cdot \mathbf{n}) dv .$$

A.2.2 Green identity

Let consider $\Omega \subset \mathbb{R}^3$ a region with boundary $\partial\Omega$, and two scalar functions φ and ψ, where φ is two times continuously differentiable on Ω and ψ is once continuously differentiable on Ω. Then,

$$\int_{\Omega} \psi \nabla^2 \varphi dV + \int_{\Omega} \nabla\psi \cdot \nabla\varphi dV = \int_{\partial\Omega} \psi (\nabla\varphi \cdot \mathbf{n}) dv .$$

is the Green's identity, which derived directly from the divergence theorem considering $\mathbf{F} = \psi\nabla\varphi$.

Appendix B

Local shape functions

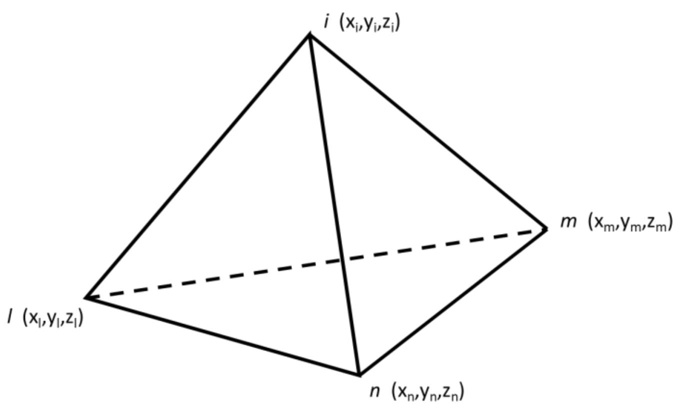

Figure B.1. Schematic of a tetrahedral element with vertices i,l,m and n.

In the 3D application of finite element methods, the domains are discretized into a mesh composed of tetrahedral elements. The functions of the basis for the functional space V_h are polynomial functions associated with the mesh and here, in all the FEM applications treated in this Thesis, the shape functions are assumed to be linear.

Let now consider the T-th tetrahedron of the mesh, which is composed by the vertices i, l, m and n, as illustrated in Figure B.1. The linear variation of ϕ_h in the tetrahedron can be expressed as a linear function of the Cartesian coordinates (x,y,z) by [1]

$$\phi_h^T(x,y,z) = \alpha_1 + \alpha_2 x + \alpha_3 y + \alpha_4 z \tag{B.1}$$

where α_1, α_2, α_3, and α_4 are unknown coefficients that depend on vertex coordinates.

Let now denote the nodal values of ϕ_h as $\hat{\phi}_i, \hat{\phi}_l, \hat{\phi}_m$ and $\hat{\phi}_n$ in the corresponding vertices, with the following nodal conditions

$$\begin{cases} \phi_h^T(x,y,z) = \hat{\phi}_i \text{ at } (x,y,z) = (x_i, y_i, z_i) \\ \phi_h^T(x,y,z) = \hat{\phi}_l \text{ at } (x,y,z) = (x_l, y_l, z_l) \\ \phi_h^T(x,y,z) = \hat{\phi}_m \text{ at } (x,y,z) = (x_m, y_m, z_m) \\ \phi_h^T(x,y,z) = \hat{\phi}_n \text{ at } (x,y,z) = (x_n, y_n, z_n) \end{cases} \tag{B.2}$$

that lead to the following system

$$\begin{cases} \hat{\phi}_i = \alpha_1 + \alpha_2 x_i + \alpha_3 y_i + \alpha_4 z_i \\ \hat{\phi}_l = \alpha_1 + \alpha_2 x_l + \alpha_3 y_l + \alpha_4 z_l \\ \hat{\phi}_m = \alpha_1 + \alpha_2 x_m + \alpha_3 y_m + \alpha_4 z_m \\ \hat{\phi}_n = \alpha_1 + \alpha_2 x_n + \alpha_3 y_n + \alpha_4 z_n \end{cases} \tag{B.3}$$

Solving the system of Eqs. (B.3), we then obtain an explicit expression for the coefficients α_1, α_2, α_3, and α_4 by the following equations

$$\alpha_1 = \frac{1}{6V_T}\left(a_i\hat{\phi}_i + a_l\hat{\phi}_l + a_m\hat{\phi}_m + a_n\hat{\phi}_n\right)$$

$$\alpha_2 = \frac{1}{6V_T}\left(b_i\hat{\phi}_i + b_l\hat{\phi}_l + b_m\hat{\phi}_m + b_n\hat{\phi}_n\right)$$

$$\alpha_3 = \frac{1}{6V_T}\left(c_i\hat{\phi}_i + c_l\hat{\phi}_l + c_m\hat{\phi}_m + c_n\hat{\phi}_n\right)$$

$$\alpha_4 = \frac{1}{6V_T}\left(d_i\hat{\phi}_i + d_l\hat{\phi}_l + d_m\hat{\phi}_m + d_n\hat{\phi}_n\right)$$

where V_T is the volume of the tetrahedron and is calculated as

$$V_T = \frac{1}{6}\begin{vmatrix} 1 & x_i & y_i & z_i \\ 1 & x_l & y_l & z_l \\ 1 & x_m & y_m & z_m \\ 1 & x_n & y_n & z_n \end{vmatrix}.$$

Moreover, we have

$$a_i = \begin{vmatrix} x_l & y_l & z_l \\ x_m & y_m & z_m \\ x_n & y_n & z_n \end{vmatrix}, \quad b_i = -\begin{vmatrix} 1 & y_l & z_l \\ 1 & y_m & z_m \\ 1 & y_n & z_n \end{vmatrix}, \quad c_i = -\begin{vmatrix} x_l & 1 & z_l \\ x_m & 1 & z_m \\ x_n & 1 & z_n \end{vmatrix}, \quad d_i = -\begin{vmatrix} x_l & y_l & 1 \\ x_m & y_m & 1 \\ x_n & y_n & 1 \end{vmatrix}$$

and the other constants can be obtained by cyclic interchange of the subscripts in the last expressions, i.e.

$$a_l = \begin{vmatrix} x_{\mathrm{n}} & y_n & z_n \\ x_m & y_m & z_m \\ x_i & y_i & z_i \end{vmatrix}, \quad b_l = -\begin{vmatrix} 1 & y_{\mathrm{n}} & z_{\mathrm{n}} \\ 1 & y_m & z_m \\ 1 & y_i & z_i \end{vmatrix}, \quad c_l = -\begin{vmatrix} x_n & 1 & z_n \\ x_m & 1 & z_m \\ x_i & 1 & z_i \end{vmatrix}, \quad d_l = -\begin{vmatrix} x_{\mathrm{n}} & y_{\mathrm{n}} & 1 \\ x_m & y_m & 1 \\ x_i & z_i & 1 \end{vmatrix},$$

$$a_m = \begin{vmatrix} x_n & y_n & z_n \\ x_l & y_l & z_l \\ x_i & y_i & z_i \end{vmatrix}, \quad b_m = -\begin{vmatrix} 1 & y_n & z_n \\ 1 & y_l & z_l \\ 1 & y_i & z_i \end{vmatrix}, \quad c_m = -\begin{vmatrix} x_n & 1 & z_n \\ x_l & 1 & z_l \\ x_i & 1 & z_i \end{vmatrix}, \quad d_m = -\begin{vmatrix} x_n & y_n & 1 \\ x_l & y_l & 1 \\ x_i & z_i & 1 \end{vmatrix},$$

$$a_n = \begin{vmatrix} x_m & y_m & z_m \\ x_l & y_l & z_l \\ x_i & y_i & z_i \end{vmatrix}, \quad b_n = -\begin{vmatrix} 1 & y_m & z_m \\ 1 & y_l & z_l \\ 1 & y_i & z_i \end{vmatrix}, \quad c_n = -\begin{vmatrix} x_m & 1 & z_m \\ x_l & 1 & z_l \\ x_i & 1 & z_i \end{vmatrix}, \quad d_n = -\begin{vmatrix} x_m & y_m & 1 \\ x_l & y_l & 1 \\ x_i & z_i & 1 \end{vmatrix}.$$

Substituting the terms above in (B.1), we find

$$\phi_h^T(x,y,z) = \varphi_i(x,y,z)\hat{\phi}_i + \varphi_l(x,y,z)\hat{\phi}_l + \varphi_m(x,y,z)\hat{\phi}_m + \varphi_n(x,y,z)\hat{\phi}_n$$

where φ_i, φ_l, φ_m and φ_n are the linear shape functions defined on the tetrahedron of vertices *i*, *l*, *m* and *n* by

$$\varphi_i = \frac{1}{6V_T}\left(a_i + b_i x + c_i y + d_i z\right)$$

$$\varphi_l = \frac{1}{6V_T}\left(a_l + b_l x + c_l y + d_l z\right)$$

$$\varphi_m = \frac{1}{6V_T}\left(a_m + b_m x + c_m y + d_m z\right)$$

$$\varphi_n = \frac{1}{6V_T}\left(a_n + b_n x + c_n y + d_n z\right)$$

Therefore, each shape function is associated to one of the mesh nodes and their relationship is expressed by the fact that the value of φ_i is 1 at node *i* and zero elsewhere. Likewise, φ_l, φ_m and φ_n are 1 only at nodes *l*, *m* and *n* respectively.

References

[1] S. S. Rao, The finite element method in engineering: Third edition, 3rd ed. Woburn, MA: Butterworth-Heinemann, 2015.

Appendix C

Micromagnetic model

The hysteresis loops of the MNPs were evaluated by means of in-house micromagnetic codes, which solve the Landau-Lifshitz-Gilbert (LLG) equation, namely:

$$\frac{\partial \mathbf{M}}{\partial t} = -\frac{\gamma}{1+\alpha^2}\mathbf{M}\times\left[\mathbf{H}_{\text{eff}} + \frac{\alpha}{M_s}\left(\mathbf{M}\times\mathbf{H}_{\text{eff}}\right)\right] \tag{C.1}$$

where **M** is the vector of magnetization, whose amplitude is constant and equal to the saturation magnetization M_s, $\gamma = 2.21 \cdot 10^5$ m/(A·s) is the absolute value of the gyromagnetic ratio, and α is the damping coefficient. $\mathbf{H}_{\text{eff}}$ is the effective field and is defined by the sum of the exchange field $\mathbf{H}_{\text{ex}}$, the magnetostatic field $\mathbf{H}_{\text{m}}$, the applied field $\mathbf{H}_{\text{a}}$, the magnetocrystalline anisotropy field $\mathbf{H}_{\text{an}}$, and the thermal field $\mathbf{H}_{\text{th}}$.

Specifically, the magnetostatic field is described by

$$\mathbf{H}_{\text{m}} = -\frac{1}{4\pi}\nabla\int_{\Omega}\nabla'\left(\frac{1}{|\mathbf{r}-\mathbf{r}'|}\right)\cdot\mathbf{M}(\mathbf{r}')\,d^3\mathbf{r}' \tag{C.2}$$

where **r** is the position of the point calculation and **r'** is the variable of integration.

The exchange field is defined by

$$\mathbf{H}_{\text{ex}} = \frac{2k_{\text{ex}}}{\mu_0 M_{\text{s}}^2} \nabla^2 \mathbf{M} \tag{C.3}$$

where k_{ex} is the exchange constant and μ_0 is the magnetic permeability of vacuum.

Regarding the magnetocrystalline anisotropy field, for the case of uniaxial anisotropy along a direction identified with the unity vector **u**, it is defined by

$$\mathbf{H}_{\text{an}} = -\frac{1}{\mu_0} \frac{\partial f_{\text{an}}(\mathbf{M})}{\partial \mathbf{M}} \tag{C.4}$$

where f_{an} is the free energy density, which is expressed by

$$f_{\text{an}}(\mathbf{M}) = \frac{2k\left[1-(\mathbf{M}\cdot\mathbf{u})^2\right]}{2M_s^2} = \frac{2k\left[1-\left(M_x u_x + M_y u_y + M_z u_z\right)^2\right]}{2M_s^2}$$

with k (J/m^3) the anisotropy constant. Considering that the derivative with respect to the x-component of **M** is expressed by

$$\frac{\partial f_{\text{an}}(\mathbf{M})}{\partial M_x} = -\frac{2k}{M_S^2}\left(M_x u_x + M_y u_y + M_z u_z\right) u_x = -\frac{2k}{M_S^2}(\mathbf{M}\cdot\mathbf{u}) u_x,$$

then, we have that the components of $\mathbf{H}_{\text{an}}$ are defined by

$$\begin{cases} H_{\text{an}_x} = \dfrac{2k}{\mu_0 M_S^2}(\mathbf{M}\cdot\mathbf{u}) u_x \\ H_{\text{an}_y} = \dfrac{2k}{\mu_0 M_S^2}(\mathbf{M}\cdot\mathbf{u}) u_y \\ H_{\text{an}_z} = \dfrac{2k}{\mu_0 M_S^2}(\mathbf{M}\cdot\mathbf{u}) u_z \end{cases}$$

Whereas, for the case of cubic anisotropy with the crystal axes that coincide with the coordinate ones, the magnetocrystalline anisotropy field is described by

$$\mathbf{H}_{\text{an}} = -\frac{2\text{K}}{\mu_0 M_{\text{s}}} \mathbf{m} \tag{C.5}$$

with **m** is the normalized magnetization vector and K is a matrix expressed as

$$\mathrm{K} = \begin{bmatrix} K_1\left(m_y^2+m_z^2\right)+K_2 m_y^2 m_z^2 & 0 & 0 \\ 0 & K_1\left(m_x^2+m_z^2\right)+K_2 m_x^2 m_z^2 & 0 \\ 0 & 0 & K_1\left(m_x^2+m_y^2\right)+K_2 m_x^2 m_y^2 \end{bmatrix}$$

with K_1 the first and K_2 the second order cubic anisotropy constants, respectively.

If included, the contribution from $\mathbf{H}_{\mathrm{th}}$ is evaluated by the following Langevin approach and the fluctuation-dissipation theorem, resulting in:

$$\mathbf{H}_{\mathrm{th}} = \boldsymbol{\eta}\left(\mathbf{r},t\right)\sqrt{\frac{2\alpha k_{\mathrm{B}} T}{\gamma \mu_0 M_{\mathrm{s}} \Delta s^3 \Delta t}} \tag{C.6}$$

where k_{B} is the Boltzmann constant, T is the absolute temperature, $\boldsymbol{\eta}$ is the stochastic vector whose components are Gaussian random numbers with zero mean value and dispersion 1 and uncorrelated in time and space, Δs is the average size of the grid for the spatial discretization, and Δt is the time-step.